UNIVERSITY OF SOUTHAMPTON

FACULTY OF PHYSICAL SCIENCES AND ENGINEERING

Optoelectronics Research Centre

Control and localisation of light with engineered nano-structures

Tapashree Roy

Thesis for the degree of Doctor of Philosophy

May 2014

UNIVERSITY OF SOUTHAMPTON

ABSTRACT

FACULTY OF PHYSICAL SCIENCES AND ENGINEERING

Optoelectronics Research Centre

Doctor of Philosophy

CONTROL AND LOCALISATION OF LIGHT WITH ENGINEERED NANO-STRUCTURES

by Tapashree Roy

In this thesis I present my research on nano-scale light control using several novel approaches.

I have demonstrated a planar metal nano-structure with cylindrical symmetry that is designed to create a super-oscillation of electromagnetic waves to focus light down to sizes smaller than the Abbe diffraction limit. For the first time this super-oscillatory lens was experimentally used for imaging of nano-structures. A pair of 0.3λ diameter nano-holes with 0.16λ edge-to-edge separation were resolved.

I have demonstrated a novel type of super-oscillatory lens which produces a continuous distribution of sub-wavelength light localisations extending over several wavelengths along the optical axis. This *'optical needle'* is also characterised by a large field of view. I have experimentally demonstrated a optical-needle-lens with 7 μm depth of focus and 16% narrower than a diffraction-limited focal spot.

I have characterised the point spread function of the above-mentioned super-oscillatory lenses, i.e., their ability to accurately image a point source. The images of the point source generated by these super-oscillatory lenses are at least 24% smaller than that produced by an ideal glass lens restrained by the Abbe diffraction limit. I have experimentally verified the imaging characteristics of the optical-needle-lens and demonstrated its ability to detect the off-axis placement of a point-like source.

I have developed the nano-fabrication processes for manufacturing the super-oscillatory lenses on thin films of metals (Au, Al, Ti) using gallium focused-ion-beam milling technology. The focusing characteristics of the fabricated structures showed very good agreement with computational predictions.

I have computationally shown that objects placed within the field of viewfocfocus of the optical-needle-lens can be imaged with super-resolution quality. This is a significant improvement over the sub-wavelength-step scanning imaging technique reported in this thesis for the other kind of super-oscillatory lens. For example, a super-oscillatory lens can resolve a *'random'* cluster of 0.15λ diameter nano-holes with the smallest edge-to-edge separation of 0.28λ.

I have experimentally demonstrated the first *prototype* of a solid-immersion super-oscillatory lens that promises to achieve a 50 nm hotspot with 405 nm illumination for applications in heat-assisted magnetic recording technology.

I have demonstrated for the first time a planar diffraction grating for *visible light* designed by arranging meta-molecules to produce a periodic phase ramp. I have also demonstrated the first ever metamaterial-based planar lens-array that produced a 2D array of sub-wavelength foci.

Finally, I have provided the first experimental evidence that photoluminescence of gold can be substantially enhanced by patterning the film with designed 2D nano-structured array (or, metamaterials). When *resonant two-photon excitation* is used the metamaterial enhances the photoluminescence by more than 76 times. I have also observed that the photoluminescence emission peaks are linked to the frequencies of absorption resonances in the metamaterials.

Contents

List of Figures

DECLARATION OF AUTHORSHIP

I, Tapashree Roy, declare that the thesis entitled "Control and localisation of light with engineered nano-structures" and the work presented in the thesis are both my own, and have been generated by me as the result of my own original research. I confirm that:

- this work was done wholly or mainly while in candidature for a research degree at this University;
- where any part of this thesis has previously been submitted for a degree or any other qualification at this University or any other institution, this has been clearly stated;
- where I have consulted the published work of others, this is always clearly attributed;
- where I have quoted from the work of others, the source is always given. With the exception of such quotations, this thesis is entirely my own work;
- I have acknowledged all main sources of help;
- where the thesis is based on work done by myself jointly with others, I have made clear exactly what was done by others and what I have contributed myself;
- parts of this work have been published as the journal papers and conference contributions listed in Appendix C.

Signed: _____

Date: _____

Acknowledgements

I would like to thank my supervisor Prof Nikolay Zheludev for giving me this opportunity to experience the best phase of my student life. I thank Prof. Zheludev for his most-able guidance at the crucial stages of my PhD, for his patience when I have been wrong, for sharing his knowledge and experience with his students.

I must thank Dr. Edward Rogers, my co-supervisor for guiding me through thick and thin. I thank Dr. Rogers for his help with my research and the numerous discussion sessions with him.

I thank both of my supervisors for my transformation from a student who was afraid to handle even a simple microscope, to a more confident researcher.

I extend my gratitude to my internal examiner Dr. Bill Brocklesby for his critical review of the intermediate stages of my PhD studies.

I consider myself lucky to be a part of this very dynamic and large research group. I would like to thank all my colleagues and friends for readily extending their help. I want to mention Dr. Nikitas Papasimakis and Dr. Jianfa Zhang for introducing me to the Comsol simulations and Mr. Bruce Ou for his never-ending help with FIB fabrication.

ORC is a wonderful place with its vast resources and infrastructures, but mostly because it is made up of very helpful and friendly people. I like to thank our cleanroom managers Neil Sessions and Dave Sager, our mechanical workshop managers Paul Allwood, Mark Lessey, and Ed Weatherby, and Christopher Craig for all their help, and make my research smooth and safe.

I thank the collaborators of the Nanoscope project, especially Dr. Yuan Guanghui for his help and support.

I thank my *partner for life* for keeping me motivated through all these years. This would not have been possible without your undivided support and love.

Finally, we have a saying in our culture that one cannot thank one's parents enough. All I want to say to my parents: *I feel blessed to be your daughter.*

1 Introduction

1.1 Motivation

Controlling light at the nano-scale is the indispensable *mantra* for the fast-evolving photonics industry.

We collect a significant amount of information about the objects around us by looking at them and the simplest devices used for the purpose are the lenses. The earliest known lenses date back to the 14^{th} century AD and ever since we have tried to better their performance to improve imaging. Since the days of Antonie van Leeuwenhoek and Robert Hooke, microscopes have come a long way. In fact, in the last century alone, four Nobel Prizes have been awarded for the development of imaging technologies [1]. Improved imaging technologies have driven discoveries and advancement across all branches of science and engineering and for majority of these applications, optical microscopes are the elegant choice of instrument. But even a modern day high resolution optical microscope is limited by the diffraction limit and cannot image features smaller than the scale of a wavelength of light. There are several existing techniques for super-resolution imaging and each of them have their own pros and cons [2–4]. Lenses designed on the basis of super-oscillation phenomena promises focal spots arbitrarily smaller than the diffraction limit at distances beyond the near-field of the lens.

A little over half a century ago Richard Feynman, in his celebrated lecture [5], invited scientists to embark on a new journey of nanotechnology. Feynman envisioned some interesting ramifications of manipulating matter at the atomic scale. Today,

exploiting the capabilities of modern nano-fabrication technologies it is possible to shape and size matter within the scale of a few atoms. This opens up the opportunity for studying the light-matter interaction at the nanoscale. Enthusiasm in this field of research was boosted with the advent of *metamaterials* just over a decade ago. Metamaterials are a special class of man-made media patterned on a sub-wavelength scale allowing precise control of electromagnetic waves to provide all sorts of exotic and useful functionalities [6]. Using *photonic metamaterials* active research is being carried on to achieve nano-scale control and localisation of light.

The following sections introduce some of the concepts and definitions that will be used in this thesis. The current state-of-the-art research based on those concepts is also briefly discussed.

1.2 Diffraction limit and optical microscopy

Diffraction is the phenomena where light spreads past an obstacle or through an aperture, instead of casting a sharp-edged shadow of the object. As well as for electromagnetic waves, diffraction happens for all kinds of waves including sound, and water waves. It is this phenomenon that causes the focal spot, even from an ideal glass lens, to appear bigger than a geometrical point.

In 1874 Ernst Abbe proposed a formula which would estimate the smallest spot size that can be produced by an ideal lens in a given medium. The focal spot size d is related to the wavelength λ and numerical aperture NA of the lens by the formula $d = 0.61\lambda/\text{NA}$[1] [7]. This fundamental limit is called the diffraction limit, and it limits the resolution of images from optical systems like microscopes, cameras or telescopes. Due to the presence of the diffraction limit, no image is as detailed as the object. A conventional lens successfully transmits the propagating components of the electromagnetic field to the image plane; however, the evanescent wave which carries the information about the finest features of the object exponentially decays from its plane of origin. The sub-wavelength details about the object are lost before forming

[1]The NA defines the maximum range of angle over which a lens can accept light (Fig. 1.1a) and is given by $\text{NA} = n\sin\theta_{\max}$; n is the refractive index of the medium, $\theta_{\max}$ is the half angle of the maximum cone of light that can enter or exit the lens. For an ideal lens operating in air ($n = 1$), the NA is less than 1.

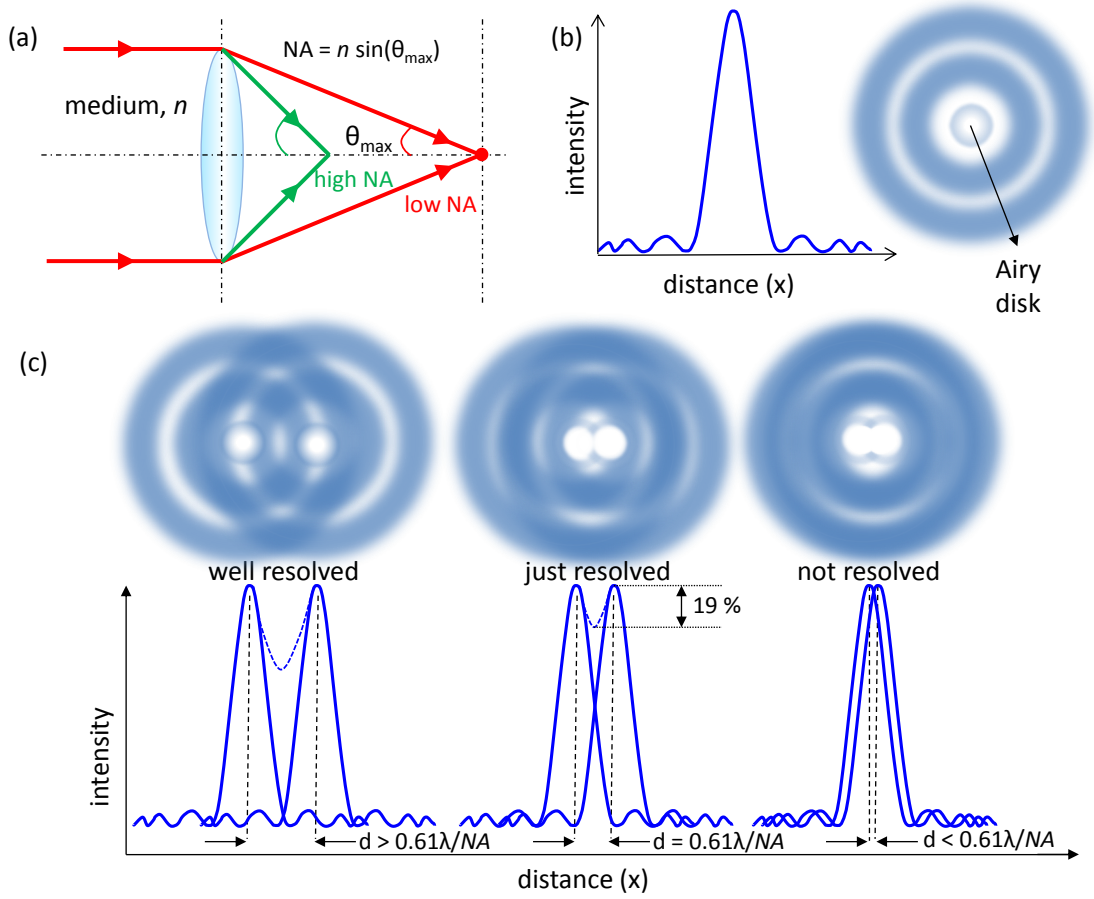

Figure 1.1: Image formation by a convex lens and resolution.(a) Numerical aperture NA = $n\sin\theta$ of a lens. The refractive index of the medium in which the lens works is n, $\theta_{\max}$ is the largest half-angle within which all diverging light rays from a point source are collected by the lens. (b) Airy pattern produced by light diffracted through a circular aperture and captured by a lens. (c) Rayleigh resolution criteria: Airy disk representing well-focused intensity profiles from two point sources. Three different cases, well resolved, just resolved, and unresolved are shown.

the image, making it look blurred compared to the object.

Figure 1.1b shows the image of an circular aperture as captured by an ordinary lens. Due to diffraction, the image is not just a circular disk, but formed from a bright central spot called the Airy disk and surrounded by less bright annular rings forming the Airy pattern. There are several resolution criteria defined for any imaging system to give an estimate of how close two point sources can be placed until they can be no more imaged as two separate sources. The most commonly used is the Rayleigh criterion [8] of resolution. According to the Rayleigh criterion two incoherent point sources of equal intensity are regarded as just resolved when the intensity peak of the Airy disk of one source, coincides with the first minimum of the second source. This distance is given

by a measure in terms of the wavelength and numerical aperture by $d = 0.61\lambda/\mathrm{NA}$, which is also the size of the focal spot as given by Abbe. At Rayleigh resolution limit the sum of intensities from two closely spaced apertures has two peaks with a central dip or saddle point which is $8/\pi^2$ times the peak intensity, i.e. 81% of the individual peak values (Fig. 1.1) [8]. There are other resolution criteria; the Sparrow criterion is the next best known, and gives a limit which allows two points to be placed closer than that given by Rayleigh, yet still call them resolved. At Sparrow resolution limit the saddle region vanishes and becomes a flat line joining the two peaks. In other words, at the Sparrow resolution limit the derivative of the intensity is zero between the two peak positions [8]. Sparrow's criterion is considered to be a more practical estimate of resolution, since human eyes are known to be sensitive to lesser intensity difference than that given by the Rayleigh's criterion. Sparrow's criterion has proved to be more useful while studying realistic situations, for example, resolving two distant stars [8].

There has been considerable research on improving the image quality to achieve higher and higher resolution. Besides improving the quality of the lenses, one of the simplest methods is to increase the refractive index of the surrounding medium. Since the NA and hence the focal spot size depends on the refractive index of the medium, using a high-index immersion medium will lead to increase in resolution. Features that are smaller than the diffraction limit in free space can be measured using an immersion lens. This technique is however limited by the availability of high refractive index materials.

Super-resolution imaging techniques

The resolution of the conventional wide-field microscope is limited to about 200 nm due to diffraction of light. However, present day science and technology demands the study, characterisation, and fabrication of structures as small as a few nanometres. In the following sections several microscopy techniques that provide resolution surpassing the fundamental limit of diffraction will be briefly discussed.

1.2.1 Scanning near-field optical microscope (SNOM)

The scanning near field optical microscope (SNOM/NSOM) is a microscopy technique that captures the finest information from the object field by scanning a sub-wavelength

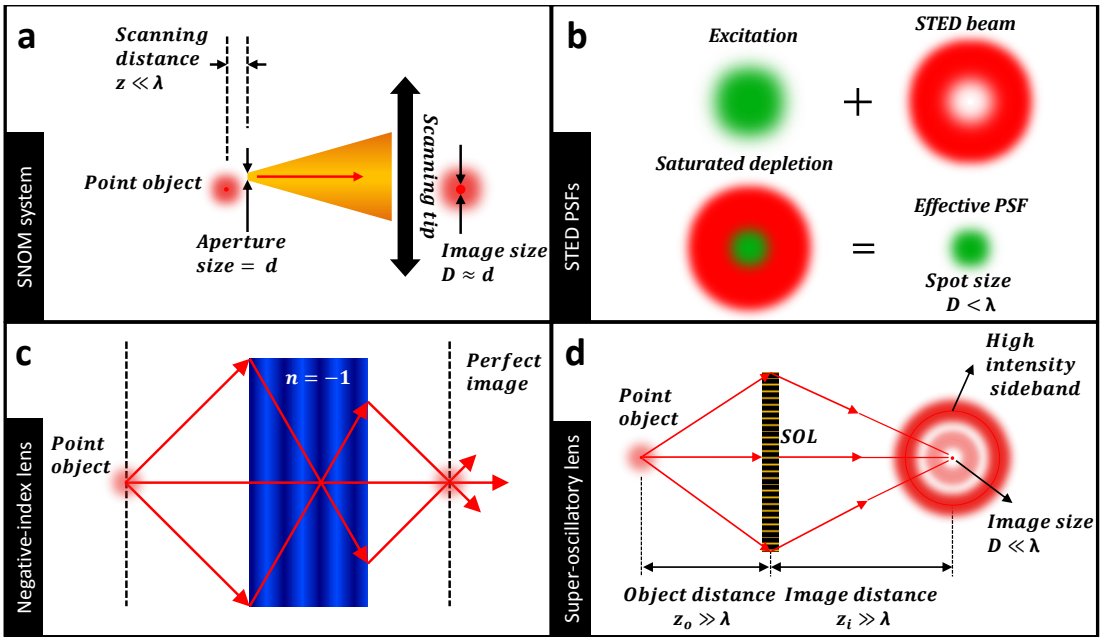

Figure 1.2: Different super-resolution techniques. (a) SNOM. A scanning tip collects both propagating and evanescent components from the object plane. The resolution is determined by the size of the aperture on the tip. (b) STED. A fluorescent imaging technique where the fluorescence from the peripheral region is depleted using a doughnut-shaped beam, resulting in a smaller than diffraction-limit point spread function. (c) A negative index superlens. The lens amplifies the exponentially decaying evanescent component so that at the image plane both propagating and evanescent components are detected. (d) A super-oscillatory lens. The focal spot is smaller than the diffraction limit, but is often surrounded by high intensity halo.

aperture in close proximity ($\ll \lambda$) to the sample (Fig. 1.2a). Resolution is limited by the diameter of the aperture. A major limitation is that the throughput of light is reduced for very narrow SNOM tip apertures.

In 1928 Synge [9] described an experimental set-up where a thin section from a biological sample was illuminated with a point source obtained by making an aperture $\sim$ 100 nm on a metal screen. He proposed that the aperture must be placed from the sample surface at a distance no greater than its diameter. The transmitted light was to be detected point by point with a sensitive photo-detector. Synge's scheme was never practically realised due to unavailability of proper technology to scan the aperture within a wavelength distance of the sample surface. In 1984 Synge's forgotten scheme was re-invented by Pohl and demonstrated with Denk and Duerig at the IBM Ruschlikon Research Laboratory [10–12]. Independently, a similar scheme was proposed and developed by Lewis *et al.*. at Cornell University [13–15]. The breakthrough was

fabricating a sharply pointed transparent tip with metal coating on the outside walls and a sub-wavelength aperture at the tip. The constant scanning height of only a few nanometres from the object was also ensured by using a feedback signal as will be discussed in the following text.

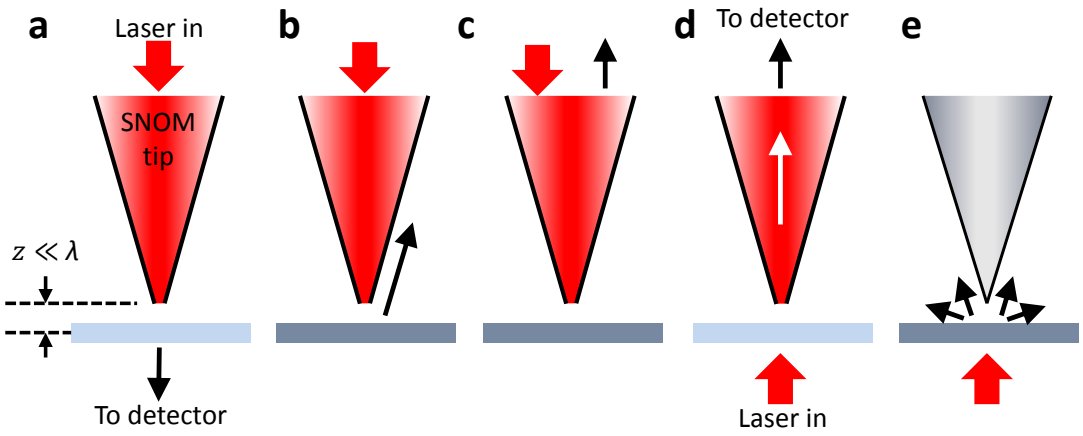

Figure 1.3: Modes of SNOM operation. (a) Illumination by the tip, collection by an external detector. (b) Illumination through the tip and collection of the scattered signal by the tip. (c) Illumination and collection of the reflected signal through the tip. (d) Illumination from an external source and collection by the tip. (e) Illumination from an external source and collection by an aperture-less SNOM.

SNOM works primarily under three modes of operation: (i) illumination mode, where a sub-wavelength point source produced by the SNOM tip illuminates the sample surface and the transmitted (Fig. 1.3a) or the scattered (Fig. 1.3b) signal is collected by an external detector like a microscope objective, or the reflected (Figs. 1.3c) signal is collected by the SNOM tip itself, (ii) collection mode, where the reflected (Figs. 1.3c) or the transmitted (Figs. 1.3d) signal is collected by the SNOM tip and (iii) aperture-less mode, where the sharp contour of an aperture-less metal tip is used as a small scatterer for the light transmitted or reflected from the sample (Figs. 1.3e). The scattered signal is then collected by a large external detector. The illumination and collection modes of SNOM operation use a sub-wavelength aperture, typically 20 nm to 100 nm, at the tip of a metal-coated tapered optical fibre.

A feedback signal unrelated to the SNOM signal is used to maintain a constant distance of a few nanometres between the sample and the probe [16]. There are two feedback mechanisms mostly used: (i) Shear force feedback where the tips are mounted on a tuning fork or a bimorph which oscillates with a resonant frequency, and its

amplitude is related to the distance from the sample. (ii) Constant force feedback where a constant force is maintained between the tip and the sample using static tip deflection as the feedback signal. This feedback mechanism is similar to the one used for atomic force microscopy (AFM).

The SNOM probe is raster scanned across the sample to collect information from all over the surface. The resolution is decided by the aperture size and not the wavelength of illumination. Resolution of $\lambda/20$ was reported by Pohl in 1984 [17]. Subsequently, a resolution of 12 nm ($\lambda/43$) was reported in 1991 [18]. Using aperture-less SNOM resolution less than 10 nm has also been reported in more recent papers [19–21].

Today SNOM represents a powerful tool for optically studying the surface properties and finds application across branches of physics, chemistry, and biology. However, SNOM suffers from some drawbacks as listed here.

- It is time-consuming due to the scanning process.
- The sample, specially soft ones often gets damaged due to proximity to the probe.
- The SNOM tips are very prone to mechanical damage.
- The wide-field image of the sample is not obtained like with an ordinary glass lens.
- The technique fails where information beyond the surface of the sample is required.

1.2.2 Fluorescence super-resolution techniques

Imaging techniques providing super-resolution with the aid of fluorescence signal from the sample are popular choices for imaging biological samples. Three commonly known fluorescence microscopy techniques, stimulated emission depletion microscopy (STED), stochastic optical reconstruction microscopy (STORM), and structured illumination microscopy (SIM) will be discussed here.

Stimulated emission depletion microscopy [2] (STED) uses fluorescent dyes to mark biological samples with fine features. Unlike SNOM, the fluorescent dye embedded into the sample can give information beyond the surface. A laser beam focused to a small spot is used to excite a specific fluorescent dye. Depending on the spot size of the laser, the dye around that region fluoresces. Next, a second laser beam at the

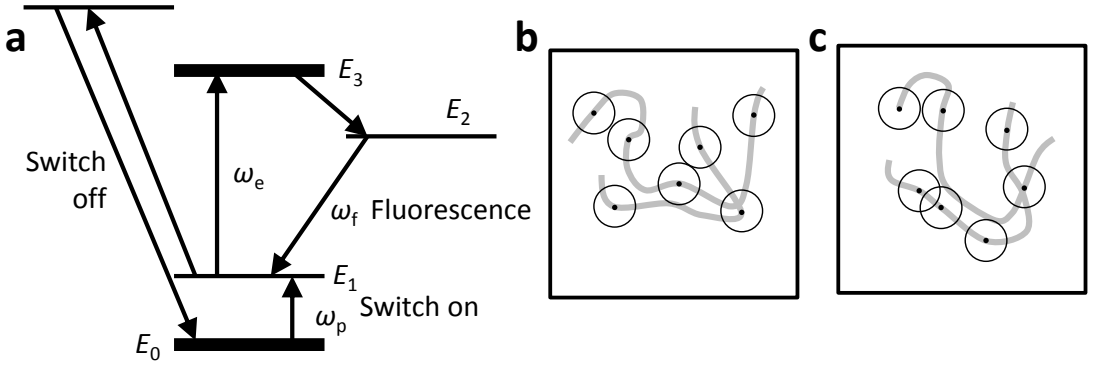

Figure 1.4: Stochastic optical reconstruction microscopy, STORM (a) Energy level diagram showing switchable fluorescence. (b) and (c) Stochasically excited fluorescent tags. The circles show the point spread function with centre of gravity shown as dots. (c) An example of overlapping point spread functions that are eliminated in data-processing. Figure after [7].

emission wavelength and with a doughnut-shaped wavefront is incident. By stimulated emission the atoms in the doughnut region are de-excited, leaving the atoms in the central position to be detected by their fluorescence only (Fig. 1.2b). With an increase in the intensity, the doughnut width increases resulting in a smaller central portion. By adjusting the intensity of the doughnut-beam the central portion, within which the fluorescent molecules emit spontaneously, can be made smaller than the diffraction limit. The limitation to the size of the central portion is imposed by damage threshold of the sample under investigation.

Another microscopy technique is stochastic optical reconstruction microscopy [7,22] (STORM). Using photo-switchable fluorescent probes this imaging technique temporally separate the otherwise spatially overlapping images of individual molecules allowing the precise localization of individual fluorescent labels on the sample. This idea can be used for imaging a dense objects, using several batches of sparse sampling points separated by distances greater than a few wavelengths. For imaging a wide region, weak pump is incident on the florescent sample which switches on a series of sparse random fluorescent tags to a metastable state (Fig. 1.4a). The fluorescence from each of these tags is then observed using P excitation pulses and the same number of (P) fluorescent images are recorded (Fig. 1.4b). This process is repeated for a new set of sparse random tags (Fig. 1.4c). Each series of P images is processed to determine the position of the individual tags with accuracy ($d = 0.5\lambda/\mathrm{NA}\sqrt{N}$). It makes use of the fact that for N number of photons emitted from a point source, the position of the

image can be determined with an accuracy $\sqrt{N}$ times better than diffraction limit. The resolution is decided by the value of N but is limited by the size of the fluorescent tag itself. Any discrepancy where two fluorescent tags are overlapping (Fig. 1.4c) are eliminated. STORM consists of many cycles of imaging processes during which fluorophores are activated, imaged, and deactivated. Hence, it is not a very fast imaging technique. Other similar imaging techniques which come under the broad class of stochastical super resolution are direct stochastic optical reconstruction microscopy d-STORM, photo-activated localization microscopy PALM, spectral precision distance microscopy SPDM.

Structured illumination microscopy (SIM) is a wide-field super-resolution imaging technique where a grid pattern is generated through interference of of sinusoidally patterned illumination and superimposed on the sample while capturing images. This technique was first proposed by Lukosz in 1966 but only recently demonstrated by Gustafsson [23]. The image of the sample that is recorded is multiplied by a sinusoid of the form $1/2[1+\cos(k_{\mathrm{p}}x)]$. This incoherent image is recorded and the Fourier transform is calculated. This is equal to the transform of the required image convoluted with the transform of the illumination, i.e., three delta functions at 0, and $\pm k_{\mathrm{p}}$. The convolution superimposes the transform of the image on repeats of itself shifted by $\pm k_{\mathrm{p}}$. This moves the high spatial frequencies, otherwise not detectable, to lower ones. According to Abbe theory the image consist of Fourier components with spatial frequencies up to $\pm 2\mathrm{NA}k_0 = \pm k_{\mathrm{m}}$. In SIM, due to the convolution, the image will now include frequencies in the range $\pm(k_{\mathrm{p}} + k_{\mathrm{m}})$, thus promising higher resolution. In 2005, the resolution from SIM has been reported to increase three-fold by using non-linear fluorescent response [24]. Using very bright illumination, the sinusoidal function becomes closer to a square wave, which includes delta functions at $\pm 3k_{\mathrm{p}}$, $\pm 5k_{\mathrm{p}}$, etc., when a resolution of $\lambda/12\mathrm{NA}$ was obtained. It must be noted, though SIM does not rely on scanning and is a wide-field illumination technique; it is not fast due to considerable computational post-processing methods.

All the above imaging techniques rely on fluorescent emission from the object under study. It must be remembered that though a large number of biological microscopy methods use fluorescent imaging techniques, nevertheless it is always preferred not to alter the sample properties by the use of dye or other chemical substances.

1.2.3 Imaging with engineered media or metamaterials

Metamaterials are artificial man-made media structured on a scale smaller than the incident wavelength, and offers exotic properties. Such structures will be discussed in details separately (section 1.3). Making use of the ability of metamaterials to design any desired material parameter profile, a new class of lenses providing resolution beyond the diffraction limit were proposed a decade ago (Fig. 1.2c). Below several such imaging schemes are briefly discussed.

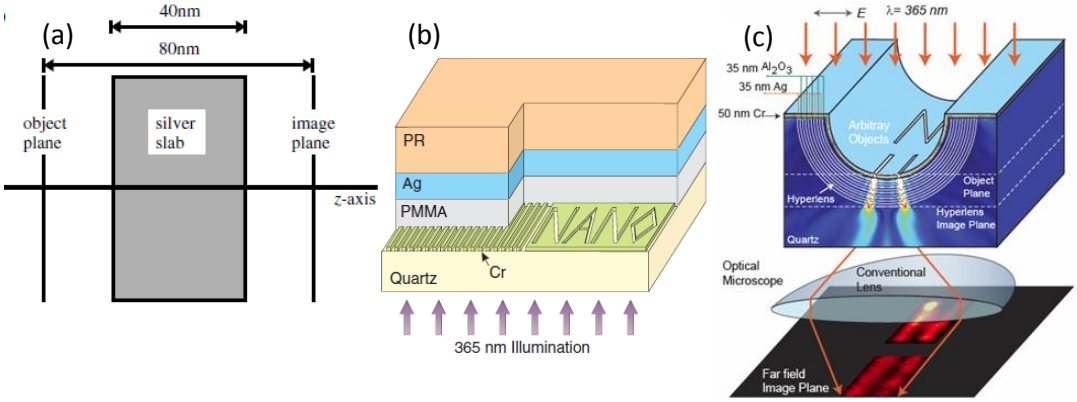

Figure 1.5: Different schemes for imaging with metamaterials(a) A superlens made of silver slab placed halfway between object and image planes [25]. (b) Optical superlensing experiment. The embedded objects are inscribed onto the 50 nm-thick chrome (Cr); at left is an array of 60 nm wide slots of 120 nm pitch, separated from the 35 nm thick silver film by a 40 nm PMMA spacer layer. The image of the object is recorded by the photoresist on the other side of the silver superlens [26]. (c) Schematic of hyperlens and numerical simulation of imaging of sub-diffraction-limited objects [27].

In the year 2000, Pendry [25] proposed that a metamaterial with negative index of refraction can be used to realise a perfect lens. The negative index metamaterials would help to amplify the otherwise exponentially decaying evanescent waves (Fig. 1.2c). A slab of silver with negative value of only permittivity (and not permeability) was proposed as a *poorman's lens*. Simulation results demonstrated that for wavelength of 356 nm, two lines of the order of a few nanometres thick can be perfectly imaged using a 40 nm thick silver slab (Fig. 1.5a). The main challenge is that the losses in the metamaterial deteriorate the theoretically proposed ideal performance and in practice it is difficult to realize a slab of lossless metamaterial. The first *poorman's lens* was demonstrated experimentally by Fang *et al.* [26]. A thin film of silver was placed with a dielectric material with equal and opposite permittivity (Fig. 1.5b). The surface

plasmon oscillations match the evanescent field frequencies leading to an enhancement of the evanescent waves. A resolution equal to $\lambda/6$ was reported. But it must be noted that in this case both the object and the image were at the near field of the lens.

In 2007, Jacob *et al.* [27] proposed the hyperlens which demonstrated high resolution imaging in the far field. The hyperlens transforms the scattered evanescent waves into propagating waves using an anisotropic metamaterial. Once the magnified feature is larger than the diffraction limit, it can be imaged to the far field with a conventional lens (Fig. 1.5c). A curved periodic stack of silver (35 nm) and Al_2O_3 (35 nm) deposited on a half-cylindrical cavity fabricated on a quartz substrate constituted the anisotropic metamaterial. The medium was designed so that the radial and tangential permittivities have different signs. Object with sub-wavelength feature size was placed in close proximity of the lens. A pair of 35 nm wide lines spaced 150 nm apart was magnified as an image with 350 nm spacing. This can be clearly resolved with an optical microscope of numerical aperture 1.4. The disadvantage that remains is that the object has to be placed very near to the hyperlens.

1.2.4 Super-oscillation and super-oscillatory lenses

Super-oscillation allows the design of lenses that can focus light to arbitrarily small spots at distances beyond the evanescent zone. Such lenses provide super-resolution imaging even when the object is not is close proximity to the lens. Major concerns of this rapidly developing technology have been the high intensity sidebands surrounding the sub-wavelength hotspot, and low energy throughput (Fig. 1.2d). Nevertheless this far-field super-resolution imaging technique opens up some exciting possibilities and is worth studying further.

Optical super-oscillation and its possible application to increase resolution of optical instruments beyond the diffraction limit was first proposed in 1952 [28] by Toraldo di Francia. This is similar to the then known concept of super-directive antennas which consist of a finite array of antennas that can direct radiation into arbitrarily narrow beams by tailoring the interference of waves emitted by different elements [29–31]. Super-oscillation is a complementary concept where a source of super-oscillatory fields, often obtained by designing a mask, interferes at a distance from the mask to produce an arbitrarily small hotspot. In both cases, the energy content in the super-directive

beam or the super-oscillatory hotspot is only a fraction of the total incident energy. In super-directivity the trade-off is the unwanted evanescent component close to the antenna array arising from the input feed. In super-oscillation the trade-off is the high intensity halo surrounding the super-oscillatory hotspot.

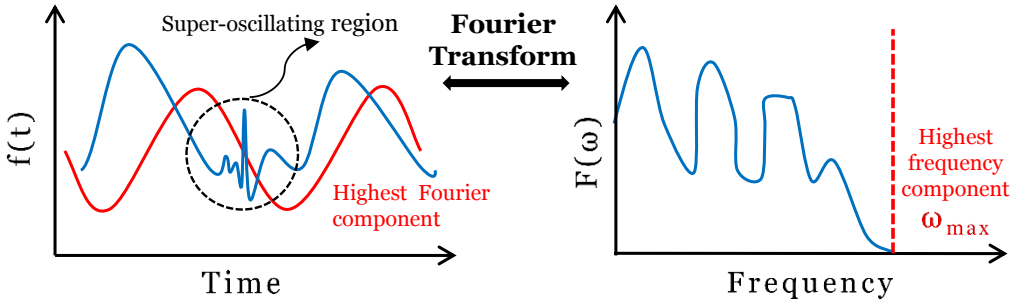

Figure 1.6: The principle of super-oscillation The highest Fourier frequency and the super-oscillatory region in the time domain. The band-limited function in the frequency domain.

The phenomenon of super-oscillation [32,33] is related to the fact that band-limited functions may oscillate arbitrarily fast within a local region, much faster than the highest Fourier component. As depicted in Fig. 1.6 the Fourier transform $F(\omega)$ of a time-varying function $f(t)$ is zero above a certain angular frequency ω_{max}; $f(t)$ is thus band-limited in the frequency domain. It is commonly known that in the temporal domain $f(t)$ could oscillate only as fast as the highest Fourier component ω_{max}. But if a super-oscillatory function, $f(t)$ has a small time window where it oscillates arbitrarily fast, even faster than ω_{max}. This is depicted in Fig. 1.6 where the red curve in time domain corresponds to the highest frequency component in the band-limited frequency domain. There exists a small region in time (encircled with dotted line) where $f(t)$ is oscillating much faster than the red curve.

However, it must be noted that in a finite energy band-limited signal, super-oscillations appear over a small spatial or temporal window but at the expense of loss of energy into neighbouring sidebands. Only a minute fraction of the total energy can exist in the super-oscillatory region. Ferreira and Kempf [34] showed that the energy dispersed into the sidebands, or regions surrounding the super-oscillating window, increases exponentially with the number of super-oscillations and polynomially with the inverse of the signal bandwidth. In optics this implies that for a super-oscillatory

hotspot surrounded by a high energy halo, the energy dispersed in to the halo increases exponentially with increase in the field of view (FOV), where FOV is defined as the area in which the sub-wavelength focal spot lies and outside which the high intensity sidebands occur (Fig. 1.8a). However, the energy dispersed into the halo increases only polynomially with decrease in the hotspot size. So from practical design consideration it is desirable to minimise the spot size rather than the field of view to get more and more of the total incident energy into the focal spot.

A simple example of one-dimensional super-oscillatory function consisting of only 6 spatial Fourier components was presented by Rogers and Zheludev [6, 35]:

$$f(x) = Ae^{i\phi} = \sum_{n=1}^{n=5} a_n e^{i2\pi nx}$$

where, a_n are the Fourier coefficients ($a_0 = 19.0123$, $a_1 = -2.7348$, $a_2 = -15.7629$, $a_3 = -17.9047$, $a_4 = -1.0000$, $a_5 = 18.4910$). Figure 1.7a shows the intensity $|f(x)|^2$ of the above function along with the fastest Fourier component $\cos(k_{max}x)$ with $k_{max} = 10\pi$. The function appears to oscillate slower than the fastest component. However the plot of the zoomed-in central portion reveals that in the low-intensity region there exist a very narrow peak, almost 10 times narrower than the fastest Fourier component. The peak demonstrates two characteristics of super-oscillation: super-oscillatory features are associated with low intensities and the phase values changes rapidly in the super-oscillatory region (shown by red-dotted line). In fact, rapidly oscillating phase has been considered as a signature of super-oscillation [36, 37]; a function is said to be super-oscillatory if the local gradient of phase ϕ, i.e., $k_{local} = d\phi/dx$ is greater than the fastest Fourier component, i.e., $k_{local} > k_{max}$. This region is shown by grey rectangles in Fig. 1.7a.

Super-oscillation can also manifest itself in random systems. It was demonstrated that statistically one-third of the area of a two-dimensional speckle pattern may be super-oscillatory [37] which was later studied for higher dimensions [36]. Figure 1.7b shows the phase and intensity of a random two-dimensional functional obtained by super-position of 100 plane waves with the same wave number k. The bright areas in the phase diagram show rapidly changing phase; the white contour traces $k_{local} = k$. The bright areas form 1/3rd of the total area which is super-oscillatory. On the intensity plot, these regions are characterised by low intensity values. Super-oscillation, though

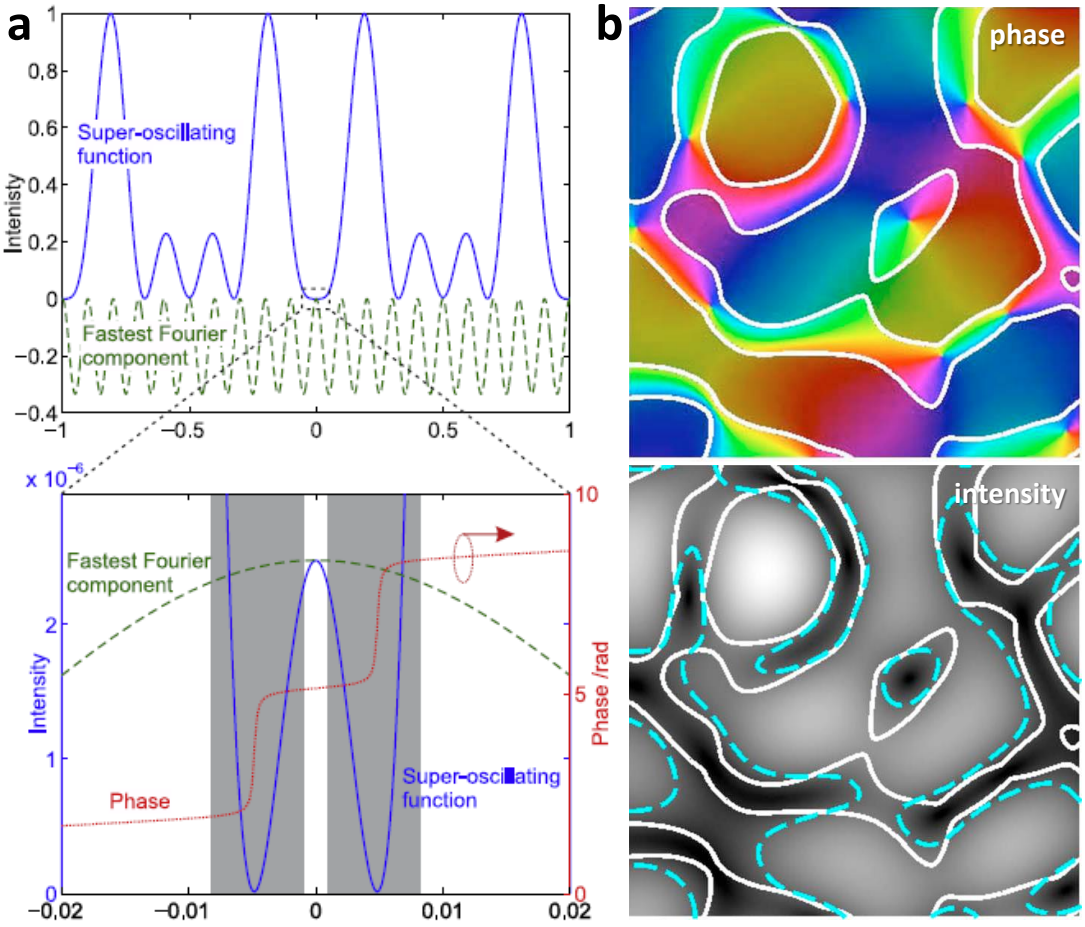

Figure 1.7: Examples of super-oscillatory functions (a) One-dimensional super-oscillation. Upper: a super-oscillatory function (solid blue line) and its fastest Fourier component (dashed green line). Lower: zoom of the function near the origin showing a narrow peak with rapidly oscillating phase (red dotted line) in the nulls on either side. The super-oscillatory region is shaded in grey. Figure reproduced from [35], ©IOP publishing. (b) Two dimensional super-oscillatory speckle pattern. Upper: Phase pattern. Lower: intensity pattern. The sub-oscillatory region is shaded with a dark filter and white outline. The intensity contour enclosing the lowest intensity pattern is shown by dashed cyan curve. This is close to the white super-oscillation contour. Figure reproduced from [37]. ©2008 OSA.

present in random speckle patterns, may not necessarily produce small features.

All optical systems are globally band-limited in the post-evanescent region by the free-space wavenumber k_0. Thus the principle of super-oscillation can be applied in optics to realize arbitrarily small focal spot beyond the evanescent zone. As mentioned in [33] a structure as simple as a diffraction grating when suitably designed, can produce super-oscillations which consist of non-evanescent features propagating considerably beyond the near field. Some prior research in this direction will be briefly discussed in the following section. In chapter 2 it will be demonstrated how a grating-like mask with circular symmetry can be designed to produce a sub-wavelength focal spots in the post-evanescent region.

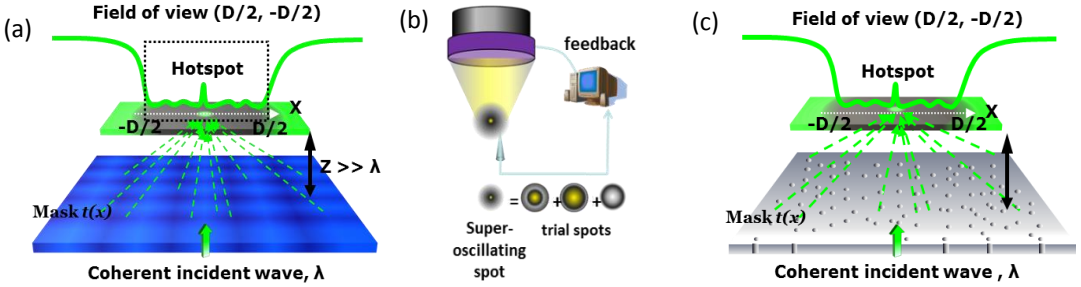

Figure 1.8: Different schemes for realising optical super-oscillation(a) continuous mask, (b) adaptive optics technique, (c) binary mask.

Optical super-oscillation has been experimentally demonstrated to localise light within an arbitrarily small confinement resulting in sub-wavelength sized focal spots that beat the diffraction limit [35, 38–41]. This is achieved by engineered interference of propagating beams only. Hence the focal distance of the sub-wavelength spot can be beyond the evanescent zone of the super-oscillatory lenses. One of the techniques for designing a super-oscillatory field with the aim of achieving sub-wavelength focusing [42] considers manipulation of both the amplitude and phase of the transmitted field (Fig. 1.8a). To arrive at the design of the mask that would result in a super-oscillatory function, the transmitted field is expressed as a series of band-limited (in spatial frequency domain) prolate spheroidal wave functions, within a limited field of view. The hotspot lies within this field of view with high intensity sidebands appearing outside the region. The series of prolate spheroidal functions is further decomposed into a series of plane waves. The complex transmission function of the mask is then

derived using scalar angular spectrum description of light propagation [43]. Once the transmission function is known the mask may be designed to produce the required amplitude and phase modulation. As a practical possibility for these kinds of masks a dielectric grating structure was suggested which would control the phase, and will be covered with varying thickness of metal films to manipulate the transmitted amplitude. But as was rightly pointed out in the same paper, in the microwave and THz regime though these amplitude-phase continuous masks are relatively easy to manufacture and robust to manufacturing defects ($\sim 0.1\lambda$), however, in the infrared and visible regime the fabrication becomes increasingly challenging.

This whole problem of manufacturing a mask for realizing super-oscillation may be circumvented by an adaptive optics approach [39, 40, 44, 45]. In such method, super-oscillatory hotspots are realized by using a spatial light modulator and a conventional optical microscope. Optical eigenmodes are used to determine the required amplitude and/or phase modulation to produce the smallest possible focal spot after the objective lens. The optical eigenmode method has been experimentally demonstrated to produce a super-oscillatory spot measuring 0.35λ [39]. Following which, super-resolution imaging was experimentally demonstrated in a low NA imaging system providing 1.3 times improvement over the diffraction-limited imaging system [40]. It must be mentioned that the spatial light modulator can also be used in the collection path of a conventional microscope for super-oscillatory filtering of the captured images, thus increasing the resolution of the imaging system [46, 47].

Super-oscillation may also be looked upon as constructive interference of forward propagating light where over a small spatial region a certain condition is satisfied i.e. local wavenumber exceeds the maximum global wavenumber. Hence, a properly designed mask which modulates only the transmission amplitude in a binary manner (i.e, either transmits or blocks light) may also result in a super-oscillating field (Fig. 1.9). In fact it has been demonstrated [38, 42, 48] that a quasi-periodic nanohole array shows super-oscillating hotspots at post-evanescent distances from the mask. In 2007 Huang and Zheludev [38] reported that 5 μm away from the nanohole array the smallest spot achieved was 0.54λ by 0.30λ, when illuminated with a laser of $\lambda = 660$ nm. This was measured by scanning a SNOM tip across the sample. SNOM or scanning near-field optical microscope tips have sub-wavelength apertures for collecting light and are de-

signed specifically to measure the near field of the sample. But in the above case the SNOM tip was used to measure the field beyond the near-field.

Shortly afterwards, it was reported by the same group [48] that sub-wavelength features are visible at different heights away from a quasi-periodic nanohole array simply through a high numerical aperture (NA) microscope objective. This shows that the sub-wavelength spot is a result of super-oscillation, since no significant evanescent component can be observed through a microscope objective. The sub-wavelength hotspot is constructed from interference of the propagating components only. Hence it can be observed with conventional microscope, even though it is smaller than the diffraction limit.

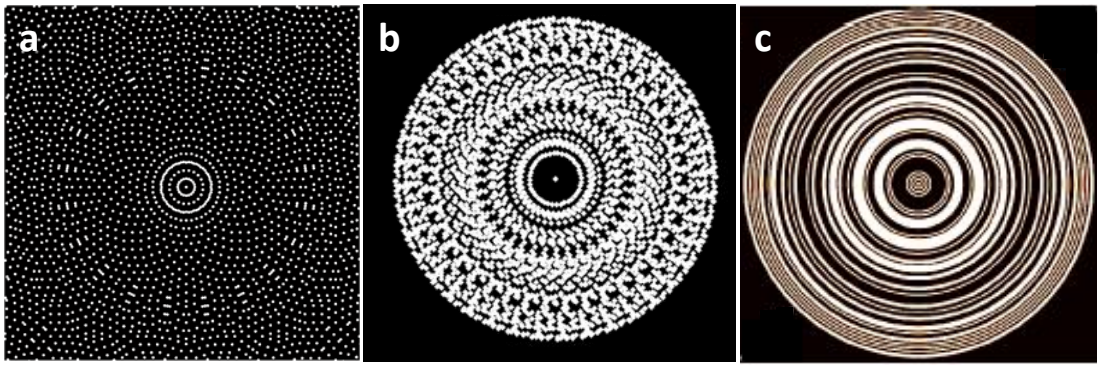

Figure 1.9: Examples of binary amplitude super-oscillatory masks (a) radially symmetric quasi periodic hole array, (b) random spiral hole array, (c) ring binary nanolens.

It must be noted that the nanohole arrays produce several sub-wavelength hotspots over a large field of view, distributed along with bigger focal spots. This result in an interesting pattern called photonic carpet [34]. This is of little interest if imaging were to be considered as a practical application of sub-wavelength hotspots. Arrangement of the nanoholes in a radially symmetric pattern (Fig. 1.9a) helps in isolating a hotspot at the centre of the field of view [49]. The so called radially symmetric quasi-periodic hole arrays though promising from the point of view of isolation of the hotspot, require intensive analytical modelling to arrive at the mask design. In another such design random spiral hole arrays (Fig. 1.9b) the holes are arranged with S-fold symmetry where S is the number of holes on each concentric circular path. This design is reported to result in better minimization of the hotspot dimension. These are relatively easier to model analytically and also show that quasi-periodicity is not essential for

achieving super-oscillation. Intuitively if the holes of the above masks are joined to form concentric circles, the throughput of the mask is increased by almost 50%. With ring-binary nanolens (Fig. 1.9c), a sub-wavelength hotspot is observed at the centre, though accompanied by annular sidebands. Such ring-type nanolenses will form the basis of Chapter 2, where the design, fabrication, and characteristics of the lenses will be presented.

1.3 Metamaterials

Metamaterials are man-made structures designed by arranging units, often periodically, on a scale smaller than a wavelength of the interacting wave. Besides electromagnetic waves [25, 50, 51] the field of metamaterial research has been active for acoustic waves [52–54] as well. In this thesis electromagnetic metamaterials, specially metamaterials for optical waves, will be considered.

In the naturally available materials the constituent atoms and molecules and their inter-spacing are much smaller than the interacting electromagnetic wavelength, thus rendering the medium homogeneous. Similarly for a metamaterial the size of the engineered building blocks — *'metamolecules'* or *'metatoms'* — and the spacing between them are made to be smaller than a wavelength of the incident wave. This ensures that the metamaterial as a whole is effectively homogeneous to the interacting waves, i.e., the effective medium theory can be applied to the artificially engineered structure. Hence, the engineered material with macroscopic *atoms* and *molecules* behaves like naturally available materials with defined material parameters, like permittivity and permeability.

The Greek word *meta* literally means 'beyond'. Metamaterials are known to exhibit properties beyond that available from ordinary or natural materials. One of the exotic properties offered by the metamaterials is negative index of refraction when the effective permittivity and permeability of the engineered medium are designed to be simultaneously negative [50, 55]. In this context it is interesting to note that negative refraction was predicted as early as 1904 by Schuster [56]. Other extraordinary outcomes achieved with metamaterials include optical chirality [57], electromagnetically induced transparency [58], cloaking [59, 60] and super-resolution imaging [25, 61, 62].

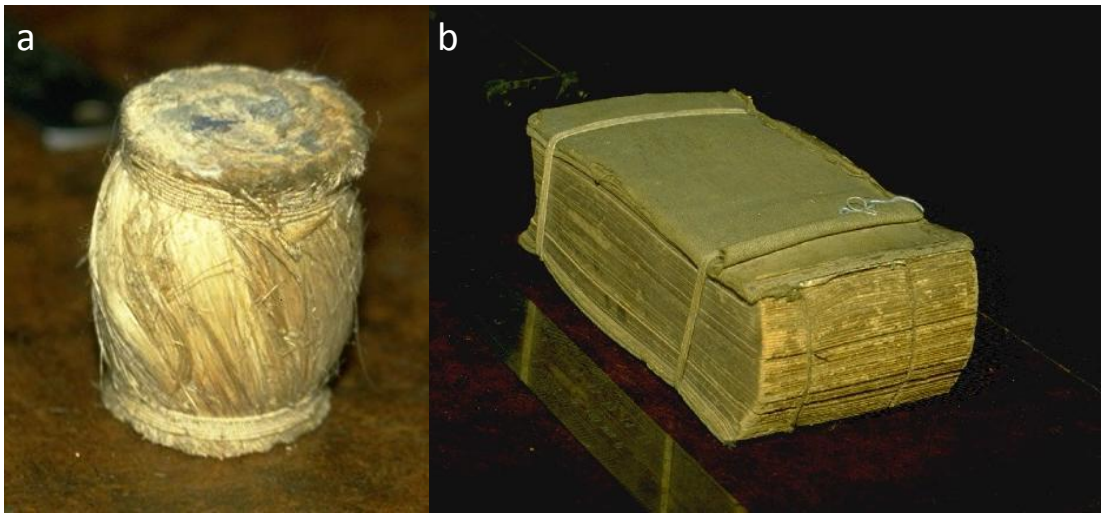

Figure 1.10: Earliest known metamaterials: works of J. C. Bose (a)One of the twisted-jute polarizers used by Bose [63]. (b) One of Bose's polarizers was a cut-off metal plate grating, consisting of a book (Bradshaw's Railway Timetable) with sheets of tinfoil interleaved in the pages [64]. Figures reproduced from [65] ©IEEE, 1997.

Interesting to note, the earliest known metamaterial may be traced back to the end of 19^{th} century when Jagadish Chandra Bose, used twisted jute bundles (Fig. 1.10a) to rotate the plane of polarisation [63]. Bose used the bundles to built a macroscopic model of polarisation rotating medium like sugar solution. This was the first know macroscopic man-made chiral molecule. Bose also demonstrated that the an ordinary book can act as a polariser to electromagnetic waves; each page is like a dielectric layer separated by thin air. He was able to enhance the function of the polariser by using tin foils in between pages (Fig. 1.10b).

Metamaterials, as they are known today, are mostly metal resonant units arranged periodically and supported by some dielectric substrate. However, all-dielectric metamaterials are an active field of research due to the inherent low loss of dielectric media [66–68]. One of the earlier forms of modern day metamaterials consisted of metal split rings to realise artificial permeability and thin metal rods to achieve artificial permittivity - first demonstrated by Smith *et al.* in 2000 [51]. Such structures are relatively easy to manufacture for microwave frequencies, and may be scaled down in dimension to operate in the terahertz and near-infrared regime. But due to increasing metal loss they cannot be simply scaled down for optical frequencies. An alternative low-loss design for shorter wavelengths was demonstrated in 2008 by Valentine *et al.* [60]. This was a fishnet type metamaterial consisting of 21 alternating layers of silver (30 nm) and

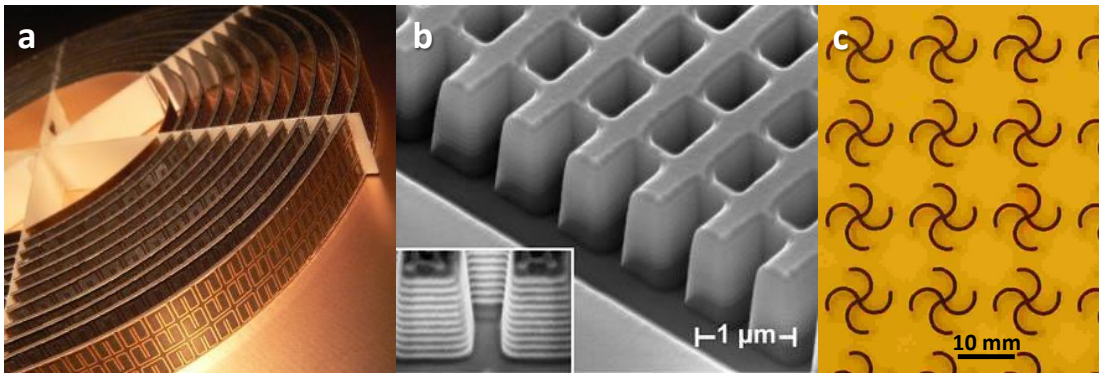

Figure 1.11: Examples of metamaterials (a) Photograph of a microwave 2D cloaking structure [59] ©AAAS. (b) SEM image of the fabricated fishnet metamaterial with the inset showing the 21 layers [60] ©NPG. (c) Photograph of part of a bi-layered metamaterial sheet. The twisted rosettes of the second layer can be seen as a shaded area due to partial transparency of the substrate [69] ©APS.

magnesium fluoride (50 nm) exhibiting negative refractive index in the optical regime (Fig. 1.11b).

To ease the fabrication difficulties of three dimensional metamaterials and deal with the unavoidable material loss a new genre of planar metamaterials emerged. These are single sheets of metals consisting of metamolecules with sub-wavelength periodicity, supported on a transparent substrate. Such planar metamaterials have been used to demonstrate some of the above mentioned properties like negative refraction due to chirality (Fig. 1.11c) and a metamaterial analogue of electromagnetically induced transparency [55, 57, 58].

1.3.1 Surface plasmon polaritons

Surface plasmon polaritons play a significant role in explaining the response of metal-dielectric metamaterials at optical frequencies [70]. It is important to study the surface plasmon excitation at metal-dielectric interfaces to understand the behaviour of plasmonic metamaterials. A brief background of surface plasmon polaritons is presented here.

At optical frequencies the free electron gas of metals can sustain surface and volume charge density oscillations called plasmons that have a distinct resonance frequency [7, 71]. The quanta of surface charge density oscillations are called surface plasmons. These surface plasmons can be coupled to photons of an external electromag-

netic wave, resulting in electromagnetic waves propagating along the metal-dielectric interface called surface plasmon polaritons (SPPs) [71]. The SPPs are strongly localised along the interface, decaying exponentially into both the media away from the interface (Fig. 1.12a). For example, for gold-air interface the decay length of SPPs transverse to the interface is 23 nm in gold and 421 nm in air, for 633 nm wavelength.

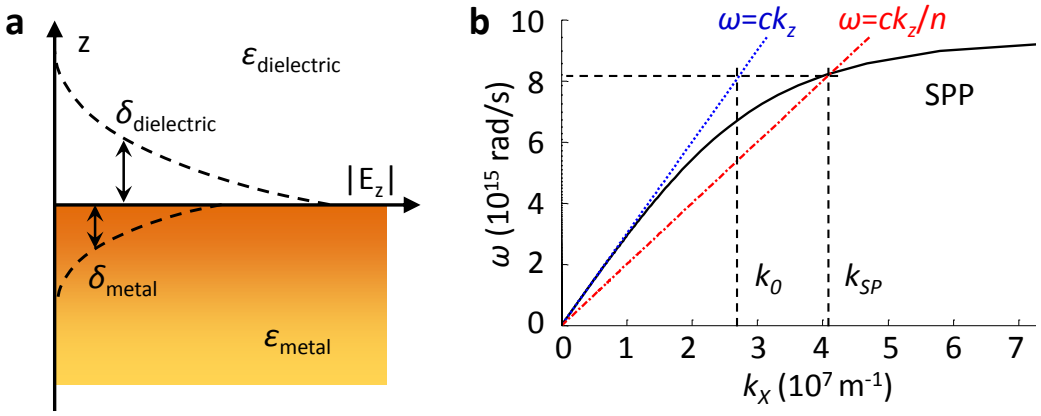

Figure 1.12: Surface plasmon polaritons. (a) The surface plasmon polaritons propagate along the interface of a metal and dielectric, with the electric field decaying exponentially away from the interface on both sides. (b) Dispersion diagram of surface plasmon polaritons (black solid curve) with free-space light line (blue dotted line) and the tilted light line in a high refractive index ($n > 1$) medium (red dash-dot line).

The SPPs propagate along the interface and are damped due to ohmic losses of the electrons participating in the SPP oscillations. The propagation length of SPPs is defined as the length over which the intensity of the SPPs decays to 1/e of its initial value. The propagation length is related to the imaginary part of the complex wave number ($k_{z,imag}$) parallel to the metal-dielectric interface and is given by $1/(2k_{z,imag})$. As an example, the propagation length of the SPPs for gold-air interface at a wavelength of 633 nm is 10 µm [71].

The real part of the complex wave number determines the SPP wavelength and is given by $\lambda_{SPP} = 2\pi k_{z,real}$. Using the same example as above, the SPP wavelength is 605 nm, when the wavelength of the excitation light is 633 nm. In other words, the wave number of SPPs is larger than that of light in free space. The dispersion relation for the surface plasmon polaritons, i.e. the relation between the complex wave number parallel to the metal-dielectric interface and the angular frequency is given by

$$k_{SPP} = \frac{\omega}{c}\sqrt{\frac{\epsilon_m(\omega)\epsilon_d}{\epsilon_m(\omega)+\epsilon_d}} \tag{1.1}$$

where $\epsilon_m(\omega)$ is the permittivity of the metal, which for the case of the Drude model is given by $\epsilon_m(\omega) = 1 - (\omega_p^2(\omega^2+\gamma^2))$, ϵ_d is the permittivity of the adjacent dielectric, ω is the angular frequency and c is the velocity of light in free space. The dispersion diagram is plotted in Fig. 1.12b using $\omega_p = 1.38\text{x}10^{15}\text{rad}s^{-1}$ as the plasma frequency and $\gamma = 1.075\text{x}10^{14}s^{-1}$ as the estimate for loss given by [71] for gold, and considering $\epsilon_d = 1$ for the neighbouring dielectric (air). The dispersion relation of an SPP is plotted (black solid line) along with the free-space light line (blue dotted line) and the tilted light line in a high refractive index ($n > 1$) medium (red dash-dot line). A feature of the SPPs, as can be observed in Fig. 1.12b, is that for a given energy ($\hbar\omega$), the momentum ($\hbar k_z$) of the SPPs is always greater than the momentum of light travelling through free space. The momentum of SPPs is increased because of the strong coupling between photons and oscillating surface charge densities. Due to this momentum mismatch SPPs cannot be excited by light propagating in free space. However when light travels through a high index medium (red dash-dot line in Fig. 1.12b), its momentum is greater than the free space value. In this situation, there exists a point on the dispersion diagram where the light line in the high index medium crosses the SPP dispersion curve. At this point the momentum of the electromagnetic wave and the surface plasmons are matched and SPPs can be excited. Below, some of the popular methods to achieve momentum enhancement of incident photons for exciting SPPs are discussed.

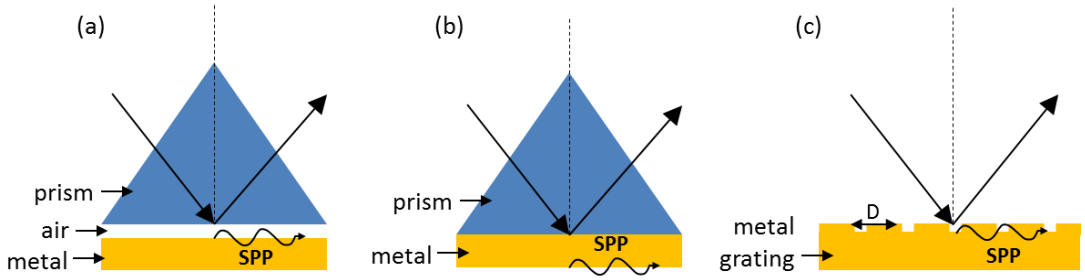

Figure 1.13: Surface plasmon - photon coupling at metal-dielectric interface
(a) Otto configuration (b) Kretschmann configuration and (c) grating coupler.

Figure 1.13 shows a schematic representation of some possible arrangements. The Otto configuration (Fig. 1.13a) uses a thin metal film placed in the evanescent zone

of a high index glass prism. For light that undergoes total internal reflection in the prism, evanescent waves are created in the air gap. If this electromagnetic field with increased momentum matches the momentum of the SPPs at the metal interface, it couples photons to the surface plasmons. This technique uses attenuated total internal reflection, and was proposed by Otto in 1968. For optimum coupling of photons to surface plasmons, the air gap must be of the order of the incident wavelength. For visible wavelengths this is difficult to achieve experimentally. In the same year 1968, Kretschmann demonstrated an alternative method for excitation of SPPs (Fig. 1.13b). A metal film is deposited on the surface of the glass prism thin enough to transmit light without significant attenuation of the SPP oscillations. The SPPs are excited on the far surface where the metal is in contact with the air. A third method uses grating coupler to excite SPPs (Fig. 1.13c). For some diffraction orders, light may diffract beyond 90° as measured from the normal to the grating surface. In such cases, light will not propagate but become evanescent. The enhanced momentum of these evanescent fields may couple radiation to the surface plasmons thus exciting SPPs. The parallel wave number is increased by an integer multiple of $2\pi/D$, where D is the grating period.

Localised surface plasmons are associated with nano-particles and nano-grooves of metals where size-scale of the structures are smaller than the incident wavelength. If the frequency of the incident electromagnetic field matches the coherent oscillations of the surface plasmons in the metal nano-structures this is manifested by a strong absorption peak [73]. For nobel metals (gold, silver, copper) this resonance lies within visible part of the spectrum. The Lycurgus cup on exhibit in the British Museum, London is one of the earliest known examples of localised surface plasmon resonance effect dating back as early as the 4^{th} century AD (Fig. 1.14a). The cup, now known to contain gold and silver colloids, looks pale green in reflection, and glows red in transmission when light is shone through it. Localized surface plasmon resonances can lead to significant local field enhancement. This is now being widely used to study applications like light concentration and manipulation [74], sensing [75–77], solar energy absorption [78–80], and ultrafast signal processing [81–84].

Localised surface plasmons are useful in describing the optical response of photonic metamaterials. A numerical [72] study of plasmonic modes of U-shaped metamaterials were presented [72], and later experimentally verified [85]. The study concluded that

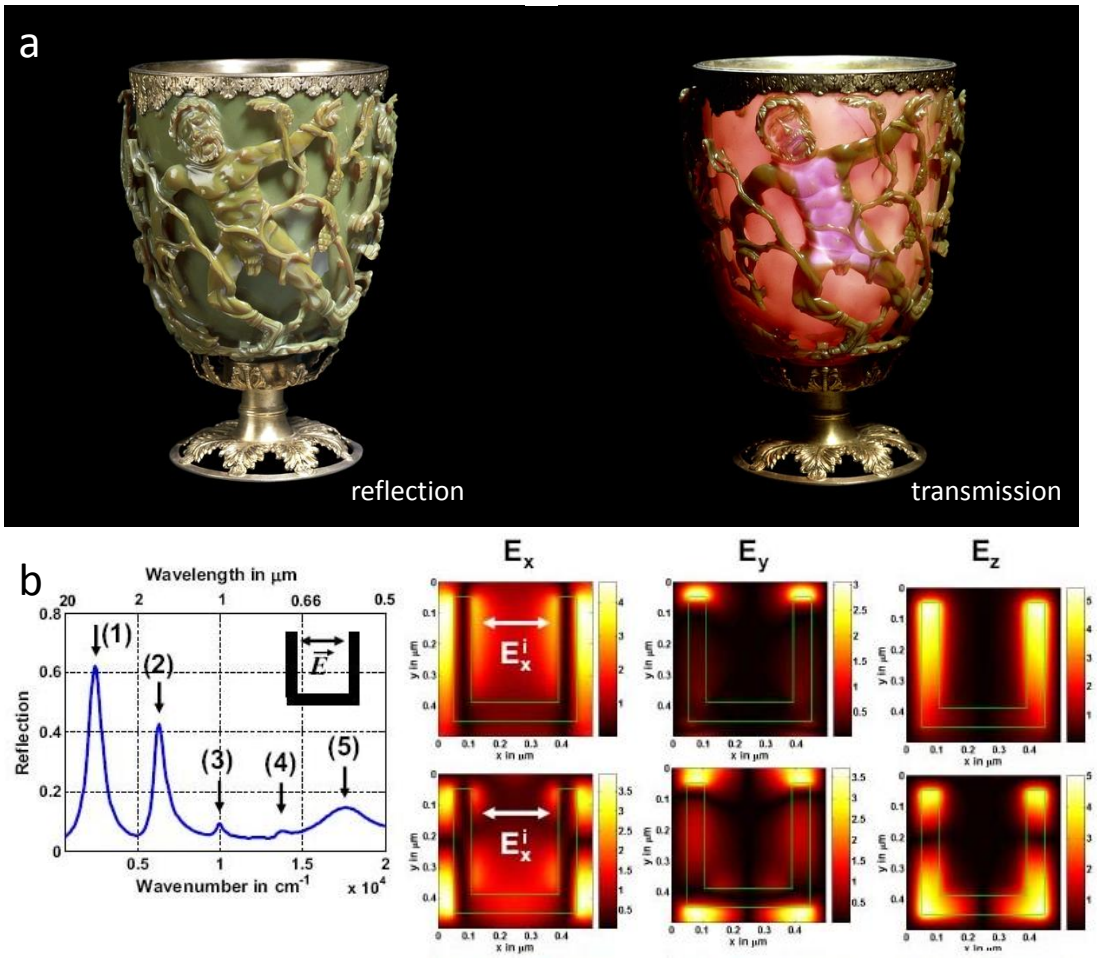

Figure 1.14: Localised surface plasmons (a) The Lycurgus cup ($4^{th} century AD$) made of silver and gold nano-particles appears green in reflection and red in transmission. Photo courtesy the British Museum website. (b) Spectral reflection response split-ring resonators for incident polarisation parallel to the gap. Colour maps show corresponding near-field distribution of magnitude of electric field for the first two resonance peaks. Figure reproduced from [72]. ©OSA, 2006.

the resonances of such plasmonic metamaterials can be explained by different higher orders of localised plasmon resonances in the nano-structure. The fundamental mode of resonance could be explained by LC-circuit model aside from which there existed other higher order modes (Fig. 1.14b).

1.3.2 Talbot effect

In 1836 Henry Fox Talbot reported [87] that alternate red and green bands were observed very near and parallel to the plane of an illuminated grating. As Talbot moved away the magnifying lens with which he observed the red-green bands, the bands

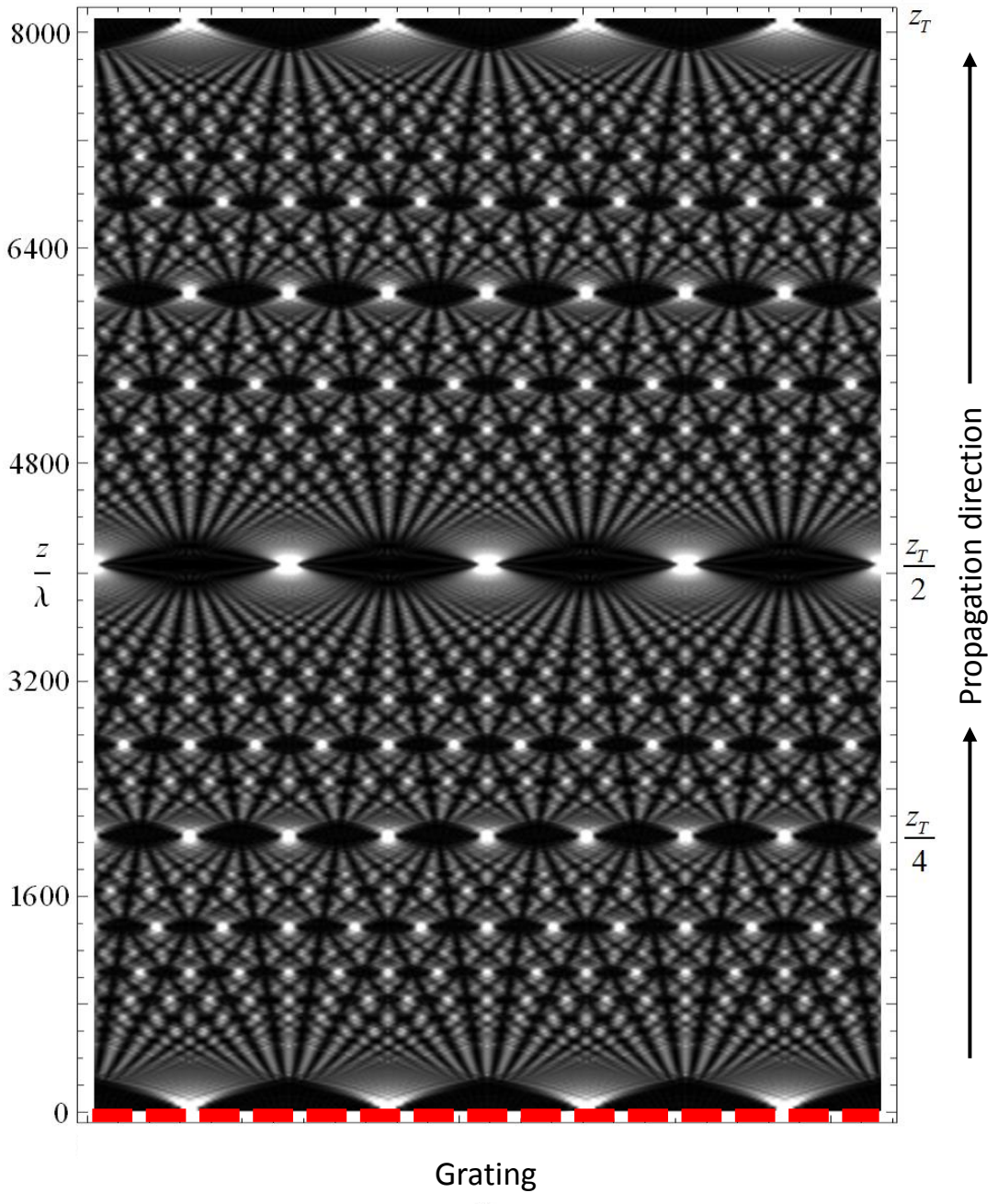

Figure 1.15: Talbot carpet Example of a Talbot carpet showing fractional Talbot images over one Talbot distance. z_T is the Talbot distance. Figure reproduced from [86].

changed to alternating blue and yellow. Further away from the grating surface the bands became red and green again. This phenomenon is now known as the Talbot effect, where a grating illuminated with plane wave images itself repeatedly at a fixed distance. The repeat distance of the grating's self-images are given by Lord Rayleigh's calculations done in 1881 [88]. For a monochromatic wave, the Talbot distance is given by:

$$z_T = (2a^2)/\lambda$$

where, a is the period of the grating, and λ is the wavelength of illumination. The Talbot effect is a natural consequence of Fresnel diffraction [87]. Revivals of the grating self-images occur at integer multiples of the Talbot distance. Later it was observed [89] and explained [90] that fractional revivals [91] occur at all rational multiples of z_T, given by $z = (p/q)z_T$ where, p and q are co-prime integer pairs. The fractional revivals of the grating image along with the full revivals result in a distribution called the "Talbot carpet" (Fig. 1.15) due to its appearance when viewed on a plane normal to the grating surface [86, 92].

The Talbot images are result of constructive interference of light from all the slits of a grating. But only under paraxial approximation when $\lambda/a \to 0$ the Talbot images are sharp. As explained [91] and observed [92], in the post-paraxial regime when $\lambda \sim a$ the Talbot images are blurred, and often result in inexact replication of the illuminated grating. Even within the paraxial-limit, the sharpness of the Talbot images requires a grating with infinite number of slits. As explained [91], for a large but finite number of N slits, the sharp edges of Talbot images are blurred by fringes with lateral scale $(az/(Nz_T))$ and the repetition of Talbot images may not be periodic [93].

Recently, Talbot effect has been studied for surface plasmons [94] which was subsequently experimentally demonstrated [93, 95, 96]. Coherently illuminated nano-holes and nano-grooves on gold films were used to launch surface-plasmons. Due to finite size of the structures, Talbot effect was studied in the non-paraxial limit for several ratios of a and λ [93]. Figure. 1.16 demonstrates Talbot carpet due to coherent illumination of gold nano-hole array in the non-paraxial limit. When $a/\lambda < 1$ no periodic pattern was observed. When $1 \leq a/\lambda < \sqrt{2}$ (Figs. 1.16a and b) periodic self-images of the grating was formed along the propagation direction. When $a/\lambda \geq \sqrt{2}$ (Figs. 1.16c and

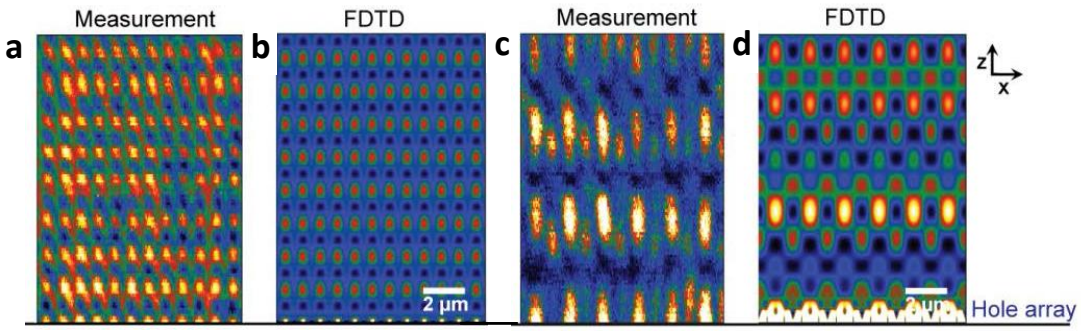

Figure 1.16: Non-paraxial Talbot effect Light patterns from Au hole array with $a/\lambda = 1.23$ ($a = 600$ nm, $\lambda = 488$ nanom) for (a) and (b),and $a/\lambda = 1.9$ ($a = 1.2$ μm, $\lambda = 633$ nm) for (c) and (d). For larger a/λ the Talbot image repetition is not periodic in z, as observed clearly from the FDTD simulation in(d). Figure reproduced from [93]. ©2012 OSA.

d) the self-images are no more periodic along the propagation direction.

1.4 Thesis overview

This thesis presents three major bodies of work: (1) Super-oscillatory lens devices and their applications, (2) Planar optical devices designed with spatially varying meta-molecules and (3) Enhanced photoluminescence due to nano-structuring of ultra-thin gold film. Each of these major sections are presented as one or more chapters. The following sections give a brief overview of the individual chapters in this thesis.

The principle of super-oscillation offers us an excellent opportunity to design optical imaging devices that can break the *diffraction limit*. In this thesis planar super-oscillatory lenses and their possible applications are studied.

Chapter 2 presents a study on super-oscillatory lenses that are designed to modulate the amplitude of the incident light. Such planar lenses focus light into sub-diffraction limited sizes beyond the near-field of the lenses. This is demonstrated experimentally in this chapter for two different designs. The first kind of super-oscillatory lens comprises of several concentric rings and produces multiple sub-wavelength foci along the optical axis. These sub-diffraction focal spots are characterised by low intensity and accompanied by an intense annular sideband. It is shown that when such a focal spot is scanned over an object in sub-wavelength steps, features as small as $1/6^{th}$ of a wavelength can be imaged bypassing the negative effect of the high intensity sideband. The second kind of super-oscillatory lens has the same design as the previous one, but with an opaque

disk blocking some of the rings in the central portion. This results in a continuous distribution of sub-wavelength foci along the optical axis giving the impression of an optical needle perpendicular to the lens surface. Additionally, the latter design has the advantage of pushing the high intensity sidebands away from the central region. This provides a larger field of view which may be used, as will be presented in chapter 3, for super-resolution imaging without the need of scanning the spot.

Chapter 3 provides a more detailed understanding about the imaging characteristics of the super-oscillatory lenses. The point spread functions of the lenses presented in chapter 2 are studied theoretically and experimentally in this chapter. This provides a measure of how accurately the super-oscillatory lenses can image a point source, compared to a conventional optical lens. A theoretical study on scan-less, direct imaging of multiple points within the extended field of view of the optical needle super-oscillatory lens is also included.

The sub-diffraction focal spot produced by the super-oscillatory lenses can be applied for focusing as well as imaging applications. Imaging has been discussed in chapters 2 & 3. Chapter 4 presents a proof-of-principle demonstration of solid-immersion super-oscillatory lens that might be integrated within a commercial hard disk drive for increasing the data storage density. Theoretical calculations presented in this chapter indicate that using a high refractive index medium like gallium phosphide, a ~ 50 nm focal spot is achievable. A focal spot this small is a pre-requisite for the cutting-edge data storage technology of heat-assisted magnetic recording. For experimental demonstration a simpler-to-fabricate solid-immersion medium with refractive index lower than gallium phosphide is chosen, and a focal spot measuring ~ 130 nm is demonstrated.

Planar metamaterials provide the opportunity to manipulate the phase and amplitude of light with sub-wavelength spatial resolution across a two-dimensional interface. Chapter 5 makes use of this concept to design a planar optical diffraction grating and a lens-array. The planar diffraction grating is formed by sub-wavelength elements with periodically variable parameters. At normal incidence the grating exhibits asymmetric diffraction for visible wavelengths. It is also demonstrated that a planar plasmonic metamaterial with spatially variable parameters can focus transmitted light into sub-wavelength hot-spots. Since the sub-diffraction foci measuring a fifth of an wavelength occur beyond the near-field of the metamaterial, this is attributed to the phenomenon

of super-oscillation.

Finally, metamaterials can be used to alter the electronic properties of the constituent material. In chapter 6 is it demonstrated how nano-structured gold films can alter and enhance the photoluminescence of an unstructured gold film. The shift in the emission peak and the substantial intensity enhancement due to the presence of the metamaterials can be related to the engineered plasmonic resonances.

Chapter 7 summaries the results presented in this thesis and provides an outlook for future research possibilities. This is followed by two appendices: appendix A gives a brief overview of the nano-fabrication technique of focused ion beam milling that has been extensively used to fabricate all the samples for this thesis, and appendix B briefly describes the finite element simulation technique used to calculate the transmission and reflection characteristics of the planar metamaterials.

2

Super-oscillatory focusing devices

The past few decades have seen extensive research on various super-resolution imaging techniques in an effort to beat the fundamental diffraction limit. The Pendry-Veselago superlens [25] invokes negative refractive index of artificial media, but faces the challenges of engineering a perfectly lossless medium and fabrication finesse. Other super-resolution techniques either require the object to be in close proximity of the imaging device [97–101] or work for a limited class of objects such as intensely luminescence samples [2, 102] or very sparse objects [103].

In this chapter a new kind of super-resolution imaging device with sub-diffraction focusing capabilities and little restriction on the placement of object from the lens will be presented. This technique makes use of the principle of super-oscillation (section 1.2.4), which was recently predicted [32, 33] and observed [48, 104–106]. Such a super-oscillatory lens is a nano-structured binary amplitude mask. The careful design of the super-oscillatory lens ensures that upon illuminating with coherent light, the interference pattern forms sub-diffraction-limited hot-spots at distances beyond the evanescent region of the lens. In the following sections two kinds of super-oscillatory lenses are presented: one that produces several isolated and laterally sub-wavelength focal spots along the optical axis with intense side-bands closely neighbouring the central hotspot, and the second kind which produces an "optical needle" shaped continuous distribution of sub-wavelength hotspots along the optical axis with an extended field of view.

2.1 Binary super-oscillatory lens: SOL

2.1.1 Introduction

In this section a super-oscillatory amplitude mask will be described in detail and experimental characterisations of such a lens will be presented. After optimising the design of the super-oscillatory lens (SOL), it is fabricated by milling a thin aluminium film with sub-wavelength features. The SOL is illuminated with monochromatic coherent light and the distribution of foci along the propagation direction is experimentally studied. At the end of this section, the appropriateness of the SOL as an useful super-resolution imaging device will be justified by performing an imaging experiment.

The design of the SOL is provided by Dr. Jari Lindberg, the fabrication, experimental characterisation and data analysis are done by the author Tapashree Roy and the experiment using SOL for imaging (section 2.1.4) is carried out by Dr. Edward Rogers.

2.1.2 Design and fabrication of SOL

The super-oscillatory binary mask is designed by using a nature-inspired optimisation algorithm called binary particle swarm optimisation (BPSO) algorithm [107]. The algorithm is described in Fig. 2.1. A swarm of N random particles scattered in an n-dimensional space are chosen. Value of each particle depends on their position in this space. For this starting position each of the N particles are evaluated and the global best value is noted. All the particles then move to a new position in the n-space with some defined velocity. The new individual values are noted and these are compared to their own previous values. The new global best value is updated. For each successive steps the particles move in a way such that each of them gets closer to the position which would give the individual best value as well allow them to provide the global best value. This is continued for a fixed number of iterations after which the particle with the global best solution is chosen.

This algorithm is applied in designing the super-oscillatory mask. The basic design of the SOL is chosen as $n = 100$ concentric annuli of equal width each of which can have transmittance value either 1 or 0. The overall diameter of the 100 annuli is fixed to be 40 μm. N=60 different kinds of SOL, i.e. with different combination of

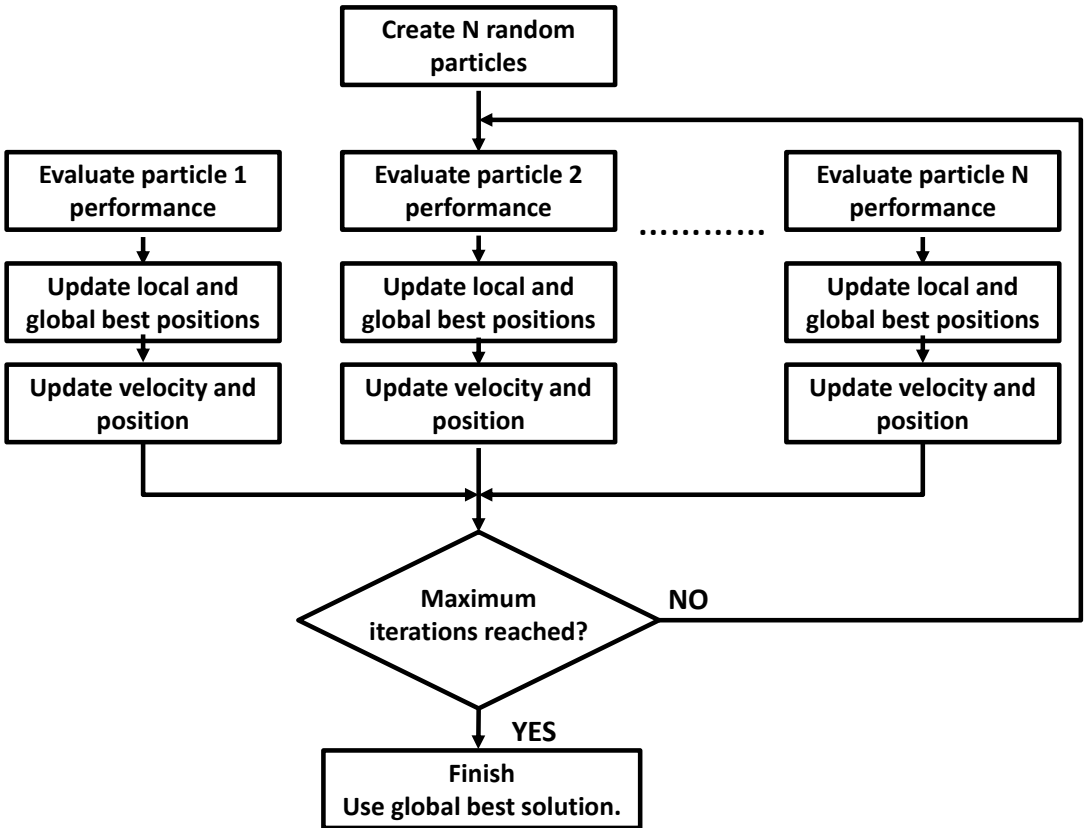

Figure 2.1: Binary particle swarm optimisation algorithm Schematic flow diagram of the particle swarm optimization algorithm used for designing a super-oscillatory lens. N particles swarm around the search space, guided by the best existing positions, converging to an optimum mask design. Figure after [35].

transmittance value for the annuli are chosen at the start. So, now there are 60 different SOLs with different focusing performances. The figure of merit for the optimising the design is chosen as the minimum achievable focal spot size at a fixed distance (10 μm) from the SOL. Further constraints imposed are the minimum value of field of view (1.2λ) and the intensity ratio between the central peak and the maximum side-band ($>$ 0.05). Performance for each of the 60 SOL designs are evaluated and compared against the figure of merits. After each iteration, the combination of transmittance value through the 100 annuli is changed so that the SOL approaches towards the optimum performance. After 10,000 iterations a single optimised design of SOL, as shown in Fig. 2.2a, is obtained. The final design consists of 25 transparent regions of varying sizes and a overall radius of 20 μm. Note that, in contrast with other algorithms assuming a fixed number of transparent region [108, 109] in this case the number can vary during the optimization process.

The SOL is fabricated by focused ion beam milling of a 100 nm thin aluminium film deposited by electron-beam assisted evaporation on a round shaped silica substrate(Fig. 2.3a). Figs. 2.2b and 2.2c shows the fabrication finesse attained with narrowest feature measuring 200 nm. The ion beam current required to mill the SOL pattern on the aluminium film is chosen after several trials to be 93 pA. This is optimised for the given metal thickness and minimum feature size on the design. It must be mentioned that the choice of metal and its thickness required for SOL fabrication is guided by the requirement for an opaque yet thin film. As will be presented later in this chapter, SOLs are also made with gold instead of aluminium. However, the metal thickness is kept the same (100 nm); any thinner than that have shown to degrade the performance of the lens due leakage of incident light through the metal film.

It must be mentioned that the fabrication finesse of the planar metal structures has an effect on the quality of hotspots produced by the super-oscillatory lenses. It has been observed that the super-oscillatory hotspots are robust to a standard deviation of a few nanometres from the designed widths of the rings. It is intuitive that if the lens is elliptical due to fabrication imperfection, the hotspots formed are also elliptical, and not round as predicted by the simulations.

2.1.3 Experimental characterisation of a SOL

To experimentally characterise the SOL it is mounted on a customised holder with a hollow centre (Fig. 2.3b). Such an assembly can easily replace any conventional objective in a standard microscope set up (Fig. 2.3c). Linearly polarised light with 660 nm wavelength from a diode laser is incident on the backside of the lens through the hollow centre of the SOL holder. The diffraction patterns produced up to 30 μm from the SOL along its optical axis are collected through a high NA (0.95, 150X) Nikon objective and recorded by a charge-coupled device (CCD) camera (Fig. 2.3d). Since the focal spots are formed by interference of only the propagating components of the waves, they can be accurately recorded by this arrangement even though they measure smaller than the diffraction limit.

Figure 2.4 shows the diffraction patterns recorded at two different focal distances from the SOL. The smallest central spot with full width at half maximum (FWHM) measuring only 0.29λ is shown in Fig. 2.4a. However this spot formed at a distance

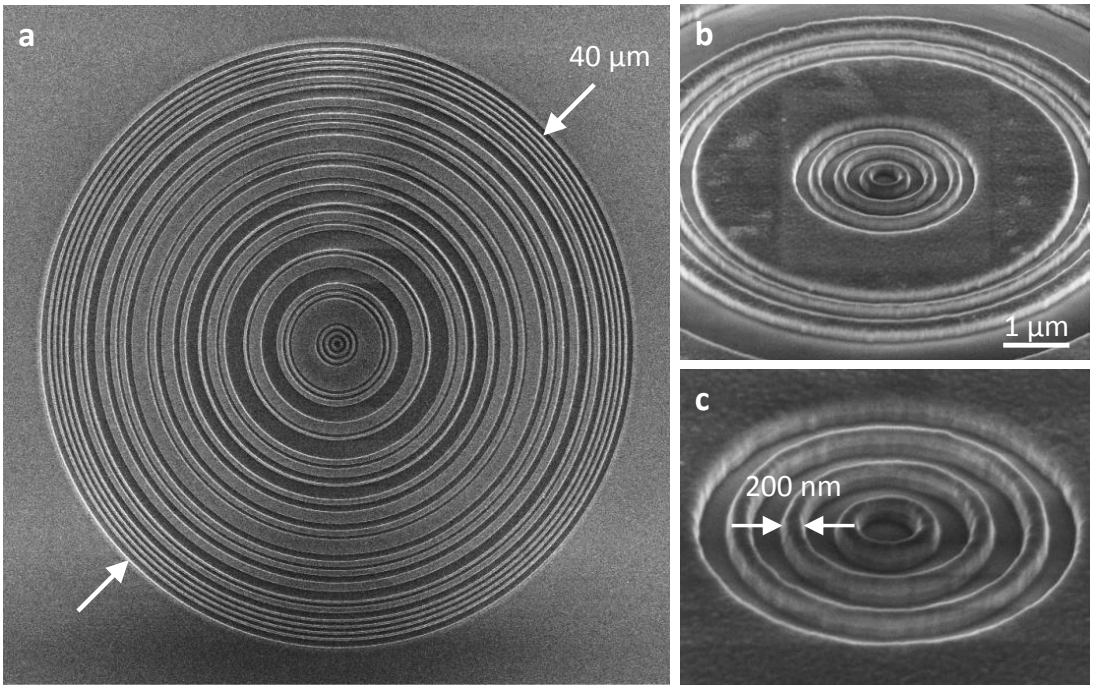

Figure 2.2: Design and structure of a SOL Scanning electron microscope images of the fabricated SOL (a) the entire mask with 40 µm diameter, (b) zoomed-in image of the central portion of the mask when the sample platform is tilted at 52°, (c) further zoomed in view showing the finest line width 200 nm.

4 µm ($\sim 6\lambda$) from the SOL, is accompanied by high intensity side-bands (Fig. 2.4c). Figure 2.4b shows a larger but just sub-diffraction-limited (FWHM $= 0.47\lambda$) spot. This spot is more intense with much lower intensity side-bands (Fig. 2.4d) and appears at 12.2 µm ($\sim 18.5\lambda$) from the SOL. As is observed from the entire experimental data set (presented later in Fig. 2.5), the smallest spots are accompanied with high intensity side-bands, which is a common characteristic of optical super-oscillation [33].

The effective NA given by a lens may be expressed as $\mathrm{NA_{eff}} = \lambda/(2\mathrm{FWHM})$. Using this formula the effective NA of the SOL at the above focal distances are calculated as $\mathrm{NA_{eff}} = 1.72$ at 4 µm and $\mathrm{NA_{eff}} = 1.06$ at 12.2 µm. It must be noted that in air, the medium used here, the maximum NA possible is 1. For comparison, the physical NA of the SOL is 0.98 at $z = 4$ µm and 0.85 at $z = 12.2$ µm where, $\mathrm{NA_{phys}} = n\sin(\tan^{-1}(r/z))$, with $n = 1$ the refractive index of air, $r = 20$ µm the radius of the SOL, and z the respective focal distances. Though the physical NA of the SOL is no better than that of the conventional lenses, the SOL provides better focusing performance when the hotspot sizes are considered.

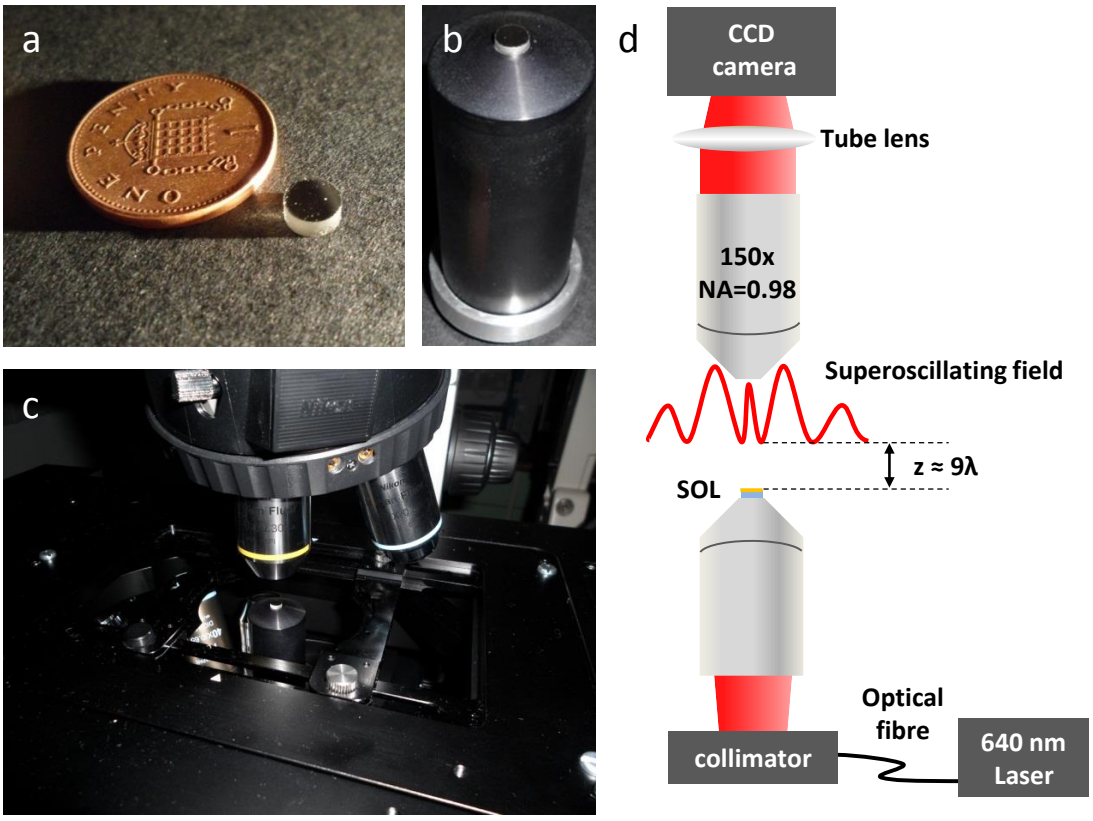

Figure 2.3: Experimental set up for SOL characterisation (a) aluminium coated round glass substrate hosting the nanofabricated SOL, (b) SOL on customised holder, (c) SOL replacing the conventional objective of an inverted microscope in a customised dual microscope set-up, (d) schematic presentation of the experimental set-up.

Figure 2.5 shows how the focal spots change along the propagation direction of the SOL. The intensity distribution across a propagation plane of the SOL is plotted. As noted by comparing Figs. 2.5a and 2.5b, there is good agreement between the experimental intensity distribution and the theoretical values obtained using scalar angular spectrum method. As seen in Fig. 2.5c smaller the the spots are, the lower their intensity. As described in section 1.2 this is a characteristic of super-oscillation. Figs. 2.5d shows the axial intensity distribution around the focal spots at 4 μm and 12.2 μm, the same spots as presented in Fig. 2.4. The smallest spot at 4 μm has very low intensity with high intensity regions along both the transverse and propagation direction. However, the spot at 12.2 μm is much more intense and looks like one produced by a conventional lens, except that it is not well localized along the propagation axis. In the later case an estimate for the focal depth is obtained to be ∼1.2 μm. In comparison, known focal depths for conventional high NA objectives are 0.4 μm for NA=0.85 and

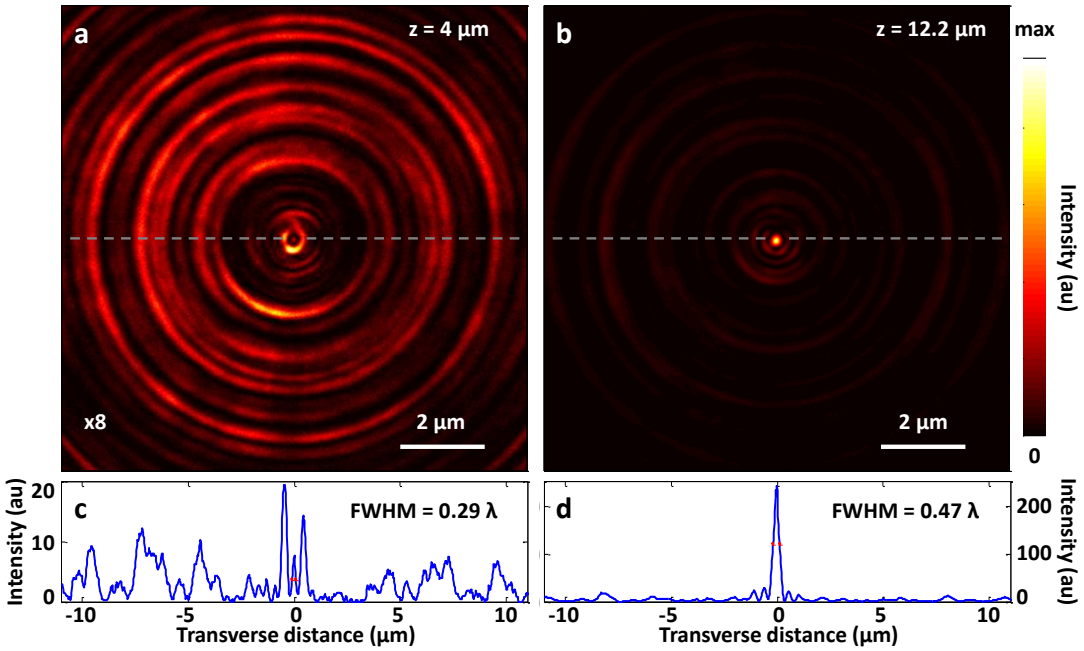

Figure 2.4: Intensity distribution produced by SOL (a) 4 µm, (b) 12.2 µm away along the optical axis. (c) and (d) shows lineout through (a) and (b) respectively providing an estimate of the central spot size, sideband intensity level, and isolation of the central spot from any high intensity sidebands.

0.19 µm for NA=0.95 [110].

2.1.4 SOL as super-resolution imaging device

Optical super-oscillation was known for some time as a means to focus light into spots smaller than the diffraction limit [28, 33, 38, 108, 109]. However, this was not seen as a practical means for achieving super-resolution imaging mainly due to the reason that the sub-wavelength hotspot is formed in a low intensity region with a neighbouring halo of much higher intensity. This was thought to have limited the field of view required for imaging. Also the energy contained in the super-oscillatory hotspot is only a small fraction of the total beam energy. Further, the type of optical super-oscillatory masks as proposed by Huang *et al* [38] demanded high precision nano-fabrication technologies which would produce a super-oscillatory mask with accurate, continuous, co-ordinate dependent phase retardation and transmission. The nano-fabrication challenge has been addressed, as presented in the sections 2.1.2 & 2.1.3, by experimentally demonstrating that a binary mask capable of modulating only the amplitude is sufficient for producing optical super-oscillation. In this section it will

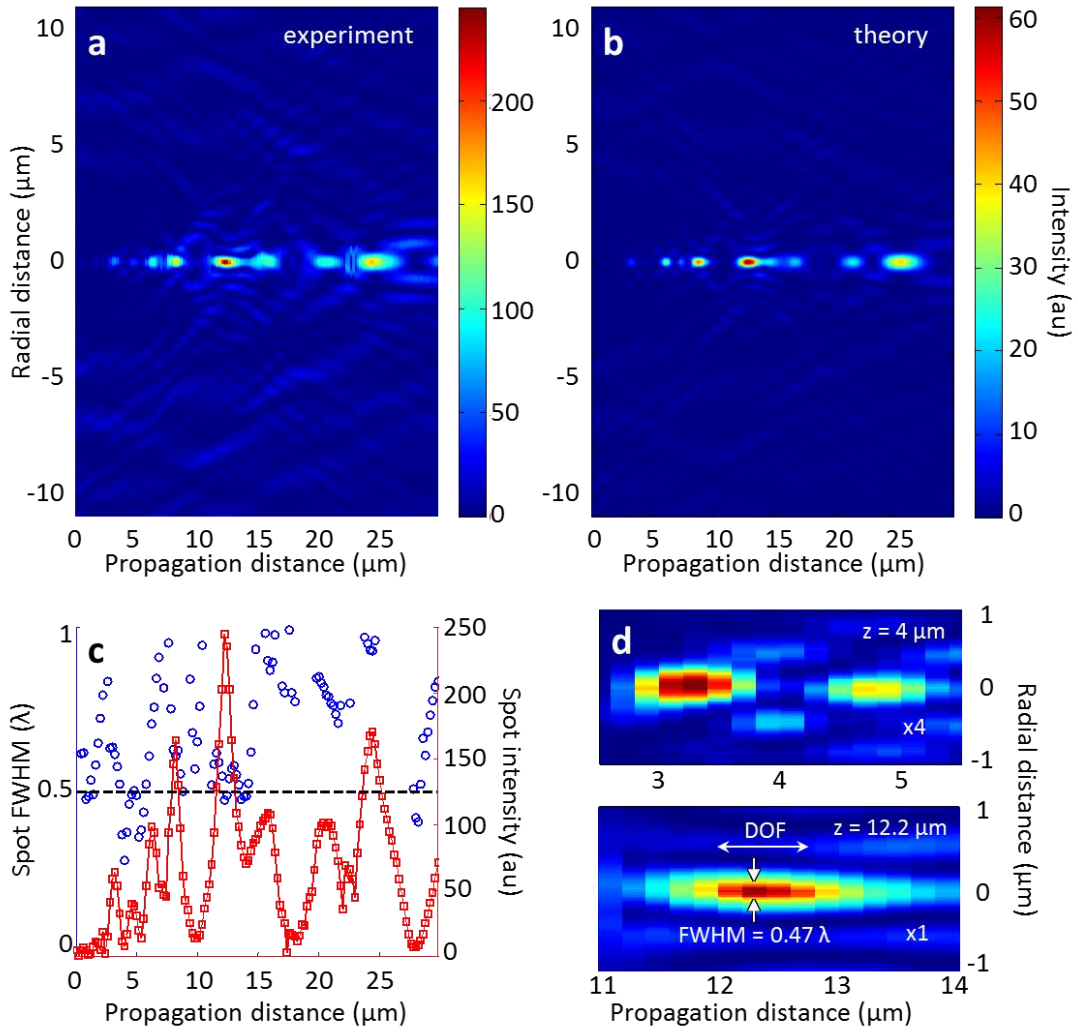

Figure 2.5: SOL intensity distribution along propagation direction (a) experimental, (b) theoretical results in good agreement with each other, (c) experimental distribution of FWHM and intensity of the central spot along propagation direction, (d) zoomed-in view of intensity distribution shown in (a) about 4 μm and 12.2 μm showing depth of focus for the later.

be demonstrated that such super-oscillatory binary masks producing sub-wavelength hotspots, even though accompanied by high intensity halos, can be useful for imagining with resolution exceeding conventional diffraction limited lenses. In fact it will be shown that the resolution achieved with the post-evanescent region super-oscillatory lens promises to exceed those demonstrated by other contemporary near-field super-resolution techniques [97, 99].

The imaging is performed by scanning the SOL generated hotspot across the object of choice. For image reconstruction the signal from the central part of the CCD detector is collected where the SOL hotspot would have been in the absence of the object. This method of scanning illumination and pinhole detection is similar to that used in confocal microscopy. This way the unwanted scattering from the annular halo around the spot is avoided.

In case of a conventional lens if the aperture is closed gradually while imaging a point-like source, the image spot size and the lens resolution will decrease. However for a SOL closing even a small part of its aperture may completely destroy the super-oscillatory intensity distribution which is formed by delicate interference of a large number of beams. It is this fragile nature of super-oscillatory hotspots that allow imaging features that cannot be otherwise resolved by diffraction-limited lenses. Even the tiniest object, smaller than the spot itself, may disturb the super-oscillatory field and hence the signal used for image reconstruction.

The SOL design used here is the same as that described above in section 2.1.2. The SOL is illuminated with 640 nm linearly polarised light, and the spots are formed in immersion oil. A spot at 10.3 μm measuring $\lambda/3.45$ in FWHM (Fig. 2.6) is selected to illuminate the objects to be imaged. The conceptual experimental set-up is schematically depicted in Fig. 2.7. In a customised dual microscope set-up, where an inverted and an upright microscope face each other along the optical axis, the SOL replaces the objective of the inverted microscope and illuminates the objects placed 10.3 μm away on a scanning sample stage. The transmitted signal from the object is detected by CCD camera through a Nikon immersion microscope objective (model VC100xH). The detector is a fast frame rate 16-bit resolution 5 megapixel Andor Neo sCMOS camera. The objects are placed on a X-Y nano-positioning piezo stage and are scanned across the SOL hotspot in 20 nm steps (Fig. 2.8b and Fig. 2.8d) or in

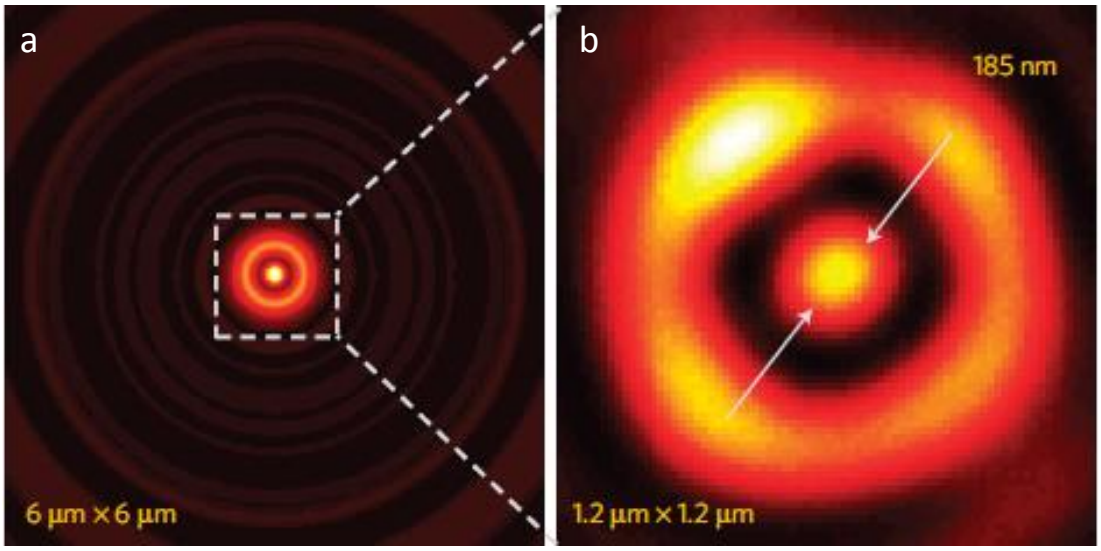

Figure 2.6: SOL hotspot for imaging (a) Theoretically predicted focal spot formed at 10.3 µm from the SOL (b) experimentally achieved focal spot. Spots formed in immersion oil ($n = 1.4$) with incident $\lambda = 640$ nm. Figure adapted from [104].

50 nm steps (Fig. 2.8g). For image reconstruction the detection region is chosen to be a factor of three smaller than the size of the hotspot on the CCD. The images (Fig. 2.8) are formed by simple point to point scanning operation without any deconvolution or post-processing, thus not requiring any prior information about the objects.

To test imaging capabilities of the super-oscillatory microscope a single slit 112 nm wide (Fig. 2.8a) and a pair of slits with 137 nm edge-to-edge separation (Fig. 2.8c) are fabricated on a 100 nm thick titanium film. The objects are scanned with 20 nm steps across the SOL hotspot. The reconstructed images are shown in Figs. 2.8b and 2.8d respectively. In the image the single slit is slightly widened to 121 nm while the gap between the pair of slits is still recognisable, measured as 125 nm. It is interesting to note that the same pair of slits are not resolved when imaged with a conventional liquid immersion lens with NA=1.4 (Fig. 2.8e). The measurements demonstrate that SOL is capable of recognising features smaller than 140 nm or $\lambda/4.5$ (with centre-to-centre distance $\lambda/2.6$) which is similar to the near-field plasmonic lens ($\lambda/3$ [97]) and 3D hyperlens ($\lambda/2.6$ [99]). But SOL has the clear advantage of placing the object beyond the near-field of the lens.

To demonstrate the ability of the SOL to image complex objects, a cluster of eight nano-holes with diameter $\sim$200 nm ($\lambda/3.2$) is fabricated on a 100 nm thick gold film with widely varying edge to edge separations (Fig. 2.8f). The hole cluster is scanned

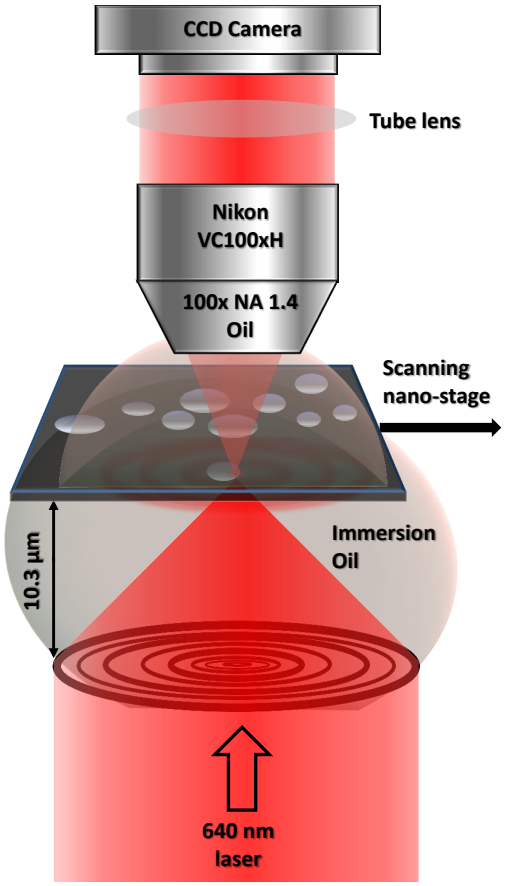

Figure 2.7: Schematic of imaging set-up with SOL Experimental set-up for imaging with SOL. Linearly polarised monochromatic light (640 nm illuminates the SOL from the backside. The sub-wavelength focal spot created by the SOL at 10.3 µm on the sample plane. The sample sits on a scanning stage with nano-scale precision, which moves the sample across the focal spot in sub-wavelength steps.

with 50 nm steps. When imaged with a SOL all major features are detected; holes separated by 105 nm ($\lambda/6$, or centre-centre distance $\lambda/2.1$) are clearly distinct. The two holes spaced 41 nm ($\lambda/15$, i.e. centre-to-centre $\lambda/2.7$) are also nearly resolved. These images indicate that scattering from the neighbouring halo into the detection area is not a major hindrance in imaging with SOL and results in hardly visible halos around the nano-holes. It may be noted that there is slight discrepancy between the SEM image of the nano-holes and the SOL image position. This is due to mechanical drift during the image acquisition process which takes 600 seconds for 2.75 µm by 2.75 µm sample area.

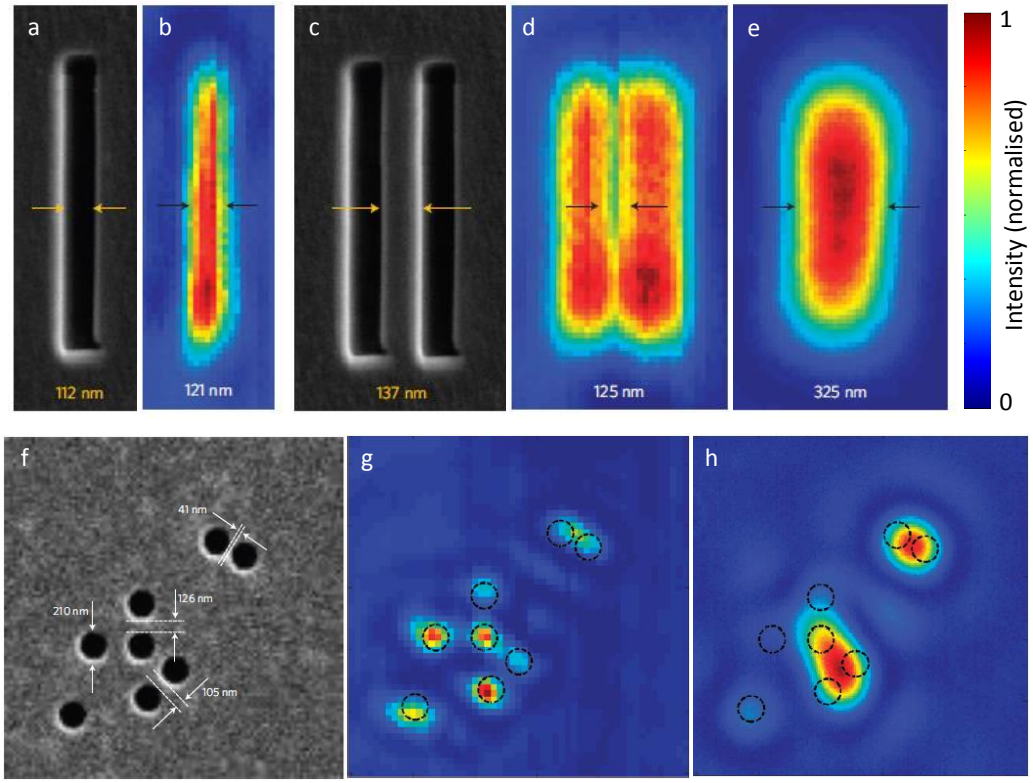

Figure 2.8: Super-resolution imaging with SOL (a) SEM image of a 112 nm slit, (b) its SOL image, (c) SEM image of a pair of slits, (d) resolved when imaged by SOL, and (e) unresolved when imaged by a conventional objective NA=1.4. (f) SEM image of a cluster of nano-holes, total field of view 2.75 μm by 2.75 μm, (g) mostly resolved when imaged by SOL, and (h) unresolved when imaged by a conventional lens NA=1.4. The dashed circles show the actual position of the holes. Figure adapted from [104]

2.1.5 Summary: SOL

To summarise, in this section a binary amplitude mask designed as a super-oscillatory lens is introduced. The SOL measures 40 μm in diameter and is fabricated on a 100 nm thin Al film. The SOL is characterised using monochromatic (λ =660 nm) plane wave illumination. Focal spots measuring smaller than the diffraction limit by up to 58% are recorded along the optical axis at several distances from the SOL. As examples, a very small spot at 4 μm and a not so small, but well isolated and brighter spot at 12.2 μm from SOL are presented. The SOL is then used as a imaging lens to study binary amplitude objects like nano-slits and cluster of nano-holes. The SOL can easily identify small features like nano-holes with edge-to-edge separation of $\lambda/6$, and can nearly resolve nano holes with $\lambda/15$ edge-to-edge separation; neither of these objects can be resolved by a conventional high NA immersion oil objective.

2.2 Optical needle super-oscillatory lens: ONSOL

2.2.1 Introduction

In this section another version of the super-oscillatory lens is introduced which, in contrast to the SOL, creates sub-diffraction-limited focal spots with high-intensity side-bands pushed farther away from the optical axis. Unlike the SOL, which produces one or more localised super-oscillatory hotspots along the optical axis, these new lenses are characterised by continuous distribution of sub-wavelength foci in the axial direction giving the impression of an 'optical needle'. Hence they are named optical needle SOLs (ONSOLs). In this section the ONSOL will be described in detail, as well as experimentally characterised in comparison with the SOL.

The concept and design of the ONSOL is provided by Dr. Salvatore Savo and Dr. Edward Rogers, the fabrication, experimental characterisation and data analysis are done by Tapashree Roy.

2.2.2 Design concept of ONSOL

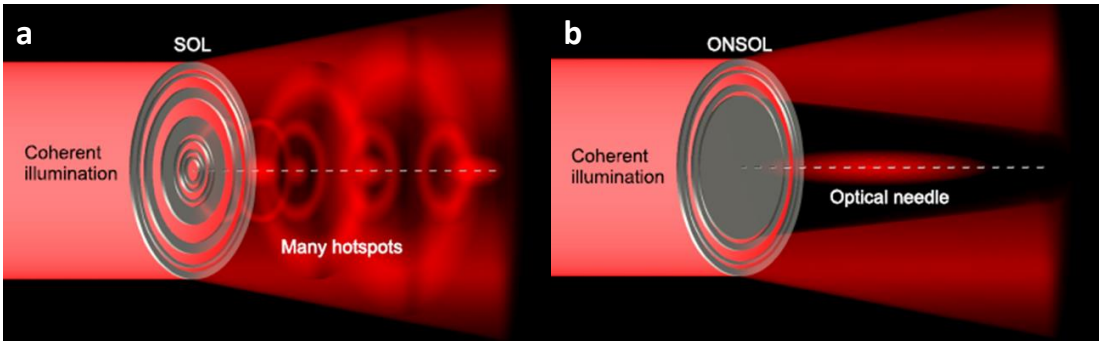

Figure 2.9: Comparison of SOL and ONSOL (a) The SOL produces a complex pattern of spots and side-bands at different distances from the lens. (b) The ONSOL produces a much simpler pattern with a sub-wavelength needle on the optical axis and side-bands far from the axis. Figure reproduced from [106], ©2013 AIP.

The design of an ONSOL is the same as that of a SOL, only difference being that the central region of an ONSOL is blocked by an opaque disk (Fig. 2.9b). The sub-wavelength spots are formed in the shadow of this central blocking region. This phenomena of forming the focal spot in the shadow of an obstacle is similar to a 200 year old concept, the Arago spot [7, 111]. In the year 1818, physicist Augustin-Jean Fresnel wrote an essay where he argued that if a point source illuminate a perfectly round

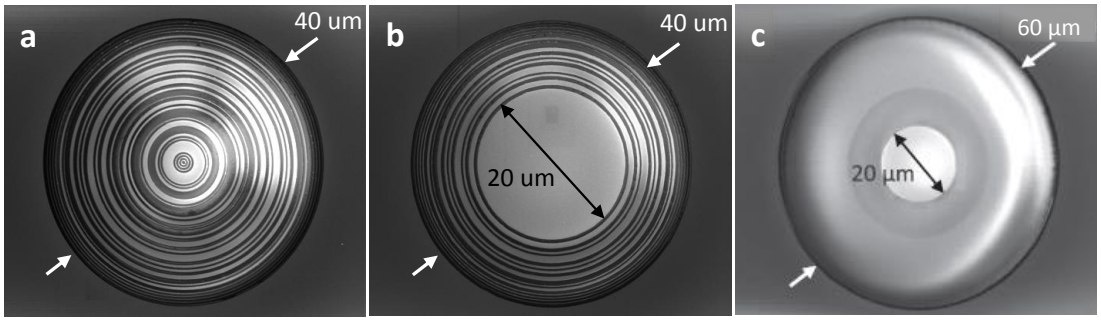

Figure 2.10: Comparison of design and structure (a) SOL, (b) ONSOL, and (c) a disk control sample with surrounding transparent region, all fabricated by milling 100 nm thick layer of gold. Figure adapted from [106]

object, there must occur a bright spot at the centre of the shadow cast by the object. This happens because the waves at the periphery must be in phase and hence the wave in the centre of the shadow must also be in phase resulting in the bright spot. After much controversy, experiments done by Fresnel and Franois Arago verified the claim. The result was also considered as a triumph of wave-theory over the then prevalent corpuscular theory of Newton. The working principle of ONSOL demonstrates that an age-old concept can be used to make a state-of-the-art imaging device.

Figure 2.10 shows the scanning electron microscope images of a SOL, an ONSOL, and a circular disk, all fabricated by milling a 100 nm thick gold film deposited on silica by thermal evaporation method. The ONSOL has 40 µm outer diameter, same as that of the SOL. The disk blocking the centre of the ONSOL measures 20 µm. A disk with 20 µm diameter within a 60 µm transparent region is also fabricated for control experiments. The design of the two super-oscillatory lenses are identical except the centre of the ONSOL is blocked by the opaque disk. The blocking region helps ONSOL push high intensity side-bands away from the central spot, while the remaining peripheral rings ensure that the high k vectors required for producing sub-diffraction-limited focal spots are preserved [106]. The increased field of view and the extended axial focal depth makes ONSOL a more practical choice over SOL for applications like photo-lithography and imaging of planar objects. However it may be noted that it is this needle like focal depth that may make imaging of 3D objects difficult for ONSOL.

2.2.3 Experimental characterisation of an ONSOL

The ONSOL is experimentally characterised and compared to the SOL and the Arago spot produced by a 20 µm diameter gold disk. All the three structures are illuminated with linearly polarised plane wave from a 640 nm wavelength laser. Diffraction patterns produced along the optical axis by each of the structures are individually recorded by a CCD camera through a high NA (0.95, 150X) Nikon objective. Figure 2.11 shows the intensity distribution across a plane in the propagation direction.

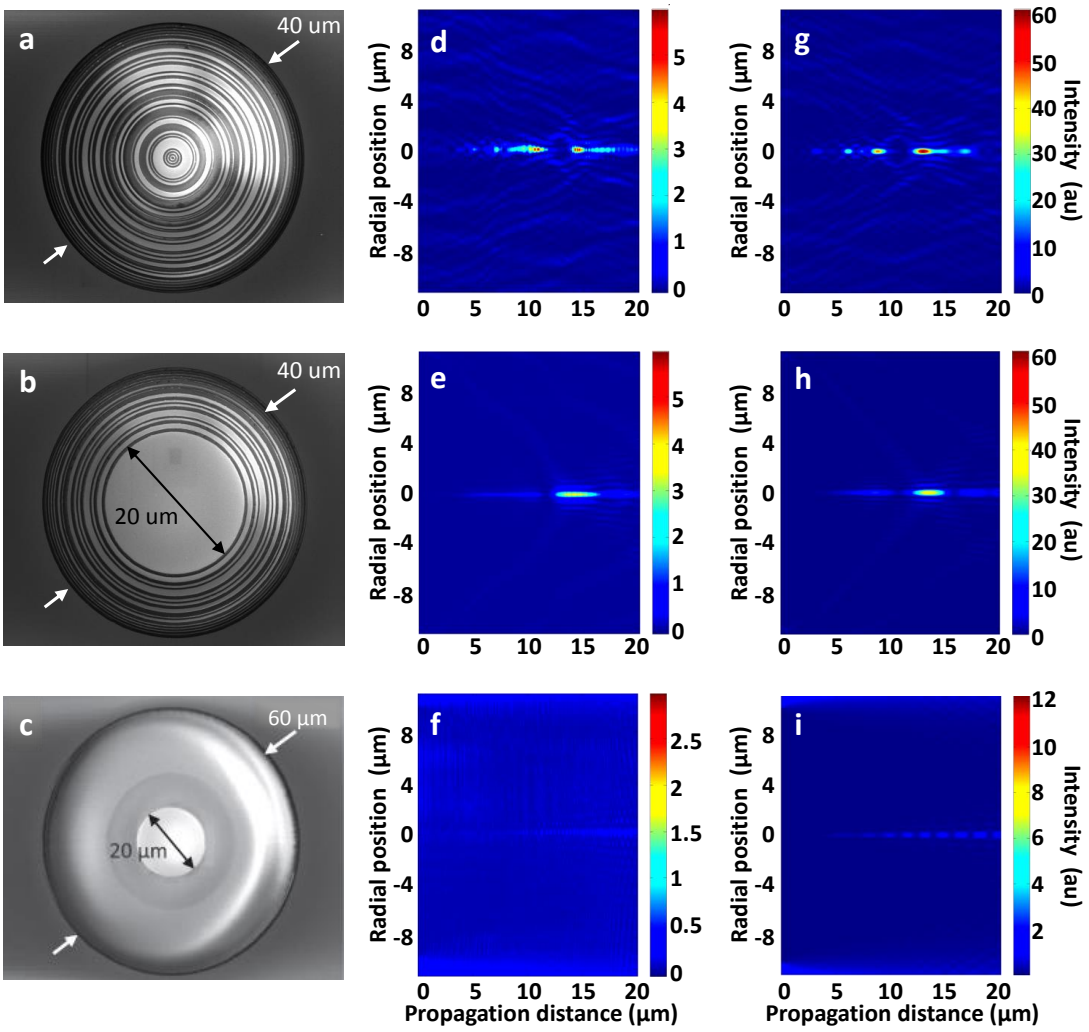

Figure 2.11: Intensity distribution along propagation direction Scanning electron micrographs of (a) SOL, (b) ONSOL, (c) control sample. (d)-(f) experimental and (g)-(i) simulated interference patterns due to SOL (d and g), ONSOL (e and h), and control sample (f and i). Note the different colour scales in (f) and (i) adjusted to improve the visibility of the very low intensity spots.

The experimental data (Figs. 2.11a - 2.11c) show good agreement with the simulated results (Figs. 2.11d - 2.11f) which are obtained using the scalar angular spectrum method (as in section 2.1). In case of the SOL (Figs. 2.11a and 2.11d) the sub-diffraction-limited focal spots appear localised at different distances along the propagation direction. But in case of the ONSOL (Figs. 2.11b and 2.11e) the focal spots remain continuously smaller than the diffraction limit for an extended distance resulting in an "optical needle". The needle starts at 4 μm from the lens, and persists for the next ∼7 μm. The control sample, as expected, forms a series of spots (Figs. 2.11c and 2.11f) but with almost 5 times lower intensity than that in the case of either SOL or ONSOL. This is an experimental manifestation of the well-known Arago spots formed in the shadow of the disc.

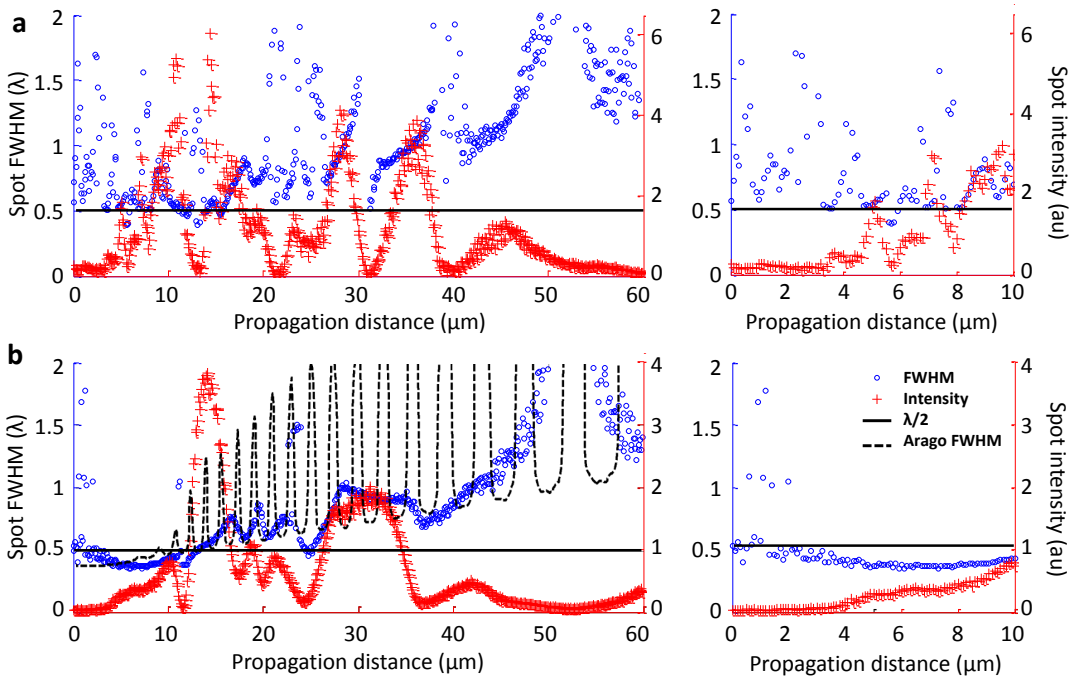

Figure 2.12: FWHM and intensity distribution along propagation direction (a) SOL, (b) ONSOL; each figure on the right hand side shows the corresponding zoomed-in view from 0 to 10 μm. The simulated FWHM of the Arago spot is shown in (b) as the dashed line.

Figure 2.12 shows the full width at half maximum and the intensity content in the focal spots as measured experimentally for both the SOL and the ONSOL. For the SOL, no sub-wavelength spots are formed beyond 15 μm. The smallest spot formed by a SOL is shown in Fig. 2.13a measuring 0.35λ at 5.7 μm from the lens.

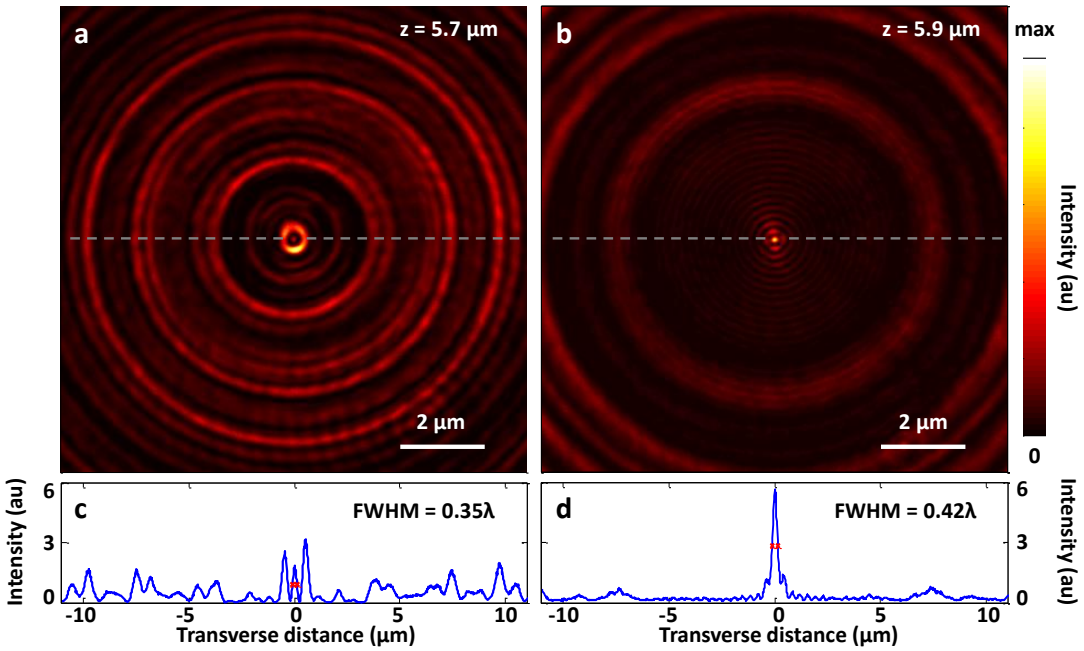

Figure 2.13: Comparing focusing of SOL and ONSOL Focal spots at (a) z =5.7 µm for the SOL and at (b) z =5.9 µm for the ONSOL. (c) and (d) show intensity profiles through the lines in (a) and (b), respectively.

The needle like formation of ONSOL intensity pattern with focal spot size smaller than the diffraction limit ($\sim \lambda/2$) is clearly demonstrated in Fig. 2.12b. The FWHM distribution of the ONSOL maintains a constant sub-wavelength width from about 4 µm to 11 µm. The intensity of this needle monotonically increases and varies by less than a factor of 2 between 5 µm and 9 µm. The smallest spot generated by ONSOL is found at 5.9 µm (Fig. 2.13b). This spot measures 0.42λ which is slightly larger than that in the case of the SOL, but has the advantage of being isolated from any significantly intense side-bands.

Interestingly, beyond 40 µm the FWHM distribution looks very similar for both the SOL and the ONSOL. The dashed line in Fig. 2.12b shows the simulated FWHM distribution for Arago spots formed by the 20 µm gold disk. The sub-wavelength spots close to the gold disc, as seen in the simulation, are of such low intensity that they cannot be measured experimentally.

Effect of central-block-size on ONSOL performance

Figure 2.14 shows simulated results on the effect of a change of blocking region diameter on the optical needle without varying the rest of the ONSOL. As might be expected from a consideration of simple diffraction effects, the main effect of increasing the size of the blocking region is to move the needle away from the ONSOL and to increase the size of the field of view around the needle. The intensity of the needle also reduces, primarily as a result of the lower overall transmission of the masks with larger blocking regions. For the diameter of 20 µm used in the experiments presented here, a reasonable compromise was achieved in terms of needle intensity and length while forming the needle far enough from the mask to be technologically useful.

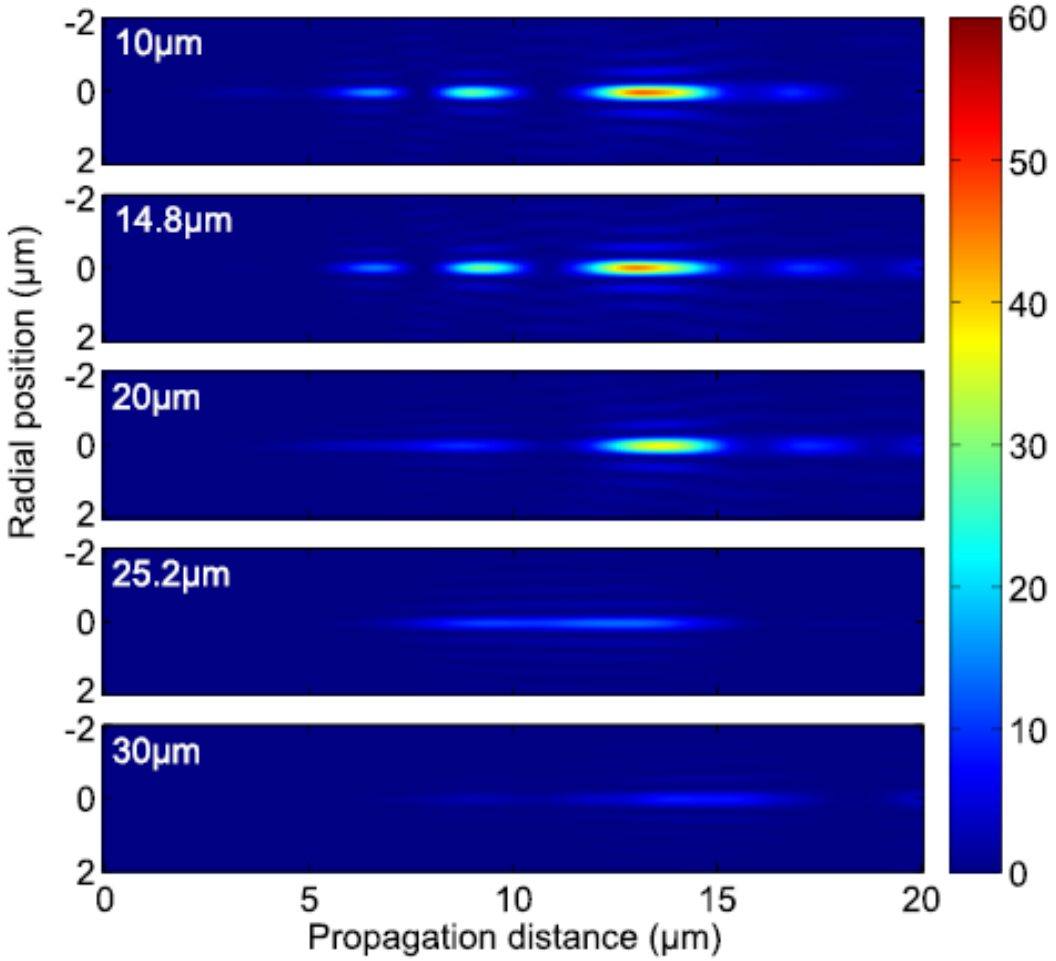

Figure 2.14: Effect of central block size on ONSOL Simulated optical needles formed by the ONSOL for various central block diameters. Figure reproduced from [106], ©2013 AIP.

2.2.4 Summary: ONSOL

To summarise, in this section an optical needle SOL is presented. The ONSOL is designed as a dark-field configuration of the standard SOL by blocking 25% of it's central area with an opaque disk. The ONSOL is studied both theoretically and experimentally in comparison to the SOL. When illuminated with monochromatic (λ =640 nm) plane wave, the ONSOL generates a continuous needle like intensity distribution along the optical axis with lateral FWHM smaller than the diffraction limit. The needle appears at a distance 4 μm from the ONSOL and remains up to 11 μm. However for SOL no such needle like distribution is observed; sub-wavelength hotspots appear at isolated positions along the optical axis. An important feature of ONSOL is that it is capable of pushing the high intense side-bands away from the optical axis, thus increasing the field of view for imaging applications. The absence of high intense side-bands and the appearance of optical needle make ONSOL a more suitable candidate than SOL for applications like photo-lithography and imaging of planar objects. However the down-side of the long depth of focus is that the ONSOL is not so suitable for imaging of 3D objects.

2.3 ONSOL performance for blue light

2.3.1 Introduction

In this section it will be demonstrated that optical needle super-oscillatory lenses produces sub-wavelength focal spots even when illuminated with light of shorter wavelength, i.e. in the blue part of the visible spectrum. For this demonstration two designs of ONSOL will be considered: (i) the already presented design, ONSOL-A (section 2.2) which is originally designed to work with 660 nm light, or red light, and (ii) a newly optimised design, ONSOL-B[1] that is designed for the purpose, to operate under blue illumination of wavelength 405 nm. Figure 2.15 shows the structures of the two ONSOLs. Both the ONSOLs are fabricated on 100 nm thick aluminium deposited by thermal evaporation on $\sim$ 170 µm thick silica substrate. Ion beam current measuring 93 pA was chosen for fabrication of both the designs.

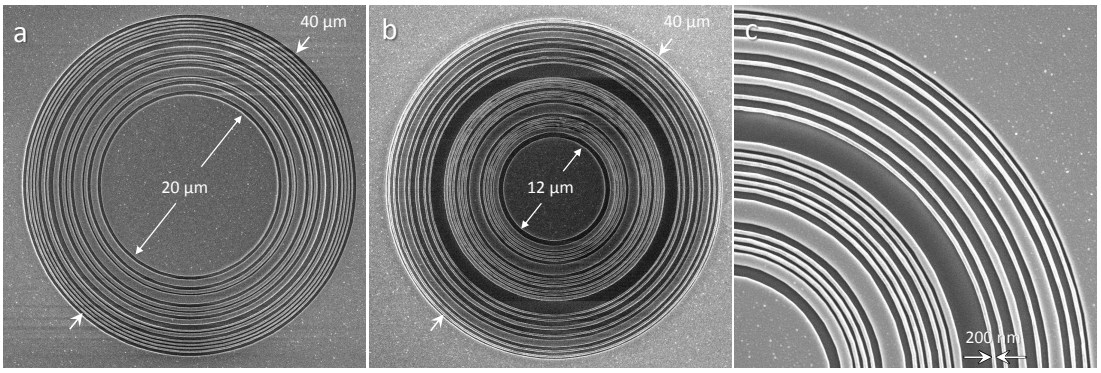

Figure 2.15: ONSOL designs for red and blue lights Scanning electron micrographs for ONSOL samples optimised for (a) 660 nm, design A and (b) 405 nm, design B. Both the samples are fabricated on 100 nm thin Al deposited on SiO_2. (c) Zoomed-in section of ONSOL B showing fabrication finesse.

In the following sections it will be experimentally demonstrated that a given ONSOL will form sub-wavelength focal spots for any illuminating wavelength, even though it is not optimised for that particular wavelength. Optimisation of an ONSOL for a particular wavelength ensures that the optical needle is formed at a prescribed location along the optical axis, with determined sub-wavelength size. However, for any other wavelength of illumination, the optical needle is likely to exist elsewhere along the optical axis.

[1]The author acknowledges contribution of Dr Yuan Guanghui for providing the design of ONSOL-B.

2.3.2 Characterisation of ONSOL-A

This section presents experimental characterisation of ONSOL-A when illuminated with 405 nm light. This particular design of ONSOL has been demonstrated (section 2.2) to form a sub-wavelength optical needle under 640 nm illumination. Here the incident illumination is changed to a shorter wavelength. The results are summarised below in Fig. 2.16.

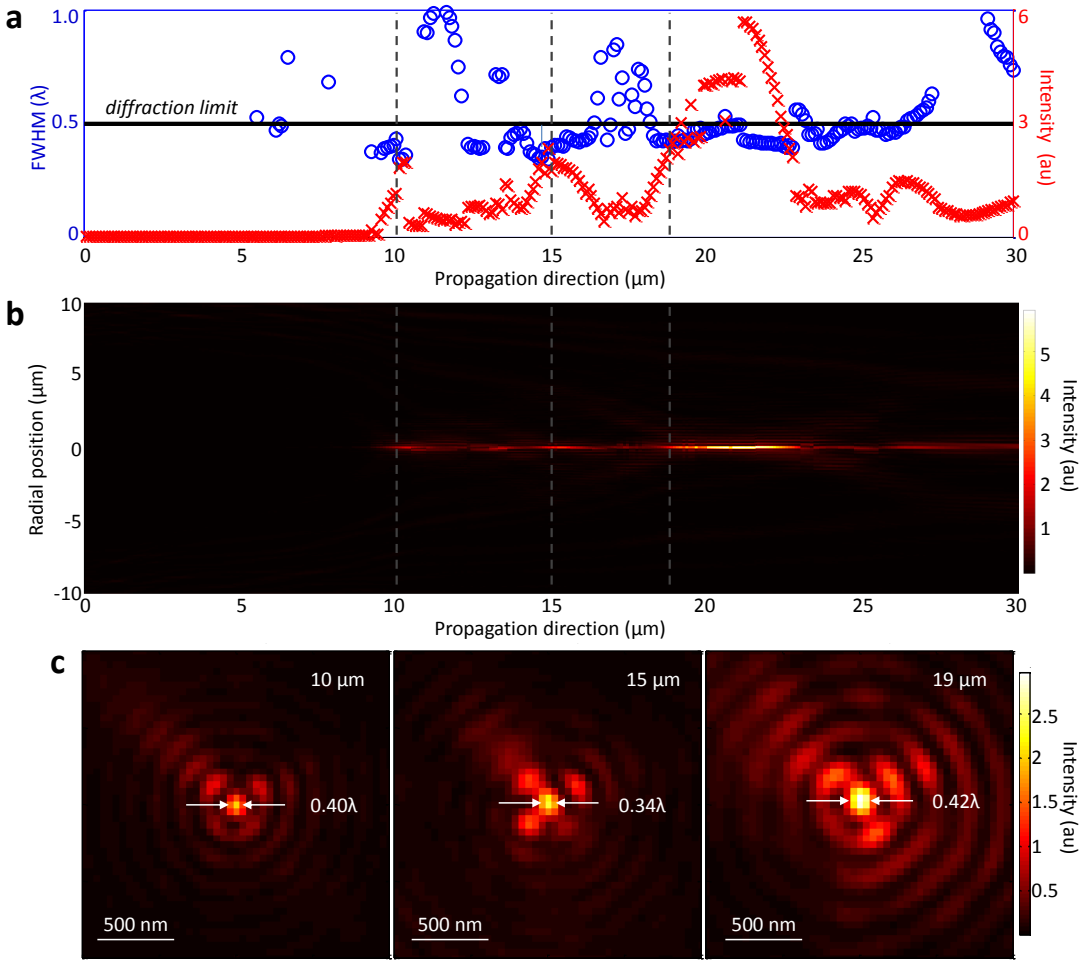

Figure 2.16: Performance of ONSOL-A with blue light (a)Experimental distribution of FWHM and intensity of the central spot along propagation direction. The solid black line shows the diffraction limit. (b) Intensity distribution along a plane through the optical axis of the ONSOL. (c) Intensity map at three representative focal planes where the spot measures smaller than the diffraction limit.

The ONSOL is illuminated with plane wave $\lambda = 405$ nm, and the transmitted intensity is recorded by a CCD camera through a high NA (150X NA 0.95) microscope-objective. The focal spots along the propagation direction is recorded up to 30 μm

while moving the ONSOL away from the objective in 100 nm steps. Figure 2.16 shows that even though not optimised for 405 nm, ONSOL-A produces optical needles with FWHM smaller than diffraction limit. The intensity (shown by red-crosses in Fig. 2.16a) is extremely low for the first 8 μm and hence no FWHM measurement can be obtained from the data. When Figs. 2.16a and 2.16b are studied together, sub-wavelength needles are observed around (i) around 10 μm extending for 1 μm along the optical axis with spots measuring 0.4λ, (ii) around 15.5 μm extending for 2 μm with spots measuring as small as 0.34λ, and (iii) around 20.5 μm extending for 4 μm with spots measuring as small as 0.42λ and with the highest intensity content compared to the former two needles. As representative images, three focal spots with their surrounding intensity distribution along a plane normal to the optical axis are shown in Fig. 2.16c. The one at 15 μm looks like the most useful, with good intensity content and the smallest FWHM amongst the three.

2.3.3 Characterisation of ONSOL-B

In this section an ONSOL will be experimentally characterised whose performance has been optimised for $\lambda = 405$ nm illumination. The ONSOL is designed using binary particle swarm optimisation, same way as described in the beginning of this chapter (section 2.1). The structure of the ONSOL is shown in Fig. 2.15b.

The ONSOL-B is experimentally characterised with linearly polarised blue light illumination in the same way as described above for ONSOL-A. The results are summarised in Fig. 2.17. By studying Figs. 2.17a and 2.17b together it is evident that there exist a long optical needle from 1 μm to 9 μm measuring as small as 0.35λ at 2.5 μm. The theoretically calculated FWHM is shown as green line in Fig. 2.17a which suggests a long continuous needle up to 10 μm from the surface of the ONSOL. The overall trend of the theoretical FWHM along the propagation direction matches well with the experimentally obtained data. Fig. 2.17c shows intensity distribution for three representative focal spots chosen from within the optical needle.

2.3.4 Summary: blue ONSOL

This section demonstrates that super-oscillatory optical needle lenses are likely to produce sub-wavelength spots somewhere along the optical axis irrespective of the wave-

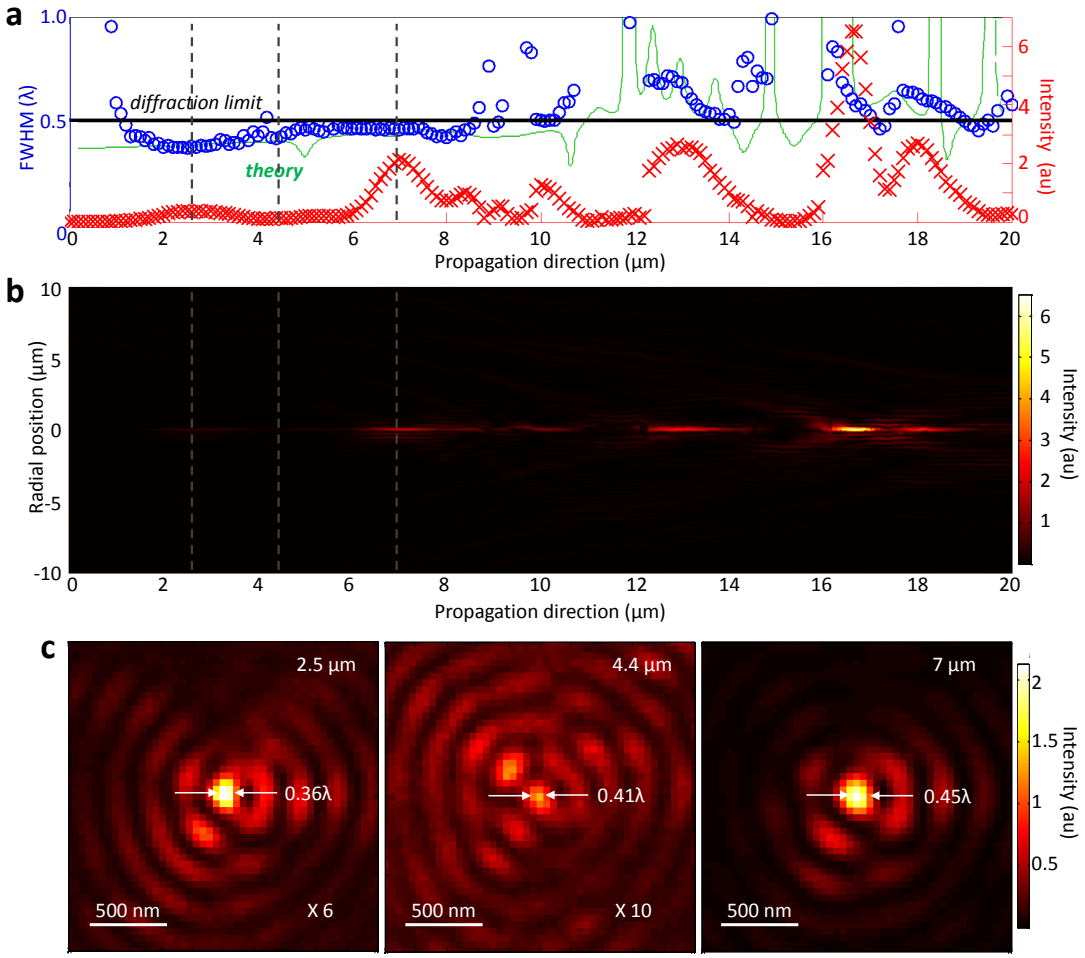

Figure 2.17: Performance of ONSOL B with blue light (a)Experimental distribution of FWHM and intensity of the central spot along propagation direction. The black line shows the diffraction limit. The green line gives the theoretically calculated value of FWHM. (b) Intensity distribution along a plane through the optical axis of the ONSOL. (c) Intensity distribution along three representative focal planes where the spot size measure smaller than the diffraction limit.

length of illumination. Even though not conclusive from a single case study, the following observation is made for ONSOL-A: when illuminated with 640 nm light (the wavelength at which it is designed), the ONSOL produces a ~ 7 μm long optical needle. But when it is illuminated with a shorter wavelength, its optical needle gets broken into smaller pieces and moves further away from the lens surface along the optical axis. The ONSOL-B is optimised for 405 nm light and produces an optical needle ~ 8 μm long; it agrees well with the simulated results.

2.4 Summary

In this chapter performances of super-oscillatory optical lenses (SOLs) are studied experimentally. SOLs are designed to make the propagating components of the incident wave interfere in a way such that the produced focal spots measure smaller than the diffraction limit. The SOLs are designed for a specified wavelength and field of view using an optimisation algorithm. The SOLs are fabricated as a binary pattern on thin (100 nm) metal (Al or Au) films which are then optically characterised with incident monochromatic, linearly polarised, coherent illumination. A SOL produces several sub-wavelength spots along the propagation direction, and the smallest focal spots are accompanied by a high intensity sideband. A suitable focal spot generated by a SOL is selected for demonstrating super-resolution imaging of binary objects. The sub-wavelength spot illuminates the object which is scanned in very small steps. Image is reconstructed from each frame as recorded by a CCD camera. The SOL can easily identify small features like nano-holes with edge to edge separation of $\lambda/6$, and can nearly tell nano holes $\lambda/15$ apart; neither of these features are resolved by a conventional high NA immersion oil objective.

A particular kind of SOL (ONSOL) demonstrates a typical behaviour forming continuous distribution of sub-wavelength hotspots along the optical axis, resulting in an optical needle. Structure-wise ONSOLs are similar to SOLs, except their centres are blocked by an opaque disk. The sub-wavelength needle forms in the shadow of this disk, which is similar to Arago spot where a diffraction-limited focal spot is formed in the shadow of an opaque disc when illuminated from behind. ONSOLs presented here has shown sub-wavelength optical needles extended for 10 μm along the optical axis. Compared to the SOLs, the ONSOLs are characterised by large field of view, i.e. the high intensity sidebands around the focal spots are pushed much farther away from the central hotspot. Hence the ONSOLs are preferable for super-resolution applications like imaging, photo-lithography and/or data storage.

Finally it is demonstrated that ONSOLs tend to produce sub-wavelength focal spots even when illuminated with wavelength for which the design was not optimised. An ONSOL if illuminated with shorter wavelength than that for which it was optimised, the optical needle breaks into several pieces and moves farther along the optical axis.

3

Super-oscillatory point-spread functions

3.1 Introduction

Diffraction causes the image of a point object to appear as a hotspot of finite radius accompanied by annular bands of weaker intensities, even when observed through an ideal lens. The intensity distribution of the image of the point object is commonly known as the point spread function (PSF) [112]. The specific form of this PSF for an ideal lens is known as the Airy pattern after the 19^{th} century astronomer Sir George Biddell Airy who was the first to describe such spreading of light [113]. The minimum radius of the hotspot of an Airy pattern is limited by diffraction, with full width at half maximum (FWHM) measuring $\lambda/2\text{NA}$ (where λ is the wavelength and NA is the numerical aperture of the microscope objective). For normal incoherent imaging, the image of an extended object is the convolution of the object with the PSF of the system and, hence, the size of the PSF determines the resolution of the microscope. Methods of reducing the size of the PSF of an optical system by using modified pupil functions were first described in 1952 by Toraldo di Francia [28] and they have since been studied extensively (a recent review article [114]) and their use in practical imaging systems has also been demonstrated [46, 47, 108, 115–118].

Recently a class of optical lenses based on the principle of super-oscillation [32, 33] has been proven to focus light smaller than the diffraction limit [35, 38–41]. One particular class of super-oscillatory lenses is an amplitude mask designed to diffract an incident plane wave into arbitrarily small hotspots at post-evanescent distances from the lens (chapter 2). These super-oscillatory lenses have been used in a scanning

imaging system [104] to demonstrate resolution surpassing that of diffraction limited systems 2.1.4. This particular type of super-oscillatory lens (SOL) is designed to focus a plane wave into several isolated sub-wavelength focal spots at different distances along the optical axis. A variation of the SOL [106] focuses light into a sub-wavelength needle and is termed the optical needle super-oscillatory lens (ONSOL) (section 2.2). In this chapter the imaging performance of a super-oscillatory microscope will be studied both numerically and experimentally. In a super-oscillatory microscope, the objective is replaced by either a SOL or an ONSOL. The performance of such microscope is measured by studying how accurately a point object can be imaged, or in other words by the measure of the PSF. It will be demonstrated here that a super-oscillatory lens reduces the size of the point spread function below the conventional diffraction limit.

In the following sections a numerical study comparing the PSF formed by a super-oscillatory lens and an optical-needle-super-oscillatory lens will be presented. It will be demonstrated that for a given object and image distance, the PSF formed by an ONSOL is more robust to any object displacement in the direction perpendicular to optical axis. After establishing that ONSOL is a better choice over SOL for practical imaging and lithography applications, an experimental study of the ONSOL imaging performance will be demonstrated. Finally, scan-less, single-capture imaging of two or more points placed within the field of view of an optical needle lens will be numerically studied, establishing that ONSOLs provide better resolution than that dictated by diffraction limit.

3.2 Imaging a point source with super-oscillatory lenses

3.2.1 Numerical study of super-oscillatory PSFs

The characteristics of super-oscillatory PSFs formed by the lenses described in chapter 2 are studied numerically in this section. A luminous point object is placed at a pre-determined distance from each of the super-oscillatory lenses (SOL and ONSOL). Light propagates from the point object through free space and illuminates either of the lenses. The lens modifies the intensity which then propagates on to the image plane and gets imaged at some distance from the lens. The image formed, as with conventional lenses, is not a point but a hotspot surrounded by annular rings. However, in this case, the size of the hotspot in the PSF is smaller than the limit set by diffraction limit. The propagation of light from the point object to the lenses and on to the image plane is simulated using scalar angular spectrum method [43], which has previously been shown to be suitable for these types of propagation problems [106].

It has been shown (chapter 2) that both types of super-oscillatory lenses (SOL and ONSOL), when illuminated with plane wave, produce sub-wavelength focal spots only at certain distances from the lens. While imaging a point object with such super-oscillatory lenses, it is intuitive that the image of the object will be sub-wavelength only under certain conditions, or at pre-determined object-image distance pair. To find a suitable object-image distance pair, for which both SOL and ONSOL would produce sub-wavelength PSFs, the following numerical experiment is performed. Monochromatic light with wavelength 640 nm from a point source (∼100 nm diameter) propagates through free space and illuminates each lens (placed at distance D_{object} from the source). The PSF formed is imaged on the other side of the lens (at a distance D_{image} from the lens). To systematise the study, a parameter ρ is introduced which is given by the ratio of D_{image} to D_{object}. For example, when $\rho = 0.5$, the image plane is half the distance of the object plane from the lens. For a given object-image distance pair the full width at half maximum (FWHM) of the hotspot of the PSF is measured. For different values of ρ Figs. 3.1b & c show how FWHM of the PSF changes as the point source is moved away from the lens.

Figure 3.1b shows for the SOL how the FWHM of the PSF changes with object distance for $\rho = 0.36, 0.5, 1, 1.5$. For any value of ρ the FWHM goes below the diffrac-

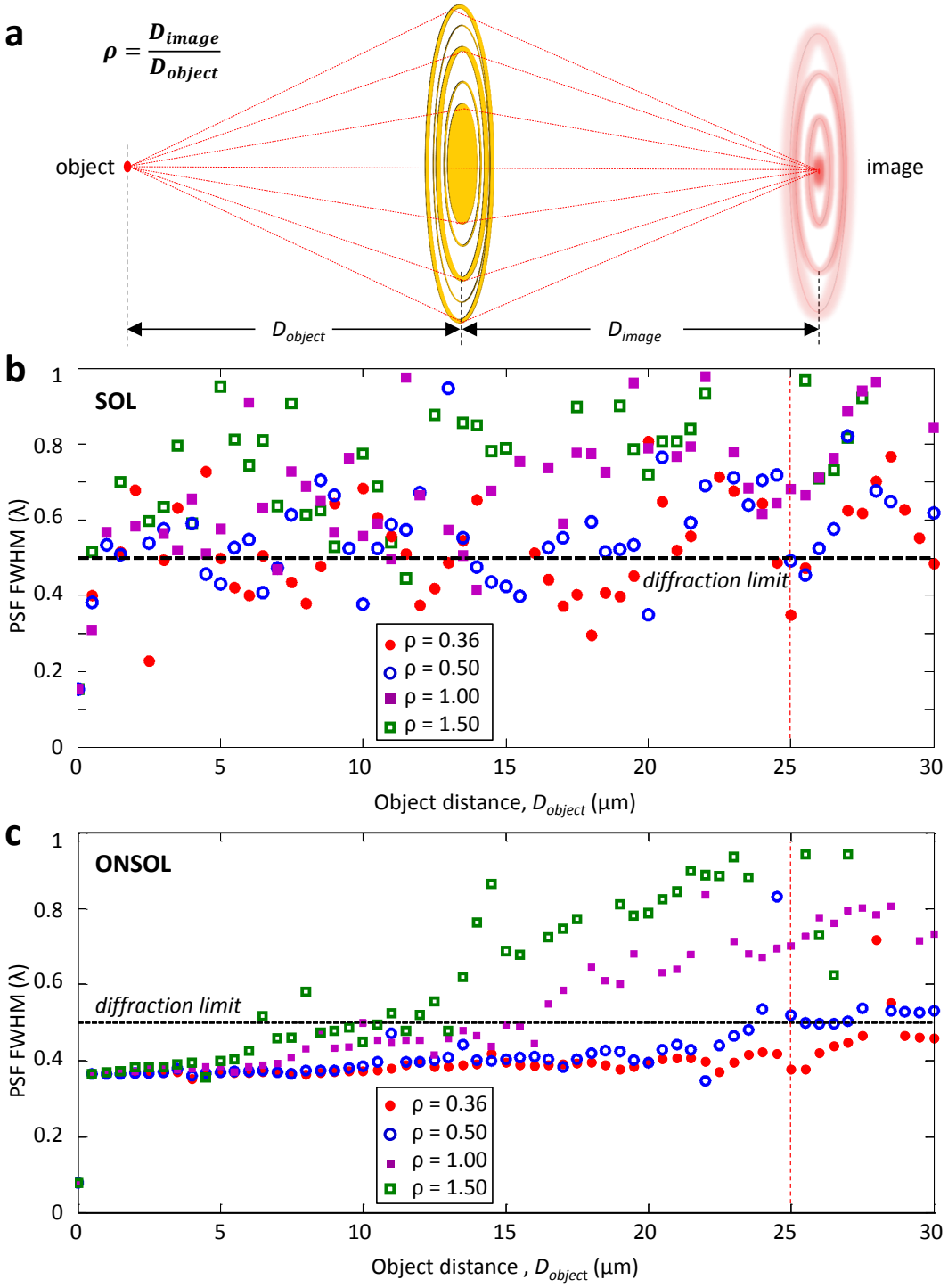

Figure 3.1: Finding object-image distance pair for imaging with SOL and ONSOL (a) Schematic representation of imaging with a super-oscillatory lens. Parameter ρ is introduced as the ratio of image distance to object distance. (b) Size of the image hotspot formed by a SOL for increasing object distance. (c) Size of the image hotspot formed by an ONSOL for increasing object distance. Different symbols in (b) and(c) represent different values of $\rho = 0.36, 0.5, 1, 1.5$.

tion limit only at isolated object distances. This is expected from the previous study of focusing characteristics of SOL (chapter 2). For increasing values of ρ the number of sub-wavelength PSFs formed at various object distances become fewer. In comparison, Fig. 3.1c shows for ONSOL the FWHM distribution with increasing object distance for the same values of ρ. For a given ρ, the FWHM remains continuously sub-wavelength until a certain object distance. The value of D_{object} until which FWHM remain sub-wavelength decreases with increasing ρ. From this study an object-image distance pair for which FWHM remain sub-wavelength for both the SOL and the ONSOL is chosen; this is shown by the vertical dotted red lines in Figs. 3.1b & c when, $D_{object} = 25$ µm and $\rho = 0.36$, i.e. $D_{image} = 9$ µm.

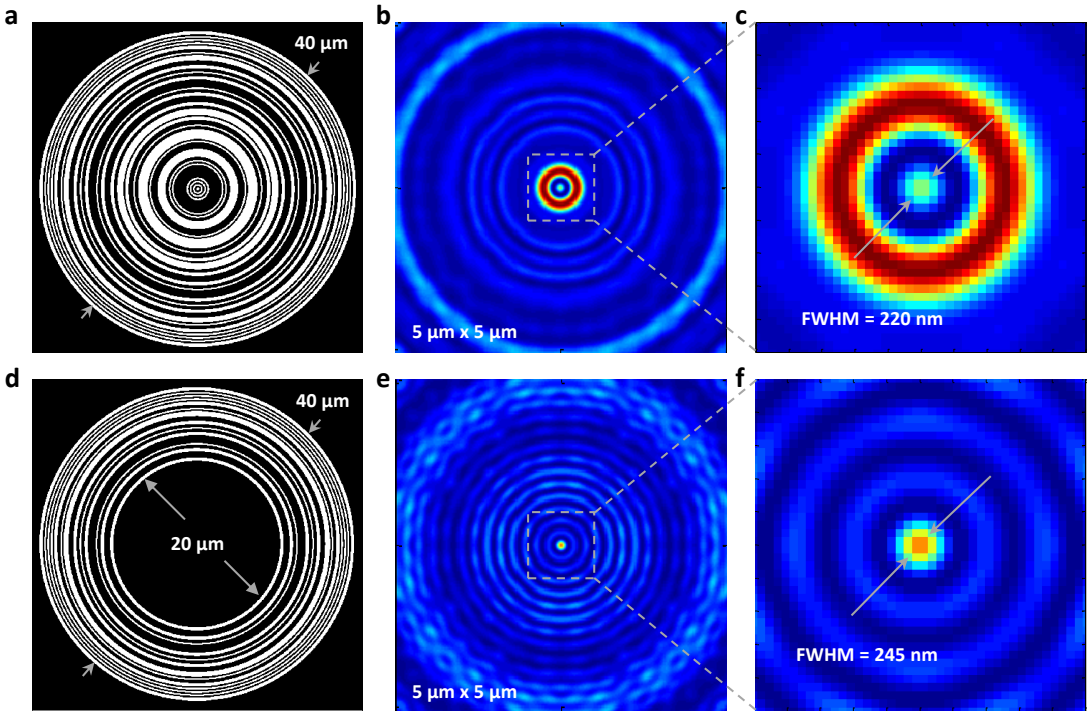

Figure 3.2: Comparison of simulated super-oscillatory PSFs formed by a SOL and an ONSOL. Mask designs of (a) SOL, and (d) ONSOL. PSF generated 9 µm away from the (b) SOL and (e) ONSOL when a 100 nm circular aperture is placed 25 µm away. Central intensity distribution of PSF generated by (c) SOL and (f) ONSOL, λ =640 nm.

Figure 3.2 presents a comparison of PSFs formed by the ordinary super-oscillatory lens and the optical-needle super-oscillatory lens for the chosen object-image distance pair ($D_{object} = 25$ µm, $D_{object} = 9$ µm). The designs of the SOL and the ONSOL are shown in Figs. 3.2a and 3.2d respectively, which are the same as previously studied in sections 2.1 and 2.2. The two designs are identical expect that the centre of the

ONSOL is blocked by a 20 μm diameter disc. This blocking region helps the ONSOL push high intensity sidebands away from the central spot, while the remaining peripheral rings ensure that the high k vectors required for producing sub-diffraction-limited focal spots are preserved [106]. Figures 3.2b and 3.2c show the PSF generated by the SOL, with a hotspot measuring 0.35λ and accompanied by an intense ring around the spot. The ONSOL generates a PSF with a hotspot measuring 0.38λ, still beating the diffraction limit but with much lower intensity annular rings (Figs. 3.2e and 3.2f). For comparison, a high NA (0.95) microscope objective would form a PSF with hotspot FWHM measuring $\sim 0.53\lambda$. For a conventional lens, the FWHM of the PSF is given by $\lambda/2\text{NA}$. Therefore, an effective NA is defined for these super-oscillatory lenses as $\text{NA}_{\text{eff}} = \lambda/2\text{FWHM}_{\text{PSF}}$. This formula gives $\text{NA}_{\text{eff, SOL}} = 1.43$ and $\text{NA}_{\text{eff, ONSOL}} = 1.31$; note that the maximum possible NA for any conventional lens in air is 1.

From the study so far, let us draw comparison between a conventional lens and the two kinds of super-oscillatory lenses (SOL and ONSOL) presented here. A conventional convex lens images a point object into a hotspot of finite size (limited by diffraction) surrounded by much fainter annular rings. A super-oscillatory lens images a point object into a hotspot measuring smaller than the diffraction limit, but with higher intensity annular sidebands. An optical-needle super-oscillatory lens still images the point object into a sub-diffraction size hotspot with an added advantage, that the high intensity sidebands are pushed far from the centre. For a fixed object distance, a conventional lens produces the best image at a fixed distance only. However, for the same situation a super-oscillatory lens may produce multiple images along the optical axis (Fig. 3.3a). This implies super-oscillatory lenses are characterised by multiple foci, unlike ordinary lenses (demonstrated in chapter 2). For this reason the conventional thin lens formula [112] $1/f = 1/u + 1/v$, (f is the focal length, u is the object distance, v is the image distance) may not be readily used for super-oscillatory lenses. The applicability of this formula for super-oscillatory lenses is tested here, as summarised in Fig. 3.3.

Figure 3.3b shows the object distance versus the image distance plot for an ordinary lens, and the two kinds of super-oscillatory lenses. In the above numerical experiment when the object is $u = 25$ μm from the super-oscillatory lens, an image is formed at $v = 9$ μm on the other side of the lens. The thin-lens formula suggests that the lens

should have an effective focal length of 6.6 μm. Figure 3.3b shows a plot of this formula for the calculated focal length. The SOL and the ONSOL matches this curve at the chosen object and image distance. It is now checked if the super-oscillatory lenses follow the ordinary lens curve away from this point. To derive the u vs. v curve for the super-oscillatory lenses a set of numerical experiments are done. For a fixed object distance (u) the size of the PSF is calculated for a number of image distances (v), as shown in Fig. 3.3a. This is repeated for a number of object distances (u = 10 μm to 32 μm). For each u, the super-oscillatory lenses form sub-diffraction images at multiple distances along the optical axis. In each case, the image distance closest to the thin-lens curve is chosen and plotted in Fig. 3.3b . As observed from Fig. 3.3b, for both the SOL and the ONSOL the image distance decreases with increasing object distance. At first glance this may seem to follow the thin-lens formula (solid black line) for slightly different f. But a much better fit is obtained using a slightly modified formula, $1/u+1/v = 1/a(1-b/uv)$, which matches the thin lens formula when $b = 0$ and $a = f$. So, the super-oscillatory lenses do not readily follow the ordinary thin lens formula. The may be explained by higher than ordinary effective-NA of super-oscillatory lenses and multiple focal lengths for a given lens design and wavelength.

Next, another lens-like behaviour of the super-oscillatory lenses is investigated. For a conventional lens if the object is displaced perpendicular to the optical axis and the corresponding image moves in the opposite direction. This characteristic will be tested for super-oscillatory lenses. For this numerical experiment the object-image distances are kept the same as above (u = 25 μm, v = 9 μm.) for both the SOL and the ONSOL. Figures 3.4a - 3.4g show the image displacement for SOL when the point source is displaced by 3 μm on either side of the optical axis. When the point source is perfectly aligned with the optical axis (Fig. 3.4d), the PSF appears same as in Fig. 3.2b; note the difference in appearance is only due to different colour scales for intensities. As the point source is displaced from the optical axis (Figs. 3.4d - 3.4g), the image moves opposite to the direction of object movement and the central spot in the PSF moves by 500 nm for every 1 μm object movement. At the same time, the central spot distorts and decreases sharply in intensity while the sidebands increase in intensity and become more and more asymmetric. When the object is displaced by 3 μm, the central spot becomes difficult to recognize (compare Fig. 3.4d with Figs. 3.4g). The trend is the

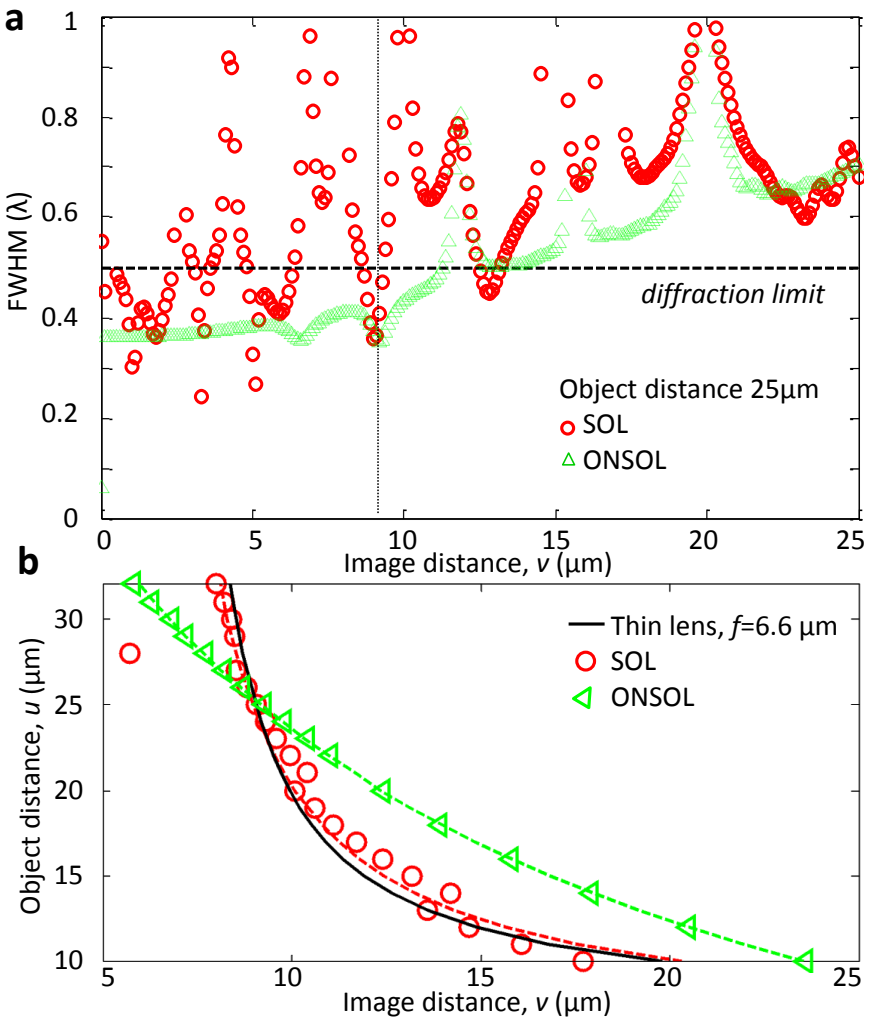

Figure 3.3: Image formation by super-oscillatory lenses (a) Size of image hotspot with increasing image distance, as imaged by a SOL and an ONSOL when a point object is placed at 25 μm . (b) Image distance vs. object distance for a conventional lens with focal length 6.6 μm compared to that for a SOL and an ONSOL.

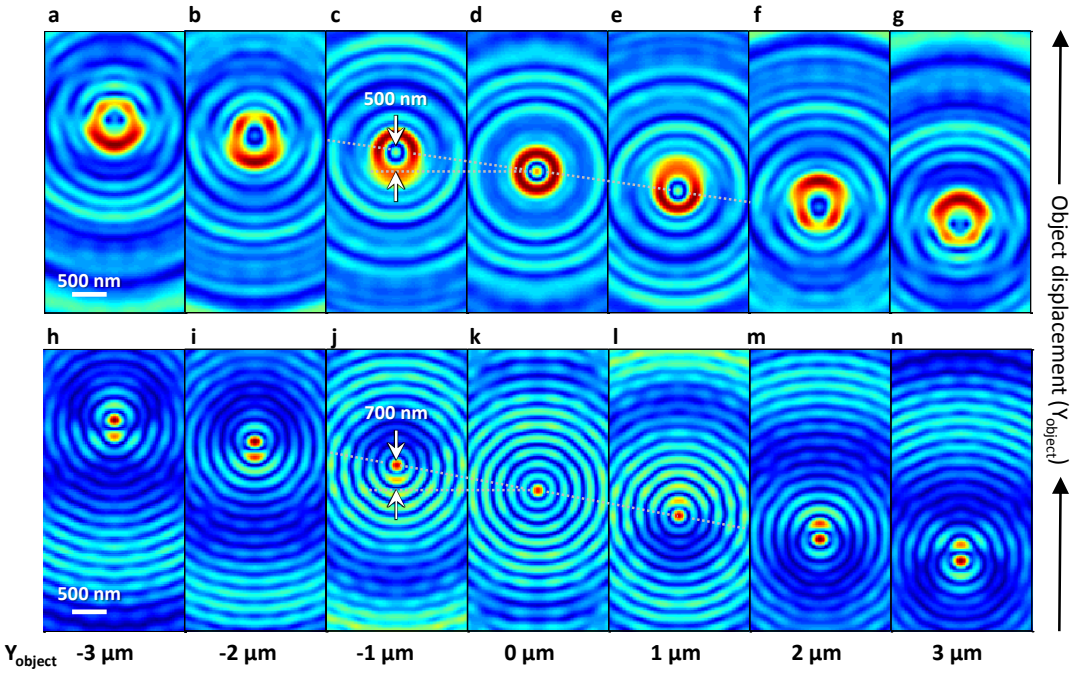

Figure 3.4: Effect of object displacement super-oscillatory PSFs A point object is displaced laterally by 3 µm on either side of the optical axis of the lenses. Corresponding displacement of the PSF formed by SOL (a-g) and ONSOL (h-k).

same as the point source moves to the other side of the optical axis (Figs. 3.4a - 3.4d). For the ONSOL, the direction of relative movement of the point source and the PSF is the same as in the case of SOL. Interestingly, the ONSOL PSF is more robust to object displacement than that of the SOL. For this particular object-image distance pair, the intensity content in the central spot of the ONSOL increases with displacement of the point source (Figs. 3.4k - 3.4n). The central spot is still recognizable when the object is displaced 3 µm off the axis, though the spot becomes slightly elliptical. In this case also, the sidebands become more and more asymmetric with increasing off-axis object placement, though most of the energy remains in the central spot. This distortion is because the super-oscillatory PSFs are formed by delicate interference of a large number of beams, and any misalignment of the point source is transferred to the image plane as distortion of the sidebands and the central spot. Note that for ONSOL the central spot in the PSF moves by 700 nm for every 1 µm object movement (Figs. 3.4j and 3.4k). This is different to that of the SOL, even though the object and image positions (u and v) remain the same. For a conventional thin lens the image displacement for a given object displacement depends on u and v, which in turn

are related by the focal length f. But as mentioned before super-oscillatory lenses though display lens-like characteristics (focusing plane wave, forming PSF, and inverse object-image displacement) cannot be simply explained by the known thin-lens formula. Amongst themselves, SOL and ONSOL function in different ways, one focusing plane wave into multiple isolated sub-wavelength foci and the other producing an extended sub-wavelength needle, through complex interference of multiple beams. Hence it is no surprise that their imaging characteristics are slightly different even for the same pair of u and v. Note that compared to the SOL, ONSOL is characterised by an increased field of view and robustness of the super-oscillatory sub-wavelength PSF to off-axis placement of the object. These features make ONSOL suitable for high speed processing applications including imaging and photolithography.

In the following section the imaging performance of the ONSOL will be experimentally demonstrated.

3.2.2 Experimental characterisation of ONSOL point spread function

The experimental arrangement for imaging a point source with an ONSOL is schematically presented in Fig. 3.5. To approximate the point source a 640 nm linearly polarised laser is coupled into a scanning near field optical microscope (SNOM) probe with 100 nm aperture at the tip. A conventional microscope with high NA objective (Nikon CFI LU Plan Apo EPI 150X, NA=0.95) is used to record the PSF created by the ONSOL. Since the super-oscillatory PSFs are formed by interference of propagating waves, they can be imaged by a conventional objective. The imaging objective is kept fixed at 9 μm from the ONSOL — as in the simulations. The SNOM tip is placed on the optical axis and moved away from the ONSOL in 100 nm steps, to find the object position that forms a PSF with sub-diffraction-limited hotspot at the pre-fixed imaging distance.

Figure 3.6 summarises the experimental imaging performance of ONSOL. The lens (Fig. 3.6a) is fabricated by focused ion beam milling of a 100 nm thick gold layer deposited on a 50 nm thick silicon nitride membrane. The lens structure is illuminated with light from the SNOM tip, which approximates a point source. As the object scans along the optical axis, the PSFs formed at the fixed imaging distance (9 μm) are recorded. A PSF with hotspot FWHM smaller than the diffraction limit appears

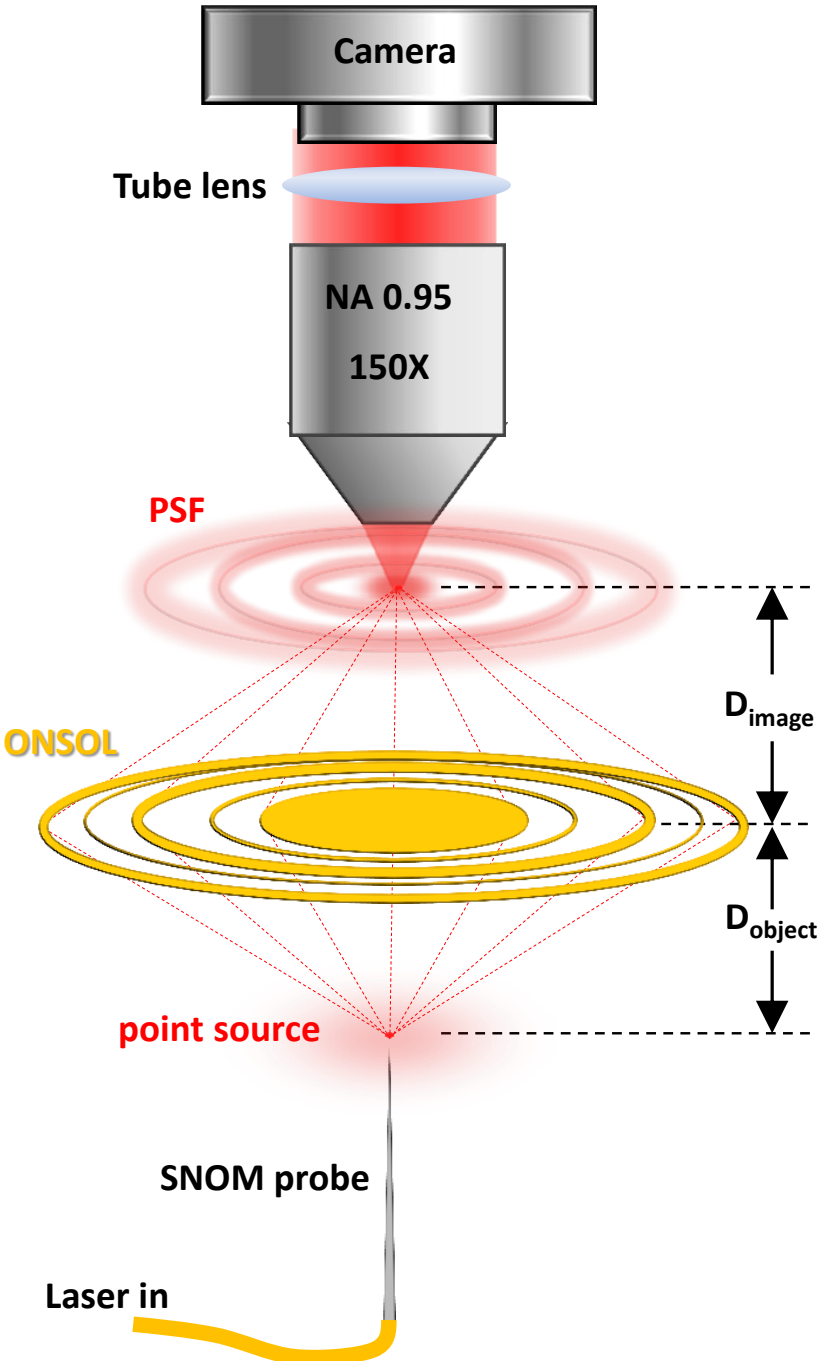

Figure 3.5: Experimental set-up for recording ONSOL PSF Linearly polarised light from a fibre-coupled laser is coupled into a SNOM probe with 100 nm aperture at the tip. The point source is imaged by the ONSOL creating a PSF. The PSF is imaged by a high NA (=0.95) microscope objective.

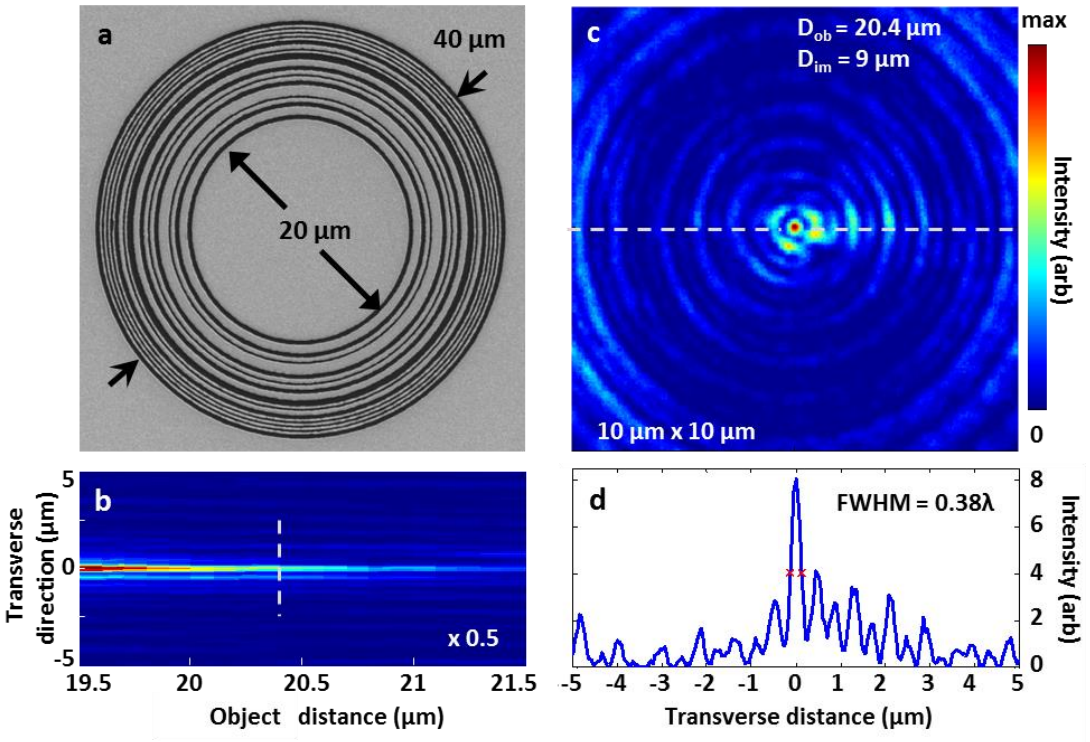

Figure 3.6: ONSOL generated PSF: experimental result. (a) SEM image of the ONSOL, (b) axial intensity distribution of the PSF showing the distance over which the hotspot remains smaller than the diffraction limit, (c) intensity distribution of PSF imaged 9 µm away when the point source is 20.4 µm on the other side of the lens, (d) intensity profile through the line in (b) & (c).

when the tip is 19.5 µm from the ONSOL. The PSF remains sub-diffraction-limited for the next 2 µm along the propagation direction (Fig. 3.6b). This extended focal depth of the ONSOL means it is not ideal for imaging of 3D objects, but is useful for imaging planar surfaces, since it would allow a large tolerance in the placement of the object. As an example of the sub-diffraction PSF in the transverse plane, the intensity distribution along the dashed line in Fig. 3.6b is plotted in Fig. 3.6c, when the point source is 20.4 µm from the lens. As in the computational results, the hotspot in the PSF has FWHM= 0.38λ (Fig. 3.6d) surrounded by low intensity sidebands. The slight asymmetry in the PSF is probably due to a small displacement of the point source from the optical axis of the lens; the same effect as seen in the simulations in section 3.2.1.

To experimentally verify the correlation between object and image displacement for the ONSOL, the lens is moved in 100 nm steps over a distance of 4 µm perpendicular to optical axis of the lens. For each position the image is recorded by the microscope and CCD camera. Figures 3.7a - 3.7e present the experimental PSFs when the ONSOL

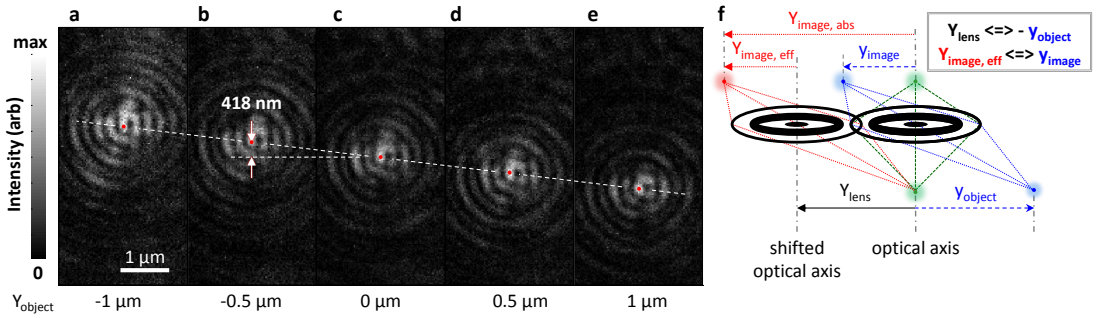

Figure 3.7: ONSOL vs. image displacement: experimental result. The ONSOL is displaced by 0.5 µm between each frame showing total 2 µm displacement between (a) and (e). (f)Schematic showing the equivalence between object displacement (in blue) and lens displacement (in red); the original undisturbed position for object, lens and image is shown in green.

moves by 2 µm. Each image is repositioned so that the the optical axis of the ONSOL is held at zero displacement to facilitate comparison with the simulations (Fig. 3.7f). The point source in this case is 17.6 µm from the ONSOL, and it is being imaged at 9 µm. The spots measure 0.48λ, still smaller than the diffraction-limit. For 500 nm displacement of the object, the image moves by 418 nm in the other direction; simulations with the same conditions show the corresponding image shift is 415 nm.

3.3 Multiple point imaging with ONSOL

An extended object might be thought of as made up of multiple point objects. In nature each of this point is either self-luminous (like a fluorescent object) or incoherently illuminated (like any scene around us). It has been discussed in the previous sections how a single point object is imaged by any lens into a point spread function (PSF). So each of the points in an extended object creates a PSF when viewed through a lens. The image of the whole object is thus the convolution of the object intensity and the PSF. The simplest way to test the resolution limit of a lens is by studying the image of two closely spaced point objects. The points are brought closer to each other until it is difficult to resolve them as two separate points from the image. Better resolution of a lens implies its ability to produce a detailed image of an extended object.

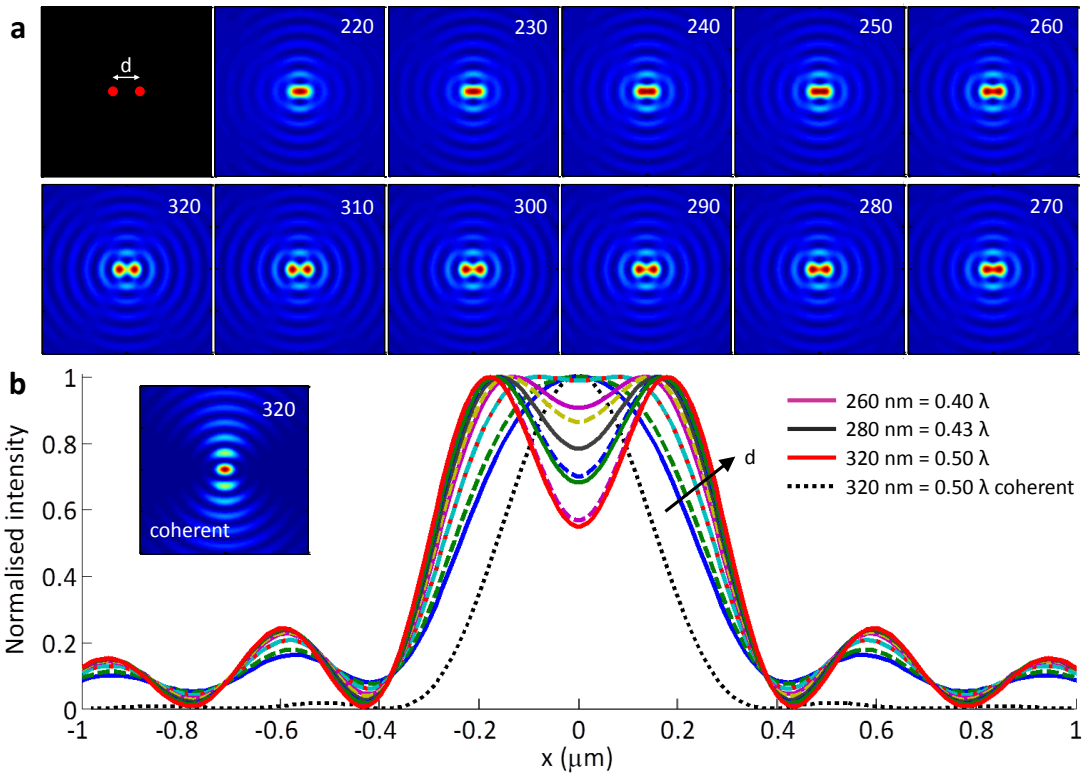

Figure 3.8: ONSOL resolution test (a) Two incoherent points (100 nm diameter) separated by distance d and their images taken by ONSOL for various values of d (220 nm to 320 nm). Each frame is 2 μm by 2 μm. (b) Intensity line-out of the images of two points for various values of d. Inset shows intensity plot for two coherent points separated by d =320 nm.

In this section the resolution limit of ONSOL will be tested by simulating the imaging of two incoherent point objects with varying centre-to-centre distances. The object

is then extended to three points and eventually to seven randomly scattered points. It must be mentioned here that if the objects are coherently illuminated, say, two point apertures illuminated with light from a laser, it is more difficult to resolve them [7]. For coherently illuminated points, their individual amplitudes (not intensities) must be added to get the image. It will be shown that when two incoherently illuminated points are very well resolved by ONSOL, the same points are not resolved when illuminated with coherent light. It is also noteworthy that the imaging method presented here is different to that done with SOL [104]. As discussed in section 2.1.4 the sub-wavelength focal spot created by a SOL was used to illuminate the object, and scanned in sub-wavelength steps to construct a super-resolution image by studying the transmission through the object in a confocal manner. This operation is time consuming and requires high stability of the object. In contrast, in this section, the images are acquired in a single capture. This is possible because the PSF of ONSOL unlike SOL is not accompanied by high intensity side-bands close to the central hotspot. As will be demonstrated in this section, the extended field of view (FOV) of ONSOL allows direct capture imaging of objects measuring smaller than the FOV. Recently Wong *et. al.* [46] experimentally demonstrated such direct, single shot imaging with very low NA but, super-oscillatory microscope, i.e. an imaging system was demonstrated where the NA is only 0.008, but the system could resolve spots closer than the corresponding diffraction limit. In comparison, the ONSOL presented here has an effective NA larger than that of an ideal conventional lens. This high-NA ONSOL will be used to demonstrate direct imaging of closely spaced points which are not otherwise resolved by a conventional lens.

Figure 3.8 shows the imaging capabilities of the ONSOL for two closely spaced points. To simulate the imaging of two points with ONSOL, angular spectrum method as described in section 3.2.1 is used. The two luminous point objects (each 100 nm diameter, centre-to-centre distance d) are placed 7 μm from the ONSOL. The transmitted intensity pattern is imaged also at 7 μm from the ONSOL. The object-image distance pair is chosen from the study in section 3.2.1 such that not only the PSF is sub-wavelength, the magnification is also 1, i.e., if the single point object is displaced by, say, 1 μm perpendicular to the optical axis the image moves by the same distance in the opposite direction. This has been confirmed by performing a numerical experiment.

For incoherent imaging of the two points, intensity from the image of individual points is added at the image plane. Otherwise, if the points were considered to be coherent with each other, the amplitude of the field at the image plane is added up.

Figure 3.8a shows the object and the image for varying centre-to-centre distances. When $d = 260$ nm, the two points can be distinguished by simply looking at the intensity pattern. This separation corresponds to 0.4λ (λ =640 nm), which is also the measure of FWHM of the PSF for this object-image distance pair. Figure 3.8b shows the x-line-out through the image frames in Fig. 3.8a. For $d = 280$ nm the dip between the two peaks is $\sim 80\%$ of the peak value, which corresponds to Rayleigh's resolution limit. However, for smaller values of d, a saddle point still exists, thus distinguishing two separate points. Due to computational pixelation, the images for $d = 240$ nm and 250 nm looks the same, where the line-out gives a flat region joining the two peaks, which is Sparrow's resolution limit [112]. However, it is safe to claim that ONSOL is capable of resolving two points separated by 260 nm or 0.4λ for the given object-image distance pair. For a conventional diffraction limited lens this limit would be $\sim 0.5\lambda$ or $d = 320$ nm. It is interesting to note, when Fig. 3.8a clearly shows that two incoherent points separated by $d = 320$ nm is well resolved, the inset in Fig. 3.8b shows that the same points are not resolved when coherently illuminated.

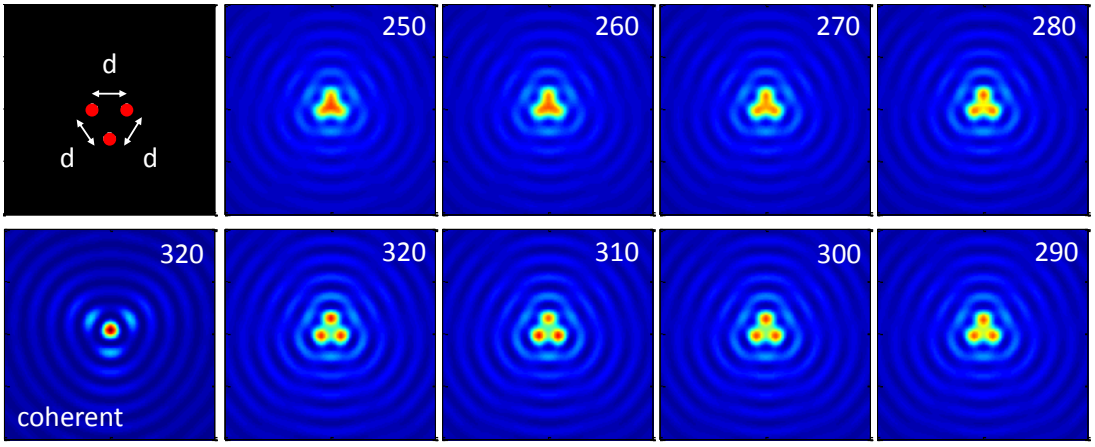

Figure 3.9: ONSOL imaging: three points Three incoherent points (100 nm diameter) placed on the vertices of an equilateral triangle with sides d. Images as captured by ONSOL for varying values of d (250 nm to 320 nm). Also shown coherent imaging of three points when $d = 320$ nm. Each frame is 2 μm by 2 μm.

Next, the object is made slightly more complex by adding a third point, so that the three points are spaced on the vertices of an equilateral triangle with sides d. Figure 3.9

shows the images formed by ONSOL for varying distances between the three points (250 nm to 320 nm). For $d = 280$ nm the three points can be resolved in the intensity plot. Note that the image is inverted with respect to the object along y-direction. This is expected from the lens-like behaviour of ONSOL. For $d = 320$ nm all the three points are very well resolved. Not surprisingly, when they are coherently illuminated, the points are not at all resolved even when spaced $d = 320$ nm apart.

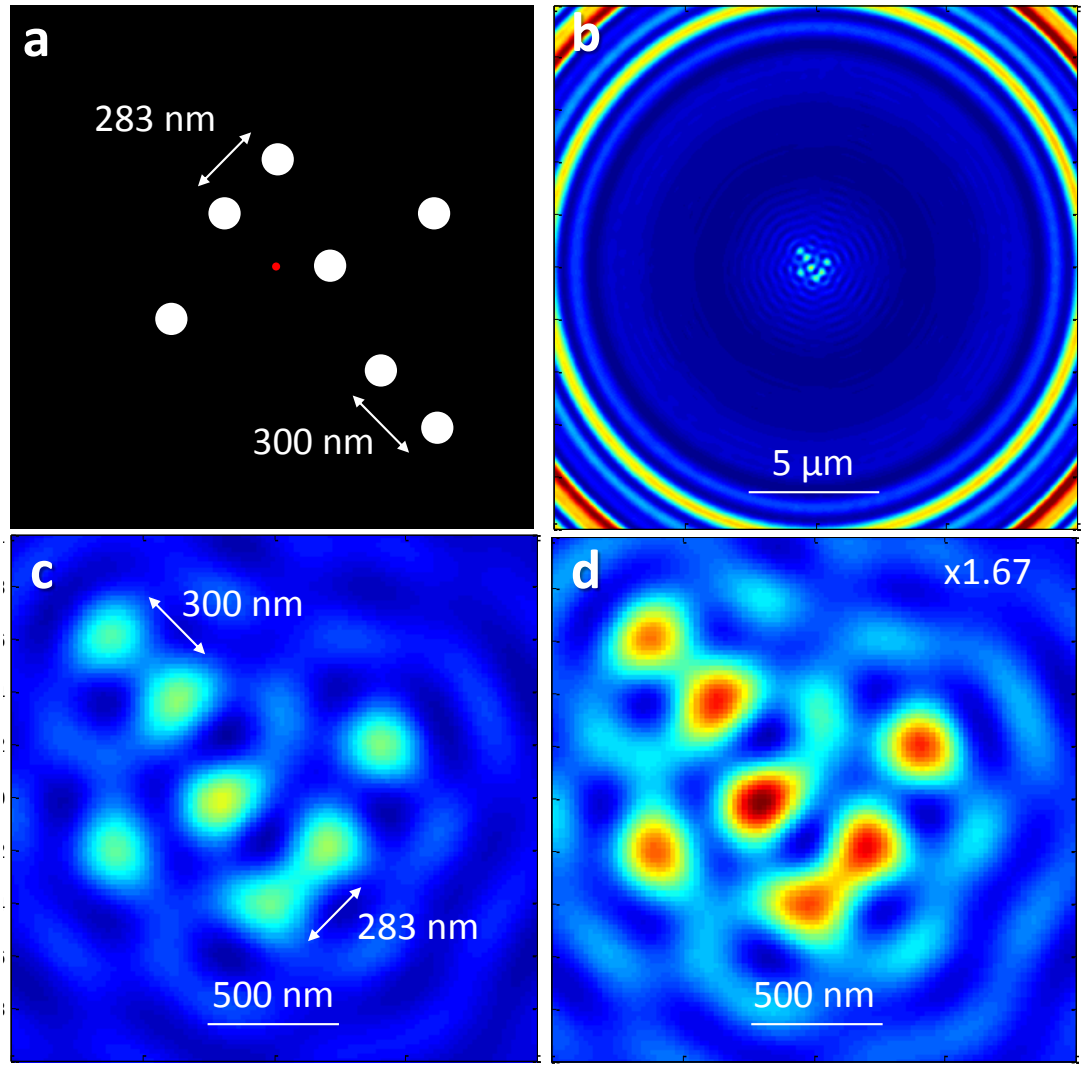

Figure 3.10: ONSOL imaging: multiple points (a) Seven randomly separated point objects (each 100 nm diameter). The red dot shows the optical axis of the ONSOL. (b) Object as imaged by ONSOL showing the large field of view. (c) Zoomed-in version of (b) showing the details of the image. (d) Enhanced colour scale used to show the intensity variation in the image depending on position of the object from the optical axis.

It has been presented how the image of a single point object gets slightly distorted

as the object is displaced perpendicular to the optical axis. This implies that for an extended object, the points that are away from the central axis of the ONSOL, the image may get more and more distorted. To test the imaging capability of ONSOL, a group of seven randomly scattered points is chosen. In Fig. 3.10a the red dot represents the centre or the optical axis of the ONSOL. The points are scattered about this centre, with a pair of points separated by nearly the resolution limit. Like in the previous experiments, each point measures 100 nm in diameter. Fig. 3.10b shows the image of the object as captured by the ONSOL. The seven points can be distinguished in the central region with low intensity side-bands around them. The field of view of the ONSOL, given by the diameter where the first intense side-band occurs is 20 μm. Figure 3.10c shows a zoomed in view of the image plane. All the seven points can be recognised, including the two closely spaced off-axis points. When the image is plotted with enhanced colour scale for better understanding (Fig. 3.10d), it is noticed that the point closest to the optical axis has the strongest intensity content.

Figure 3.11 demonstrates the robustness of the ONSOL imaging with off-axis placement of a complex object. The cluster of seven points is moved away from the optical axis (red dot) in steps of 1 μm (Figs. 3.11a- 3.11c). The object and image distances from the ONSOL are both kept at 7 μm as in the previous numerical experiments. The images of the clusters as captured by the ONSOL are shown in Figs. 3.11d- 3.11i. Figures 3.11a, 3.11d, 3.11g are the same as that presented previously in Fig. 3.10. As discussed, all the seven points are imaged faithfully in this case. Now, when the cluster is moved 1 μm from the optical axis (Figs. 3.11b, 3.11e, 3.11h), all the points are still well-resolved. However, Fig. 3.11h shows that the distant high-intensity side-bands have become asymmetric in intensity distribution along the axis of the object displacement. When the cluster moves by 2 μm from the optical axis (Figs. 3.11c, 3.11f and 3.11i) not all points are truly imaged. Ambiguity in the position of the image arises for points that lie outside the 2 μm radius about the optical axis(dotted circle in Figs. 3.11c and f). This 2 μm confirms with the distance beyond which the PSF starts getting significantly distorted, as discussed earlier in section 3.2.1. Note that the off-axis placement of the complex object are also indicated by the asymmetric intensity distribution of the distant high-intensity side-bands which are at-least 10 μm away from the optical axis (Fig. 3.11i).

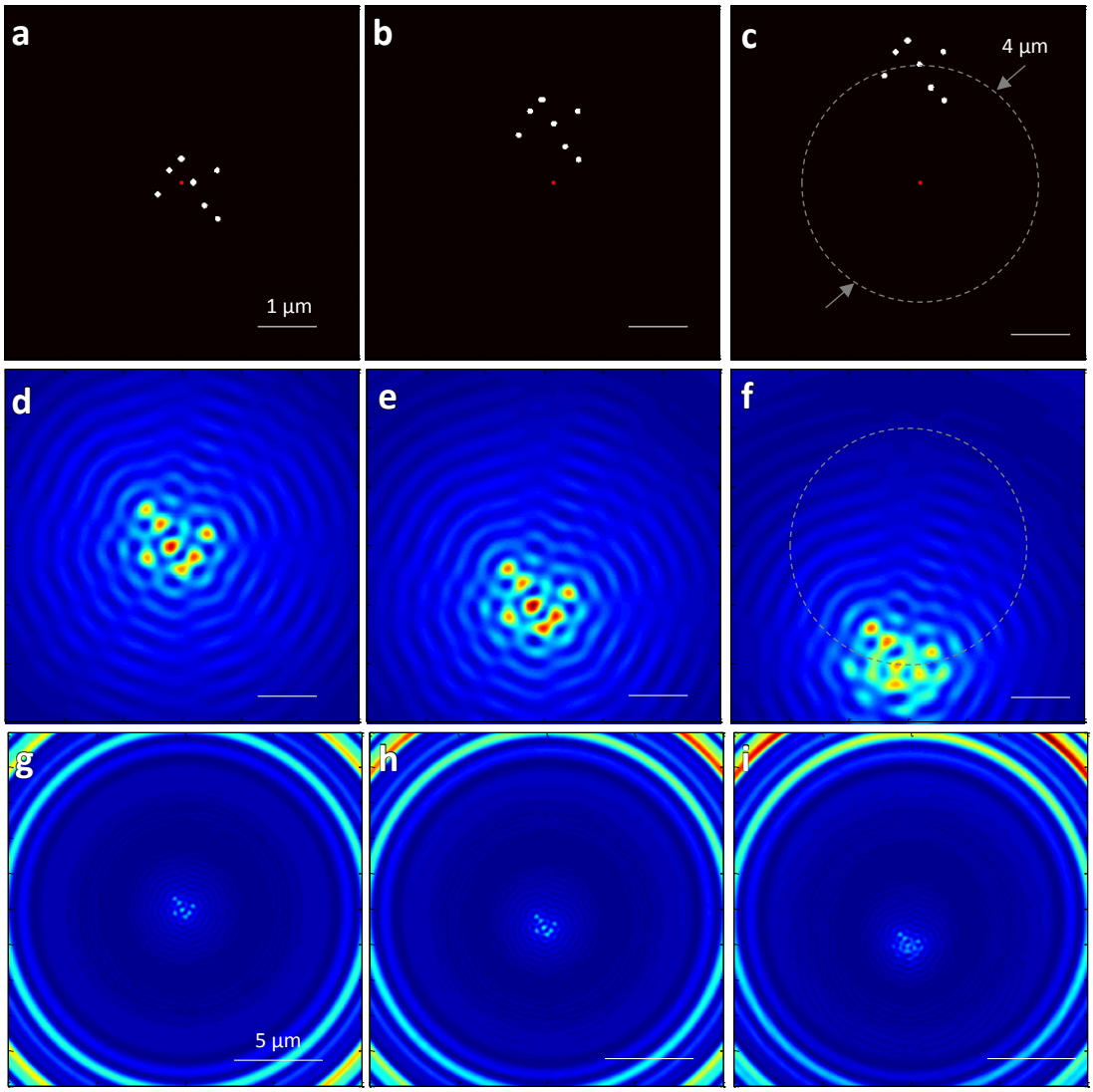

Figure 3.11: ONSOL imaging: off-axis complex object Cluster of seven points, each 100 nm diameter, placed (a) about the optical axis, (b) 1 µm from the optical axis, and (c) 2 µm from the optical axis. (d-f) Images of the respective clusters shown in (a-c) as imaged by an ONSOL. (g-i) 5 times zoomed-out area showing images of the clusters along with the high-intensity distant side-bands. Dotted circle shows the limit beyond which images may become unreliable. $D_{image} = D_{object} = 7$ µm.

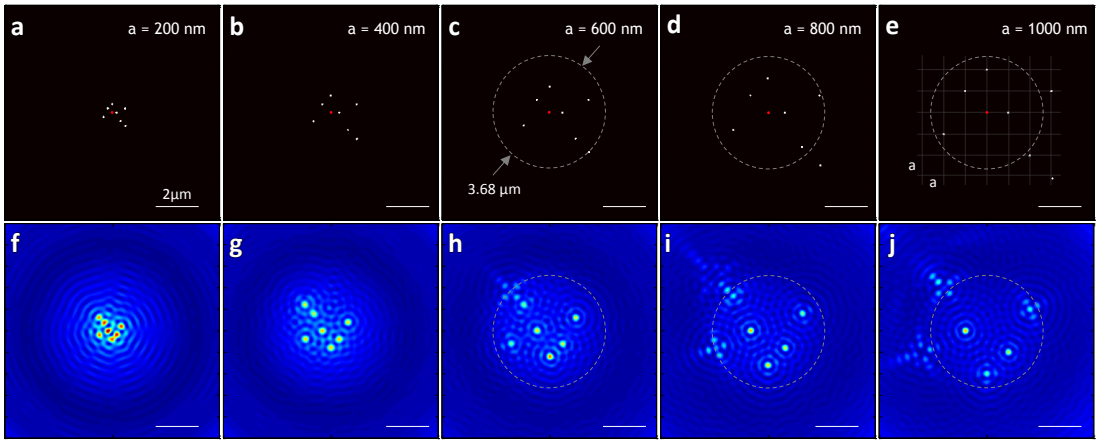

Figure 3.12: ONSOL imaging: sparsely distributed point objects (a-e) Point objects placed with increasing distance from the optical axis. The distance scales by N times with respect to the frame in (a), where N = 1 to 5. (f-j) Respective objects as imaged by an ONSOL. Dotted circle shows the limit beyond which images become unreliable. $D_{image} = D_{object} = 7$ μm.

Next, the imaging capability of ONSOL for sparsely distributed point objects are studied. The cluster of seven points presented in Fig. 3.10 is considered as the starting object for the test. The points are then moved apart from the centre by N times, where N = 1 to 5. For example, looking at Figs. 3.12a and b, the points are twice as farther from the optical axis (red dot) in the second frame, compared to the first. Image of each of these five (Figs. 3.12a - 3.12e) objects are recorded as formed by the ONSOL when the object and image distance are both 7 μm. As is observed from the images (Figs. 3.12f- 3.12j) there is no problem in recognising the points for $a = 200$ nm and 400 nm (Figs. 3.12f and 3.12g). When $a = 600$ nm the farthest point, which is 1.84 μm from the centre, is imaged as a spot with four lobes around it (Fig. 3.12c and 3.12h). From the next two increments $a = 800$ nm and 1000 nm it is clear that object points that lie beyond the dotted circle are not imaged faithfully. Note that the diameter of this circle is ~ 4 μm, as in the previous case (Fig. 3.11c). This demonstrates the fact that for this ONSOL and at this particular object-image distance pair, only objects placed within 2 μm radius from the optical centre can be imaged without ambiguity and with resolution better than the diffraction limit.

3.4 Summary

In this chapter the imaging capabilities of super-oscillatory lenses are studied numerically and experimentally. The point spread functions produced by a SOL and an ONSOL are studied numerically to determine the accuracy with which these lenses might image an extended object; smaller PSF implies better resolving capability of the lens. Of the two types of SOL investigated, the ONSOL creates PSF with less intense sidebands and is more robust to off-axis object placement than a standard SOL. This makes ONSOL a promising choice for super-resolution microscopy of planar objects and photo-lithography. Next the PSF generated by an ONSOL is experimentally studied. The results agree with the simulations. It is demonstrated that PSF generated by the ONSOL have hotspot radii 24% smaller than the diffraction-limited lenses and that the effective numerical aperture of the ONSOL in air is 1.31. This justifies their usefulness for super-resolution imaging applications. Finally, the ability of the ONSOL to resolve two closely spaced points and to image multiple points is studied numerically. The ONSOL demonstrates the ability to resolve points with centre to centre distance as small as 0.4λ, for $\lambda = 640$ nm; for conventional lenses the limit is 0.5λ. The ONSOL is also robust enough to image directly (without scanning) multiple points spaced randomly within the large field of view of the lens with resolution exceeding that of diffraction-limited lenses. However, for the object-image distance pair studied here, the points must be placed within a 2 μm radius from the optical axis of the ONSOL to be imaged reliably.

4

Solid-immersion super-oscillatory lens

4.1 Motivation: Heat assisted magnetic recording

Hard disk drive (HDD) is a data storage device used for storing and retrieving digital data and it forms an essential part of modern computers. HDD writes data by magnetising tiny areas, called bits, of a thin film of ferromagnetic material. The storage capacity of a HDD depends on how small a bit can be. In 1998 it was demonstrated at IBM Almaden Research Centre that perpendicular magnetic recording (PMR) has clear advantage of higher data storage density over its predecessor longitudinal magnetic recording. With longitudinal recording maximum storage density was limited to 40 Gbit/inch^2, while with PMR a storage density of 100 Gbit/inch^2 [119] could be realised. This was achieved by arranging the magnetic bits perpendicular to the storage disk, rather than on the plane of the disk. The architecture of PMR allows the use of magnetic material with higher coercivity[1] leading to more thermally stable magnetic bits packed with higher areal density. However, the superparamagnetic limit imposes an upper limit to storage densities in magnetic recording. This is because in very small domains magnetization may flip randomly due to thermal fluctuations [120], which in turn limits the storage density even with perpendicular recording. In 2012 Seagate announced [121] a proof-of-principle demonstration of 1 Tbit/inch^2 storage capacity using the next-generation recording technology — heat-assisted magnetic recording (HAMR). HAMR [122] offers a new degree of freedom in the currently used perpendicular magnetic recording (PMR) to circumvent the problem caused by superparamagnetism. It

[1] Coercivity is a measure of the strength of external magnetic field required to magnetise the bits; a stronger field implies higher coercivity

makes use of even higher coercivity ferromagnetic material to circumvent the thermal instability. But this requires higher writing fields than that can be delivered by the HDD writing heads. In HAMR, this high-coercivity magnetic medium is temporarily and locally heated so that the coercivity can be lowered below the available magnetic write field. Hence more thermally stable yet smaller magnetic recording bits can be realised with the HAMR technology.

To deliver a sub-diffraction limited hotspot for heating up small bits of magnetic disk Kryder [122] proposed a near-field transducer. The hotspot needs to be small so that it remains on the magnetic bit that needs to be magnetised; larger hotspots may erase the already stored data in the neighbouring bits. For areal density of 1 Tbit/inch^2 the track pitch of the magnetic medium needs to be < 50 nm. Near-field plasmonic transducer appears to be a good choice for concentrating light in such small domains and a proof-of-principle HAMR has been experimentally demonstrated using this technology with an areal density of 245 Gbit/inch^2 in 2009 [123] and 1 Tbit/inch^2 in 2012 [121]. However, the plasmonic transducer presents considerable manufacturing challenges, for example the transducer dimensions and separation from the substrate waveguide must be precisely controlled to ensure a high coupling efficiency. Low optical throughput is another problem of near-field transducers; tapered waveguides used in the near-field scanning optical microscopy have the capability to achieve a resolution of 100nm or better, but their applications are limited due to the dramatic attenuation of light transmitted through the subwavelength aperture: typical optical throughput is of the order of $10^{-4} - 10^{-5}$ [124]. Other subwavelength focusing methods based on near-field evanescent waves include the superlens [26, 97, 99] and nanoscale spherical lenses [98, 101], but all these methods require the lens to be in the immediate proximity of object, typically within distances much less than the wavelength. On the other hand, it has already been experimentally demonstrated that far-field sub-diffraction-limit focusing can be achieved using super-oscillatory lenses [41, 104, 106, 125, 126]. Even though the throughput for super-oscillatory lenses is only a few percentage in the central field of view [127], it has the obvious advantage of comfortable placement within the hard disk drive architecture. Amplitude mask type super-oscillatory lenses have demonstrated sub-wavelength focal spots $\sim \lambda/3$ for 640 nm and 405 nm wavelengths (Chapter 2). In combination with solid immersion technology, which is commonly used for high-density

optical storage [128] and a short wavelength of illumination (405 nm) a focal spot of ~ 50 nm becomes readily achievable, better than can be achieved with a conventional lens and solid immersion medium.

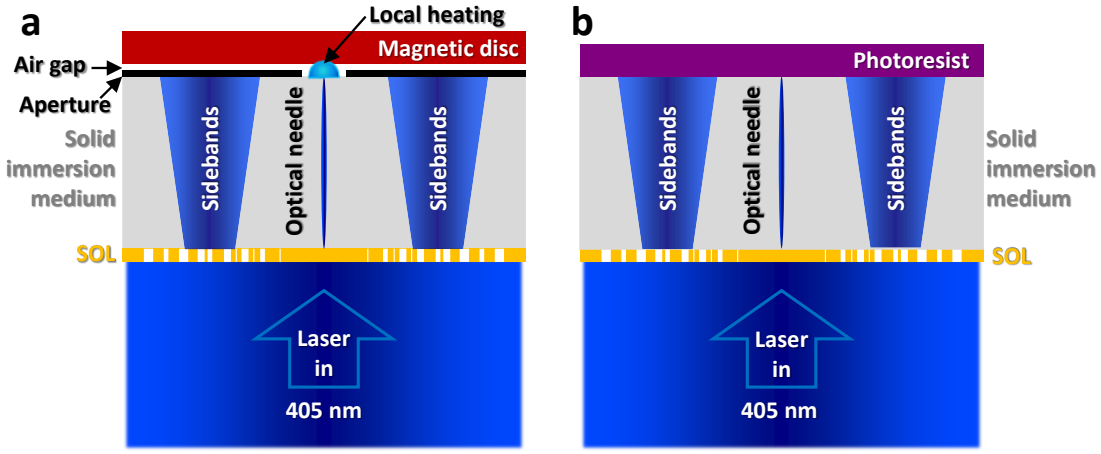

Figure 4.1: Solid-immersion super-oscillatory lens for HAMR application. (a) Conceptual representation of super-oscillatory spot assisted local heating of a magnetic medium. (b) Simplified configuration for testing the performance of super-oscillatory lens in a solid-immersion medium; photoresist replaces magnetic medium as the registration layer.

In this chapter the performance of an optical needle super-oscillatory lens (presented in chapters 2 & 3) will be investigated in a solid-immersion environment. A conceptual schematic of optical needle lens for HAMR application is shown in Fig. 4.1a. The super-oscillatory lens (SOL) fabricated on a thin metal layer is followed by a solid-immersion layer of a few micron thickness such that at the immersion-air interface a sub-wavelength hotspot is formed. Following a small air-gap measuring only a few nanometres, the magnetic disk is placed for recording data. This air-gap is present in a realistic HDD architecture between the writing head and recording medium to avoid damaging of either the head or the rotating disk [122]. As discussed in chapter 2 the super-oscillatory lenses produce sub-wavelength hotspots surrounded by high intensity halos. To cut-off the unwanted contribution from these sidebands an aperture block or an highly absorbing medium with a window is placed allowing only the desired hotspot through the central portion. As a first step in integrating the super-oscillatory lens into the hard disk drive architecture, the performance of this lens in solid-immersion medium must be tested. It must be ensured that the delicate super-oscillatory hotspot survives after travelling through micron-thick layer of a solid medium. For this test the

design of the sample is simplified as shown in Fig. 4.1b. The aperture, air-gap and the magnetic medium is replaced by a photoresist film where the sub-wavelength hotspot along with the surrounding sidebands will be registered.

In the following sections, design of the solid-immersion optical needle lens and its preliminary experimental demonstration will be presented.

4.2 Material selection for immersion medium

Solid immersion material	λ=405nm		λ=473nm	
	n	*k*	*n*	*k*
GaP *	4.15	0.256	3.71	0.014
TiO_2 **	3.25	---	2.76	---
ZnS *^	2.74	---	2.64	---
GaN *^	2.55	---	2.46	---
Diamond *^	2.46	---	2.43	---
TeO_2 *^	2.43	---	2.34	---
ZrO_2 ^^	2.27	---	2.23	---
ZnO *^	2.10	---	2.07	---
ITO ^^	2.10	0.042	2.00	0.041
AZO **^	2.10	0.006	1.95	0.002
HfO_2 ^^	1.98	---	1.95	---
Y_2O_3 *^	1.98	---	1.95	---

Table 4.1: Solid-immersion material selection. Table comparing values of refractive index and losses for various solid medium at different wavelengths of operation. Values obtained from: $*$ [129], $**$ [130], $*\wedge$ [131], $\wedge\wedge$ [132], $**\wedge$ [133].

Before optimising the design of the solid-immersion optical needle lens the operating wavelength and the solid-immersion medium must be selected. For the smallest possible optical hotspot, the incident wavelength is chosen to be in the blue part of the spectrum; simulations are done with 473 nm and/or 405 nm, where diode lasers are commercially available and which also happens to be the wavelength for commercially available data storage devices. For the experimental demonstration the 405 nm is used. For the solid-immersion medium, a high refractive index but low loss material for these wavelengths

is desired. This is to ensure that significant reduction in the hotspot size is obtained without much energy loss. Table 4.1 shows a table of materials suitable as solid-immersion media for optical lenses. Gallium phosphide (GaP) has been the medium of choice for solid-immersion lenses [134] and has a complex refractive index of $n_{\mathrm{GaP}} = 3.71 + 0.01i$ at 473 nm [129]. From the above table 4.1 it is readily seen that GaP is the best choice of solid-immersion medium with high refractive index and low loss at that wavelength. In the following sections the performance of the optical needle lens in GaP is simulated and it will be shown that it is possible to focus light of wavelength 473 nm down to only 57 nm. However, for the proof-of-principle experimental demonstration, aluminium-doped-zinc-oxide (AZO) is chosen as the material for the immersion medium and the operating wavelength is chosen to be 405 nm. As seen from table 4.1, AZO has a smaller value of the real part of refractive index compared to GaP, but at the same time is also characterised by lower losses. So it is a good enough choice for the first proof-of-principle demonstration of the solid-immersion super-oscillatory lens.

4.3 Numerical simulation

In this section performance of super-oscillatory lenses in solid-immersion media is simulated. The optical-needle lens is designed[2] using binary particle swarm optimization algorithm (BPSO) as described in chapter 2. The mask is illuminated with a circularly (rather than linearly) polarised beam to avoid unwanted polarisation effects that result in an elliptical focal spot [127, 135].

4.3.1 Sub-wavelength optical needle for HAMR application

As discussed in the introductory section, the pre-requisite for application in high storage density heat-assisted magnetic recording is a focal spot measuring ~ 50 nm. To demonstrate that super-oscillatory lenses can produce such a focal spot when illuminated with 473 nm light, performance of an optical needle super-oscillatory lens is studied in gallium phosphide[3]. Figure 4.2 summarises the characteristics of the designed optical needle lens in GaP suitable for interfacing with magnetic hard disk drive. The lens is

[2]The author is thankful to Dr. Guanghui Yuan for providing the optimised designs of the super-oscillatory lenses

[3]The author is thankful to Dr. Guanghui Yuan for providing the simulations presented in this sub-section.

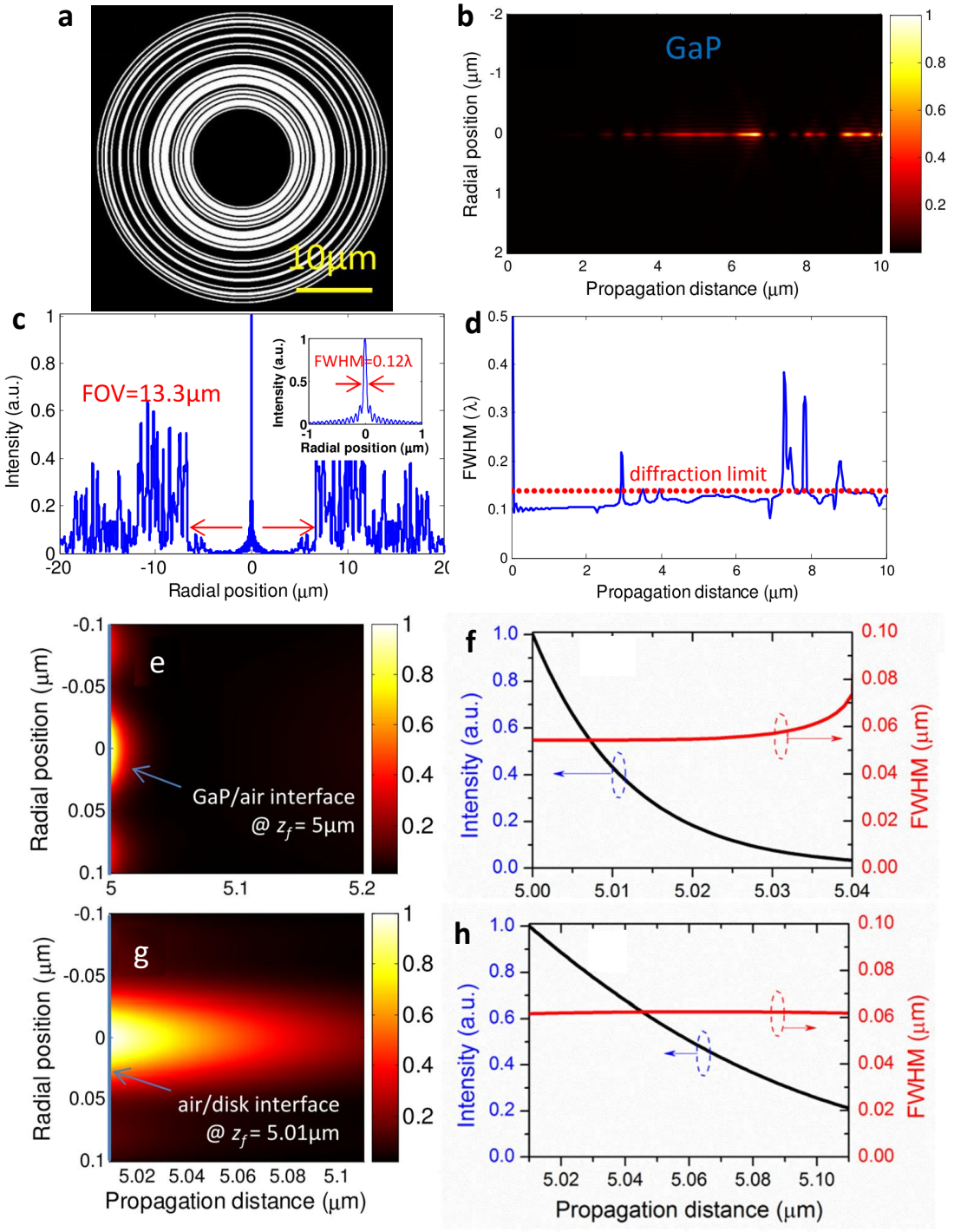

Figure 4.2: Sub-wavelength optical needle in GaP (a) Radial transmittance (white 1, black 0) distribution of the binary mask designs. (b) Normalized total electric field intensity distribution. (c) Line-out of electric field intensity along the mask diameter at $z_f = 5$ μm. (d) Variation of FWHM of light spot with propagation direction. Performance of super-oscillatory optical needle (e) after GaP/air interface at $z_f = 5$ μm and (g) air/magnetic disk after $z_f = 5.01$ μm. Electric field intensity (black line) and FWHM (red line) distribution along the axial direction (f) after GaP/air interface at $z_f = 5$ μm and (h) air/magnetic disk after $z_f = 5.01$ μm. Figure adapted from [127]. ©OSA 2014.

optimised to produce a sub-wavelength optical needle about a predefined focal length z_f = 5 μm for a chosen depth of focus DOF= 4 λ. Figure 4.2a shows the design of the lens with outer radius r_{max} = 20 μm, central block radius r_{block} = 6 μm and the smallest line width 200 nm.

The propagation characteristics of the lens in the immersion medium is calculated using the complex refractive index $n_{GaP} = 3.71 + 0.01i$ at 473 nm [129]. Figure 4.2b, shows the intensity distribution formed by the ONSOL in the GaP layer. An optical needle is formed with full-width at half maximum of 57 nm ($\sim$ 0.12 λ or 0.45 λ_{eff}) at z_f = 5 μm (Fig. 4.2c). At this focal length, the field of view (FOV) within which the sub-wavelength spot is formed is 13.3 μm. Here, the FOV is defined as the separation between the two nearest sidebands with 10 % intensity of the central peak. This extended FOV of more than 13 μm allows the use of an opaque aperture to prevent the unwanted high intensity sidebands from heating the magnetic medium in HAMR architecture. The estimated optical power within the FOV is 1.8 % of the overall optical power in the observation plane at z_f = 5 μm. It may also be noted that the peak intensity of the sidebands outside the FOV are 64 % of the central peak. Figure 4.2d shows the full-width at half maximum (FWHM) of the central spots formed along the propagation distance. The diffraction limit in GaP is calculated as $\lambda_{eff}/(2n\sin\theta_{max}) \approx 0.14\ \lambda$, where, θ_{max} is the maximal focal angle determined by the mask aperture r_{max} and focal length z_f through the relation $\tan\theta_{max} = r_{max}/z_f$. It should also be noted that smaller focal spots can be found at shorter focal lengths, for example the FWHMs at the two other foci at z=3.24 μm and z=2.66 μm are 52 nm and 50 nm respectively.

In a HAMR hard disk architecture, as shown in Fig. 4.1a, the solid-immersion medium would be followed by a narrow air-gap which would allow spinning of the magnetic disk without causing damage. It is important to study the coupling of the sub-wavelength super-oscillatory spot from the solid-immersion to the magnetic disk through the intermediate air-gap. Figures 4.2e,f show the simulated performance of super-oscillatory optical needle after the GaP/air interface, where the GaP is terminated after z_f = 5 μm. A detailed analysis of the axial electric field intensity (Fig. 4.2f) indicates that the 1/e intensity penetration depth in air is 12 nm. Within this distance the FWHM keeps almost invariant at 55 nm. Although the penetration depth of 12 nm seems to be small, the proof-of-concept HAMR system [123] had a physical air gap be-

tween the bottom of carbon overcoat of the recording head and the top of the lubricant on the magnetic disk of only ~ 2 nm. For practical HAMR applications, the dielectric properties of the magnetic disk must be considered for accurate calculation of the area of disk heated by the spot. For this purpose, the optical properties of a commercial hard disk drive platter are extracted using ellipsometry measurements[4]. At wavelength of 473 nm, its complex refractive index is found to be 4.71+0.455i. Using this data the electric field intensity distributions in the recording layer is calculated assuming 10 nm air gap between the GaP layer and magnetic disk surface. Figures 4.2g,h show that the achievable spot size in the magnetic recording layer is evaluated to be ~ 62 nm with a penetration depth of 60 nm. This spot size is comparable with that reported in [123], which seems to be the most promising HAMR technology in the industry so far.

4.3.2 Solid-immersion optical needle for experimental demonstration

For experimental demonstration of solid-immersion super-oscillatory lens, a new design with reduced overall size ($r_{\max} = 10$ μm, $r_{\text{block}} = 3$ μm, line width 200 nm) is optimised. The propagation characteristics of this lens is studied in GaP, AZO, and air. The incident wavelength is chosen as 405 nm and refractive indices are chosen as $n_{\text{GaP}} = 4.15 + 0.25i$, [129] $n_{\text{AZO}} = 2.1 + 0.006i$ [133] and $n_{\text{air}} = 1$. Figure 4.3a shows the intensity distribution along the propagation direction and at $z_{\text{f}} = 4.6$ μm for each of the three media. Just by looking at the three plots of intensity distribution along the propagation direction, it is evident that the optical needles formed in GaP are the narrowest compared to those formed in AZO and air, in that order. At 4.6 μm after the lens, the radial distribution of intensity shows the smallest and the most intense central spot formed in GaP and the largest and the dimmest spot in air. Figure 4.3b shows the FWHM distribution of the central spots along the propagation direction. It must be noted that for each medium, smaller spots exist at shorter focal lengths. This particular distance of 4.6 μm is chosen to match the experimentally deposited AZO layer thickness. It is also evident that in air the focal spots always remain larger in size than in either of the solid-immersion media. But between GaP and AZO, even though AZO has lower refractive index, the spot sizes appear comparable up to about 3 μm. However, it must be added that in both the media, region up to 3 μm is also

[4]The author would like to thank Dr. Behrad Gholipour for the ellipsometry measurements

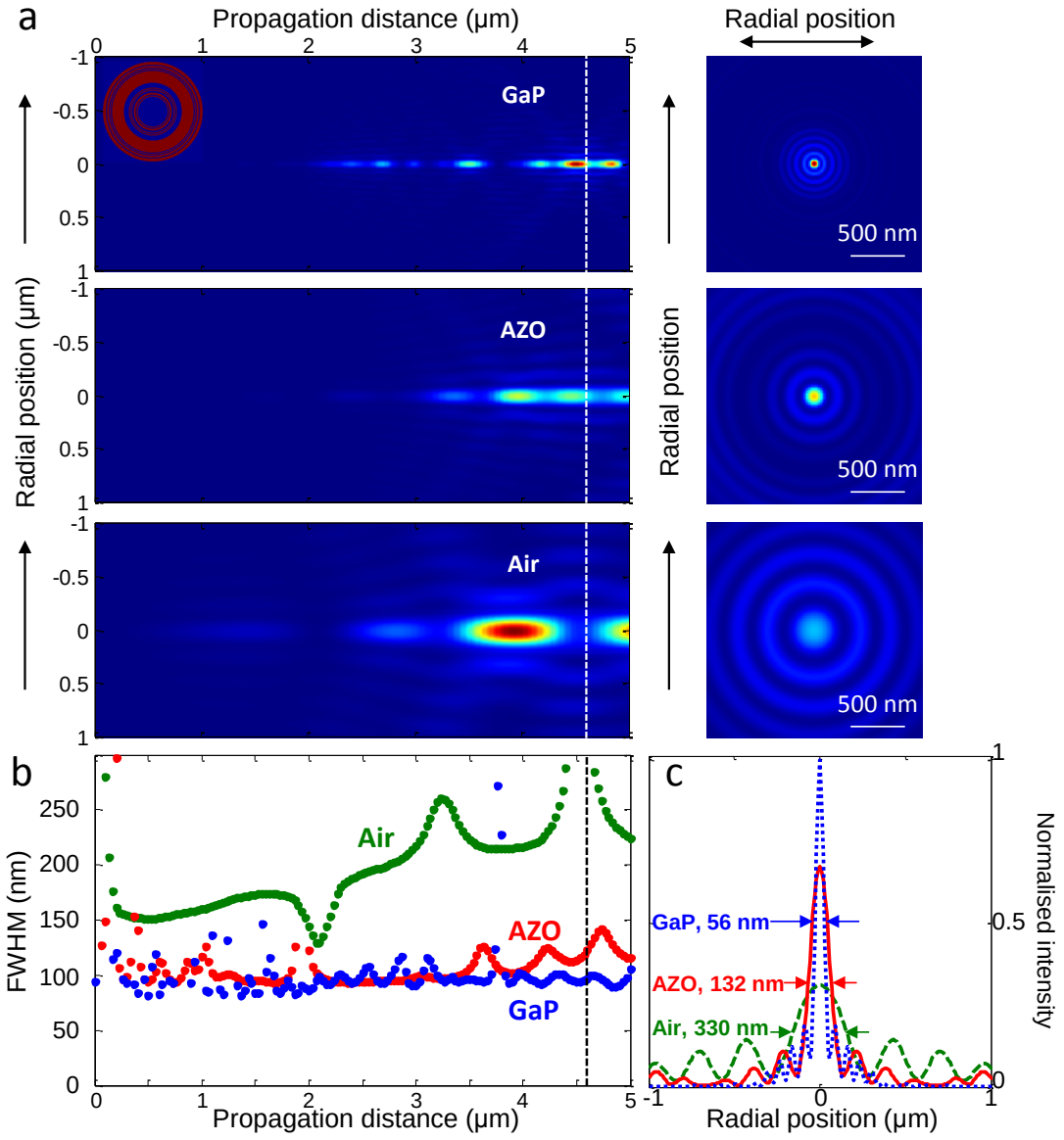

Figure 4.3: Sub-wavelength optical needle in different media (a) Intensity distribution produced by optical needle lens (inset) in gallium phosphide (top row), aluminium-doped-zinc oxide (middle row) and air (bottom row). (b) Central spot FWHM distribution along propagation direction in the three media. (c) Intensity lineout across the lens diameter at $z_f = 4.6$ μm showing spot sizes in the three media.

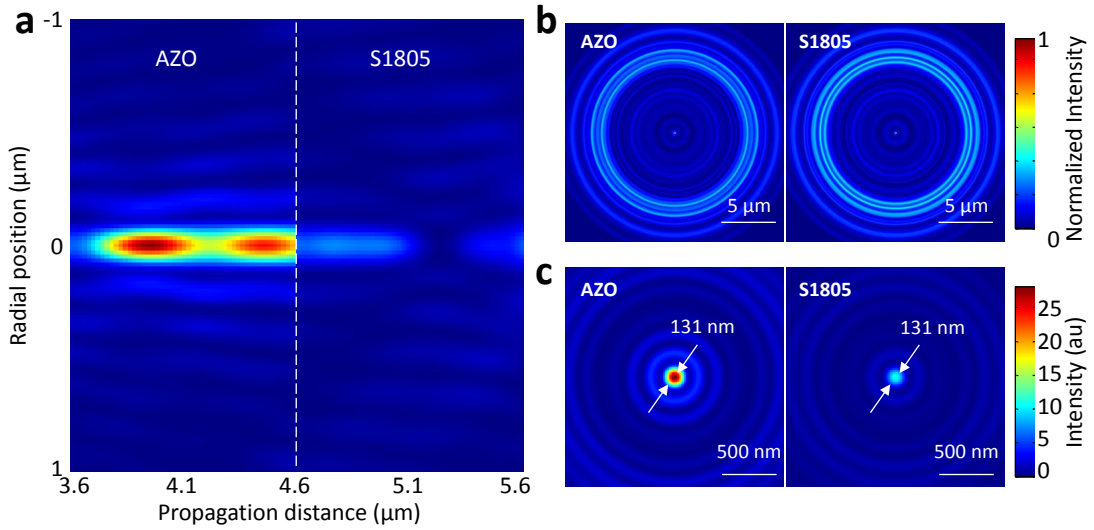

Figure 4.4: Optical needle at solid-immersion-photoresist interface (a) Intensity distribution produced by optical needle lens across the AZO-photoresist interface. (b) Radial distribution of normalised intensity at the exiting face of solid-immersion (z=4.6 μm) and thereafter traversing through 200 nm of photoresist (z=4.62 μm)(c) Zoomed in view of (b) showing the spot sizes at the AZO end face and after 200 nm of photoresist.

characterised by very low intensity and hence there may remain ambiguity in calculation of the spot size. Beyond this distance the spots formed in AZO is larger than those formed in GaP. Figure 4.3c shows a comparison between the spot sizes as produced in GaP, AZO and air at 4.6 μm. In GaP, the spot size is 56 nm, comparable to the larger lens design presented in section 4.3.1. In AZO, the spot size measures 132 nm due to lower refractive index of this medium compared to GaP. In air the spot is 330 nm. Another interesting measure is the ratio between the central spot intensity to the first annular sideband intensity. For air, the central spot is 2.16 times stronger than the first sideband. While the central spot is 6.18 times stronger in AZO and 5.35 times stronger in GaP.

For experimental demonstration of the solid-immersion lens, AZO is chosen as the material for the immersion medium. A positive photoresist (S1805) is chosen as the registration layer. It is important to simulate the performance of the optical needle at the AZO-photoresist interface. The refractive index of the photoresist is 1.71 [136] which is close to that of the AZO at 405 nm. As shown in Fig. 4.4a, due to low mismatch between the refractive index of the solid-immersion and the photoresist, the optical needle retains its shape across the interface; though almost 4 times intensity is lost in the photoresist. The radial distribution of the intensity after 4.6 μm of AZO is

shown in Fig. 4.4b. AZO is truncated after this distance and followed by the photoresist layer. The radial distribution of the intensity after 200 nm of photoresist looks very similar to that exiting the solid-immersion medium. Figure 4.4c shows the comparison of the size and intensity of the central spot in the AZO and after traversing through the photoresist. As mentioned before, though the intensity is diminished in the photoresist, the size of the spot remains the same.

4.4 Fabrication

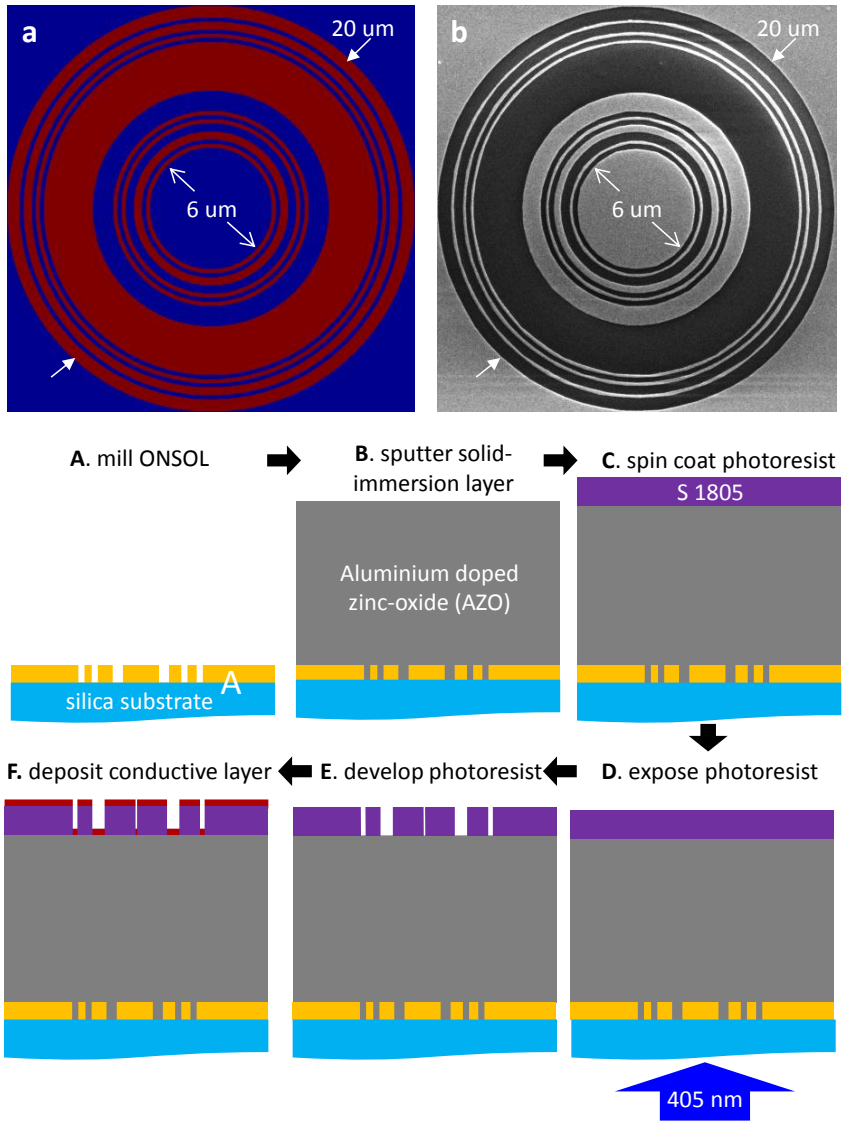

Figure 4.5: Fabrication of solid-immersion super-oscillatory lens (a) Binary design of the lens. (b) SEM image of the fabricated sample on 100 nm gold. (A)-(F) Steps for fabricating the solid-immersion lens.

The lens is fabricated using focused-ion-beam milling of 100 nm thick layer of metal (Au or Al) deposited on silica substrate by resistive evaporation method (Fig. 4.5b, A). The nano-structured sample is then used as a substrate to sputter deposit[5] a several micron thick layer of AZO (Al_2O_3 2%, ZnO 98% by weight, Fig. 4.5B). The AZO layer thickness is measured as 4.6 μm by making a cross-section of the layer with focused-ion-beam and measuring the scanning electron microscope image. For the registration layer, positive photoresist (S1805) is spin-coated on the AZO layer (Fig. 4.5C). The photoresist is spun at the recommended speed of 5000 rpm to get $\sim$ 500 nm thick layer [136].

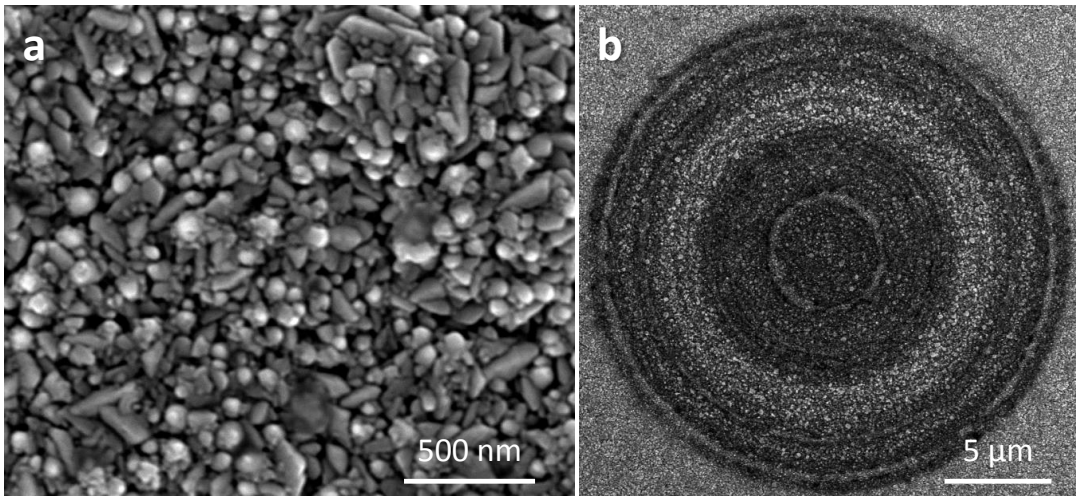

Figure 4.6: Quality of AZO layer. SEM image of (a) top-layer of AZO sputtered on 100 nm Al film and (b) top-layer of AZO directly above the super-oscillatory lens after being exposed to several doses of laser radiation.

For a solid-immersion super-oscillatory lens, the major concern could be the film quality of the solid-immersion layer itself. If this layer is rough and grainy, it may destroy the delicate super-oscillatory spot altogether. Figure 4.6a shows the scanning electron microscope image of the top surface of the 4.6 μm thick AZO layer. The AZO film shows grain sizes ranging from $\sim$ 40 nm to above 200 nm. The larger grains are comparable to the super-oscillatory hotspot dimension and may scatter the hotspot. Thus before proceeding with experimental demonstration of solid-immersion super-oscillatory lens, the film quality of the immersion layer needs to be studied and perfected. This would be an important future work. In this context it may be noted that in reference [137] the as-deposited AZO film quality is very similar to Fig. 4.6a.

[5]The author is grateful to Mr. Christopher Craig for his help with sputtering.

The aforementioned paper reports that thermal annealing in vacuum helps in reduction of the grain sizes of AZO from 100s of nanometre to the nanometre range, resulting in denser and more uniform distribution of the crystallites. It must also be kept in mind that incident high power laser may change the morphology of the as-deposited solid-immersion medium. As observed in Fig. 4.6b the top layer of the AZO film directly above a super-oscillatory lens shows various grain size distribution after being repetitively exposed to high power laser.

4.5 Experimental characterisation

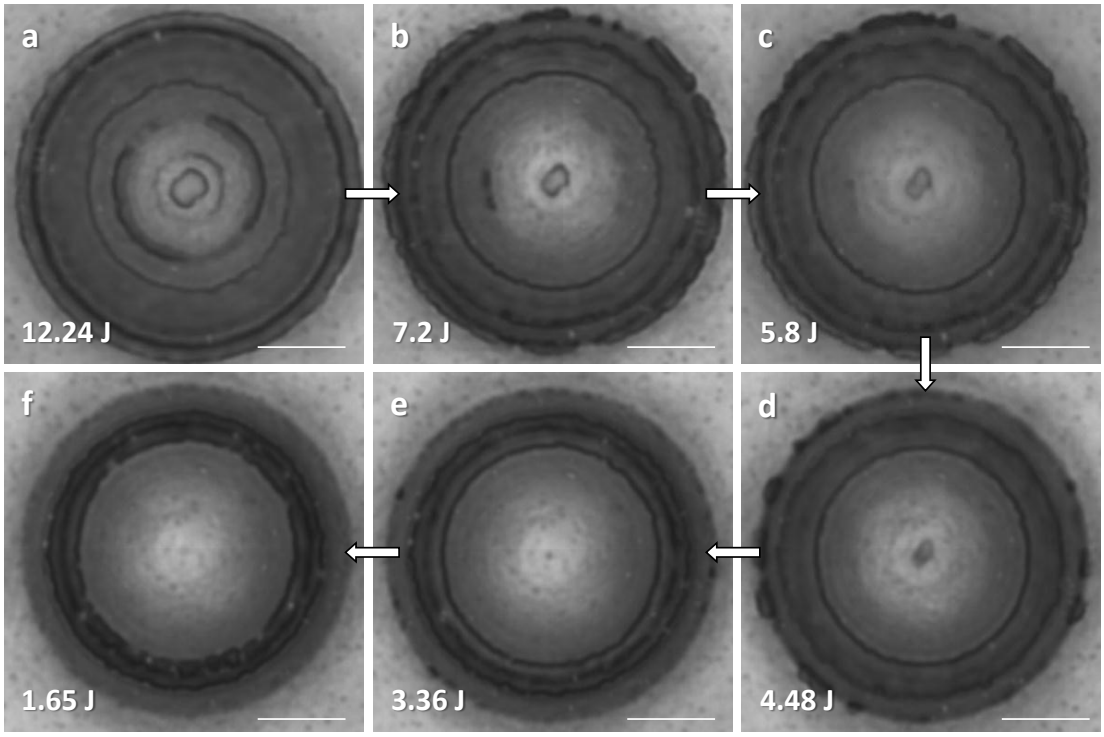

Figure 4.7: Hotspots registered on the photoresist. Optical microscope images of the developed photoresist layer for different incident energy.

For experimentally registering the super-oscillatory spot on the photoresist layer, the sample is exposed from the silica side (Fig. 4.5D) with circularly polarised light ($\lambda = 405$ nm). The incident beam size is much larger (at least 100 times) than the sample size and hence ensures uniform illumination across the sample. The exposed photoresist is developed and inspected under white light illumination in reflection mode (Fig. 4.5E) with a high NA objective. For the final inspection under the scanning

electron microscope, the developed photoresist needs to be coated with a thin ($\sim$ 5 nm) conductive layer of metal (Fig. 4.5F).

To test the correct dose of exposure, the developed photoresist is inspected optically with a high NA (0.95, 150x) microscope under white light in reflection. Figure 4.7 shows the optical microscope images for different exposure doses. After each test, the photoresist is washed off in acetone bath followed by iso-propanol and de-ionised water. The sample is then coated with afresh layer of photoresist and recycled for the next exposure test. The challenge in inspecting the solid-immersion lens performance optically is to look for a feature (131 nm) smaller than the resolution limit of the microscope ($\sim$ 213 nm). To eliminate the ambiguity in optical inspection, several doses of incident energy are tested, starting with an overexposed central spot (Fig. 4.7a). The exposure energy is then decreased, iteratively moving towards smaller and smaller spots until no feature in the central portion of the lens is noticed suggesting under-exposure (Fig. 4.7f). Figure 4.7e with 3.36 J incident energy shows an optical image where a feature in the centre is just visible. At this stage the sample is coated with 5 nm gold to inspect under the scanning electron microscope for proper assessment of the size of the central spot.

Figure 4.8 summarises the experimental performance of the solid-immersion super-oscillatory lens. A large part of the sample is exposed to 405 nm light with 3.36 J energy. But only a small fraction of this illuminates the super-oscillatory lens. Figure 4.8a shows the simulated intensity distribution in the photoresist. Figure 4.8b shows the developed photoresist under the optical microscope. Figures 4.8c,d show the high resolution scanning electron microscope images of the developed photoresist coated with 5 nm gold layer. The registered intensity pattern matches well with the simulated distribution (compare Figs. 4.8a & c). The zoomed-in view of the central spot (Fig. 4.8d) shows that the spot measures 131 nm as simulated in Fig. 4.4c. Very close to the spot, an arc-like feature is present in the experiment. This feature is not there in the simulation and is unwanted. This is discussed further in the section 4.6.

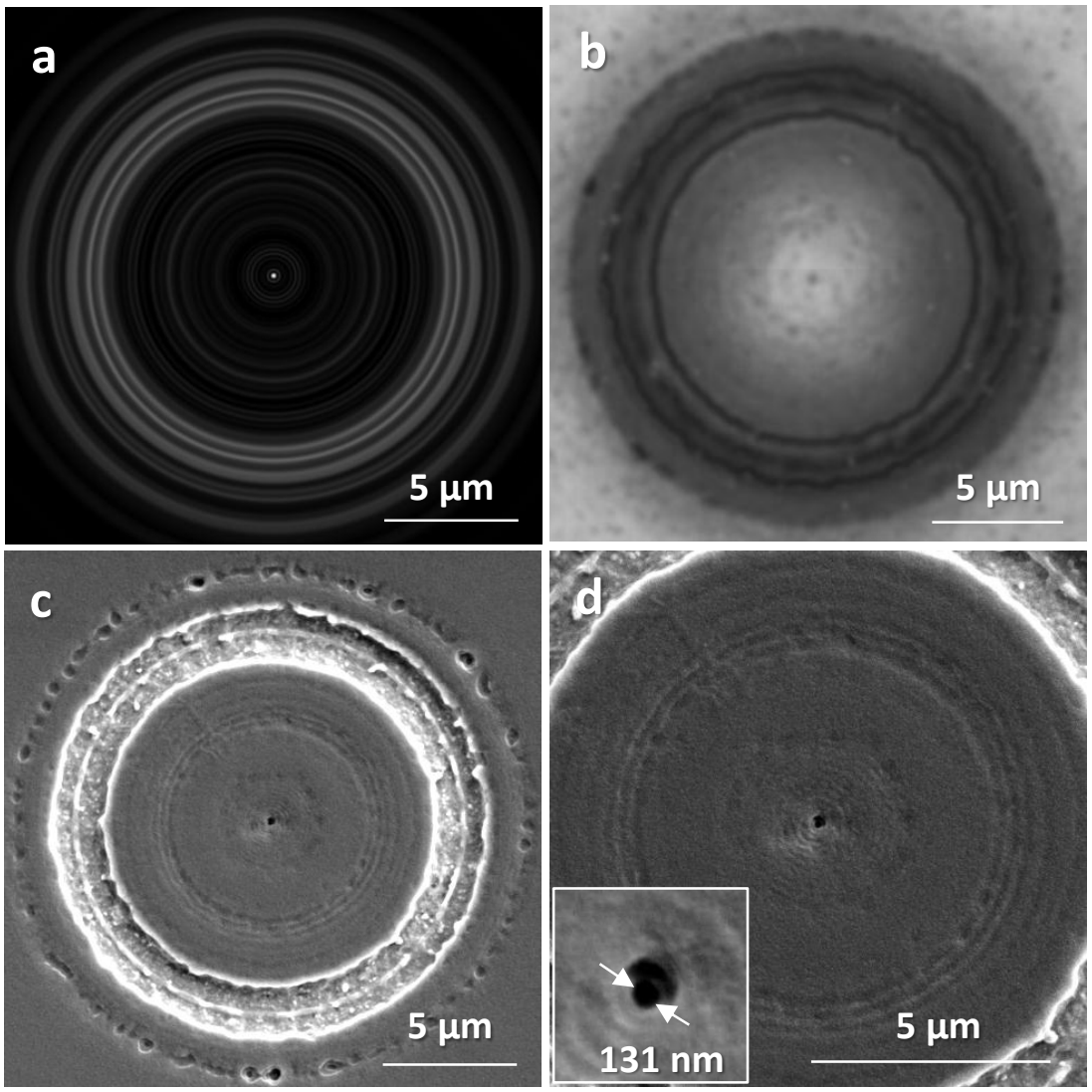

Figure 4.8: Experimental demonstration of solid-immersion super-oscillatory lens (a) Simulated intensity distribution after 4.6 µm AZO followed by 200 nm photoresist. (b) Developed photoresist imaged optically under white light in reflection. (c) Scanning electron microscope image of the developed photoresist coated with 5 nm gold. (d) Zoomed-in view of (c) showing details of the features registered in the central portion; inset shows the central spot measuring 131 nm.

4.6 Discussion

The aim of this chapter was to establish that super-oscillatory lenses remain functional even after the addition of a thick solid-immersion layer. To experimentally demonstrate this, aluminium-doped-zinc oxide (AZO) was chosen as the low-loss high-index immersion medium and a positive photoresist was chosen as the registration layer. The experiment would be considered successful if the central spot registered in the photoresist matches the theoretically predicted hotspot dimension, and this is the case presented in Section 4.5. However, this method of testing the performance of solid-immersion super-oscillatory lens has its own challenges and needs to be perfected for future continuation of the project.

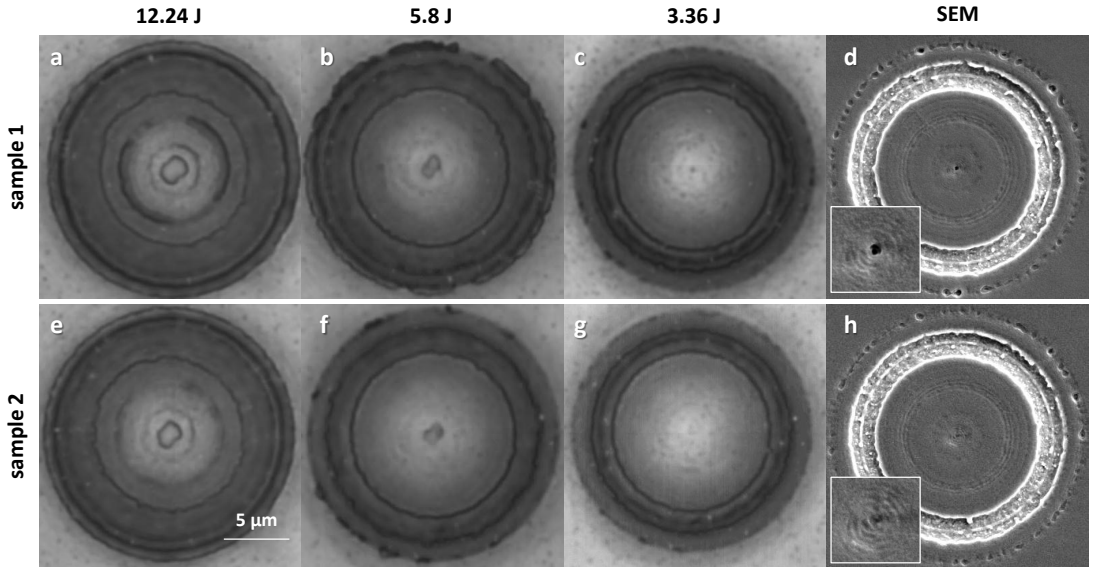

Figure 4.9: Uncertainty in the performance of the AZO-super-oscillatory lens. Optical microscope images for different incident energies for (a)-(c)sample 1 and (e)-(g)sample 2. SEM image of final stage of (d)sample 1 and (h)sample 2. The two samples are 100 µm apart on the same substrate.

Probably due to the variation in the AZO film quality across the substrate, even two neighbouring super-oscillatory lenses may not perform the same. Figure 4.9 shows an example of two super-oscillatory lenses separated by only 100 µm on the same substrate. Note that sample 2, though similar to sample 1 for different incident energies, is not identical. The final SEM image reveals there is no clear central spot formed for sample 2. This may be due to slight variation of AZO film thickness over 100 µm, but this is less likely. Another more probable reason is the occurrence of larger AZO grains

$\sim$ 200 nm in the central portion of sample 2 which scatters away the delicate super-oscillatory spot. Scattering from large sized AZO grains may also be the reason for the appearance of the arc-like feature close to the central hotspot seen in Fig. 4.8d (which is the same as Fig. 4.9d).

Finally, as the registration/recording layer for the sub-100 nm hotspots there may be a better alternative to photoresist. Registering such small spots in photoresist with nanometre accuracy would depend on the right choice of the photoresist which should support such high spatial resolution. We have briefly tried chalcogenide glass (GST) as the recording layer which upon laser exposure changes its phase from amorphous to crystalline state. The crystalline GST is more reflective compared to the amorphous form and also shows change in thermal and electrical conductivity. To read out the sub-wavelength super-oscillatory spot registered in the GST layer, atomic force microscopy may be used. However, grain size of the crystalline GST is $\sim$ 50 nm and hence may not be suitable to register a sub-100 nm spot with adequate resolution. Also since it is not trivial to change the phase of crystallised GST to amorphous, dosage testing needs a fresh sample for each exposure, unlike the recyclable photoresist sample.

4.7 Summary

In this chapter the concept of solid-immersion super-oscillatory lens is introduced. Such a configuration of the super-oscillatory lens will be of particular interest for applications like heat-assisted magnetic recording, a new technology for high density data storage in the magnetic hard disk drives. The performance of a solid-immersion super-oscillatory lens is simulated and experimentally demonstrated. The proof-of-principle experimental result shows a central hotspot measuring 131 nm registered on a positive photoresist through an immersion layer of aluminium-doped-zinc oxide. The experimental result matches the simulated intensity pattern well. It must be mentioned that this is only an initial effort to prove the working principle of solid-immersion super-oscillatory lenses. Further experimental work needs to be done to optimise the performance in terms of immersion material selection and film characteristics, better designs of the super-oscillatory lenses, and selection of better registration layer if available.

5

Planar diffractive meta-devices for visible spectrum

Recently, metallic-nanostructure-based metamaterials have provided a way of realising resonant, dispersive response of both amplitude and phase by the virtue of surface plasmon polaritons (discussed in section 1.3.1). The planar metamaterials, which are designed by patterning ultra-thin ($\ll \lambda$) plasmonic metal films, support plasmonic resonances characterised by the geometries of the individual sub-wavelength units or meta-molecules. By stitching the response of spatially varying meta-molecules arbitrary wave-front shaping may be realised. In this chapter polarisation insensitive ring-type meta-molecules are used to design a blazed diffraction meta-grating and an array of sub-micron sized meta-lenses producing focal spots smaller than the diffraction limit.

It is noteworthy that wavefront shaping has been achieved with diffractive optical elements (DOEs). These are commercially available thin dielectric devices that utilise micro-structured surface relief profile of two or more levels to modulate the phase in arbitrary manner. The micro-structures required for achieving desired phase profile are either etched in silica or quartz or embossed in polymers. DOEs provide high transmission efficiency due to weak interaction of light with the dielectric medium. Though much more compact than their refractive counterparts, DOEs require high aspect ratio topography to achieve desired phase modulation. In comparison, planar metamaterials use plasmonic resonance that can be designed by control of geometry of the metal films and thanks to modern nano-technologies free standing, i.e. metal film without any substrate (like 50 nm free-standing gold film [138]) makes it possible to realise devices in even more compact and miniaturised form.

For metamaterials (as discussed in section 1.3) the individual building blocks and

their inter-spacing are much smaller than the wavelength, so that the effective medium theory can be applied to the artificially engineered structures. The diffracting optical devices based on metamaterials, uses basic units which are smaller than the interacting wavelength; these sub-wavelength units are then arranged into larger sub-units which are comparable to or larger than the wavelength, and hence diffracting. In other words, arbitrary diffracting units are designed using sub-wavelength meta-atoms or meta-molecules.

5.1 Meta-diffraction-grating for visible light

5.1.1 Introduction

In 2003 it was demonstrated experimentally that periodic arrays of meta-molecules can exhibit polarization sensitive diffraction which is efficiently controlled by designing the constituent meta-molecules [139]. Some intriguing properties of diffraction from such arrays, like, asymmetric polarization conversion in opposite direction of propagation have been predicted [140]. Recently, planar diffractive optical elements based on metamaterials with variable parameters have attracted substantial attention [141–146]. In particular anomalous refraction and reflection has been observed in the far infra-red [143] and near-infrared [145] region of the spectrum. In earlier work, diffraction was observed on arrays of identical meta-molecules [139] and recent demonstrations [141–146] are concerned with the infra-red part of the spectrum. In contrast, this chapter presents a planar plasmonic meta-grating with periodic continuous variation of spatial meta-molecular parameters which operates in the visible part of the spectrum. At normal incidence the grating exhibits preferential blazing into one of the first orders of diffraction. It is interesting to note that a paper dated 1968 had presented analytical solution for diffraction from multi-element arrays of metal strips [147]. Each grating element consisted of monotonically decreasing length of metaL strips, which is similar to the concept used here; monotonically decreasing size of ring slots constitute a single grating element. In this section a planar blazed transmission grating operating in the visible part of the spectrum and designed by utilising the resonant properties of polarisation-insensitive meta-molecules will be described; the design concept of the meta-grating and the experimental demonstration of its performance will be presented.

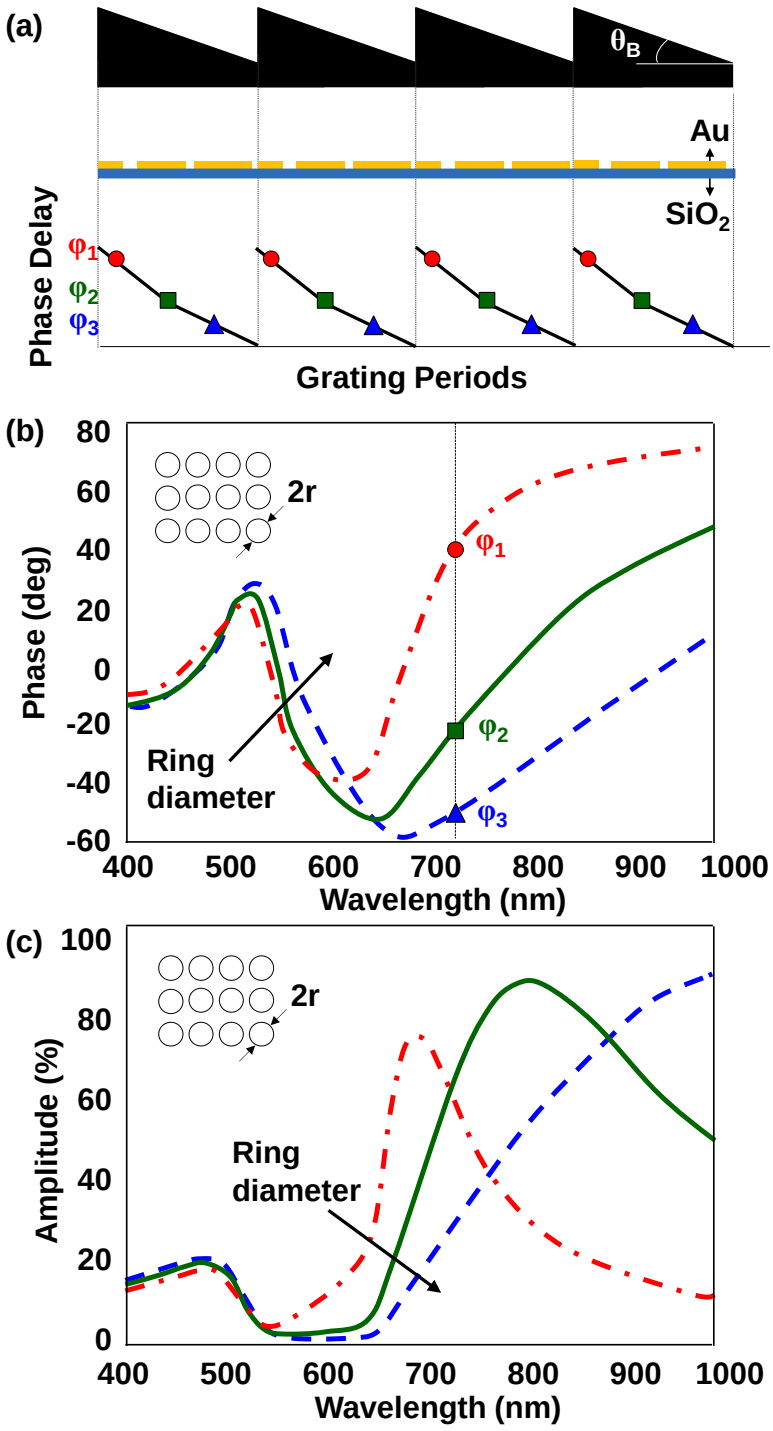

Figure 5.1: Design concept of a meta-grating (a) Phase response of a bulk blazed grating mimicked by a meta-grating. Transmission (b) phase delay and (c) amplitude of an infinite array of identical ring meta-molecules as a function of wavelength; different colours are for different diameters of the rings (dimensions of individual rings r_1 =64 nm; r_2 =90 nm; r_3 =112 nm, all with 45 nm line width).

5.1.2 Design and fabrication of a meta-grating

The design concept of the meta-grating is summarized in Fig. 5.1. A plane wave passing through a blazed grating, where each grating element has a triangular profile made out of high refractive index medium like silica or quartz, will acquire a phase delay depending on the thickness of the medium the light is traversing through. To mimic this phase ramp across a planar interface, the size dependent resonant response of a ring shaped meta-molecule is used. By gradually changing the size of the rings in a periodic fashion, the phase of the incident wave is controlled over sub-wavelength distances so that an asymmetric triangular phase profile is achieved (Fig. 5.1a).

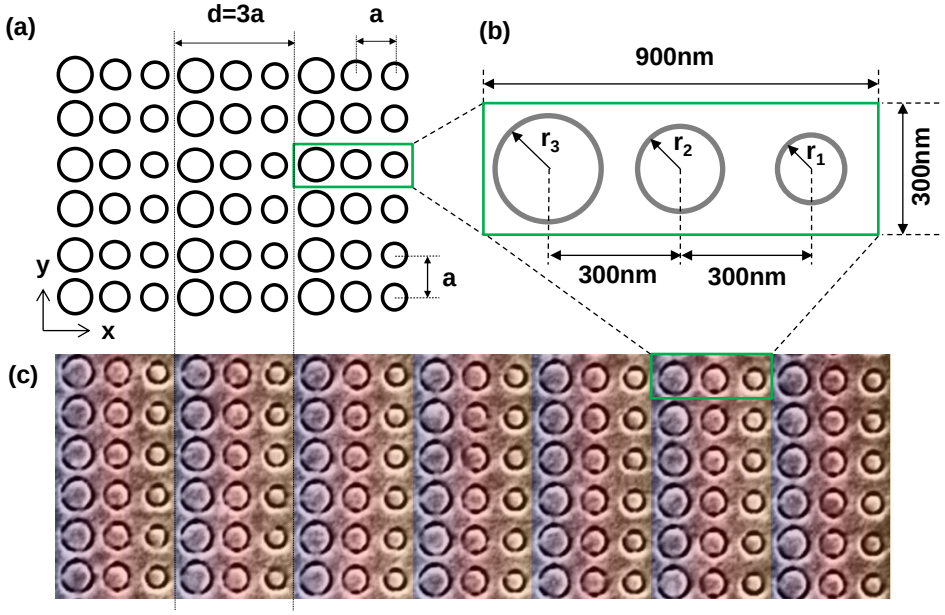

Figure 5.2: Structure of meta-grating(a) Schematic of the rings forming a planar meta-grating, (b) single meta-grating unit (dimensions of individual rings r_1 =64 nm; r_2 =90 nm; r_3 =112 nm), and (c) SEM image showing 7 periods of the fabricated structure; line width $\sim$ 30 nm. False colour shows the different elements contributing to the phase ramp.

Selection of appropriate sizes of meta-molecules for building a meta-grating unit requires the study of the resonant characteristic of each element. The ring-type meta-molecule chosen here have minimal crosstalk between neighbouring elements when arranged as an infinite array of identical units [148,149]. Using this property, the response of an isolated meta-molecule can be approximated by studying a planar array made of it; an infinite array is easier to compute. In what follows, a number of metamaterials are studied, each made out of different sizes of ring slots. Also, the choice of polarisation

insensitive meta-molecules ensure that any observed polarisation dependency arising in the grating transmission is due to the spatial arrangement of the meta-molecules only and not due to the individual building blocks.

The uniform metamaterials are simulated by solving Maxwell's equations in three dimension by finite element method (Comsol Multiphysics 3.5a). The metamaterials are designed as ring slots on ultra-thin ($\sim$ 50 nm) layer of gold supported by silica (n=1.46) substrate. The spectral dependence of transmission phase (Figs. 5.1b) and amplitude (Fig. 5.1c) of the two dimensional arrays, each made up of ring slots of different diameters, is computed for incident plane wave. For a given wavelength, the phase contribution from each array is different. At λ =740 nm phase shift of π is estimated for only 90 nm increment in diameter of the ring slots between two different meta-material array. The phase values at this particular wavelength when plotted for three different metamaterial array, with increasing meta-molecule size, resembles a phase ramp of a blazed grating (Fig. 5.1a).

To study the response of the meta-grating an infinitely planar periodic structure made out of units as shown in Fig. 5.2b is simulated (Appendix B). By periodically arranging the three ring slots with monotonically decreasing diameters as computed from the study of uniform metamaterials, the required transmission modulation is obtained. This particular combination of three different ring slots is chosen after studying the phase and amplitude of a number of different sizes of ring-slots (not presented here). Plane wave with polarisation parallel to the narrow dimension (y-axis) of the unit is incident on the meta-grating structure. Figure 5.3 shows for three different wavelengths the phase of the electric field (E_y) across a plane normal to the meta-grating surface. After passing through the meta-grating plane, the phase gets tilted at different angles for the three different wavelengths. Due to limited size of the simulation volume (2 μm on the transmission side) it is difficult to predict from the Comsol model the behaviour of the meta-grating in the Fraunhofer zone. To get a basic understanding of the far-field response, the complex electric field at 1.5 μm from the meta-grating surface is extracted from the Comsol model along a line in the x-direction. This is done for a wide range of incident wavelengths (550 nm to 850 nm) and for two orthogonal incident polarisations. This information about electric field though generated by an grating infinite in x-y direction, it is approximated to be given by an isolated grating element. The

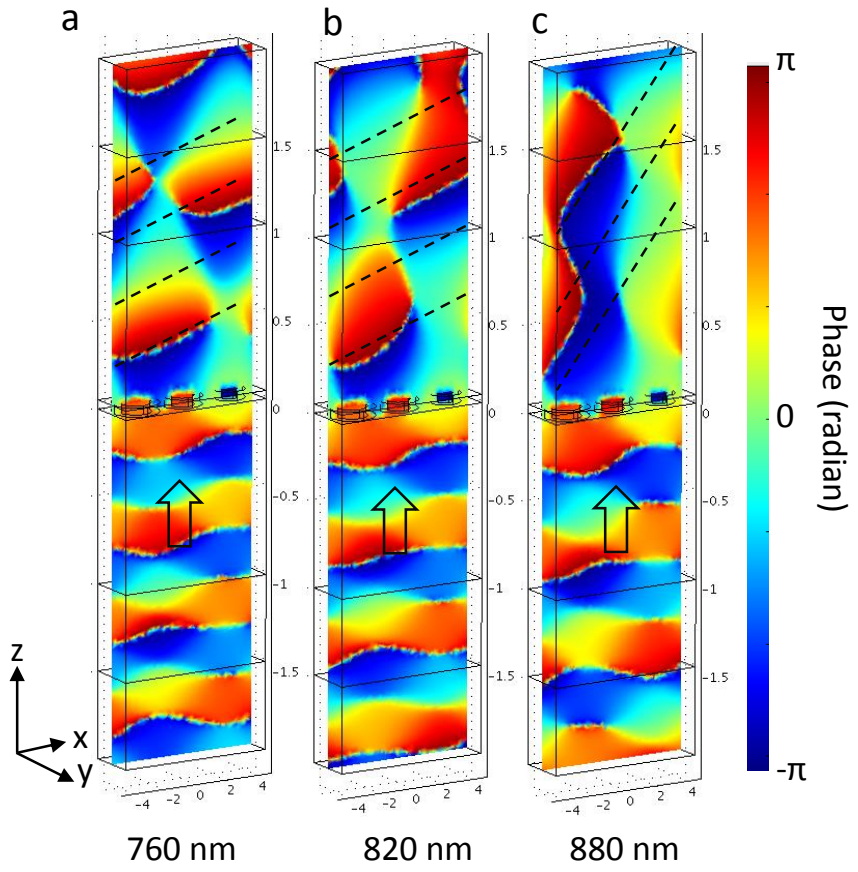

Figure 5.3: Spectral dependence of phase tilt for the meta-grating. Phase of the electric field across a plane normal to the meta-grating surface for incident wavelength (a) 760 nm, (b) 820 nm, and (c) 880 nm. The incident electric field was polarised along y-direction, parallel to the effective grating grooves. Arrow shows the direction of the incident electric field. Dotted lines are guide for phase tilt.

complex electric field is then repeated by a finite number along x-direction to simulate a finite but large grating. By taking Fourier transform of this complex electric field an approximation of the far-field intensity distribution, as diffracted by the meta-grating is obtained (Fig. 5.4). For the polarisation parallel to the effective grating grooves, there appears blazing in the diffracted intensity distribution (Fig. 5.4a). For 750 nm wavelength at an angle 50° towards left from the grating normal (order $m = -1$) the intensity is the most pronounced. In comparison, to the right of the grating normal (order $m = +1$) the intensity diffracted for all the wavelengths is much less. Simulation for the incident polarisation perpendicular to the effective grating grooves shows that the most of the intensity is concentrated in the zero-th order, with no significant blazing on either side of the normal (Fig. 5.4b). This polarisation dependence is also expected

from a conventional blazed grating.

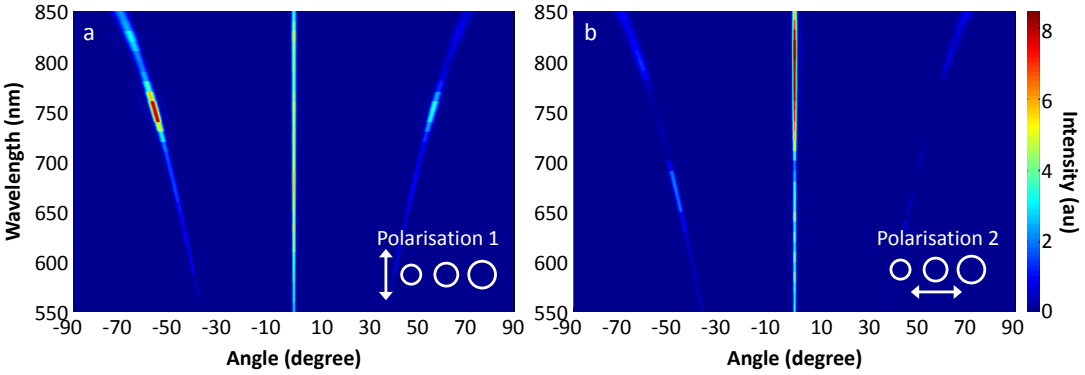

Figure 5.4: Simulated diffracted intensity distribution (a) for incident polarisation parallel to the effective grating grooves (see inset) and (b) polarisation perpendicular to the effective grating grooves (see inset). The meta-grating is blazed for 750 nm wavelength and incident polarisation as in (c). Insignificant blazing observed in (b).

The meta-grating structure is fabricated by focused ion beam milling of a 50 nm thin gold film. The gold film is deposited on a quartz substrate using resistive evaporation. While milling, the ion-beam current is selected by several trials to be 9.7 pA such that the line-width of individual rings measure ∼30 nm. The fabricated structure has 900 nm grating period as designed, and consists of 30 grating elements with overall device dimension of 27 µm by 27 µm. A scanning electron micrograph of a section of the fabricated meta-grating structure is shown in Fig. 5.2c. The measured line-width of the ring slots is ∼30 nm. The false colour on the SEM image depicts each column of sub-wavelength meta-molecules that contributes a particular phase value; the three colours show three monotonically varying phase values periodic in the x-direction.

5.1.3 Experimental characterization: meta-grating

The optical experimental set-up used for characterization of the meta-grating is depicted schematically in Fig. 5.5[1]. The structure is illuminated from the substrate side with white light (450 nm-2000 nm) from a super-continuum laser. The beam coming out of the laser is focused to ∼30 µm by reflecting off a 90° parabolic mirror, such that it just overfills the fabricated meta-grating structure. The light diffracted by the meta-device needs to be measured with both angular and spectral resolution. For this a

[1]The author acknowledges Dr. Andrey Nikolaenko's help with setting up the experiment for the meta-grating characterisation.

fibre collimator mounted on a rotation stage is used to collect the light from the sample in 1° angular steps. The fibre is connected to a spectrum analyser which records the output from the meta-grating over a spectral range of 400 nm to 1000 nm.

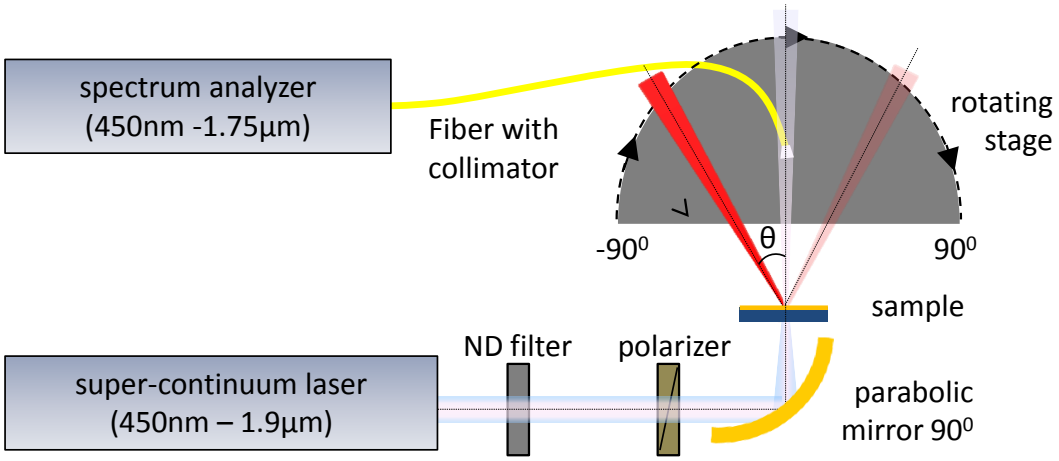

Figure 5.5: Experimental set-up for meta-grating characterisation. Light from super-continuum laser incident on the meta-grating. Diffracted light collected over ±90° angle by a fibre collimator and recorded by a spectrum analyser

Figure 5.6 shows the intensity of light diffracted by the meta-grating into the first diffraction order, normalized to the intensity of light transmitted normal to the sample. The light diffracted to the right of the normal is denoted as positive order and that to the left as negative order. As expected from the effective grating period, no intensity is diffracted for incident wavelengths greater than 900 nm. The meta-grating shows higher efficiency for y-polarization, when the electric field is parallel to the effective grating grooves. For y-polarization (Fig. 5.6a) blazing is the most prominent for wavelength 736 nm, with 1.4% of the transmitted light diffracted at an angle of $-55°$ to the grating normal. Very little light is diffracted in the positive order. The effect of blazing in this case is redistribution of energy from the positive first order to the negative first order. The inset of Fig. 5.6a shows that the spectral peak in the negative order corresponds to a spectral dip in the positive order.

For x-polarization (Fig. 5.6b) the blazing is much less prominent and the peak efficiency is about 4 times lower than that for y-polarization. Mutual coupling between neighbouring rings, which arises due to varying sizes of meta-molecules along one direction, may cause the observed polarization dependence of the transmission meta-grating. As can be seen from Figs. 5.6a and 5.6b the experimental data matches well with the

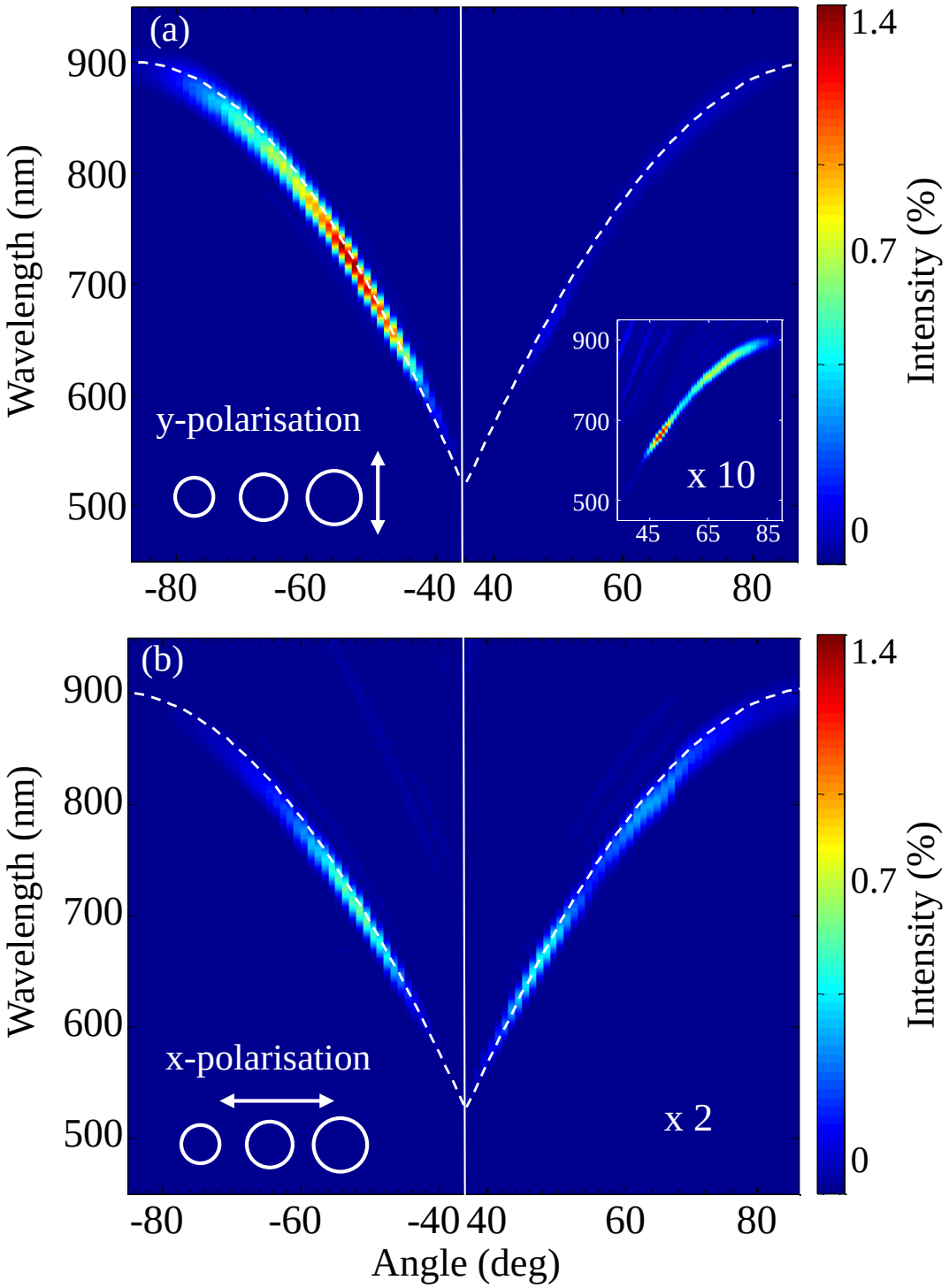

Figure 5.6: Experimental demonstration of the meta-grating. Intensities of light diffracted into first order for (a) y-polarization and (b) x-polarization. In (b) the intensities are multiplied by 2 for presentation clarity. The inset in (a) shows the diffracted light for the positive first order with 10 times enhanced intensity. The white dashed line is the theoretical plot of the grating equation.

theoretical plot of the grating equation [8]: $m\lambda = d(sin(\theta_i) + sin(\theta_r))$ (where, $m = \pm 1$ is the order of diffraction, d =900 nm is the grating period, $\theta_i = 0$ for normal incidence and θ_r are the angles at which the light is diffracted).

To estimate for the meta-grating efficiency, the spectral distribution of the diffracted intensities into the negative first order for the two incident polarizations is plotted in Fig. 5.7a. This is a plot of intensity versus wavelength along the white dashed line in Figs. 5.6a and 5.6b for the negative first order only. The beam diffracted into the negative first order for incident y-polarization is 4 times more intense than that for x-polarization. Fig. 5.7b illustrates the ratio of intensities diffracted into the negative first order to that into the positive first order. It is observed that for the more efficient y-polarisation, at the blazing wavelength, the intensity diffracted into the $m = -1$ order is around 25 times the intensity that is diffracted into $m = +1$ order.

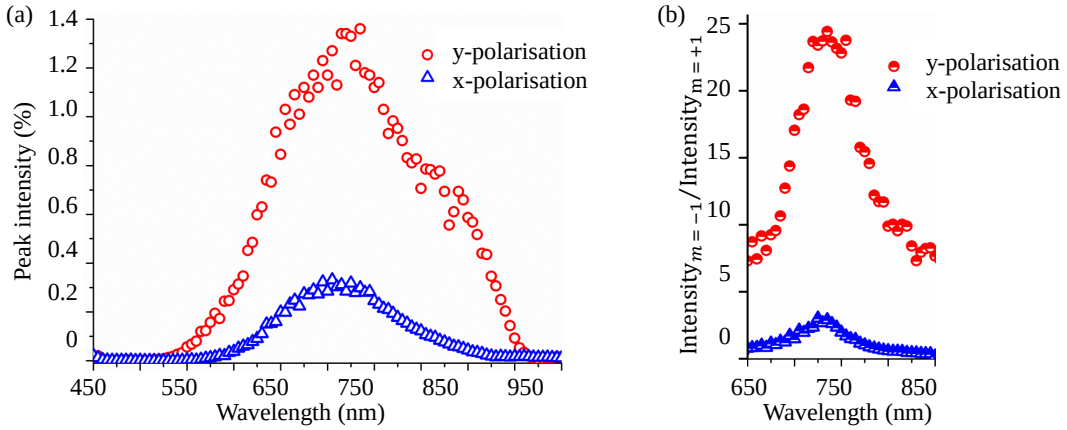

Figure 5.7: Meta-grating efficiency(a) Spectrum of diffracted intensity for negative first order and (b) ratio of intensity between orders $m = -1$ and $m = +1$.

It is worth suggesting that the transmission meta-grating structure may also be used in reflection configuration, as mentioned in [150]. Due to the spectral dependencies of reflectivity of the constituent meta-molecules blazing will occur at a wavelength which may be different to the transmission blazing wavelength. The blazing efficiency in the reflection configuration may be optimized by selecting the proper angle of incidence.

5.1.4 Summary: meta-grating

A blazed diffraction grating is designed with planar resonant meta-molecules. As a grating element, 3 meta-molecules with monotonically varying sizes are used to obtained

3 different transmission phase values within sub-wavelength spacing, resulting in a continuous phase ramp. The meta-grating exhibits blazing for 736 nm wavelength at negative first order, which is 25 times stronger compared to the light diffracted in to the positive first order.

5.2 Subwavelength focusing meta-lens array

5.2.1 Introduction: meta-lens array

It is known that metamaterials promise sub-wavelength focusing through negative refraction (section 1.2.3). In a different method where planar metamaterials can be employed to design arbitrary wavefronts, flat lenses designed with V-shaped meta-molecules have been demonstrated at telecommunication wavelengths with diffraction limited performance [146]. In this section it will be demonstrated how metamaterials can be utilised to focus light into sub-diffraction limited spots beyond the near-field and without invoking negative refraction.

Recently it was shown that precisely tailored diffraction of light on a binary mask can create a sub-wavelength optical hotspot that can be used for optical imaging with resolution far exceeding that of conventional optical instruments (Chapter 2). This is possible due to the phenomenon of super-oscillation (section 1.2.4) where interference of propagating components of light may create arbitrarily small hot spots. In practice, however, a super-oscillatory binary mask has not been demonstrated to deliver hotspots smaller than $\lambda/3$, where λ is the wavelength of light. Super-oscillatory masks with the ability to continuously control intensity and phase of the transmitted wave has been reported to create hotspots of any size [48]. Unfortunately manufacturing of such masks, which should have optical thickness and density defined with nano-scale lateral resolution across a device of tens of microns, is still an unattainable technological challenge. In this section it is shown how planar metamaterials can provide a way to manufacture a super-oscillatory mask with spatially variable transmission and phase. The principle is illustrated with a simple example of metamaterial super-oscillatory lens array. The super-oscillatory meta-lens, as will be described here, is designed as a cluster of five polarization independent meta-molecules. It has been previously shown [6] that even relatively simple systems with as few as 6 degrees of freedom can exhibit super-oscillation. It must be mentioned that array of lenses made of polystyrene micro-spheres has already been demonstrated as useful for making repetitive micrometer patterns [151]. It is envisioned that the nano-scale meta-lens arrays, as presented here, producing sub-wavelength hotspots will be better suited to such photo-lithographic processes, and will also find application in high resolution parallel imaging, and optical

data storage. In the following sections the working principle, design, experimental methods and observations for the meta-lens arrays are discussed.

5.2.2 Design and fabrication: meta-lens array

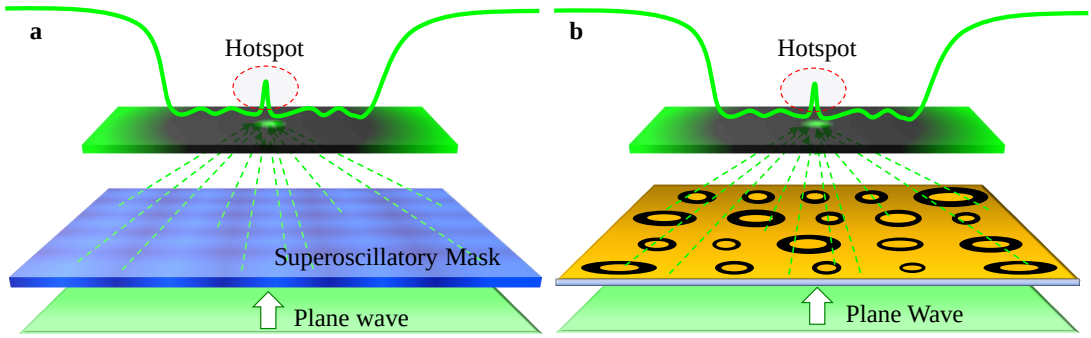

Figure 5.8: Super-oscillatory mask vs. meta-lens Design and performance of (a) an hypothetical continuous superoscillatory mask, and (b) superoscillatory meta-lens generator, both producing arbitrarily small hot spots at post-evanescent distances from the surface.

The principle of a metamaterial super-oscillatory generator is illustrated on Fig. 5.8 and compared with a conceptual super-oscillatory continuous mask [48]. An arbitrarily small hot spot, as predicted by super-oscillation principle, is produced by a plane wave incident on a hypothetical super-oscillatory mask. The mask is designed with lateral resolution on the wavelength scale enabling continuous control of the transmission and retardation. In comparison, the metamaterial super-oscillatory generator exploits the resonant behaviour of the individual sub-wavelength meta-atoms. Each of the meta-atoms can scatter light with defined amplitude and phase depending on its design and position in an array, resulting in transmission with any arbitrary modulation. Indeed, the spectral dependencies of phase retardation and intensities are in general different and thus, in principle, it is possible to design a meta-atom with a prescribed combination of scattering characteristics. In practice, however, this is difficult and is complicated by three factors namely, absorption losses, finite size of the arrays of meta-atoms and mutual interactions between them. In the view of these challenges the optimum design for the metamaterial focusing device is investigated using an empirical combinatorial approach [152] and the results compared against three-dimensional finite-element simulations (Comsol Multiphysics 3.5a)

The stages of designing a meta-lens array starting from a regular metamaterial

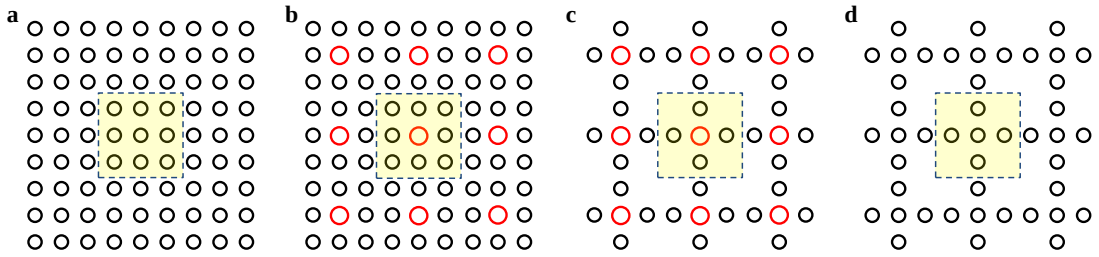

Figure 5.9: Design stages of meta-lens array (a) A regular metamaterial, (b) meta-lens array formed by changing the central ring size in a 3x3 section, (c) meta-lens array formed by changing the central ring size in a 3x3 section and omitting the 4 corner meta-molecules, and (d) meta-lens array formed by omitting the 4 corner meta-molecules in a 3x3 section of a regular metamaterial.

may be understood by following Fig. 5.9. For a regular metamaterial (Fig. 5.9a) incident plane wave results in unmodulated phase and intensity distribution, as shown in Fig. 5.10a-e. However, in a section of 3x3 meta-molecules, if the central unit is made slightly larger(Fig. 5.9b) the phase and intensity are modulated giving a lens like distribution. This is because, for a regular metamaterial made of ring slot type meta-molecules, the cross-talk between neighbouring units is negligible. As soon as, some of the meta-molecules are made slightly larger than others, coupling with its neighbours are no longer insignificant. For a certain wavelength, when the larger central meta-molecule contributes higher phase and intensity values than its surrounding smaller neighbours, a convex lens like distribution forms in the 3x3 sub-unit, resulting in a periodic distribution of such convex lenses. Since the meta-molecules have dispersive phase and amplitude response, depending on the wavelength it may be so that a concave lens is formed by the sub-unit, when the larger central meta-molecule contributes lower phase value than its surrounding neighbours. To test the concept further, within the 3x3 sub-unit if the 4 corner meta-molecules are made absent(Fig. 5.9c), it continues to function like a lens. In designing the lens unit the major role is played by coupling between neighbouring elements. When the meta-molecules at the 4 corners are omitted, the 4 peripheral meta-molecules couples to the central one owing to absence of nearest neighbour to one side only. Using this property a meta-lens unit is designed where all the meta-molecules are of same size, but units are spatially arranged to form a lens (Fig. 5.9d). These were the design steps followed to arrive at the final configuration as presented here.

The meta-lens array presented here is designed with meta-molecules which are ring

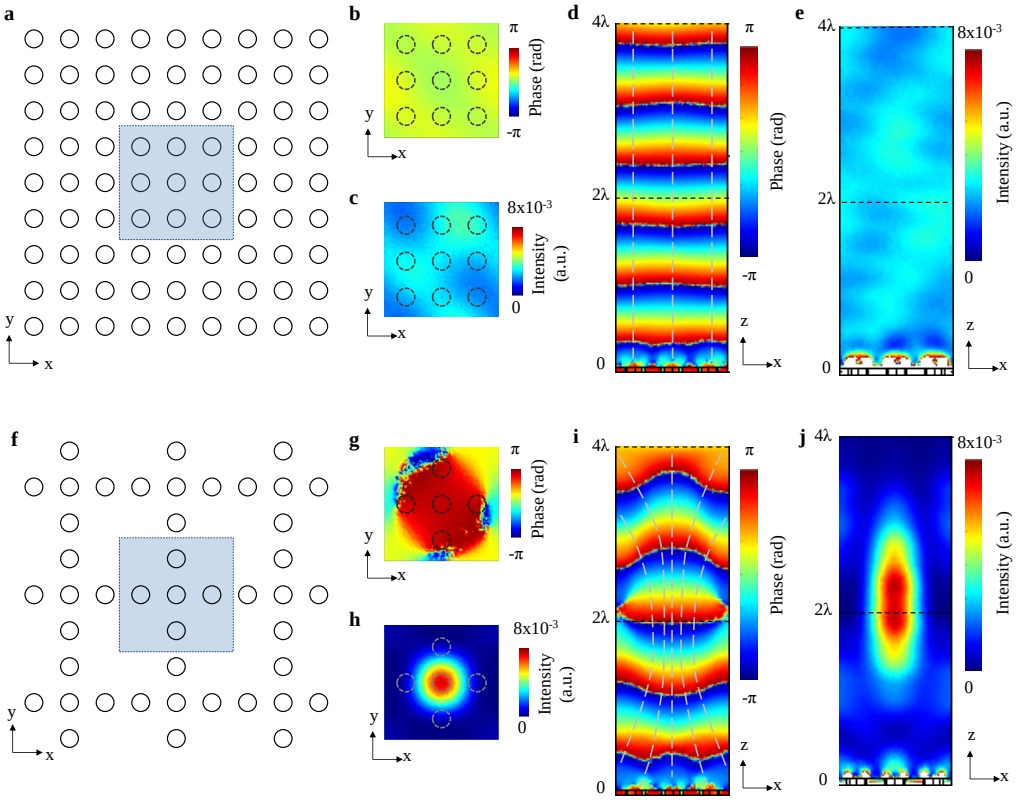

Figure 5.10: Simulating performance of a meta-lens array Regular metamaterial vs. meta-lens array: (a) Section of an infinite planar array of ring meta-atoms. (b) Phase and (c) intensity, over 3 x 3 meta-atoms, at 2λ from the surface. (d) Phase and (e) intensity in the propagation direction over the 3 x 3 meta-atoms. (f) Section of an infinite meta-lens array. (g) Curved phase front and (h) focused intensity profile over a meta-lens unit, at 2λ from the surface. Note that phase wrapping occurs in (g). (i) Phase profile like that of a converging lens and (j) intensity showing a focal spot in the propagation direction over a meta-lens unit.

slots in a 50 nm thin gold film; each ring slot has 20 nm line width. To understand the design of a meta-lens array, an infinite array of meta-atoms with regular sub-wavelength periodicity (Fig. 5.10a) and illuminated by a plane wave, is studied. The transmitted wave retains a plane wavefront as illustrated in Figs. 5.10b - 5.10e. However, when the arrays are constructed such that cluster of 5 ring slots are periodically repeated (Fig. 5.10f), the transmitted wavefront no longer remains flat, but is modulated. The light passing through the central part of each cluster experiences a different phase delay than that passing through its outer area: the transmitted light wavefront becomes curved. The wave front curvature is controlled by the ring dimensions, their mutual position in the cluster and depends on the incident wavelength and polarization. As the central part of the ring cluster provides higher phase delay than its outer part, it forms

a convex meta-lens and transmitted light converges to a focus several wavelengths away from the meta-lens surface. A hot-spot is formed directly above the central ring, as illustrated on Fig. 5.10h. The planar array of foci repeats itself at fixed distances along the propagation direction due to Talbot effect [87] (discussed in section 1.3.2).

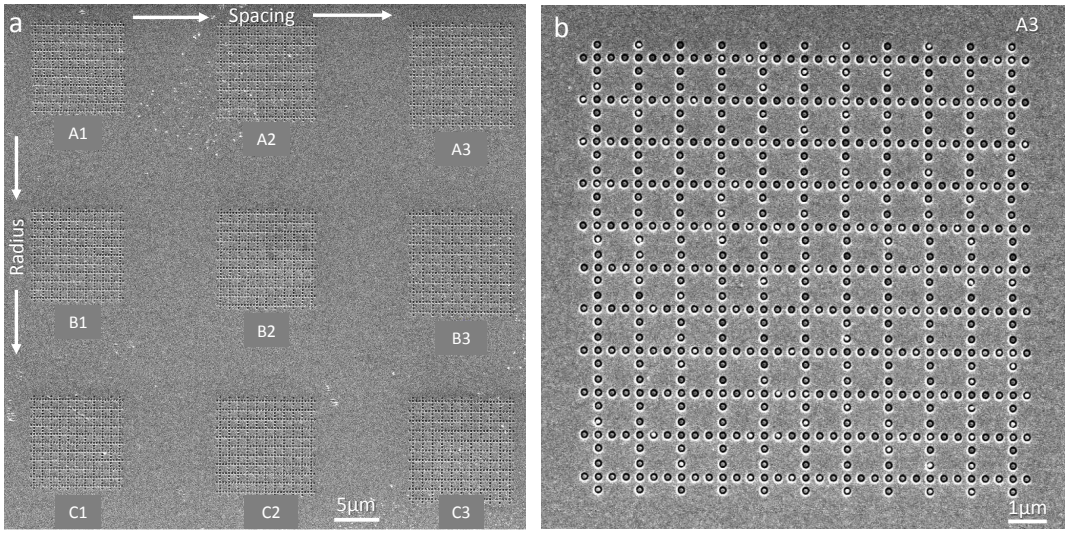

Spacing *a* / Radius *r*	1	2	3
A	75; 300	75; 320	75; 340
B	80; 300	80; 320	80; 340
C	85; 300	85; 320	85; 340

Figure 5.11: Scanning electron microscope image of the fabricated combinatorial meta-lens sample (a) Matrix of nine samples with varying inter-ring spacing and ring radii. (b) Sample A3 consisting of 11x11 meta-lens units; a single unit is marked with red box. Table shows the radii and centre-to-centre separation between neighbouring rings for each of the 9 meta-lens arrays.

The sample used for demonstrating the proof-of-principle super-oscillatory meta-lens consisted of a combination of nine different meta-lens arrays with varying parameters, each with 11x11 meta-lenses. The dimension of individual rings and the centre-centre to spacing between the nearest neighbours are depicted in a tabular form in Fig. 5.11. Looking at the scanning electron micrograph of the fabricated combinatorial sample (Fig. 5.11a), the radii of constituent ring slots measure 75 nm for all meta-lens arrays along the top row and increases in 5 nm steps for each successive rows. The centre-to-centre distance between the neighbouring meta-atoms is 300 nm for all meta-lens arrays on the left most column and increases in 20 nm steps for consecutive columns. The meta-lens arrays are fabricated by focused ion beam milling of a 50 nm

thin gold film deposited on a silica substrate by resistive evaporation. For all the rings slots the line width measures ∼34 nm.

5.2.3 Experimental characterisation and results: meta-lens array

The performance of the meta-lenses is investigated for 750, 800 and 850 nm wavelengths with a circularly polarized laser beam illuminating the arrays from the substrate side. Circular polarization is used rather than linear polarization to eliminate any asymmetry in the resulting focal spots. A linearly 45° polarised light has shown similar results in the computation. However, in the experiment it is non-trivial to ensure the polarisation is exactly at 45° to the axis of the meta-lenses. For any other angle of linear polarisation, it may be commented from computational studies that, the result will be elliptical shaped focal spots.

The intensity pattern on the transmission side of the meta-lens arrays is imaged in immersion oil by a CCD camera through a liquid immersion microscope objective (60X, NA=1.4). The formation of foci and the reconstruction of the array at periodic distances from the meta-lens arrays are observed. The best results are found with 800 nm illumination on meta-lens structure A3 (Fig. 5.11b) and are presented here.

Figure 5.12 presents a summary of the experimental characterization of meta-lens A3. The intensity distribution on the surface of the sample, when illuminated with plane wave, is shown on Fig. 5.12a. The foci above each meta-lens unit re-appears after every z'_T =2.8 μm along the propagation direction. This is presented on Fig. 5.12b where the intensity distribution directly above a meta-lens unit is plotted along the propagation direction. It is noteworthy that the classical Talbot effect predicts repetition distance for focal spots to be z_T =3.6 μm. This is calculated from the relation [88] $z_T = \lambda_{medium}/1 - \sqrt{1 - (\lambda_{medium}/d)^2}$, where $\lambda_{medium} = \lambda_0/n, n = 1.5$ is the refractive index of the immersion oil in which the intensity pattern is formed and d is the meta-lens unit period. The discrepancy between the calculated classical Talbot distance and the measured repetition distance may be explained by the following reasons: (i) classical Talbot effect is defined and observed for infinite grating, and (ii) the above formula and its well known approximation ($z_T = 2d^2/\lambda_{medium}$), holds true in the paraxial limit when $d/\lambda >> 1$. In this case of the meta-lens array neither of the two reasons required for observing classical Talbot effect holds true. The meta-lens period (1020 nm)

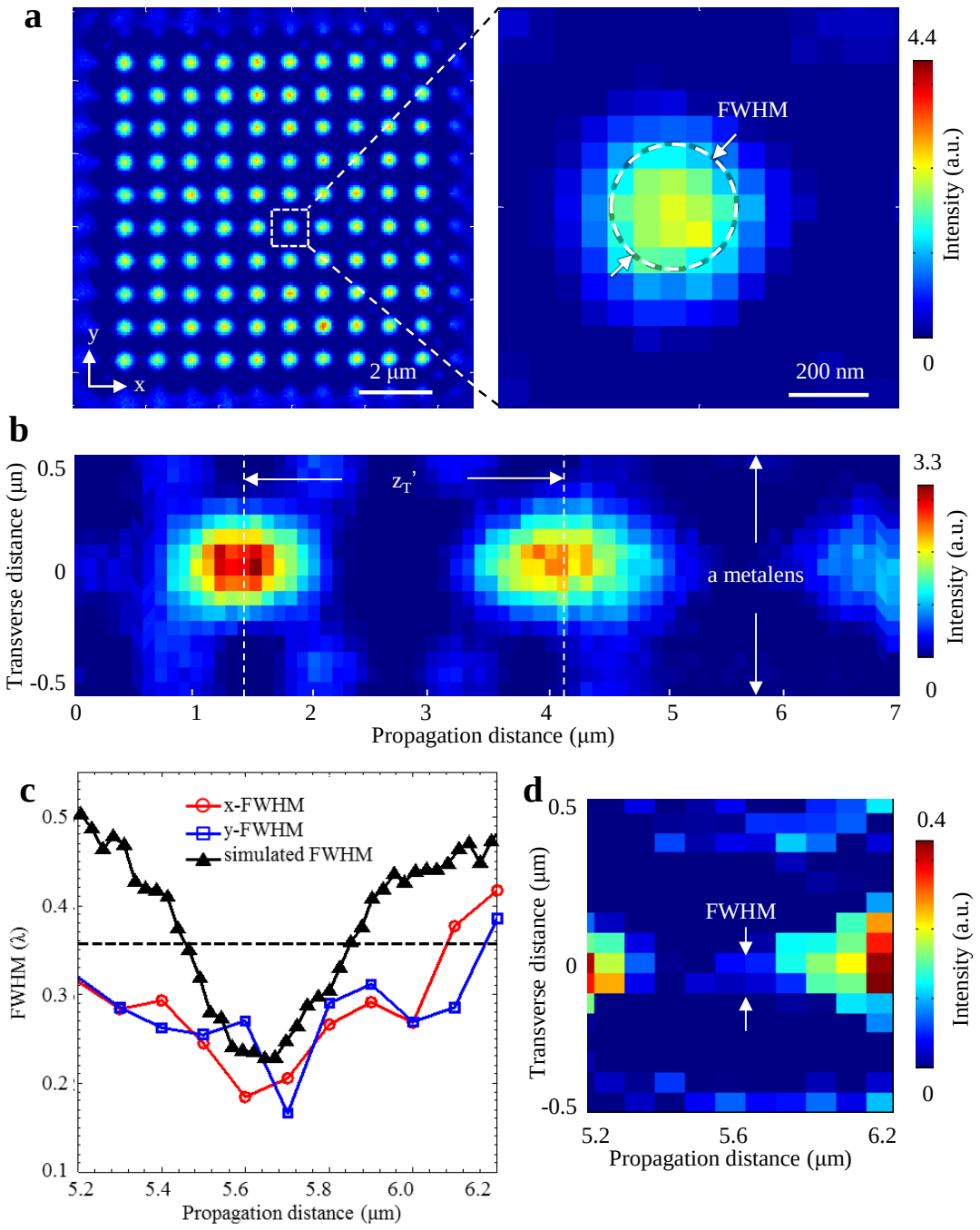

Figure 5.12: Experimental focusing with meta-lens A3 (a) Intensity distribution on the surface of the meta-lens array; (right) over a meta-lens unit. (b) Intensity plot over one meta-lens unit showing repeated formation of focal spots along the propagation direction with Talbot distance $z_{T'}$. (c) FWHM of a spot along the propagation distance. The focal spot is below diffraction limit (dashed line). (d) Zoom of (b) showing low intensity region over which focal spot is smaller than the diffraction limit.

is of the order of wavelength (800 nm) and the grating is made of only 11 periods, or $\sim 14\lambda$, which is of finite extent. Such deviation from classical Talbot distance in the non-paraxial limit for nano-structures has been observed and reported by other researchers [93, 96].

To analyse the sub-wavelength characteristics of the hot-spots, a single spot directly over a meta-lens unit is chosen and the full width at half maximum (FWHM) is measured for each position along the propagation direction. Figure 5.12c shows a plot of the FWHM, as measured and simulated, along the propagation direction where small spot sizes were observed. The smallest spot (FWHM = 176 nm) occurs at 5.7 μm with low intensity levels (Fig. 5.12d). In fact, all the spots smaller than the diffraction limit (dotted line in Fig. 5.12c) were found in the low intensity region and several wavelengths away from the meta-lens surface which are characteristic features of optical super-oscillations [104].

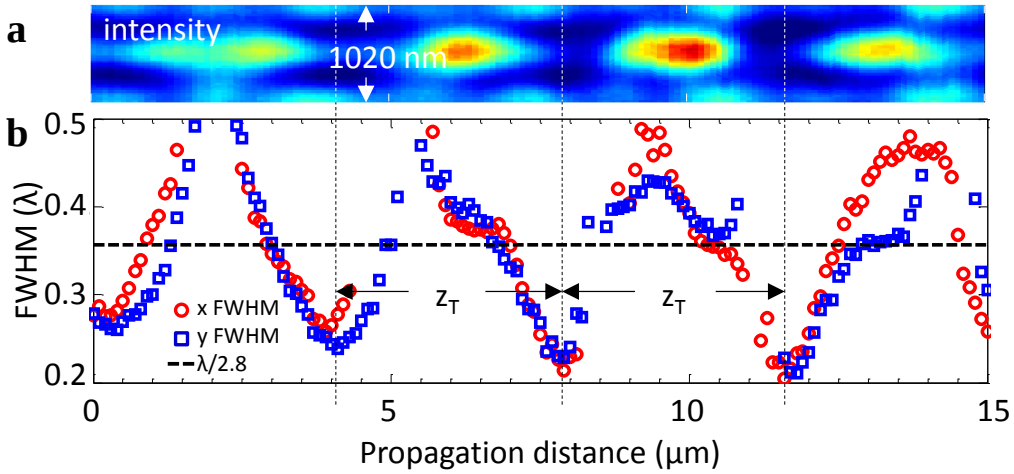

Figure 5.13: Long-range performance of a super-oscillatory meta-device (a) Experimentally measured intensity and (b) FWHM from a sample formed by 30 by 30 meta-lenses. Hot-spots measuring $\sim 0.2\lambda$ at 11.7 μm from the lens with Talbot distance of 3.8 μm are observed.

In the above experiment, due to the finite size of each of the samples in the combinatorial array, the distance up to which the hot-spots could be characterized was limited by strong edge diffraction effects. To address this, a large array consisting of 30 by 30 meta-lenses is fabricated with each meta-lens unit measuring 1.02 μm by 1.02 μm. When illuminated with an 800 nm circularly polarized laser, hot-spots measuring as small as ∼160 nm is observed as far as 11.7 μm from the metamaterial lens

surface (Fig. 5.13b). The hot-spots were repeated along the propagation distance with a repetition distance of 3.8 μm, which is significantly different from that observed in case of the smaller array. As noted earlier, the finite size of the meta-lens array affects the self-imaging distance, or repetition distance of the focal spots. Changing this finite extent may change the distance at which the focal spots re-appear. However, similar to the smaller array of meta-lenses, in this case also, the smallest spots appeared in the low intensity region; the size of the high intensity spots is around the diffraction limit.

5.2.4 Summary: meta-lens array

A super-oscillatory meta-lens array made of clusters of ring slots milled on a thin gold film is designed and experimentally demonstrated. The design of the lens-like phase and intensity pattern relies on coupling between the nearest neighbours of cluster. The meta-lens arrays act as a focusing device depending on the parameters of the meta-atoms and optical wavelength and can generate arrays of sub-wavelength foci as small as $\lambda/5$ at a distance 14.7λ from the meta-lens surface. Such planar arrays of meta-lenses can find applications in high resolution parallel imaging, photo-lithography, and data storage.

5.3 Summary

This chapter presents how resonant properties of spatially varying sub-wavelength meta-molecules can be utilised to design planar optical devices. As examples of diffractive planar optics, a blazed transmission meta-grating operating at visible wavelengths, and an array of meta-lenses focusing light in to sub-diffraction limited spots are demonstrated.

The blazed transmission meta-grating is designed using polarisation insensitive ring-type meta-molecules, which are spatially arranged with varying parameters to mimic periodically varying phase ramp. Each meta-grating unit consists of 3 meta-molecules arranged with monotonically decreasing diameters, such that, a specified phase delay is obtained from each meta-molecule within sub-wavelength spacing. The meta-grating with 900 nm grating period diffracts white light incident with linear polarisation. The strongest blazing is observed for 736 nm wavelength when incident electric field is parallel to the effective grating grooves. At the blaze wavelength the negative first order shows 25 times more intensity compared to that diffracted in to the positive first order.

The meta-lens array is designed by arranging ring-type meta-molecules spatially such that coupling between the nearest neighbours is enhanced resulting in a lens-like intensity and phase distribution. Each meta-lens unit consist of a cluster of 5 meta-molecules and is arranged in to a planar array. When illuminated with circularly polarised light, array of sub-wavelength focal spots are formed at repeated distances along the propagation direction. The focal spot distribution though similar to Talbot effect, the repetition distance is different from the calculated Talbot distance. This may be attributed to Talbot effect in the non-paraxial limit, when the period of the units are comparable to the incident wavelength. At certain distances beyond the near field of the meta-lens surface, the focal spots measure smaller than the diffraction limit. This is attributed to the phenomena of optical super-oscillation which says that light may be focused in to arbitrarily small spots and this has been demonstrated to be done by designed interference of propagating components only [104]. It is demonstrated here that a meta-lens made of ring-type metamolecules with unit measuring 1.02 μm by 1.02 μm, can focus incident monochromatic light (800 nm) to a spot measuring 0.2λ at a distance $\sim 14.7\lambda$ from the device surface.

6 Nano-structure-enhanced photoluminescence

6.1 Introduction

6.1.1 Photoluminescence

One of the possible outcomes of light-matter interaction is photoluminescence, which is defined as emission of light from a matter due to radiative recombination of electrons (with holes) from a higher energy level which were excited by absorbing photons. The emission of light from matter is called luminescence, and in this case it is induced by external photons, hence the name *photo*-luminescence [153].

To explain further, upon irradiation by an external light source the atoms in a material may absorb the incident energy. If the incident photons have energy larger than the electronic band gap, the electrons from the ground state S_0 are excited to the higher energy conduction band S_1 (Fig. 6.1a) leaving holes behind. Each energy state is made up of several closely spaced vibrational levels shown as 0, 1, 2, etc. in the diagram. The energised electrons may reach higher vibrational levels of the excited state from where they will quickly ($\sim 10^{-12}$ sec) relax to the lowest level of that state (white arrows in Fig. 6.1a). This is a non-radiative process and hence no process can be detected externally. From the lowest level of S_1 the excited electrons will now relax to S_0, ending up mostly in the highest energy level available in this state. The recombination of the electrons with the holes in level S_0 might be a radiative process when photoluminescence is detected. Since some of the absorbed energy is expended in non-radiative processes, the wavelength (energy) of the photoluminescence is often larger (smaller) than the wavelength (energy) of excitation.

The first observation of photoluminescence was reported as early as 1845 by Sir John Herschel [154, 155]. He observed a *'beautiful celestial blue colour'* from an otherwise colourless quinine solution when held under sunlight. It must be noted here that photoluminescence may be classified [155] as fluorescence and phosphorescence depending on the nature of excited state. For fluorescence emission occurs from the excited singlet states, from where transition to the ground state is allowed, and has a typical emission rate 10^8 s^{-1}. For phosphorescence the emission occurs from the excited triplet states from where transition to the ground state is forbidden, and emission is rather slow (10^3 to $10^0 s^{-1}$). In this chapter, all emission processes will be referred to as luminescence or photoluminescence.

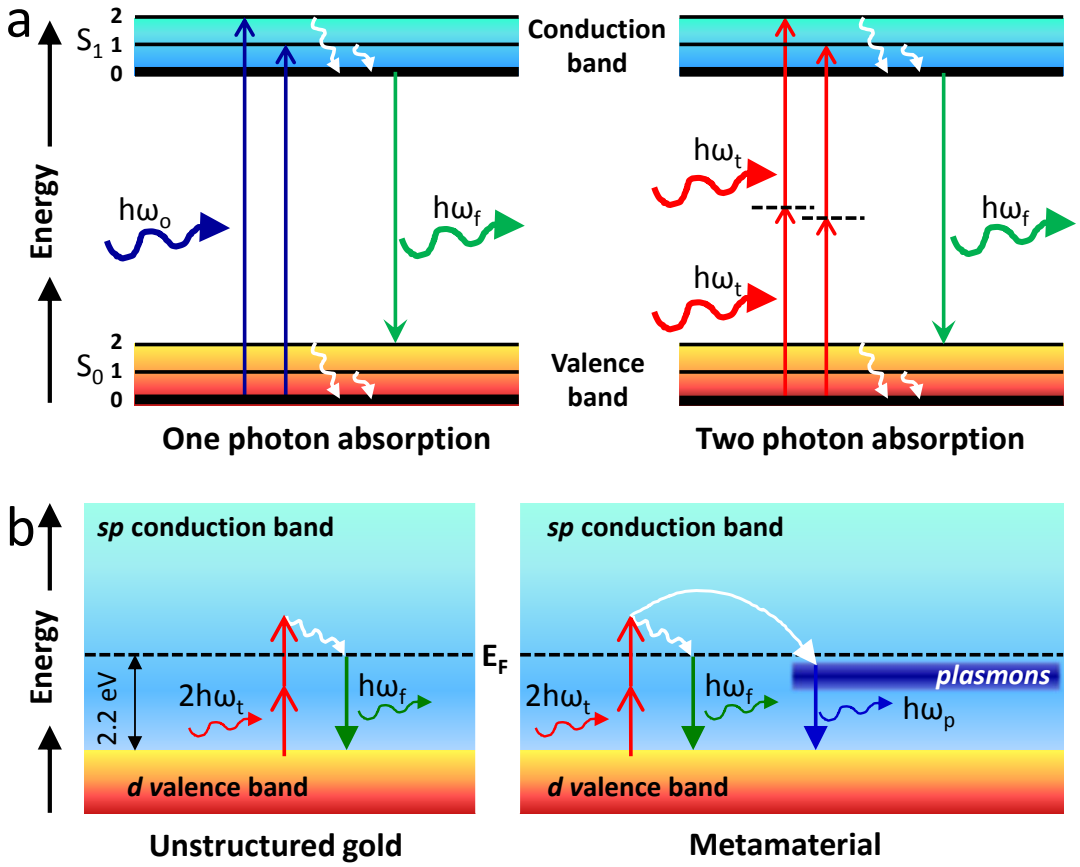

Figure 6.1: Jablonski diagram explaining photoluminescence (a) Single and two-photon photoluminescence (b) Photoluminescence from unstructured gold and metamaterials.

The process of exciting an atom from the ground state to higher energy levels can also take place by simultaneous absorption of two photons with same or different

energies, such that sum of their energies is sufficient to overcome the band gap. After being excited to higher energy states, the relaxation processes, and hence emission may follow the same steps as in the case of single photon absorption. Maria Goeppert-Mayer predicted two-photon absorption process in 1931 [156] as a part of her doctoral thesis. It was not until 30 years later that two-photon absorption was experimentally verified by Kaiser and Garret [157]. The wait was for the availability of an intense illumination source which became possible with the first functioning laser in 1960 [158]. Two-photon excitation requires more incident energy than that is required in the single photon case. This is because two-photon absorption occurs when there is a high probability of two photons being in the same place at the same time [155]. Hence the power density required is considerably higher than that needed for single photon excitation. The probability of two-photon absorption is much lower than single photon absorption and as calculated originally by Maria Goeppert-Mayer [156] is proportional to the square of incident intensity. Whereas, the probability of single photon absorption is proportional to the incident intensity.

6.1.2 Photoluminescence of metals

In 1969 Mooradian reported the first observation of photoluminescence from metals such as gold and copper, as well as gold-copper alloys [159]. For gold at room temperature, Mooradian reported a luminescence peak around 540 nm when illuminated with a 488 nm continuous wave laser. He proposed that the luminescence resulted from direct recombination of *sp* conduction band electrons just below the Fermi level (E_F) with the upper *d* band holes. In 1986 Boyd *et al.* [160] reported new features in the emission spectra of the metals used by Mooradian for different excitation energies, which they attributed to different interband transitions. In the same paper, they reported increased luminescence on roughened surfaces of metals due to localised surface plasmons. They also investigated two-photon luminescence of rough gold and other metals. Since then surface plasmon enhanced photoluminescence from gold has been used to study various light-matter interaction and physical phenomena. Infrared luminescence from intraband transitions in gold was studied using rough gold films [161]. The field distributions of gold nanoparticles were studied by observing surface plasmon enhanced two-photon luminescence from the structures [162]. It may be noted

that a large body of work exists on the effect of surface plasmon-polaritons on gold nanoparticles and nanorods and on the nature of photoluminescence from such systems [73,163–169]. Surface plasmon enhanced two-photon luminescence is of particular interest in biomedical imaging applications.

In this chapter, the two-photon excited photoluminescence from an ultra-thin film of gold, continuous and structured, will be experimentally studied. Figure 6.1b shows the Jabolonski diagram explaining two-photon excited luminescence from continuous and structured gold. Two photons are absorbed simultaneously exciting the electrons across the Fermi energy of gold (2.2 eV [159]). The energised electrons in the *sp* band recombine radiatively with holes in the *d* band. When the gold film is structured in a specific way, localised surface plasmon-polaritons are introduced. In the presence of these plasmonic resonances the density of electronic states is increased over certain energy levels. The plasmonic energy states may couple with those of gold leading to different emission energies compared to bulk gold. In section 6.2.1 two-photon excitation of an unstructured gold film is studied. The emission peak is measured at 535 nm which agrees with the original studies by Mooradian [159] and Boyd [160]. At higher intensities of excitation beam, non-quadratic behaviour of two-photon luminescence is observed. In section 6.2.2 the two-photon excited emission spectra and luminescence intensity is then studied for periodically nano-structured gold films or metamaterials. A significant shift in the emission peak and a significant enhancement in luminescence intensity is observed for the metamaterials when compared with unstructured gold film. This is linked to the plasmonic absorption peaks of the nano-structured films.

6.2 Nano-structure-enhanced two-photon luminescence

6.2.1 Two-photon luminescence from continuous gold film

In this section, two-photon luminescence from ultra-thin gold films will be experimentally studied. It will be demonstrated that under strong incident intensity, two-photon luminescence from the gold film displays a non-quadratic response to the incident power.

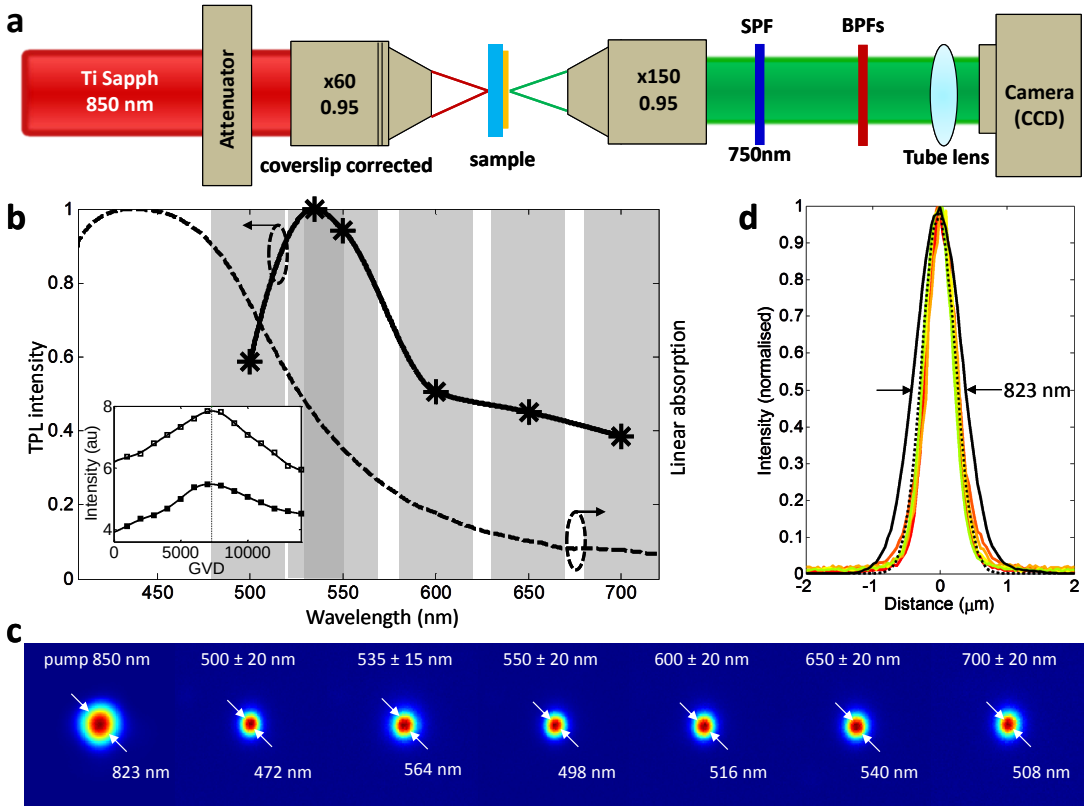

Figure 6.2: Two-photon luminescence from thin gold film (a) Experimental set-up for measuring two-photon luminescence. SPF: short pass filter, BPF: band pass filter. (b) Linear absorption and two-photon emission spectra. Inset: Luminescence dependence on group velocity dispersion of the pump laser. (c) Normalised intensity images of the excitation spot, and the luminescence detected from 50 nm gold film with different spectral filters. (d) Line-out through each frame in (c). The pump beam corresponds to the black continuous line, black dotted line is the square of the pump beam intensity.

Figure 6.2a shows a schematic representation of the experimental set-up used for measuring the spectrally and spatially resolved luminescence. For excitation of the gold film, ultra-short pulses (pulse duration τ =75 fs, repetition rate R=80 MHz) from a Ti-Sapphire laser (Chameleon Vision-S) are used. High numerical aperture microscope objectives are used for focusing the excitation beam and imaging the luminescence in

transmission. The luminescence is spectrally resolved by using a series of band-pass filters. A low-noise CCD camera (16-bit resolution 5 megapixel Andor Neo sCMOS) is used as a detector. The sample is prepared by thermally depositing a 50 nm thin film of gold on a 170 μm coverslip (SiO_2) substrate. The gold film when illuminated with tightly focused (NA=0.95, 60x, coverslip corrected) infrared (850 nm) pulses, the *d* band electrons are excited to the *sp* conduction band by absorbing two photons of 850 nm wavelength [160, 161]. The photoluminescence is detected in transmission through band-pass filters over different wavelengths (500 nm to 700 nm) in addition to a short-pass filter (cut off 750 nm), to block the excitation beam.

To detect the emission spectra from the gold film an excitation beam with an average power (P_{avg}) of 31 mW, as measured before the focusing objective, is used. The pump beam spot on the sample plane is shown in Fig. 6.2d (frame 1) with full width at half maximum measuring 820 nm. This gives an average power density of $\sim 5.86\,\mathrm{MW/cm^2}$, or peak power density of $\sim 0.98\,\mathrm{TW/cm^2}$ incident on the sample (assuming insignificant energy loss between the place where power is measured and the sample plane).

Inset in Fig. 6.2b shows the experimental data used for compensating group velocity dispersion (GVD) introduced by the optical components of the set-up. The Chameleon Vision-S laser system comes with a group velocity pre-compensator based on the prism approach [170]. By adjusting the relative positions of the in-built prisms the laser's processor can precisely adjust the amount of negative GVD required for delivering the shortest laser pulses at the sample plane. This is what is shown in Fig. 6.2b. With a given spectral filter, the luminescence spot on the gold film is imaged for different GVD values of the laser. For a fixed incident average power, the shortest pulse will deliver the highest peak power, resulting in the most intense luminescence spot under the given conditions. This is studied using two different spectral filters and in both the cases the optimal pre-compensated value of GVD is found to be $\sim 7300\,\mathrm{fs^2}$. For all the following experiments in this chapter, this value of GVD is used.

Figure 6.2b shows the linear absorption and the normalised emission spectra of two-photon excited luminescence from the ultra-thin gold film. The linear absorption for the gold film is calculated from the measured values of transmittance and reflectance obtained using a commercial spectrophotometer (Craic Technologies). For the emission

spectra, each grey coloured rectangle depicts the bandwidth of the spectral filter used for detection of the luminescence. The measurement conditions (incident power, camera exposure time, etc.) are kept the same for each band-pass filter. However, the imaging objective is refocused to take into account the chromatic aberration from the filters. An emission peak is detected around 535 nm which is supported by previous reports on photoluminescence from gold [159–161]. It may be noted that the luminescence peak is red-shifted with respect to the linear absorption peak. This difference between the absorption and emission wavelengths is called the Stoke's shift [155, 171], which arises mostly due to non-radiative energy loss in the excited state before the emission process. Further, the excited electron may decay to higher vibrational level of the ground state accounting for lower energy (higher wavelength) of emission compared to absorption.

Figure 6.2c shows the intensity images for the pump beam (without filters in the detection path), and the luminescence from the gold film at different emission wavelengths. The luminescence spots are smaller than the excitation spot size, which is more clearly depicted in Fig. 6.2d where the line-outs through each of the frames of Fig. 6.2c is plotted. To verify that the luminescence spots result from the two-photon excitation of the atoms, the square of the excitation beam lineout (black dotted) is also plotted in Fig. 6.2d. This supports the quadratic dependence of two-photon excited luminescence on the incident intensity.

To further study the nature of excitation of this photoluminescence on gold film, the change in luminescence intensity with incident average power (hence, incident intensity) is recorded. Figure 6.3a shows the results of an open-aperture z-scan done with three different spectral filters (different colours and line styles) for increasing incident average power. The sample is mounted on a piezo-driven xyz stage which is moved in the z direction, i.e., along the optical axis of the excitation spot, in 100 nm steps for ± 2 μm. The average power is varied from ~ 10 mW to ~ 60 mW. The luminescence intensity for each $z = 0$ position, when the excitation spot is focused on the sample, is plotted in Fig. 6.3b. For purely two-photon excitation the luminescence intensity should follow a quadratic relationship with excitation intensity [172]. But as seen here in Fig. 6.3b, luminescence intensity follows a power five relationship (fitted solid lines) with increasing incident average power. Non-quadratic behaviour of two-photon luminescence at high incident intensity has been reported for various materials like zinc-oxide nano-

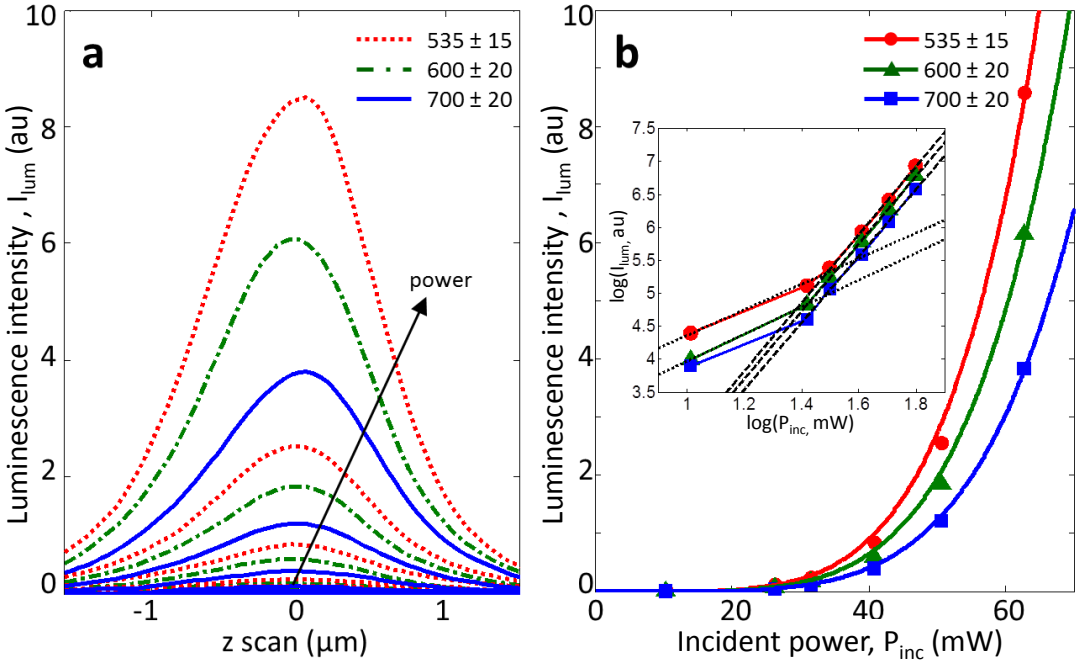

Figure 6.3: Nature of nonlinear response from gold film (a) Open aperture z-scan and power dependence for different emission wavelengths. (b) Luminescence intensity distribution with incident laser power. The solid lines are luminescence intensity to the power 5, fitted to the experimental data points. Inset shows log-log plot for luminescence intensity versus incident laser power. For lower incident power the slope of the (dashed) lines are ~ 2; for higher incident power the slope of the (solid) lines are ~ 5

rods [173], organic chromophores [174,175], organic molecules [176] and proteins [177], ammonia [178] and is often attributed to two-photon-induced excited state absorption resulting in higher order dependence of luminescence intensity with incident intensity. However, in this case looking at the log-log plot of the luminescence intensity versus the incident power (inset Fig. 6.3b) it is found that for lower incident power, the slope is $\sim$2, while with incident power more than 40 mW the slope is $\sim$5. From this it can be confirmed that on 50 nm gold film under the given experimental conditions, pure two-photon excitation is observed with average incident power $\leq$ 30 mW (i.e., incident peak power density of ≤ 0.98 TW/cm^2). This can also be confirmed from the previously discussed luminescence spot size presented in Fig. 6.2d.

6.2.2 Two-photon luminescence from nano-structured gold film

In this section, two-photon luminescence from planar metamaterials will be studied. The metamaterials are designed to engineer localised surface plasmon-polariton resonance on ultra-thin gold film. The two-photon luminescence on such structured gold

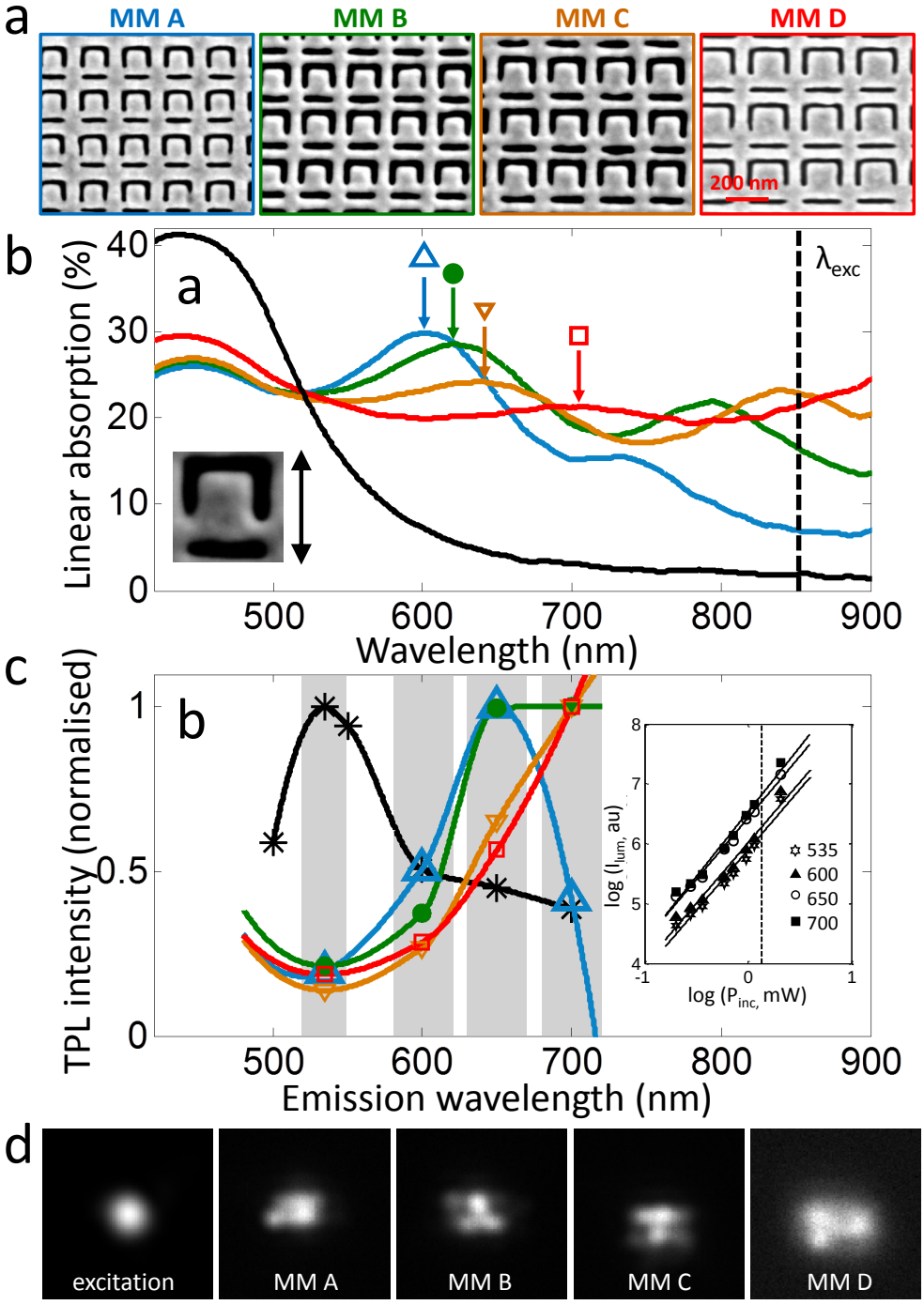

Figure 6.4: Two-photon luminescence from nano-structured gold (a) Scanning electron micrographs of metamaterials with different unit-cell size. (b) Linear absorption spectra of plain gold film and different planar metamaterials. The vertical dashed line shows the wavelength for two-photon excitation. Inset shows incident polarisation with respect to the metamaterial unit-cell. (c) Two-photon emission spectra of metamaterials compared to plain gold film. Inset shows power dependence for the metamaterial C for different detection spectral range. (d) Excitation spot on continuous gold film and luminescence from the different metamaterials detected at 700 ±20 nm.

films is a coupled effect of two-photon luminescence of the bulk gold as well as the surface plasmon-polariton-assisted local-field enhancement at both the emission and excitation wavelengths. This results in a spectral shift and large enhancement of intensity of the two-photon induced luminescence from the metamaterials.

Figure 6.4 summarises the linear absorption and two-photon luminescence spectra of the planar metamaterials compared to unstructured gold. Four different metamaterials with gradually increasing unit-cell sizes (Fig. 6.4a) are fabricated by focused-ion-beam milling of 50 nm thin gold films deposited on silica substrates (coverslips) by thermal evaporation. The unit-cell size ranges from 210 nm to 270 nm in 20 nm steps. The fabricated area of each metamaterial measures $\sim$ 24 μm by 24 μm comprising of $\sim$8000 metamolecules.

The linear absorption spectra of the metamaterials (Fig. 6.4b) is calculated from the transmittance and reflectance measured by a spectrophotometer (Craic Technologies). The absorption spectra of the gold film, measured from the unstructured areas neighbouring the metamaterials, shows a single peak around 450 nm. However nano-structuring of the same gold film introduces additional resonance peaks in the red/near-IR spectral range. The absorption resonance peaks red-shift with increasing metamolecule size.

As in the case of a continuous gold film, for two-photon excitation of the metamaterials, tightly focused ultra-short pulses of wavelength 850 nm are used. It must be noted that for two-photon excitation of the unstructured gold film, the lowest and the highest average power incident were $\sim$ 10 mW and $\sim$ 60 mW respectively. However for the nano-structured part of the gold film, an incident average power of $\sim$ 1 mW is sufficient to record a bright luminescence. The damage threshold for the metamaterials is $\sim$ 3 mW. With an average incident power of $\sim$ 1.35 mW, i.e., a peak power density of 40 GW/cm^2, the emission spectra of luminescence from the metamaterials are recorded (Fig. 6.4c). This power density is almost 25 times lower than that used for recording luminescence from the continuous gold film. As will be shown in the following sections, with this incident power level, no luminescence can be detected from the unstructured gold. In spite of this, the emission spectra from the metamaterials can be compared here. Introduction of surface plasmon resonances shifts the emission peaks to longer wavelengths. Metamaterial A, the one with the smallest unit-cell (210 nm), shows a

clear emission peak within the spectral range of 650 ±20 nm. For the other three metamaterials with larger unit-cell sizes, the emission peaks are within or beyond the range 700 ±20 nm. In this measurement, a short pass filter with cut-off at 750 nm has been used. Due to significant leakage of the excitation beam (850 nm), luminescence beyond the range 700 ±20 nm could not be faithfully measured. Hence a definitive emission peak could not be inferred for the metamaterials B, C and D. However, looking at the trend of the emission spectra in Fig. 6.4c it may be speculated that the emission peak of the metamaterial B lies somewhere in between 650 nm and 700 nm, while for the metamaterials C and D, the emission peaks lie within or beyond the detection range 700 ±20 nm.

The question remains about the excitation nature of luminescence from the metamaterials. As may be observed from Fig. 6.4d, the luminescence spots on the metamaterials are not nicely localised as they were for continuous gold film (Fig. 6.2c). So, two-photon excitation cannot be inferred by studying the size of the luminescence spot with respect to the excitation spot for the metamaterials. As an alternative, the power dependence of the metamaterial luminescence is studied. The inset in Fig. 6.4c shows the log-log plot of power dependence of metamaterial C for four different detection spectral ranges. The data points fit to a straight line with slope of 2.09 ± 0.07, implying a purely two-photon excitation process.

Besides the spectral shift of the emission peak, the introduction of localised surface plasmon-polariton resonances by nano-structuring of the continuous gold film led to huge enhancement of the luminescence intensity. This is represented in Fig. 6.5 where the excitation spot with peak power density 40 GW/cm^2 illuminates the unstructured gold and moves on to the metamaterial as the sample is scanned in 100 nm steps. At this incident energy, the luminescence from gold is undetectable even with a exposure time of 4 s for the camera. The luminescence intensity becomes detectable and begin to rise as soon as the excitation beam spot hits the edge of the metamaterials. While scanning over the metamaterial surface, a fluctuation of luminescence intensity is observed. This may be due to either one or a combination of the following reasons: (1) The excitation spot illuminates ~ 4 by 4 to ~ 3 by 3 metamolecules depending on the unit-cell size. The luminescence arising from this excitation area may be subjected to fabrication imperfection as the beam scans over the surface. (2) The metamaterials are

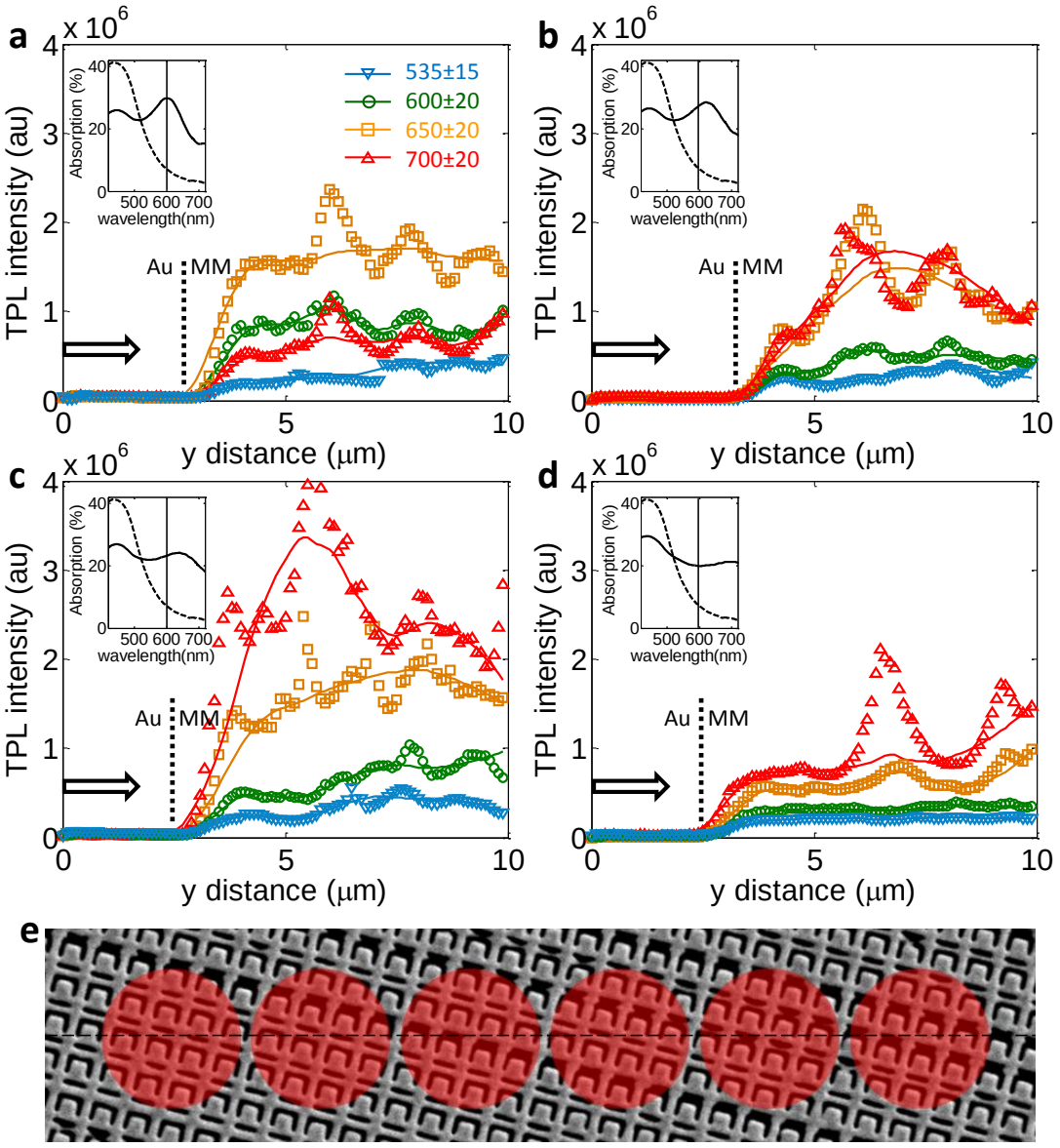

Figure 6.5: Luminescence intensity from nano-structured gold Measured two-photon luminescence intensity as the excitation spot is scanned from plain gold film on to the structured metamaterials with unit-cell size (a) 210 nm, (b) 230 nm, (c) 250 nm, and (d) 270 nm. Different detection spectral filters are given by different colours and symbols (see legend (a)). Insets show the respective linear absorption spectra compared to plain gold. (e) Possible orientation of the metamaterial with respect to the excitation beam spot.

mounted slightly oblique with respect to the axis of the sample stage. From Fig. 6.5e it may be understood that the centre of the excitation beam may move through regions between two adjacent rows as the sample is scanned over the spot. This would create difference in the overlap between the excitation spot and the number of excited meta-molecules resulting in fluctuation of the detected luminescence intensity. However, the comparative level of average luminescence from each metamaterial, detected with different spectral filters remain unambiguous and well above the noise level. From initial observation of the Figs. 6.5a-d it may be inferred that the presence of the metamaterials enhance the intensity of the luminescence from the continuous gold film, even at the emission peak (535 ±20 nm) of gold (blue inverted triangles). The enhancement of intensity increases as the detection spectral range is moved over the emission peak of the individual metamaterials. The metamaterial A showed a clear emission peak within 650 ±20 nm (Fig. 6.4c). This is supported by Fig. 6.5a where the highest enhancement in luminescence is obtained while using the same detection filter. For metamaterial B the emission spectra showed similar intensity level for the two detection ranges centred around 650 nm and 700 nm. This is also supported from the corresponding emission spectra in Fig. 6.5b. Observing Fig. 6.5c for metamaterial C, and comparing with Figs. 6.5a,b,d it is inferred that the metamaterial C shows the highest intensity level within the spectral range 700 ±20 nm, among all other metamaterials.

To further quantify the luminescence enhancement from the metamaterials, the enhancement factor is calculated for the different detection spectral ranges (Fig. 6.6). This is calculated using data from Fig. 6.5 by averaging over a number of points on the individual metamaterials for respective detection spectral range and dividing by the average signal level from the continuous gold film. It may be noted that with the level of incident illumination used for this experiment, the luminescence from the continuous gold film is below the noise floor. So the enhancement factor is the least figure expected due to the presence of the metamaterials. As seen in Fig. 6.6, the luminescence from the continuous gold film is enhanced by at least 76 times due to the presence of the metamaterial C for the spectral range 700 ±20 nm. The minimum enhancement obtained is ∼6 times due to the metamaterial D for the detection spectral range 535 ±20 nm.

One may argue that this enhancement is simply due to the nano-structured region

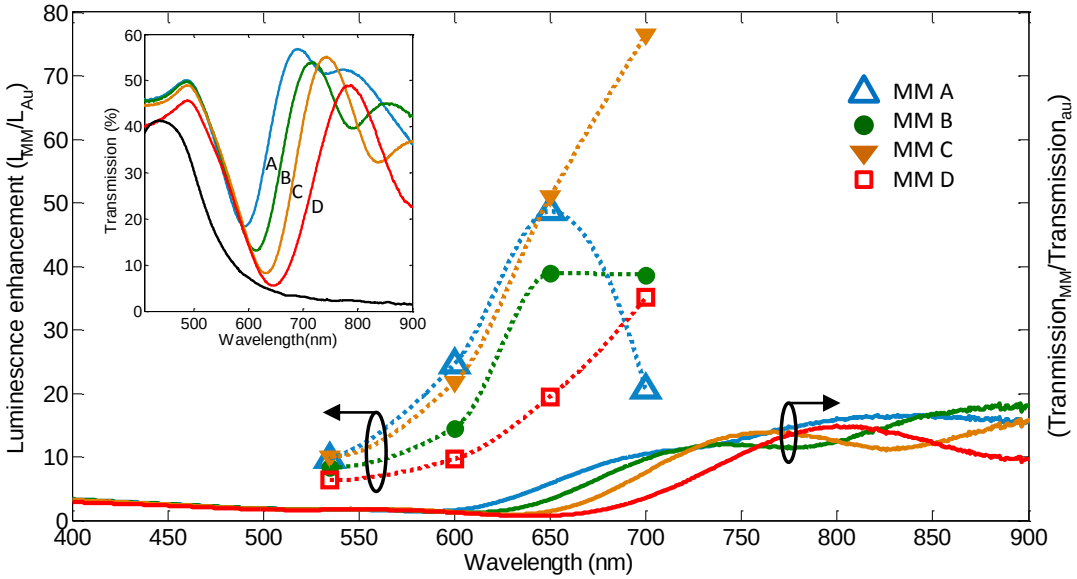

Figure 6.6: Enhanced luminescence intensity from nano-structured gold film
Enhancement of two-photon induced luminescence from the metamaterials. Solid lines show the ratio of linear transmission of the metamaterials to the gold film. Inset shows the absolute spectra of linear transmission of plain gold and the metamaterials.

being more transmissive than the unstructured gold. To investigate this issue, the ratio of linear transmission from the metamaterials to the continuous gold film is plotted on the same graph. The metamaterials are more transmissive than the gold over the spectral range shown in the plot. But this difference in transmission is not as strong as suggested by the enhanced luminescence. In fact, the position of the transmission peak does not directly affect the luminescence enhancement; as seen from the inset of Fig. 6.5 metamaterial A shows a transmission peak very close to 700 nm, but provides the least enhancement of luminescence at that wavelength compared to the other metamaterials which have transmission peak progressively further away from 700 nm.

Finally, the luminescence from the unstructured and structured gold is imaged with a colour CCD camera for different excitation wavelengths. Previous experiments reported here have shown that the emission peak for continuous gold is in the green region of visible spectrum, whereas for the metamaterials the emission peak shifted to red/near-IR part of the spectrum. When imaged with a 750 nm short-pass filter (Fig. 6.7 first 3 columns), the luminescence spots on continuous gold look yellowish. This may be due to the mixture of the predominant green luminescence with other longer wavelengths; it may be noted no band-pass filters are used for the colour images.

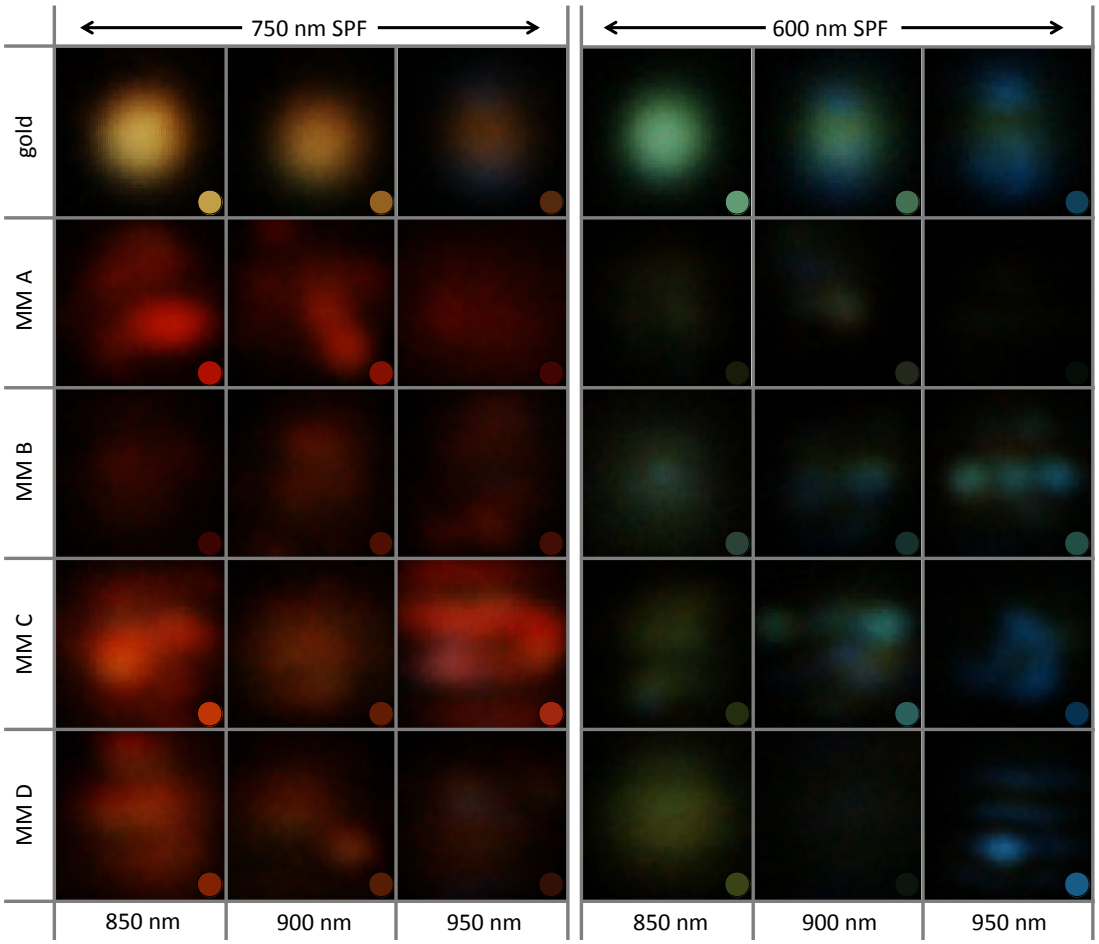

Figure 6.7: Colours of photoluminescence Two-photon luminescence imaged in RGB with a colour CCD camera for gold, and the four metamaterials. The predominant colour is shown as a dot in the bottom-right corner of each frame. The first three columns are imaged with 750 nm short pass filter, and the last three columns are imaged with 600 nm short pass filter. Each column represents different excitation wavelength.

For the metamaterials the luminescence spots are mostly red. When a short-pass filter with 600 nm cut-off wavelength is used (Fig. 6.7 last 3 columns), vivid green-blue colour of gold luminescence is captured. It may be interesting to note that metamaterial A, which has an emission peak around 650 nm shows insignificant luminescence in the green part of the spectrum. Another interesting observation is the structuring of the luminescence spots on the metamaterials. Not much can be deduced about the intensity content or the spot size from these colour images, because the camera has a highly non-linear response to photon counts, and hence does not give a reliable measure of image intensity.

It may be noted that for the thin film of gold, the colour of emission as detected by

the camera changes from green (wavelength $\sim$ 530 nm) to blue (wavelength $\sim$ 470 nm), i.e. from lower to higher energy, when the excitation wavelength (energy) is increased (decreased). This is counter-intuitive because, if the excitation energy is decreased (i.e. for the longer wavelengths) the electrons from higher states of *d*-bands will be excited, or will reach lower energy states above the Fermi energy. In the recombination process, these weakly excited electrons will emit smaller energy (i.e. longer wavelength). In short, longer excitation wavelength may lead to longer emission wavelength and not the other way round, as seen here in the colour images. However, Boyd [160] reported emission peaks near the blue part of the spectrum in addition to the well-known green emission peak, when he excited the gold films with single photons of $\sim$ 350 nm wavelength. One might also note that for a sample with metal-dielectric interface (silica-gold-air) there would exist propagating surface plasmon-polaritons (as discussed in chapter 1). Additionally, as the gold film is only a few hundreds of atomic layers thick (only 50 nm) there may remain significant surface roughness due to non-uniform growth of the film. This would introduce localised surface plasmon-polaritons in the presence of which the emission characteristics of the gold film may not conform totally to those of the bulk gold. This is worth investigating, and is suggested as a future experiment. The effect of surface plasmons on the luminescence characteristics of ultra-thin gold film may be studied in greater details by measuring the emission spectra for different excitation wavelengths using a spectrometer.

6.2.3 Discussion on mechanisms of luminescence enhancement

Enhancement of photoluminescence in the proximity of noble metal nanoparticles due to strongly localised surface plasmons has been reported in several media like rare-earth ions [179], and cadmium sulphide nanoparticles [180]. Surface plasmon enhanced photoluminescence has been studied in silver nanowires [181] and gold nanoparticles and nano-sea-urchins [182]. In fact strong photoluminescence due to two-photon excitation of roughened surfaces of noble metals has been studied almost 30 years ago by Boyd *et al.* in 1986 [160]. This enhancement in photoluminescence from rough surfaces under multi-photon excitation had been attributed to local-field enhancement due to surface plasmon-polaritons. Planar metamaterials are known to support strongly localised surface plasmon-polaritons and the nature of plasmonic excitation has been

studied [72]. Planar metamaterials consisting of unit-cell pattern as used here, have also been reported to enhance nonlinearity of carbon nanotubes [183], quantum dots [184], graphene [185], and the planar gold film itself [186].

The origin of photoluminescence for the case presented in this chapter is discussed below. In this case, the presence of metamaterials have altered the photoluminescence characteristics of an ultra-thin gold film in two ways: (1) red-shift of emission peak, and (2) intensity enhancement of the photo-luminescence over the whole detection spectral range. In general, local-field enhancement due to the presence of localised surface plasmon-polariton will have an impact on both the excitation and emission fields leading to overall intensity enhancement of the emission from the metamaterials. A strong correlation between emission spectra and linear absorption spectra suggests surface plasmon-polaritons play an active role in enhancing the photoluminescence from structured gold films.

By structuring a periodic array of interacting nanocavities on the gold film, a large density of states is created within the Fermi sea at energy levels corresponding to the plasmonic resonance peak of the metamaterials (see Fig. 6.1b). For gold, the excited electrons in the *sp* band would decay to the lower energy *d* band by emitting photons in the process. Depending on the presence of a metamaterial, a certain spectral component of this luminescence is selectivity enhanced owing to the availability of engineered density of states within the Fermi sea. Hence the shift in the emission peak.

The metamaterial resonances would play a role on enhancing the contribution of the excitation field as well. Among the four different metamaterials used here, metamaterial C shows the strongest enhancement of luminescence, specially at the emission wavelength of 700 nm. It is not a coincidence that this particular metamaterial is characterised by a transmission dip and an absorption peak (Fig. 6.8a) at the wavelength of excitation (850 nm). The transmission dip is related to the closed plasmonic mode of the metamaterial which is very weakly coupled to the free space, and helps to design high quality factor absorption resonances in thin surfaces [187]. For a negative or complementary metamaterial, like the one used in this thesis, dark-modes of surface plasmons can be excited by incident polarisation parallel to the axis of symmetry of the metamolecule, which however vanishes for the orthogonal polarisation (Fig. 6.8a). The resulting non-symmetric resonance (see transmission in Fig. 6.8a) is well-known as

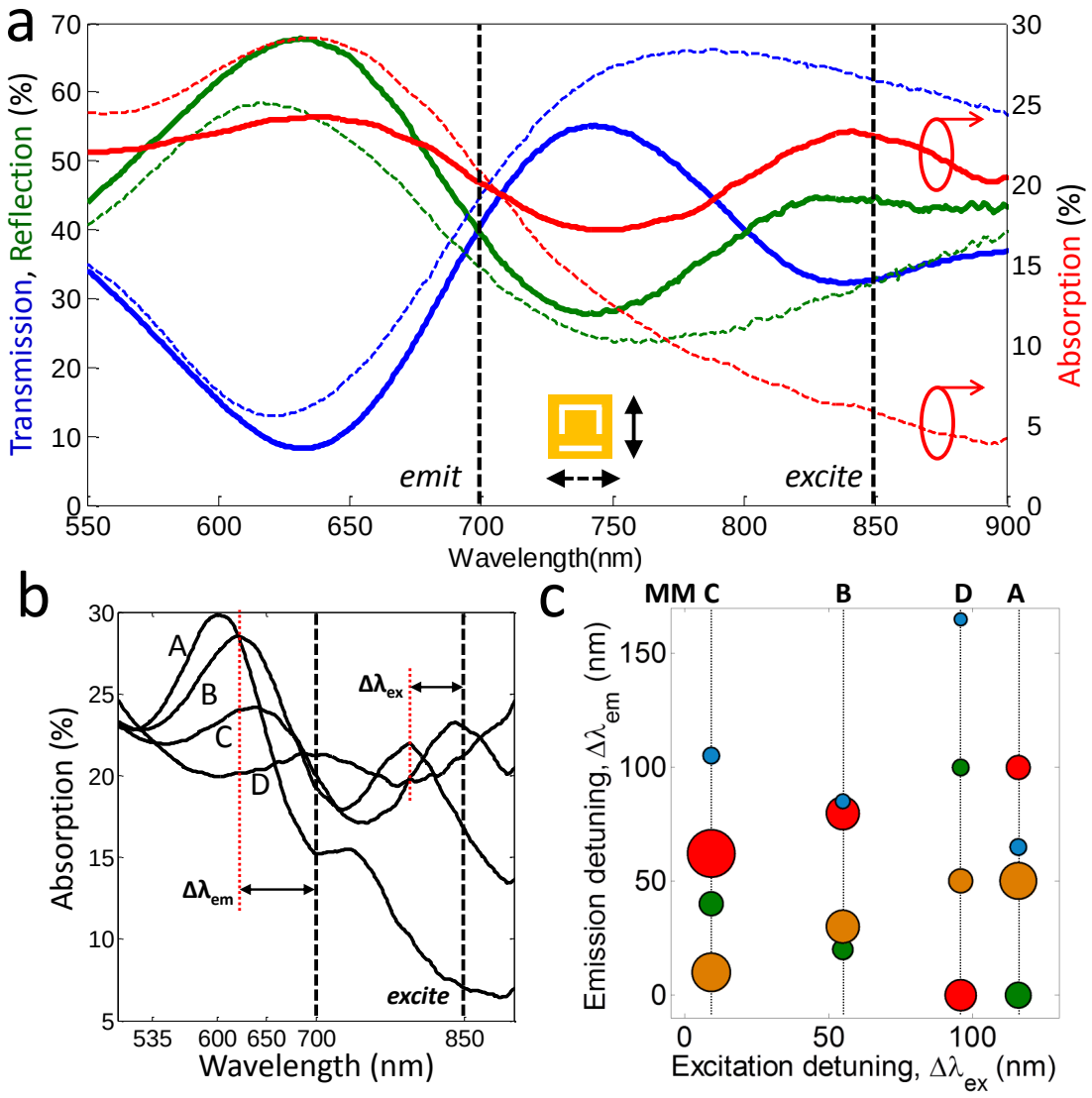

Figure 6.8: Plasmonic resonance vs. luminescence enhancement (a) Linear spectral response of metamaterial C for two orthogonal incident polarisation. The excitation and emission wavelengths for two-photon experiment are marked with vertical black lines. (b) Representative plot showing detuning parameters defined for emission and excitation wavelengths. (c) Luminescence enhancement as a function of emission and excitation detuning. Different colours represent different detection wavelength for luminescence; Red $\rightarrow$ 700 nm, Yellow $\rightarrow$ 650 nm, Green $\rightarrow$ 600 nm, and Blue $\rightarrow$ 535 nm. The size of the bubbles represent strength of luminescence enhancement.

Fano resonance [187–189] which arises from the asymmetry in the metamolecule design. For metamaterial C the wavelength of two-photon excitation occurs at the absorption peak of Fano-resonance resulting in huge field enhancement of the excitation beam. The localised fields at this resonance wavelength do not suffer from background radiation and act on the constituent gold atoms in the near-field regime to enhance their resultant photoluminescence [190].

When excited with excited with linearly polarised white light each metamaterial shows several absorption peaks. From the linear absorption spectra of the metamaterial C (Fig. 6.8a) it is seen that the first absorption peak is present for both the incident polarisations orthogonal with respect to the axis of symmetry of the metamolecule. This is attributed to a bright mode of plasmonic resonance with non-zero dipole moment, that couples well to the far-field and is easily excited with external illumination. It has been demonstrated in section 6.2.2 that the emission spectra of the metamaterials is related to this dipole-absorption peak. The difference in the position of this absorption peak from the corresponding emission wavelength is defined by a detuning parameter $\Delta\lambda_{em}$ (Fig. 6.8b). The second absorption peak in Fig. 6.8a can be excited only by the polarisation parallel to the axis of symmetry of the metamolecule and is related to the dark plasmonic mode that is weakly coupled to the far-field. The difference in the position of this Fano-absorption peak from the excitation wavelength is defined by another detuning parameter $\Delta\lambda_{ex}$, also shown in Fig. 6.8b.

Figure 6.8c presents a comprehensive plot summarising the effect of detuning of the absorption peaks on the luminescence enhancement from the metamaterials. Each vertical column represents each metamaterial, because the excitation wavelength and hence the corresponding $\Delta\lambda_{ex}$ remain the same for each metamaterial irrespective of $\Delta\lambda_{em}$. Different colours of the bubbles represent different emission wavelength and the relative size of the bubbles give a measure of the luminescence enhancement. The first vertical column of the plot represents the metamaterial C which has the least $\Delta\lambda_{ex}$ among all the metamaterials. The metamaterial C shows maximum enhancement at 700 nm, though $\Delta\lambda_{em}$ is minimum for 650 nm. This may be explained by Stoke's shift as discussed in section 6.2.1. Next, looking at the column for the metamaterial B, where $\Delta\lambda_{ex}$ is slightly more than 50 nm, it is seen that the enhancement is similar for 650 nm and 700 nm, but neither as large as for the metamaterial C at 700 nm. In fact,

among all the recorded enhancement, the one due to the metamaterial C at 700 nm is the highest. It is interesting to note that for the metamaterial D the luminescence enhancement at 700 nm is weaker than the metamaterial C even though $\Delta\lambda_{em} = 0$ for the former. Observing the overall trend of luminescence enhancement presented in the Fig. 6.8c it may be inferred that it is crucial to provide excitation at the closed-mode of plasmonic resonance of the metamaterial.

For the metamaterials (A, B, and D) whose Fano-absorption peak is far from the excitation wavelength, an interesting theory on luminescence enhancement may be considered as given by Dulkeith *et al.* [191]. While studying gold nanoparticles Dulkeith *et al.* observed that the enhancement in photoluminescence cannot be simply explained by the local-field enhancement due to surface plasmon-polaritons. They proposed that the dominant contribution to the photoluminescence originated from radiative relaxation of particle-plasmons which were created by hot carriers [192]. In Dulkeith's system, only interband transitions were excited and not plasmonic resonances. Hence no local-field enhancement was expected from the excitation process. This is similar to the case of all the metamaterials except C. The emission process was, however, influenced by plasmonic resonance. Radiative decay of surface plasmons has been reported by others [193]. This may be one of the probable processes explaining the enhanced luminescence from planar metamaterials, and is worth investigating as a future work.

6.3 Summary

This chapter presents a study on two-photon excited photoluminescence from an ultra-thin film of gold. This has been compared with the luminescence from nano-structured gold films. For continuous film of gold photoluminescence is observed in the green part of the visible spectrum. This is attributed to radiative recombination of excited *sp* conduction band electrons with *d* band holes. For high incident power density, deviation from the quadratic nature of two-photon luminescence is observed which is related to the excited state absorption. In the subsequent experiment on luminescence from metamaterials, the gold film is structured with periodic pattern of nano-slits which displays geometry dependent plasmonic resonances. Four different metamaterials are fabricated to investigate the effect of plasmonic resonance on two-photon excited photoluminescence. The emission peaks from the metamaterials are found to be red-shifted compared to continuous gold film and followed respective plasmonic resonance peaks. Also, a huge enhancement of luminescence intensity is observed from the nano-structured film. It has been demonstrated that the enhancement is not solely due to increased transmission through the nano-slits. The increased luminescence is related to the local-field enhancement due to localised surface plasmon-polaritons. For the metamaterial with an absorption peak at excitation wavelength the luminescence enhancement is maximum — at least 76 times more than that of the continuous gold film. This is related to excitation of dark plasmon modes and subsequent enhancement of the emission field.

7 Conclusions

7.1 Summary

This thesis presents several novel approaches to control light using engineered nanostructures. In the following sections, the results are summarised by the different areas of problems that have been addressed in this thesis.

7.1.1 Super-oscillatory lens device

Nanoscale localisation of light is an important requirement for applications like microscopy and high-density data storage. This thesis makes use of the phenomena of super-oscillation to design and demonstrate planar optical lenses that are capable of focusing light down to sizes below the diffraction limit. Prior to the research reported here, the phenomena of optical super-oscillation was known and initial experimental demonstrations of optical super-oscillation were reported. This thesis reports a number of theoretical and experimental advances in developing a super-oscillatory lens device:

- A super-oscillatory planar lens which modulates the amplitude of light to produce sub-diffraction foci along the optical axis has been designed and experimentally demonstrated. The super-oscillatory lens is characterised experimentally for visible light illumination (660 nm). It produces multiple sub-diffraction foci along the optical axis with the smallest spot measuring 58% smaller than the diffraction limit. The sub-diffraction super-oscillatory focal spot is used to demonstrate super-resolution capabilities, imaging features as small as $1/6^{th}$ of a wavelength. This is achieved by scanning the focal spot over the object in sub-wavelength

steps, and building up the overall image by selecting information from the central part of the individual image field.

- The inherent problem of low-intensity super-oscillatory spot accompanied by high-intensity sidebands and hence a limited field of view is solved by implementing an innovative improvement over the existing designs of super-oscillatory lens. Besides producing a large field of view around the sub-diffraction focal spot, this new design of super-oscillatory lens results in very long depth of focus giving the impression of a 'needle' along the optical axis of the lens; hence the name optical needle super-oscillatory lens.

- The super-resolution imaging capabilities of the both kinds of super-oscillatory lenses are investigated theoretically and experimentally by studying the point spread functions. The super-oscillatory lenses can image a point source more accurately than a diffraction-limited conventional lens. It is also confirmed that these super-oscillatory masks perform other lens-like functions — when the object is moved in one direction, the corresponding image moves in the opposite direction, both movements being parallel to the plane of the lens.

- The extended field of view of the optical needle super-oscillatory lens has been used to demonstrate scan-less, direct-capture, super-resolution imaging, within the field of view. For simulating such a performance of the super-oscillatory lens, binary objects made of nano-holes with increasing complexity are used. A random cluster of 0.15λ diameter nano-holes with the smallest edge-to-edge separation of 0.28λ was resolved.

- Finally, the optical needle super-oscillatory lens is investigated for its suitability in the cutting-edge technology of heat-assisted magnetic recording. This technology is being developed for increasing the density of data storage on magnetic hard disk drive and demands a device for optically heating an area as small as 50 nm. In conjunction with a high refractive index, low loss, solid immersion media like gallium phosphide, this thesis proves that it is possible to use an optical needle super-oscillatory lens to produce ~ 50 nm focal spot. For the proof-of-concept experimental demonstration of solid-immersion super-oscillatory lens, a lower in-

dex solid-immersion medium (aluminium-doped zinc-oxide) is used. Following a 4.6 μm thick layer of the immersion medium, a $\sim$ 130 nm spot was successfully registered on a positive photoresist; the registered diffraction pattern and the spot size agrees well with the simulated results.

7.1.2 Planar diffractive meta-devices

Planar metamaterials provide the opportunity to manipulate the phase and amplitude of light with sub-wavelength spatial resolution across a two-dimensional interface. Contemporary to the work of this thesis, several successful attempts have been made to design meta-surfaces for wavefront shaping. This thesis presents a simplistic approach of designing planar optical devices using the resonant properties of spatially varying sub-wavelength meta-molecules. This thesis focuses on using the simplest polarisation-insensitive unit and the least number of meta-molecules for deigning the planar devices.

- A blazed transmission meta-grating operating at visible wavelengths is designed using polarisation insensitive meta-molecules, which are spatially arranged with varying parameters to produce a periodically varying phase ramp. The meta-grating with 900 nm grating period diffracts linearly polarised white light displaying the strongest blazing for 736 nm wavelength. The blazing is observed when the incident electric field is parallel to the effective grating grooves, where 25 times more intensity is diffracted in to the negative compared to the positive first order.

- An array of meta-lenses focusing light in to sub-diffraction limited spots at distances beyond the near-field of the meta-surface is demonstrated. When illuminated with circularly polarised light, an array of sub-wavelength focal spots with period of the meta-lens array, are formed at repeated distances along the propagation direction. Since the sub-diffraction foci are formed beyond the near-field of the lens array and are mostly associated with low intensity regions, this is attributed to the phenomena of optical super-oscillation which demonstrates similar characteristics. It is demonstrated that a meta-lens array with individual lens unit measuring 1.02 μm by 1.02 μm can focus incident monochromatic light (800 nm) to a spot measuring 0.2λ at a distance $\sim 14.7\lambda$ from the device surface.

7.1.3 Metamaterial enhanced photoluminescence

Metamaterials are used to engineer surface-plasmon resonances of the constituent metals. Prior to this thesis a large body of work exist on enhancement of photoluminescence in the presence of surface plasmons. Enhanced luminescence has been reported due to localised surface plasmons resulting from roughness of planar metal films. In this thesis, gold films are nano-patterned in a controlled fashion to engineer metamaterials with pre-determined plasmonic resonances. These planar metamaterials are used to alter and enhance the photoluminescence characteristics of two-photon excited gold film.

- It is experimentally demonstrated that the nano-structuring of an ultra-thin film of gold red-shifts the peak of the photoluminescence emission spectra. The shift in the emission peak can be linked to the plasmonic resonance peak of the corresponding metamaterial.

- It is also demonstrated that the metamaterial results in a significant enhancement of the luminescence intensity compared to the unstructured gold film. The enhancement is maximised when the closed-mode of surface plasmons are excited. Under the best condition, the photoluminescence of the plain gold film is enhanced by at least 76 times in the presence of the metamaterial.

7.2 Outlook

This thesis presents proof-of-concept demonstrations of several photonic planar devices. These devices can be developed further to be useful for cutting-edge applications like super-resolution microscopy and high-speed photolithography, high density data storage, planar miniaturised optical components and so on that would aid in the evolution of photonic industry.

The super-oscillatory lenses have been used to demonstrate super-resolution imaging by scanning the sub-diffraction limited hotspot across the object in sub-wavelength steps. This is a time consuming process and may not be applicable to samples with short lifetime (like biological samples). A real-time super-resolution imaging scheme using the optical needle super-oscillatory lens may be a better alternative. The optical-needle lens has already been demonstrated to produce an extended sub-wavelength needle along the optical axis and has the advantage of extended field of view. Objects within this field of view may be directly imaged with super-resolution capabilities. However, such lenses are not entirely without high intensity sidebands which may occur within tens of microns from the central axis. This puts a limitation on the size of the objects being imaged. To overcome this impediment, the direct imaging scheme may be combined with large-step scanning to stitch several super-resolution images of an extended objects. Even better, an array of such lenses would help to image large areas by scanning the array across the sample in large steps. This would be an important step towards high-speed super-resolution image acquisition over extended sample area.

The proof-of-principle demonstration of solid-immersion super-oscillatory lens is only one step forward towards proving the suitability of such devices for heat-assisted magnetic recording technology. The requirement for a sub-50 nm focal spot from an optical lens that needs to be integrated within the existing hard-disk drive architecture is a demanding proposition. The performance of the solid-immersion super-oscillatory lens needs to be investigated more thoroughly. Further experimental work needs to be done to optimise the performance of the lens device in terms of immersion material selection and film characteristics, better designs of the super-oscillatory lenses, and selection of a better registration layer. In this thesis a positive photoresist is used as the layer for recording the super-oscillatory focal spot just after the solid-immersion

medium. However, registering such small spots in photoresist layer with nanometre accuracy would depend on the right choice of the photoresist that would support high spatial resolution. Chalcogenide glass thin films may be used as the alternative registration layer. Since chalcogenides change phase from amorphous to crystalline prescribed by a threshold temperature, the phase change would give an estimate of the heating power of the super-oscillatory optical needle.

The planar meta-devices presented in this thesis are far from being optimised for commercial applications. One persistent problem with metal-dielectric meta-surfaces is the inherent Joule loss in the metal layers. This can be overcome by using all dielectric metamaterials [66] for wavefront shaping. One may think of a reconfigurable all-dielectric meta-device [194] that can be controlled by external stimuli like electricity, magnetic field and/or heat to manipulate wavefront shaping properties of the interface.

Finally, the enhanced photoluminescence from the nano-structured gold film can be used for sensor applications. Sensing applications with metamaterials based on the change of high quality factor Fano-resonances have been discussed by other researchers. In this thesis it has been demonstrated that nonlinearity or multiphoton photoluminescence of gold film is sensitive to the structuring of the film. Also, the presence of the metamaterials leads to requirement of much lower excitation power and results in enhanced photoluminescence intensities. This photoluminescence spectra and intensity can be highly sensitive to the addition of foreign bodies and may be developed in to sensors. For the re-usability of the metamaterial sensor a dielectric film cover may be coated on gold surface.

A

Focused ion beam milling

The nano-structures presented in this thesis are fabricated using focused ion-beam milling (FIB) of thin metal films. FIB lithography is a direct write, mask-less, serial, nano-fabrication tool that uses focused ions to sputter or mill out sample surface with nanometre precision [195, 196]. FIB can also be used for high-resolution microscopy where the working principle is similar to scanning electron microscopes, and can be used for ion-beam assisted chemical vapour deposition of materials as well. Here, FIB (FEI Helios Nanolab dual beam FIB/SEM) is used for patterning thin films (50 nm or 100 nm) of metals (like, gold, aluminium, titanium) with feature sizes as small as 25 nm. The machine allows high-precision nano-fabrication coupled with high-resolution electron microscope images.

A.1 Working principle of FIB milling

Figure A.1 shows a schematic of the different components of a FIB machine. FIB uses liquid metal ion source (LMIS) to provide charged ions for the beam. The LMIS (Fig. A.1a) consist of a metal-source (in this case Gallium) which is heated-up such that it flows down and wets a sharp tungsten tip. Depending on the applied extraction voltage the liquid metal can be pulled in to an extremely sharp cone called the Taylor-Gilbert cone [195–197]. The liquid tip radius can be as small as a few nanometres which may be achieved by balancing the electrostatic forces produced by the extraction voltage and the surface tension of the liquid gallium. Ions are extracted from the tip of this cone by field emission. The parts of an ion-beam column is shown in Fig. A.1b. Electrostatic lenses are used to focus the ion-beam into a small and bright spot required

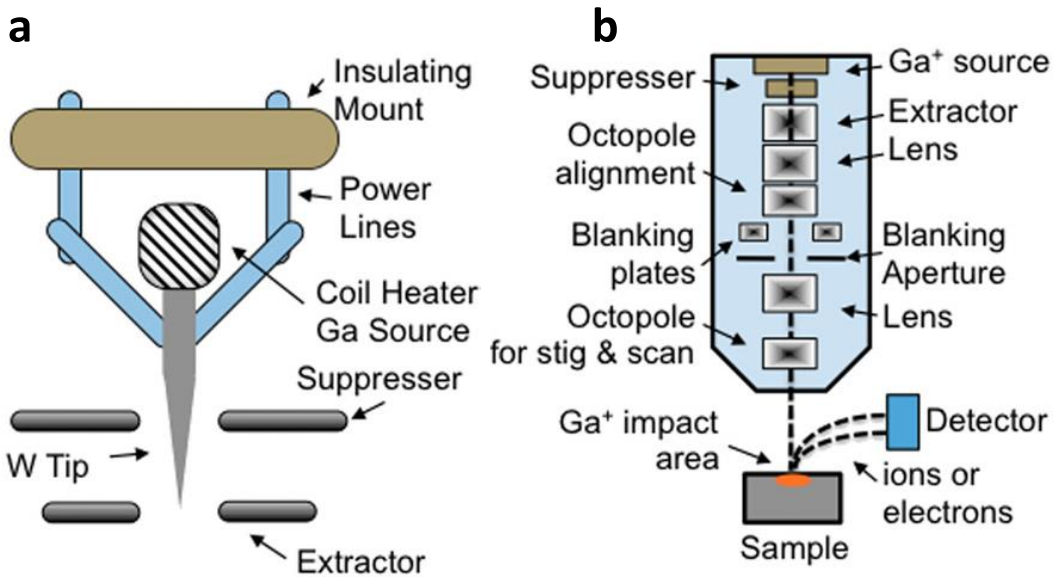

Figure A.1: Schematic of a FIB system (a) Gallium liquid metal ion source. (b) A typical FIB system showing ion-column with lenses, beam-blanker, sample and detector for imaging. Figure after [195] ©IOP, 2012.

for milling, imaging or other metal deposition. The ion beam have typical accelerating voltage of tens of kilovolts and the beam currents may range from picoamps to several nanoamps. The beam spot size can range from $\sim$ 5 nm up to 1 µm depending on the ion-column optics, the ion source and the beam current. A fast beam-blanker is used for patterning the sample surface. The design to be milled can be drawn as simple bitmaps using the software available with FIB, or for more complicated structures CAD files can be imported. During milling of a substrate, per incident ion is capable of removing approximately one to five atoms depending on the substrate and the ion energy. Secondary electrons are also released as a by product of the milling process that can be used for imaging. The shape of the milled groove does not simply depend only on the Gaussian shape of the ion-beam spot. It also depends on re-deposition of milled material, and the end product may significantly vary in quality depending on whether the milling was a single step process or repeated multiple times. Depending on the pattern to be milled the best set of steps for the process may differ. In brief, the FIB milling quality depends on the material, the ion-beam incident angle and energy, re-deposition of sputtered materials and even the crystal orientation. In FEI dual beam system the FIB and SEM intersect at 52 deg angle such that while the milling is done with normally incident ion-beam, simultaneous electron-beam imaging can be achieved.

A.2 Examples of FIB milling

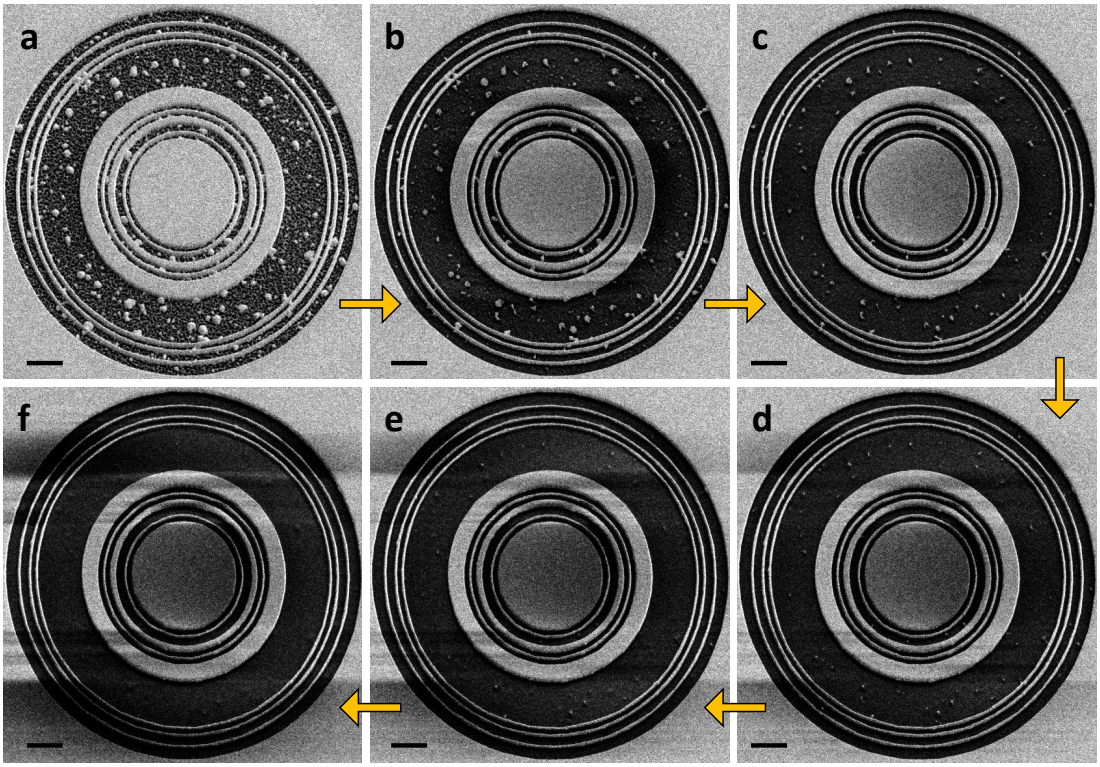

Figure A.2: Stages of FIB milling of an ONSOL. (a)-(e) Intermediate stages of milling the structure. The whole design is scanned multiple times by the ion-beam, each time removing only small amount of the material. (f) The end structure shows clean milled area with predefined un-milled regions. The scale bar is 2 μm.

Figure A.2 shows the stages of milling an optical needle super-oscillatory lens (presented in chapter 4). For this example, a CAD file was designed which was imported to the FIB software. The design is drawn as a set of concentric circles with 200 nm linewidth, only some of which have value '1' (to be milled), the rest have value '0' (not to be milled). The ion-beam with a chosen beam-current and hence spot-size starts raster scanning the area to be milled. In each step it mills a small amount of the substrate which is 95 nm gold film with 5 nm chromium adhesion layer deposited by thermal evaporation on 170 μm silica coverslip. The blanker stops the beam when design with value '0' is encountered. For the part where successive points have value '1' a fast beam blanker operates between the spatial shift of the ion beam. The spot size, and the centre-centre distance between two successive spots are so chosen that they overlap ensuring that the milled region is not pixelated. The raster scan is repeated a num-

ber of times until the desired regions are milled through leaving the un-milled regions with predefined dimensions (Fig. A.2f). The multiple pass ensures that re-deposition of material is minimal in the end.

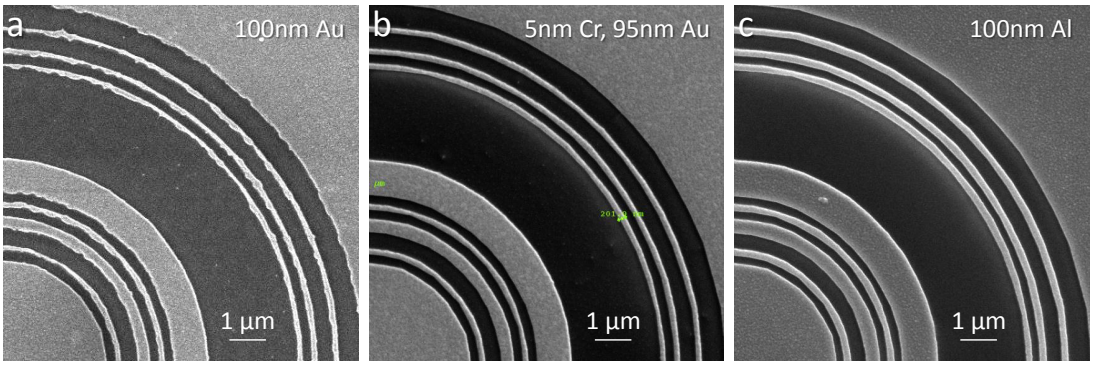

Figure A.3: Milling different metals. (a) Structure milled on 100 nm gold on silica shows rough edges. This is due to bad adhesion quality of gold to silica. (b) 5 nm chromium adhesion layer followed by 95 nm gold gives a better sample. Some residual metal can be seen in the clean-milled area. (c) Aluminium (100 nm) on silica gives the best looking sample with clean milling of area as small as 200 nm. It takes more number of passes to mill aluminium compared to gold.

Figure A.3 shows the effect of milling on different types of metal films. Due to poor adhesion of gold with silica, Fig. A.3a shows rough edges of milled area. However using chromium adhesion layer (Fig. A.3b) reduces the problem significantly. The best milling result is obtained using aluminium (Fig. A.3c) in spite of the larger grain sizes of the thin metal layer (see neighbouring regions). However it must be mentioned that it takes longer time, or more number of passes to mill the same thickness of aluminium film compared to gold, keeping other ion-beam parameters the same.

Figure A.4 shows the example of a periodic structure - a metamaterial- fabricated by milling 50 nm gold film deposited on silica. The line-width is only 25 nm. Here each unit cell (shown by the white box in Fig. A.4a) is milled completely before moving on to the next one. After each horizontal line is finished the ion beam moves down to the next line. While milling a unit cell, the inverted-U-shaped structure is milled through and then the horizontal bar. However each entity, say the horizontal bar is milled in multiple passes just like the ONSOL structures described above to minimise re-deposition, rough edges and hence get the finest possible milling. Figure A.4b shows an edge of the metamaterial imaged by electron beam microscope when the sample is at 52 ° angle. The dome-shaped appearance implies that the nano-trenches do not have

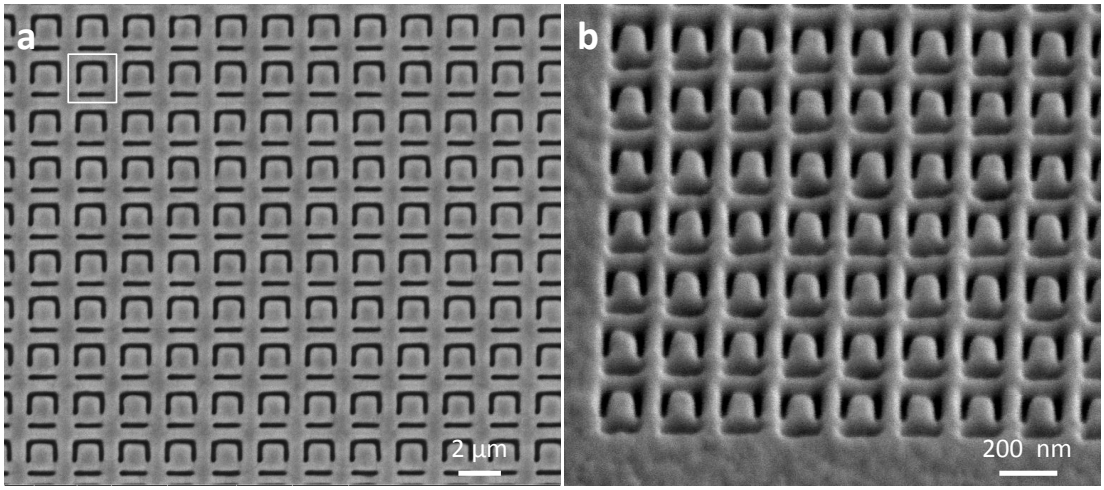

Figure A.4: Milling periodic structures. (a) 50 nm gold on silica milled with linewidth measuring 25 nm. The white box shows one unit cell measuring 210 nm. (b) SEM image of the edge of the metamaterial when the sample is at 52 deg angle with the electron-beam.

steep 90 ° edges even for a metal film as thin as 50 nm. This is because of the Gaussian shape of the ion-beam spot.

B

Comsol simulation

In this thesis the electromagnetic properties of photonic metamaterials are simulated by using a commercial software package Comsol Multiphysisc 3.5a. Comsol Multiphysics can be used to solve any physics-based problem using the different available modules. The software also offers an extensive interface to MATLAB and its toolboxes for a large variety of programming, preprocessing and post-processing possibilities [198]. For electromagnetic simulations presented here the RF module is used. The RF module provides a unique environment for the simulation of electromagnetic waves in two and three dimension. It uses finite element method to solve Maxwell's equations. In this thesis three dimensional simulations of periodic planar metamaterials are presented. A brief description of modelling such a problem is outlined here.

The first step to model a metamaterial in Comsol is to define the structure. All metamaterials presented in this thesis comprised of planar interface made up of periodic unit cells. With the help of periodic boundary condition perpendicular to the plane of the metamaterial an infinite planar structure of the metamaterial is simulated by solving over only one unit cell. In the example shown in Fig. B.1 the unit cell is made up of ring-slots of three different diameters on a 50 nm thick film of gold. This corresponds to the meta-grating geometry as described in chapter 5. The unit cell is surrounded by several rectangular blocks on either side along the propagation direction.

The second step in modelling is to define the domain material parameters like permittivity and permeability and to define the boundary conditions. All the metal structures simulated in this thesis are gold, and the values of complex dielectric parameters are used from Ref. [199]. In order to account for the presence of a substrate

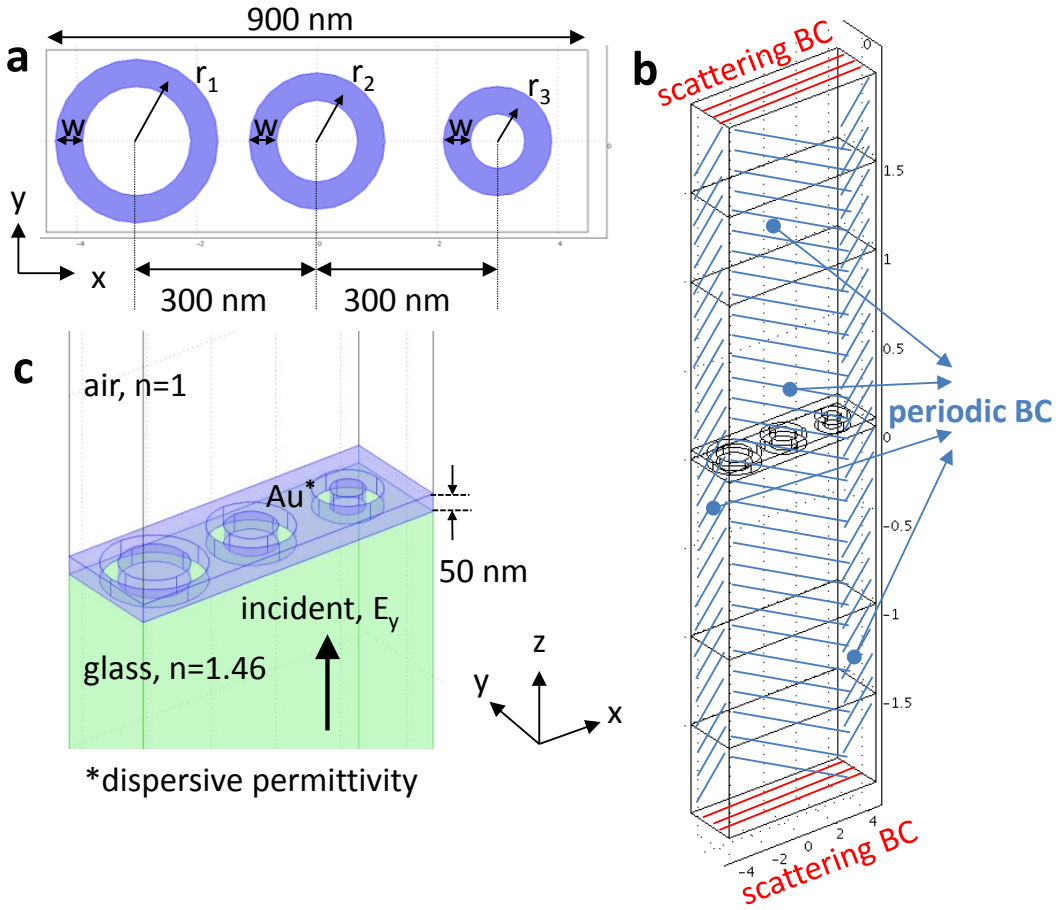

Figure B.1: Modelling a metamaterial with Comsol Multiphysics. (a) Example of an unit cell of a periodic metamaterial. (b) 3D view showing different materials defined in different sections of the model. (b) Boundary conditions imposed on the 3D model to solve for a periodic metamaterial infinite in x and y.

the rectangles below the thin gold slab are assigned the material parameter of the substrate of choice, like for silica refractive index 1.46 is used (Fig.B.1c). As mentioned earlier, periodic boundary conditions are applied for both x and y boundaries. In the z-direction, scattering boundary conditions are employed for the two external boundaries (Fig.B.1b). All internal boundaries are chosen as 'continuity'. The incident wave with its polarisation is defined at one of the scattering boundaries. In most situations, the scattering boundary condition is good enough to minimize the scattering at the boundary. However, perfectly-matched-layers could be added at the top and bottom boundaries in z-direction to further reduce the scattering if necessary.

The third step is to mesh the model such that the maximum element size in each domain is one tenth of wavelength or smaller (this means mesh in domains with high refractive index should be finer than in the air). For metallic areas, a maximum mesh element size of 25 nm is used. Care must be taken to appropriately mesh the areas with fine features. However, the element size of mesh is limited by the capability of the simulation platform (Comsol simulations in this thesis are performed with a 16 processor, 64 bit, 128 GB linux workstation). For periodical boundary conditions the mesh nodes on each pair of periodical boundaries must be identical. This can be achieved by meshing one boundary first and then copying the mesh to the other.

Finally, the simulation wavelength or frequency is set and a suitable solver parameter is chosen. After the simulation is complete, the field distributions can be obtained by post-processing. For obtaining the spectral variation of transmission, reflection and absorption, a Matlab code is generated for the solved model. By incorporating the required changes for calculating transmission, reflection using the data of power flow at suitable internal boundaries, the Matlab script can be integrated with Comsol model to solve over a specified range of wavelengths.

C Publications

C.1 Journal publications

C.1.1 Published

1. E. T. F. Rogers, J. Lindberg, T. Roy, S. Savo, J. Chad, M. R. Dennis, and N. I. Zheludev. "Super-oscillatory lens optical microscope: breaking the diffraction limit". *Nature Materials*, 11, 432 435 (2012).

2. T. Roy, E. T. F. Rogers, and N. I. Zheludev. "Subwavelength focussing meta-lens". *Optics Express*, 21, 6, 7577 - 7582 (2013).

3. T. Roy, A. E. Nikolaenko, and E. T. F. Rogers. "A meta-diffraction-grating for visible light". *Journal of Optics*, 15, 08510 (2013).

4. E. T. F. Rogers, S. Savo, J. Lindberg, T. Roy, M. R. Dennis, and N. I. Zheludev. "Super-oscillatory optical needle". *Applied Physical Letters*, 102, 031108 (2013).

5. Q. Wang, J. Maddock, E. T. F. Rogers, T. Roy, C. Craig, K. F. MacDonald, D. W. Hewak and N. I. Zheludev, "$1.7 Gbit/inch^2$ gray scale continuous-phase-change femtosecond image storage", *Applied Physics Letters*, 104, 121105 (2014).

6. G. Yuan, E. T. F. Rogers, T. Roy, Z. Shen and N. I. Zheludev, "Flat Super-oscillatory Lens for Heat-Assisted Magnetic Recording with sub-50nm resolution", *Optics Express*, 22, 6, 6428 - 6437 (2014).

7. T. Roy, E. T. F. Rogers, G. Yuan, and N. I. Zheludev. "Point spread function of the optical super-oscillatory lens", *Applied Physics Letters*, 104, 231109 (2014).

C.1.2 Under preparation or review

- T. Roy, E. T. F. Rogers, and N. I. Zheludev. "Nanostructure-enhanced two-photon luminescence from ultra-thin gold film", *under preparation.*
- T. Roy, E. T. F. Rogers, G. Yuan and N. I. Zheludev. "Nanoscale imaging with super-oscillatory optical-needle lens", *under preparation.*
- T. Roy, G. Yuan, E. T. F. Rogers, and N. I. Zheludev. "Solid-immersion flat optical-needle lens", *under preparation.*
- G. Yuan, E. T. F. Rogers, T. Roy, G. Adamo, Z. Shen, and N. I. Zheludev. "Planar super-oscillatory lens for sub-diffraction optical needle at violet wavelength", *under review.*

C.2 Patents

- N. I. Zheludev, S. Savo, T. Roy, V. Savinov, M. R. Dennis, E. T. F. Rogers, J. Lindberg. "Super-oscillatory lens device" publication number WO 2013114075 A1, Feb 2012.

C.3 Conference Contributions

oral T. Roy, G. Yuan, E. T. F. Rogers, and N. I. Zheludev, "Solid-immersion Super-oscillatory Lens for Heat Assisted Magnetic Recording Technology and Nanoscale Imaging", *CLEO: 2014*, San Jose, United States, 08 13 June 2014.

oral G. Yuan, E. T. F. Rogers, T. Roy, L. Du, Z. Shen and N. I. Zheludev, "Plasmonic Super-oscillations and Sub-Diffraction Focusing", *CLEO: 2014*, San Jose, United States, 08 13 June 2014.

oral Q. Wang, J. Maddock, E. T. F. Rogers, T. Roy, C. Craig, K. F. Macdonald, D. W. Hewak and N. I. Zheludev, "2D cognitive optical data processing with phase change materials", *CLEO: 2014*, San Jose, United States, 08 13 June 2014.

invited G. Yuan, E. T. F. Rogers, T. Roy, Z. Shen and N. I. Zheludev, "Optical super-oscillation: towards the far-field super-resolution focusing and imaging", *META14*,

Singapore, 20 23 May 2014.

invited K. F. MacDonald, W. Qian, J. Maddock, E. T. F. Rogers, T. Roy, C. Craig, B. Mills, D. Hewak, and N. I. Zheludev, "Volatile and non-volatile switching in dielectric metamaterials", *META14*, Singapore, 20 23 May 2014.

poster W.Qian, J. Maddock, B. Mills, C. Craig, E. T. F. Rogers, T. Roy, K. F. MacDonald, D. W. Hewak, and N. I. Zheludev, "Femtosecond multi-level phase switching in chalcogenide thin films for all-optical data and image processing", *SPIE Photonics Europe*, Brussels, Belgium, 14-17 April 2014

oral G. Yuan, E. T. F. Rogers, T. Roy, B. Lafferty, M. Mooney, Z. Shen and N. I. Zheludev, "Super-oscillatory optical needle for heat-assisted magnetic recording", *CLEO: 2013*, San Jose, United States, 09 14 June 2013.

poster T. Roy, E. T. F. Rogers, and N. I. Zheludev, "A superoscillatory metalens array", *Nanometa 2013*, Seefeld, Austria, 3-6 January 2013.

poster E. T. F. Rogers, T. Roy, N. I. Zheludev, J. Lindberg, and M. Dennis, "Exploring the limits of super-oscillatory imaging", *Nanometa 2013*, Seefeld, Austria, 3-6 January 2013.

keynote E. T. F. Rogers, J. Lindberg, T. Roy, S. Savo, J. E. Chad, M. Dennis, and N. I. Zheludev, "Superoscillatory lens far-field to far-field optical microscope: breaking diffraction limit", *SPIE Congress*, San Diego, USA, 12-16 Aug 2012.

oral T. Roy, A. E. Nikolaenko, E. T. F. Rogers, N. I. Zheludev, "A planar metamaterial superoscillatory lens?", *Nanolight*, London, United Kingdom, 08 Jun 2012.

oral T. Roy, A. E. Nikolaenko, E. T. F. Rogers, N. I. Zheludev, "Transformation optics with planar metamaterials: diffraction grating and lens", *CLEO: 2012*, San Jose, United States, 06 - 11 May 2012.

poster T. Roy, A. E. Nikolaenko, E. T. F.Rogers, N. I. Zheludev, "Engineering interface singularities with metamaterials: planar optical prism and diffraction grating", *SPIE Photonics Europe*, Brussels, Belgium, 16 - 19 Apr 2012.

poster T. S. Kao, T. Roy, M. Ren, N. Papasimakis, F. DeAngelis, E. DiFabrizio, A. E. Nikolaenko, N. I. Zheludev, "Light localization, linear and nonlinear properties of disordered plasmonic metamaterials", *SPIE Photonics Europe*, Brussels, Belgium, 16 - 19 Apr 2012.

poster E. T. F. Rogers, T. Roy, T. S. Kao, J. Y. Ou, V. Savinov, S. Savo, J. Lindberg, M. R. Dennis and N. I. Zheludev, "The super-oscillating superlens", *Nanometa 2011*, Seefeld, Austria, 3 – 6 January 2011.

C.4 Awards and Honours

- EPSRC Doctoral Prize Fellowship, 2014.
- HIGHLIGHTS of 2013. "A meta-diffraction-grating for visible light" *Journal of Optics*, 15, 08510 (2013).
- The Best-Student-Presentation award. "The super-oscillating superlens", *Nanometa 2011*, Seefeld, Austria, 3 – 6 January 2011.

C.5 Media Coverage

- A meta-diffraction-grating for visible light, europhysicsnews Highlights, Vol 44, No.5, Oct 2013
- Beyond the limit, Nature Photonics, May 2012
- Superoscillatory lens captures evanescent waves for super images, ars technia, Scientific method, April 2012
- Findings from university of Southampton in materials science reported, High-Beam Research, May 2012

References

[1] Nobelprize.org. "Microscopes Time Line", 2014.

[2] Stefan W Hell. "Toward fluorescence nanoscopy.". *Nature Biotechnology*, 21(11):1347–55, 2003.

[3] Lothar Schermelleh, Rainer Heintzmann, and Heinrich Leonhardt. "A guide to super-resolution fluorescence microscopy". *The Journal of Cell Biology*, 190(2):165–175, 2010.

[4] Diane S. Lidke and Keith A. Lidke. "Advances in high-resolution imaging techniques for three-dimensional imaging of cellular structures". *Journal of Cell Science*, 125(11):2571–2580, 2012.

[5] Richard P. Feynman. "There's Plenty of Room at the Bottom". *Engineering and Science*, 23:5, 1960.

[6] Nikolay I Zheludev. "What diffraction limit?". *Nature Materials*, 7(6):420–2, 2008.

[7] Ariel Lipson, Stephen G Lipson, and Henry Lipson. *Optical Physics*. Cambridge University Press, 2010.

[8] Eugene Hecht. *Optics*. Addison Wesley, San Fransisco, CA, 4^{th} edition, 2002.

[9] Heinrich G. Frey, Fritz Keilmann, Armin Kriele, and Reinhard Guckenberger. "Enhancing the resolution of scanning near-field optical microscopy by a metal tip grown on an aperture probe". *Applied Physics Letters*, 81(26):5030, 2002.

[10] Richard D. Schaller, Preston T. Snee, Justin C. Johnson, Lynn F. Lee, Kevin R. Wilson, Louis H. Haber, Richard J. Saykally, Thuc-Quyen Nguyen, and Benjamin J. Schwartz. "Nanoscopic interchain aggregate domain formation in conjugated polymer films studied by third harmonic generation near-field scanning optical microscopy". *The Journal of Chemical Physics*, 117(14):6688, 2002.

[11] O. Sqalli, I. Utke, P. Hoffmann, and F. Marquis-Weible. "Gold elliptical nanoantennas as probes for near field optical microscopy". *Journal of Applied Physics*, 92(2):1078, 2002.

[12] Bjorn T. Rosner and Daniel W. van der Weide. "High-frequency near-field microscopy". *Review of Scientific Instruments*, 73(7):2505, 2002.

[13] R Hillenbrand and F Keilmann. "Material-specific mapping of metal semiconductor dielectric nanosystems at 10 nm resolution by backscattering near-field optical microscopy". *Applied Physics Letters*, 80(1):25, 2002.

[14] N. Landraud, J. Peretti, F. Chaput, G. Lampel, J.-P. Boilot, K. Lahlil, and V. I. Safarov. "Near-field optical patterning on azo-hybrid sol-gel films". *Applied Physics Letters*, 79(27):4562, 2001.

[15] A. Frass and P. Hess. "Excitation of elastic surface pulses by fiber optics and near-field optical devices". *Journal of Applied Physics*, 90(10):5090, 2001.

[16] A. Lewis, M. Isaacson, A. Harootunian, and A. Muray. "Development of a 500Åspatial resolution light microscope: I. light is efficiently transmitted through $\lambda/16$ diameter apertures". *Ultramicroscopy*, 13(3):227 – 231, 1984.

[17] D. W. Pohl, W. Denk, and M. Lanz. "Optical stethoscopy: Image recording with resolution $\lambda/20$". *Applied Physics Letters*, 44(7):651, 1984.

[18] E. Betzig, J. K. Trautman, T. D. Harris, J. S. Weiner, and R. L. Kostelak. "Breaking the Diffraction Barrier: Optical Microscopy on a Nanometric Scale". *Science*, 251(5000):1468–1470, 1991.

[19] John Wessel. "Surface-enhanced optical microscopy". *J. Opt. Soc. Am. B*, 2(9):1538–1541, 1985.

[20] S Patane, G P Gucciardi, M Labardi, and M Allegrini. "Apertureless near-field optical microscopy". *Rivista Nuovo Cimento*, 27(1):1–46, 2004.

[21] Alpan Bek, Ralf Vogelgesang, and Klaus Kern. "Apertureless scanning near field optical microscope with sub-10nm resolution". *Review of Scientific Instruments*, 77(4):043703, 2006.

[22] Eric Betzig, George H Patterson, Rachid Sougrat, O Wolf Lindwasser, Scott Olenych, Juan S Bonifacino, Michael W Davidson, Jennifer Lippincott-Schwartz, and Harald F Hess. "Imaging intracellular fluorescent proteins at nanometer resolution.". *Science (New York, N.Y.)*, 313(5793):1642–5, 2006.

[23] Mats G. L. Gustafsson, David A. Agard, and John W. Sedat. "Doubling the lateral resolution of wide-field fluorescence microscopy using structured illumination". *SPIE Proceedings*, 3919:141–150, 2000.

[24] Mats G L Gustafsson. "Nonlinear structured-illumination microscopy: wide-field fluorescence imaging with theoretically unlimited resolution.". *Proceedings of the National Academy of Sciences of the United States of America*, 102(37):13081–6, 2005.

[25] J.B. Pendry. "Negative refraction makes a perfect lens". *Physical Review Letters*, 85(18):3966–9, 2000.

[26] N Fang, H Lee, C Sun, and X Zhang. "Sub-Diffraction-Limited Optical Imaging with a Silver Superlens". *Science*, 308(5721):534–537, 2005.

[27] Zubin Jacob, Leonid V Alekseyev, and Evgenii Narimanov. "Optical Hyperlens: Far-field imaging beyond the diffraction limit.". *Optics Express*, 14(18):8247–56, 2006.

[28] G Toraldo Di Francia. "Super-Gain Antennas and Optical Resolving Power". *Il Nuovo Cimento*, 9(3), 1952.

[29] S. A. Schelkunoff. "A Mathematical Theory of Linear Arrays". *Bell System Technical Journal*, 22(1):80–107, 1943.

[30] A. M H Wong and G.V. Eleftheriades. "Adaptation of Schelkunoff's Superdirective Antenna Theory for the Realization of Superoscillatory Antenna Arrays". *Antennas and Wireless Propagation Letters, IEEE*, 9:315–318, 2010.

[31] A. M H Wong and G.V. Eleftheriades. "Sub-Wavelength Focusing at the Multi-Wavelength Range Using Superoscillations: An Experimental Demonstration". *Antennas and Propagation, IEEE Transactions on*, 59(12):4766–4776, 2011.

[32] A Kempf. "Black holes, bandwidths and Beethoven". *Journal of Mathematical Physics*, 41(4):2360, 2000.

[33] M V Berry and S Popescu. "Evolution of quantum superoscillations and optical superresolution without evanescent waves". *Journal of Physics A: Mathematical and General*, 39(22):6965–6977, 2006.

[34] P.J.S.G. Ferreira and A. Kempf. "Superoscillations: Faster Than the Nyquist Rate". *Trans. Sig. Proc.*, 54(10):3732–3740, 2006.

[35] E T F Rogers and N I Zheludev. "Optical super-oscillations: sub-wavelength light focusing and super-resolution imaging". *Journal of Optics*, 15(9):094008, 2013.

[36] M V Berry and M R Dennis. "Natural superoscillations in monochromatic waves in D dimensions". *Journal of Physics A: Mathematical and Theoretical*, 42(2):022003, 2009.

[37] Mark R Dennis, Alasdair C Hamilton, and Johannes Courtial. "Superoscillation in speckle patterns.". *Optics letters*, 33(24):2976–8, 2008.

[38] Fu Min Huang, Nikolay Zheludev, Yifang Chen, and F. Javier Garcia de Abajo. "Focusing of light by a nanohole array". *Applied Physics Letters*, 90(9):091119, 2007.

[39] J Baumgartl, S Kosmeier, M Mazilu, E T F Rogers, N I Zheludev, and K Dholakia. "Far field subwavelength focusing using optical eigenmodes". *Applied Physics Letters*, 98(18):181109, 2011.

[40] S Kosmeier, M Mazilu, J Baumgartl, and K Dholakia. "Enhanced two-point resolution using optical eigenmode optimized pupil functions". *Journal of Optics*, 13(10):105707, 2011.

[41] Tapashree Roy, Andrey E Nikolaenko, and Edward T F Rogers. "A meta-diffraction-grating for visible light". *Journal of Optics*, 15(8):085101, 2013.

[42] F M Huang and N I Zheludev. "Super-resolution without evanescent waves.". *Nano Letters*, 9(3):1249–54, 2009.

[43] Joseph W Goodman. *Introduction to Fourier Optics*. Roberts & Company Publishers, 3rd revised editions edition, 2005.

[44] M Mazilu, J Baumgartl, S Kosmeier, and K Dholakia. "Optical eigenmodes; exploiting the quadratic nature of the energy flux and of scattering interactions.". *Optics Express*, 19(2):933–45, 2011.

[45] K Piché, J Leach, A. S. Johnson, J. Z. Salvail, M. I. Kolobov, and R. W. Boyd. "Experimental realization of optical eigenmode super-resolution". *Optics Express*, 20:26424–26433, 2012.

[46] A M H Wong and G V Eleftheriades. "An optical super-microscope for far-field, real-time imaging beyond the diffraction limit.". *Scientific Reports*, 3:1715, 2013.

[47] R K Amineh and G V Eleftheriades. "2D and 3D sub-diffraction source imaging with a superoscillatory filter.". *Optics Express*, 21(7):8142–56, 2013.

[48] Fu Min Huang, Yifang Chen, F Javier Garcia de Abajo, and Nikolay I Zheludev. "Optical super-resolution through super-oscillations". *Journal of Optics A: Pure and Applied Optics*, 9(9):S285–S288, 2007.

[49] V Savinov. "Subwavelength focusing of light by nanohole array". Masters thesis, University of Southampton, 2010.

[50] V G Veselago. "The electrodynamics of substances with simultaneously negative values of ϵ and μ". *Soviet Physics Uspekhi*, 10(4):509, 1968.

[51] D R Smith, W J Padilla, D C Vier, S C Nemat-Nasser, and S Schultz. "Composite medium with simultaneously negative permeability and permittivity". *Physical Review Letters*, 84(18):4184–7, 2000.

[52] Zhengyou Liu, Xixiang Zhang, Yiwei Mao, Y. Y. Zhu, Zhiyu Yang, C. T. Chan, and Ping Sheng. "Locally Resonant Sonic Materials". *Science*, 289(5485):1734–1736, 2000.

[53] Jensen Li and C. T. Chan. "Double-negative acoustic metamaterial". *Phys. Rev. E*, 70:055602, 2004.

[54] Shu Zhang, Leilei Yin, and Nicholas Fang. "Focusing Ultrasound with an Acoustic Metamaterial Network". *Phys. Rev. Lett.*, 102:194301, 2009.

[55] J.B. Pendry, a.J. Holden, D.J. Robbins, and W.J. Stewart. "Magnetism from conductors and enhanced nonlinear phenomena". *IEEE Transactions on Microwave Theory and Techniques*, 47(11):2075–2084, 1999.

[56] A Schuster. *An introduction of the theory of optics.* Edward Arnold, London, 1904.

[57] E Plum, V A Fedotov, and N I Zheludev. "Optical activity in extrinsically chiral metamaterial". *Applied Physics Letters*, 93(19):191911, 2008.

[58] N. Papasimakis, V. Fedotov, N. Zheludev, and S. Prosvirnin. "Metamaterial Analog of Electromagnetically Induced Transparency". *Physical Review Letters*, 101(25):253903, 2008.

[59] D Schurig, J J Mock, B J Justice, S a Cummer, J B Pendry, a F Starr, and D R Smith. "Metamaterial electromagnetic cloak at microwave frequencies.". *Science (New York, N.Y.)*, 314(5801):977–80, 2006.

[60] Jason Valentine, Jensen Li, Thomas Zentgraf, Guy Bartal, and Xiang Zhang. "An optical cloak made of dielectrics.". *Nature Materials*, 8(7):568–71, 2009.

[61] Anthony Grbic and George Eleftheriades. "Overcoming the Diffraction Limit with a Planar Left-Handed Transmission-Line Lens". *Physical Review Letters*, 92(11):117403, 2004.

[62] Zhaowei Liu, Hyesog Lee, Yi Xiong, Cheng Sun, and Xiang Zhang. "Far-Field Optical Hyperlens Magnifying". *Science*, 315, 2007.

[63] Jagadis Chunder Bose. "On the Rotation of Plane of Polarisation of Electric Waves by a Twisted Structure". *Proceedings of the Royal Society of London*, 63:146–152, 1898.

[64] Jagadis Chunder Bose. "On the selective conductivity exhibited by some polarising substances". *Proceedings of the Royal Society of London*, 60:433, 1896.

[65] D T Emerson. "The work of Jagadis Chandra Bose: 100 years of mm-wave research". In *Microwave Symposium Digest, 1997., IEEE MTT-S International*, volume 2, pages 553–556 vol.2, 1997.

[66] Jianfa Zhang, Kevin F. MacDonald, and Nikolay I. Zheludev. "Near-infrared trapped mode magnetic resonance in an all-dielectric metamaterial". *Optics Express*, 21(22):26721–26728, 2013.

[67] Gennady Shvets, Chihhui Wu, NIhal Arju, Glen Kelp, Burton Neuner, Gregory Ten Eyck, Michael B. Sinclair, and Igal Brener. "All-Dielectric Metamaterials: Path to Low Losses and High Spectral Selectivity". In *CLEO: 2013*, page QW1P.2. Optical Society of America, 2013.

[68] Parikshit Moitra, Yuanmu Yang, Zachary Anderson, Ivan I. Kravchenko, Dayrl P. Briggs, and Jason Valentine. "Realization of an all-dielectric zero-index optical metamaterial". *Nature Photonics*, 7, 2013.

[69] E. Plum, J. Zhou, J. Dong, V. Fedotov, T. Koschny, C. Soukoulis, and N. Zheludev. "Metamaterial with negative index due to chirality". *Physical Review B*, 79(3):035407, 2009.

[70] S. A. Maier. *Plasmonics: fundamentals and applications*. Springer, 2007.

[71] Lukas Novotny and Bert Hecht. *Principles of Nano-Optics*. Cambridge University Press, 2006.

[72] Carsten Rockstuhl, Falk Lederer, Christoph Etrich, Thomas Zentgraf, Jürgen Kuhl, and Harald Giessen. "On the reinterpretation of resonances in split-ring-resonators at normal incidence". *Optics Express*, 14(19):8827–8836, 2006.

[73] Stephan Link and Mostafa A. El-Sayed. "Optical properties and ultrafast dynamics ofmetallic nanocrystals". *Annu. Rev. Phys. Chem*, 54:33166, 2003.

[74] Jon A. Schuller, Edward S. Barnard, Wenshan Cai, Young Chul Jun, Justin S. White, and Mark L. Brongersma. "Plasmonics for extreme light concentration and manipulation". *Nature Materials*, 9, 2010.

[75] Julia M. Bingham, Jeffrey N. Anker, Lauren E. Kreno, and Richard P. Van Duyne. "Gas Sensing with High-Resolution Localized Surface Plasmon Resonance Spectroscopy". *Journal of the American Chemical Society*, 132(49):17358–17359, 2010.

[76] Shunping Zhang, Kui Bao, Naomi J. Halas, Hongxing Xu, and Peter Nordlander. "Substrate-Induced Fano Resonances of a Plasmonic Nanocube: A Route to Increased-Sensitivity Localized Surface Plasmon Resonance Sensors Revealed". *Nano Letters*, 11(4):1657–1663, 2011.

[77] Julia A. Ruemmele, W. Paige Hall, Laura K. Ruvuna, and Richard P. Van Duyne. "A Localized Surface Plasmon Resonance Imaging Instrument for Multiplexed Biosensing". *Analytical Chemistry*, 85(9):4560–4566, 2013.

[78] Linfang Qiao, Dan Wang, Lijian Zuo, Yuqian Ye, Jun Qian, Hongzheng Chen, and Sailing He. "Localized surface plasmon resonance enhanced organic solar cell with gold nanospheres". *Applied Energy*, 88(3):848 – 852, 2011.

[79] Xiangnan Dang, Jifa Qi, Matthew T. Klug, Po-Yen Chen, Dong Soo Yun, Nicholas X. Fang, Paula T. Hammond, and Angela M. Belcher. "Tunable Localized Surface Plasmon-Enabled Broadband Light-Harvesting Enhancement for High-Efficiency Panchromatic Dye-Sensitized Solar Cells". *Nano Letters*, 13(2):637–642, 2013.

[80] Xiao-Yu Wang, Jin-Liang Wang, and Hai Wang. "Improvement of the efficiency and power output of solar cells using nanoparticles and annealing". *Solar Energy*, 101(0):100 – 104, 2014.

[81] G. A. Wurtz, R. Pollard, W. Hendren, G. P. Wiederrecht, D. J. Gosztola, V. A. Podolskiy, and A. V. Zayats. "Designed ultrafast optical nonlinearity in a plasmonic nanorod metamaterial enhanced by nonlocality". *Nature Nanotechnology*, 6, 2011.

[82] Martti Kauranen and Anatoly V. Zayats. "Nonlinear plasmonics". *Natue Photonics*, 6, 2012.

[83] Pter Dombi, Anton Hrl, Pter Rcz, Istvn Mrton, Andreas Trgler, Joachim R. Krenn, and Ulrich Hohenester. "Ultrafast Strong-Field Photoemission from Plasmonic Nanoparticles". *Nano Letters*, 13(2):674–678, 2013.

[84] Xu Fang, Ming Lun Tseng, Jun-Yu Ou, Kevin F. MacDonald, Din Ping Tsai, and Nikolay I. Zheludev. "Ultrafast all-optical switching via coherent modulation of metamaterial absorption". *Applied Physics Letters*, 104(14):–, 2014.

[85] Chia-Yun Chen, Shich-Chuan Wu, and Ta-Jen Yen. "Experimental verification of standing-wave plasmonic resonances in split-ring resonators". *Applied Physics Letters*, 93(3):–, 2008.

[86] skullsinthestars. "Rolling out the (optical) carpet: the Talbot effect". *http://skullsinthestars.com/2010/03/04/rolling-out-the-optical-carpet-the-talbot-effect/*, 2010.

[87] H. F. Talbot. "Facts relating to optical science. no. IV". *Philosophical Magazine Series 3*, 9:401–407, 1836.

[88] Lord Rayleigh. "XXV. On copying diffraction-gratings, and on some phenomena connected therewith". *Philosophical Magazine Series 5*, 11(67):196–205, 1881.

[89] E. A. Heidemann and M. A. Breazeale. "Secondary interference in the Fresnel zone of gratings". *J. Opt. Soc. Am.*, 49:372–375, 1959.

[90] J T Winthrop and C R Worthington. "Theory of Fresnel Images . I . Plane Periodic Objects in Monochromatic Light ". *Journal of the Optical Society of America*, 55(4), 1965.

[91] M. V. Berry and S. Klein. "Interger, fractional, and fractal Talbot effects". *Journal of Modern Optics*, 43(10):2139–2164, 1996.

[92] J D Mills, C W Hillman, B H Blott, and W S Brocklesby. "Imaging of free-space interference patterns used to manufacture fiber bragg gratings.". *Applied optics*, 39(33):6128–35, 2000.

[93] Yi Hua, Jae Yong Suh, Wei Zhou, Mark D Huntington, and Teri W Odom. "Talbot effect beyond the paraxial limit at optical frequencies.". *Optics Express*, 20(13):14284–91, 2012.

[94] Mark R Dennis, Nikolay I Zheludev, and F Javier García de Abajo. "The plasmon Talbot effect.". *Optics Express*, 15(15):9692–700, 2007.

[95] Weiwei Zhang, Chenlong Zhao, Jiayuan Wang, and Jiasen Zhang. "An experimental study of the plasmonic Talbot effect.". *Optics Express*, 17(22):19757–62, 2009.

[96] Myun-Sik Kim, Toralf Scharf, Christoph Menzel, Carsten Rockstuhl, and Hans Peter Herzig. "Talbot images of wavelength-scale amplitude gratings.". *Optics Express*, 20(5):4903–20, 2012.

[97] Xiang Zhang and Zhaowei Liu. "Superlenses to overcome the diffraction limit.". *Nature Materials*, 7(6):435–41, 2008.

[98] Ju Young Lee, Byung Hee Hong, Woo Youn Kim, Seung Kyu Min, Yukyung Kim, Mikhail V. Jouravlev, Ranojoy Bose, Keun Soo Kim, In-Chul Hwang, Laura J. Kaufman, Chee Wei Wong, Philip Kim, and Kwang S. Kim. "Near-field focusing and magnification through self-assembled nanoscale spherical lenses". *Nature*, 460(7254):498–501, 2009.

[99] Junsuk Rho, Ziliang Ye, Yi Xiong, Xiaobo Yin, Zhaowei Liu, Hyeunseok Choi, Guy Bartal, and Xiang Zhang. "Spherical hyperlens for two-dimensional sub-diffractional imaging at visible frequencies.". *Nature Communications*, 1:143, 2010.

[100] Igor I Smolyaninov, Yu-Ju Hung, and Christopher C Davis. "Magnifying superlens in the visible frequency range.". *Science (New York, N.Y.)*, 315(5819):1699–701, 2007.

[101] Zengbo Wang, Wei Guo, Lin Li, Boris Luk'yanchuk, Ashfaq Khan, Zhu Liu, Zaichun Chen, and Minghui Hong. "Optical virtual imaging at 50 nm lateral resolution with a white-light nanoscope.". *Nature Communications*, 2:218, 2011.

[102] F M Huang, T S Kao, V A Fedotov, Y Chen, and N I Zheludev. "Nanohole array as a lens.". *Nano Letters*, 8(8):2469–72, 2008.

[103] Snir Gazit, Alexander Szameit, Yonina C. Eldar, and Mordechai Segev. "Super-resolution and reconstruction of sparse sub-wavelength images". *Optics Express*, 17(26):23920–23946, 2009.

[104] E T F Rogers, J Lindberg, T Roy, S Savo, J E Chad, M R Dennis, and N I Zheludev. "A super-oscillatory lens optical microscope for subwavelength imaging.". *Nature Materials*, 11(5):432–5, 2012.

[105] Tapashree Roy, Edward T F Rogers, and Nikolay I Zheludev. "Sub-wavelength focusing meta-lens.". *Optics Express*, 21(6):7577–82, 2013.

[106] E T F Rogers, S Savo, J Lindberg, T Roy, M R Dennis, and N I Zheludev. "Super-oscillatory optical needle". *Applied Physics Letters*, 102(3):031108, 2013.

[107] Nanbo Jin and Yahya Rahmat-Samii. "Advances in Particle Swarm Optimization for Antenna Designs: Real-Number, Binary, Single-Objective and Multiobjective Implementations". *IEEE Transactions on Antennas and Propagation*, 55:556–567, 2007.

[108] Z S Hegedus and V Sarafis. "Superresolving filters in confocally scanned imaging systems". *JOSA A*, 3(11):1892–1896, 1986.

[109] Haifeng Wang, Luping Shi, Boris Lukyanchuk, Colin Sheppard, and Chong Tow Chong. "Creation of a needle of longitudinally polarized light in vacuum using binary optics". *Nature Photonics*, 2(8):501–505, 2008.

[110] Kenneth R Spring and Michael W Davidson. "Nikon Microscopy U". *http://www.microscopyu.com/articles/formulas/formulasfielddepth.html*, 2013.

[111] A J Fresnel. *OEuvres Completes d' Augustin Fresnel*. Imprimerie imperiale, 1866.

[112] E Hetch. *Optics*. Addison-Wesley, 4^{th} edition, 2002.

[113] G B Airy. "On the diffraction of an object-glass with circular aperture". *Transaction of the Cambridge Philosophical Society*, 5:283–291, 1835.

[114] J Lindberg. "Mathematical concepts of optical superresolution". *Journal of Optics*, 14(8):083001, 2012.

[115] Z S Hegedus. "Annular Pupil Arrays". *Optica Acta: International Journal of Optics*, 32(7):815–826, 1985.

[116] M Bertero, P Boccacci, R E Davies, F Malfanti, E R Pike, and J G Walker. "Super-resolution in confocal scanning microscopy: IV. Theory of data inversion by the use of optical masks". *Inverse Problems*, 8(1):1, 1992.

[117] M M Corral, P Andres, J O Castaneda, and G Saavedra. "Tunable axial superresolution by annular binary filters. Application to confocal microscopy". *Optics Communications*, 119(56):491 – 498, 1995.

[118] M M Corral, P Andres, C J Z Rodrigues, and C J R Sheppard. "Improvement of three-dimensional resolution in confocal scanning microscopy by combination of two pupil filter". *Optik*, 107(4):145–148, 1998.

[119] S K Khizroev, M H Kryder, Y Ikeda, K Rubin, P Arnett, M Best, and D A Thompson. "Recording heads with track widths suitable for 100 Gbit/in^2 density". *Magnetics, IEEE Transactions on*, 35(5):2544–2546, 1999.

[120] Barry C. Stipe, Timothy C. Strand, Chie C. Poon, Hamid Balamane, Thomas D. Boone, Jordan A. Katine, Jui-Lung Li, Vijay Rawat, Hiroaki Nemoto, Akemi Hirotsune, Olav Hellwig, Ricardo Ruiz, Elizabeth Dobisz, Dan S. Kercher, Neil Robertson, Albrecht Thomas R., and Bruce D. Terris. "Magnetic recording at 1.5 Pb m2 using an integrated plasmonic antenna". *Nature Photonics*, 4:484 – 488, 2010.

[121] Seagate. "Seagate Reaches 1 Terabit Per Square Inch Milestone In Hard Drive Storage With New Technology Demonstration". *News Room, Press Releases*, 2012.

[122] Mark H Kryder, Edward C Gage, Terry W Mcdaniel, William A Challener, Robert E Rottmayer, Ganping Ju, Yiao-tee Hsia, and M Fatih Erden. "Heat Assisted Magnetic Recording". *Proceedings of the IEEE*, 96(11), 2008.

[123] W A Challener, Chubing Peng, A V Itagi, D Karns, Wei Peng, Yingguo Peng, Xiaomin Yang, Xiaobin Zhu, N J Gokemeijer, Y Hsia, G Ju, Robert E Rottmayer, Michael A Seigler, and E C Gage. "Heat-assisted magnetic recording by a near-field transducer with efficient optical energy transfer". *Nature Photonics*, 3(April), 2009.

[124] Phan Ngoc Minh, Takahito Ono, and Masayoshi Esashi. "High throughput aperture near-field scanning optical microscopy". *Review of Scientific Instruments*, 71(8):3111, 2000.

[125] Bo Huang, Wenqin Wang, Mark Bates, and Xiaowei Zhuang. "Three-dimensional super-resolution imaging by stochastic optical reconstruction microscopy.". *Science (New York, N.Y.)*, 319(5864):810–3, 2008.

[126] Elad Greenfield, Ran Schley, Ilan Hurwitz, Jonathan Nemirovsky, Konstantinos G. Makris, and Mordechai Segev. "Experimental generation of arbitrarily shaped diffractionless superoscillatory optical beams". *Optics Express*, 21(11):13425–13435, 2013.

[127] Guanghui Yuan, Edward T F Rogers, Tapashree Roy, Zexiang Shen, and Nikolay I Zheludev. "Flat Super-oscillatory Lens for Heat-Assisted Magnetic Recording with sub-50nm Resolution". *Optics Express*, 22:64286437, 2014.

[128] S. M. Mansfield and G. S. Kino. "Solid immersion microscope". *Applied Physics Letters*, 57(24):2615–2616, 1990.

[129] D. E. Aspnes and A. A. Studna. "Dielectric functions and optical parameters of Si, Ge, GaP, GaAs, GaSb, InP, InAs, and InSb from 1.5 to 6.0 eV". *Phys. Rev. B*, 27:985–1009, 1983.

[130] J. R. Devore. "Refractive Indices of Rutile and Sphalerite". *J. Opt. Soc. Am.*, 41(6):416–417, 1951.

[131] M Bass, C DeCusatis, J Enoch, V Lakshminarayanan, G Li, C MacDonald, V Mahajan, and E. V. Stryland. *Handbook of Optics*, volume 4. McGraw Hill Professional, 3 edition, 2009.

[132] S. A. Sopra. "Optical Data from Sopra SA", 2008.

[133] Materion.com. "BrochuresAndDataSheets/AZO transparent conductive coating", 2008.

[134] Qiang Wu, G.D. Feke, Robert D. Grober, and L.P. Ghislain. "Realization of numerical aperture 2.0 using a gallium phosphide solid immersion lens". *Applied Physics Letters*, 75(26):4064–4066, 1999.

[135] Djenan Ganic, Xiaosong Gan, and Min Gu. "Focusing of doughnut laser beams by a high numerical-aperture objective in free space". *Optics Express*, 11(21):2747–2752, 2003.

[136] Shipley. "Data sheet: Microposit S1800 G2 series photoresists".

[137] G. J. Fang, D. J. Li, and B. L. Yao. "Effect of Vacuum Annealing on the Properties of Transparent Conductive AZO Thin Films Prepared by DC Magnetron Sputtering". *Phys. Stat. Sol. (a)*, 193(1):139152, 2002.

[138] Jianfa Zhang, Kevin F MacDonald, and Nikolay I Zheludev. "Controlling light-with-light without nonlinearity". *Light: Science & Applications*, 1(7):e18, 2012.

[139] A. Papakostas, A. Potts, D. Bagnall, S. Prosvirnin, H. Coles, and N. Zheludev. "Optical Manifestations of Planar Chirality". *Physical Review Letters*, 90(10):107404, 2003.

[140] S. Prosvirnin and N. Zheludev. "Polarization effects in the diffraction of light by a planar chiral structure". *Physical Review E*, 71(3):037603, 2005.

[141] B. Walther, C. Helgert, C. Rockstuhl, and T. Pertsch. "Diffractive optical elements based on plasmonic metamaterials". *Applied Physics Letters*, 98(19):191101, 2011.

[142] Benny Walther, Christian Helgert, Carsten Rockstuhl, Frank Setzpfandt, Falk Eilenberger, Ernst-Bernhard Kley, Falk Lederer, Andreas Tünnermann, and Thomas Pertsch. "Spatial and spectral light shaping with metamaterials.". *Advanced Materials (Deerfield Beach, Fla.)*, 24(47):6300–4, 2012.

[143] Jean-Philippe Tetienne Nanfang Yu, Patrice Genevet, Mikhail A. Kats, Francesco Aieta and Zeno Gaburro Federico Capasso. "Light Propagation with Phase Reflection and Refraction". *Science*, 334:333–337, 2011.

[144] Yu-ju Tsai, Talmage Tyler, Guy Lipworth, Nan M Jokerst, and David R Smith. "Design and fabrication of a metamaterial gradient index diffraction grating at Abstract". *Optics Express*, 19(24):5156–5162, 2011.

[145] Xingjie Ni, Naresh K Emani, Alexander V Kildishev, Alexandra Boltasseva, and Vladimir M Shalaev. "Broadband light bending with plasmonic nanoantennas.". *Science (New York, N.Y.)*, 335(6067):427, 2012.

[146] Francesco Aieta, Patrice Genevet, Mikhail a Kats, Nanfang Yu, Romain Blanchard, Zeno Gaburro, and Federico Capasso. "Aberration-free ultrathin flat lenses and axicons at telecom wavelengths based on plasmonic metasurfaces.". *Nano Letters*, 12(9):4932–6, 2012.

[147] A. I. Ena, L. N. Litvinenko, and V. P. Shestopalov. "Diffraction properties of nonsymmetrical metal strip arrays". *Radiophysics and Quantum Electronics*, 11(1):62–68, 1968.

[148] N. Papasimakis, Y. H. Fu, V. a. Fedotov, S. L. Prosvirnin, D. P. Tsai, and N. I. Zheludev. "Metamaterial with polarization and direction insensitive resonant transmission response mimicking electromagnetically induced transparency". *Applied Physics Letters*, 94(21):211902, 2009.

[149] N. Papasimakis, V. Fedotov, Y. H. Fu, D. P. Tsai, and N. Zheludev. "Coherent and incoherent metamaterials and order-disorder transitions". *Physical Review B*, 80:041102, 2009.

[150] Sergey L Prosvirnin and Nikolay I Zheludev. "Analysis of polarization transformations by a planar chiral array of complex-shaped particles". *Journal of Optics A: Pure and Applied Optics*, 11(7):074002, 2009.

[151] Ming-Hsien Wu and George M. Whitesides. "Fabrication of arrays of two-dimensional micropatterns using microspheres as lenses for projection photolithography". *Applied Physics Letters*, 78(16):2273, 2001.

[152] E Plum, K Tanaka, W T Chen, V a Fedotov, D P Tsai, and N I Zheludev. "A combinatorial approach to metamaterials discovery". *Journal of Optics*, 13(5):055102, 2011.

[153] International Union of Pure and Applied Chemistry. *Compendium of Chemical Terminology: Gold Book*. International Union of Pure and Applied Chemistry, 2014.

[154] John Frederick William Herschel. "On a Case of Superficial Colour Presented by a Homogeneous Liquid Internally Colourless". *Philosophical Transactions of the Royal Society of London*, 135:143–145, 1845.

[155] Joseph R. Lakowicz. *Principles of fluorescence spectroscopy*. Springer, 2006.

[156] Maria Goeppert-Mayer. *Uber Elementarakte mit zwei Quantensprungen*. PhD thesis, University of Gottingen, Germany, 1931.

[157] W. Kaiser and C. G. B. Garrett. "Two-Photon Excitation in $CaF^2 : Eu^{2+}$". *Phys. Rev. Lett.*, 7:229–231, 1961.

[158] T. H. Maiman. "Stimulated optical radiation in ruby". *Nature*, 187(4736), 1960.

[159] A Mooradian. "Photoluminescence of Metals". *Physical Review Letters*, 22(5):5–7, 1969.

[160] G. T. Boyd, Z. H. Yu, and Y. R. Shen. "Photoinduced luminescence from the noble metals and its enhancement on roughened surfaces". *Phys. Rev. B*, 33:7923–7936, 1986.

[161] Michael Beversluis, Alexandre Bouhelier, and Lukas Novotny. "Continuum generation from single gold nanostructures through near-field mediated intraband transitions". *Physical Review B*, 68(11):115433, 2003.

[162] Alexandre Bouhelier, Michael R. Beversluis, and Lukas Novotny. "Characterization of nanoplasmonic structures by locally excited photoluminescence". *Applied Physics Letters*, 83(24):5041, 2003.

[163] Kohei Imura, Tetsuhiko Nagahara, and Hiromi Okamoto. "Photoluminescence from gold nanoplates induced by near-field two-photon absorption". *Applied Physics Letters*, 88(2):023104, 2006.

[164] Da-Shin Wang, Fu-Yin Hsu, and Chii-Wann Lin. "Surface plasmon effects on two photon luminescence of gold nanorods.". *Optics Express*, 17(14):11350–9, 2009.

[165] Jonas Beermann, Sergey M Novikov, Tobias Holmgaard, René L Eriksen, Ole Albrektsen, Kjeld Pedersen, and Sergey I Bozhevolnyi. "Polarization-resolved two-photon luminescence microscopy of V-groove arrays.". *Optics Express*, 20(1):654–62, 2012.

[166] Xiao-Fang Jiang, Yanlin Pan, Cuifeng Jiang, Tingting Zhao, Peiyan Yuan, T. Venkatesan, and Qing-Hua Xu. "Excitation Nature of Two-Photon Photoluminescence of Gold Nanorods and Coupled Gold Nanoparticles Studied by Two-Pulse Emission Modulation Spectroscopy". *The Journal of Physical Chemistry Letters*, 4(10):1634–1638, 2013.

[167] Wei Tao, Hongchun Bao, and Min Gu. "Two-photon-excited photoluminescence and heating of gold nanorods through absorption of supercontinuum light". *Applied Physics B*, 112(2):153–158, 2013.

[168] Tianyi Wang, David Halaney, Derek Ho, Marc D Feldman, and Thomas E Milner. "Two-photon luminescence properties of gold nanorods". *Biomedical Optics Express*, 4(4):584–595, 2013.

[169] Tingting Zhao, Xiaoqin Shen, Lin Li, Zhenping Guan, Nengyue Gao, Peiyan Yuan, Shao Q Yao, Qing-hua Xu, and Guo Qin Xu. "Gold nanorods as agents for two-photon photodynamic therapy". *Nanoscale*, pages 7712–7719, 2012.

[170] Coherent. “Chameleon Vision S The Next Generation of One-Box Ti:Sapphire Lasers”, 2012.

[171] G. G. Stokes. “On the Change of Refrangibility of Light”. *Royal Society of London Philosophical Transactions Series I*, 142:463–562, 1852.

[172] Robert W. Boyd. *Nonlinear Optics*. Academic Press, 2008.

[173] Jun Dai, Jian-hua Zeng, Sheng Lan, Xia Wan, and Shao-long Tie. “Competition between second harmonic generation and two-photon-induced luminescence in single , double and multiple ZnO nanorods”. *Optics Express*, 21(8):459–463, 2013.

[174] Delmar S Larsen, Mikas Vengris, Ivo H M van Stokkum, Michael a van der Horst, Frank L de Weerd, Klaas J Hellingwerf, and Rienk van Grondelle. “Photoisomerization and photoionization of the photoactive yellow protein chromophore in solution.”. *Biophysical Journal*, 86(4):2538–50, 2004.

[175] C H Wang, Oliver Y-H Tai, Yuxiao Wang, Tsung-Hsiu Tsai, and Nein-Chen Chang. “Non-quadratic-intensity dependence of two-photon absorption induced fluorescence of organic chromophores in solution.”. *The Journal of Chemical Physics*, 122(8):84509, 2005.

[176] Kevin D Belfield, Mykhailo V Bondar, Ciceron O Yanez, Florencio E Hernandez, and Olga V Przhonska. “One- and two-photon stimulated emission depletion of a sulfonyl-containing fluorene derivative.”. *The Journal of Physical Chemistry B*, 113(20):7101–6, 2009.

[177] Emmanouil Papagiannakis, Ivo H M van Stokkum, Mikas Vengris, Richard J Cogdell, Rienk van Grondelle, and Delmar S Larsen. “Excited-state dynamics of carotenoids in light-harvesting complexes. 1. Exploring the relationship between the S1 and S* states.”. *The Journal of Physical Chemistry B*, 110(11):5727–36, 2006.

[178] Odd Magnar Hole. “Development and application of measurement techniques for the detection of ammonia Measuring ammonia”. Master’s thesis, Department of Physics, University of Lund, Sweden, 2012.

[179] V A G Rivera, F A Ferri, and E Marega Jr. *Plasmonics - Principles and Applications*. InTech, 2012.

[180] Changwoo Nahm, Dae-Ryong Jung, Seunghoon Nam, Hongsik Choi, Saeromi Hong, Taehyun Hwang, Taeho Moon, and Byungwoo Park. "Photoluminescence Enhancement by Surface-Plasmon Resonance: Recombination-Rate Theory and Experiments". *Applied Physics Express*, 6(5):052001, 2013.

[181] Min Song, Gengxu Chen, Yan Liu, E Wu, Botao wu, and Heping Zeng. "Polarization properties of surface plasmon enhanced photoluminescence from a single Ag nanowire". *Optics Express*, 20(20):22290–22297, 2012.

[182] Yen Hsun Su, Sheng-Lung Tu, Shih-Wen Tseng, Yun-Chorng Chang, Shih-Hui Chang, and Wei-Min Zhang. "Influence of surface plasmon resonance on the emission intermittency of photoluminescence from gold nano-sea-urchins". *Nanoscale*, 2:2639–2646, 2010.

[183] Andrey E. Nikolaenko, Francesco De Angelis, Stuart A. Boden, Nikitas Papasimakis, Peter Ashburn, Enzo Di Fabrizio, and Nikolay I. Zheludev. "Carbon Nanotubes in a Photonic Metamaterial". *Phys. Rev. Lett.*, 104:153902, 2010.

[184] K. Tanaka, E. Plum, J. Y. Ou, T. Uchino, and N. I. Zheludev. "Multifold Enhancement of Quantum Dot Luminescence in Plasmonic Metamaterials". *Physical Review Letters*, 105(22):227403, 2010.

[185] Andrey E. Nikolaenko, Nikitas Papasimakis, Evangelos Atmatzakis, Zhiqiang Luo, Ze Xiang Shen, Francesco De Angelis, Stuart A. Boden, Enzo Di Fabrizio, and Nikolay I. Zheludev. "Nonlinear graphene metamaterial". *Applied Physics Letters*, 100(18):–, 2012.

[186] Mengxin Ren, Baohua Jia, Jun-Yu Ou, Eric Plum, Jianfa Zhang, Kevin F MacDonald, Andrey E Nikolaenko, Jingjun Xu, Min Gu, and Nikolay I Zheludev. "Nanostructured plasmonic medium for terahertz bandwidth all-optical switching.". *Advanced materials (Deerfield Beach, Fla.)*, 23(46):5540–4, 2011.

[187] Sergey Prosvirnin and Said Zouhdi. "Resonances of Closed Modes in Thin Arrays of Complex Particles". In Sad Zouhdi, Ari Sihvola, and Mohamed Arsalane,

editors, *Advances in Electromagnetics of Complex Media and Metamaterials*, volume 89 of *NATO Science Series*, pages 281–290. Springer Netherlands, 2002.

[188] Nikitas Papasimakis and Nikolay I. Zheludev. "Metamaterial-Induced Transparency:Sharp Fano Resonances and Slow Light". *Opt. Photon. News*, 20(10):22–27, 2009.

[189] Boris Luk'yanchuk, Nikolay I Zheludev, Stefan a Maier, Naomi J Halas, Peter Nordlander, Harald Giessen, and Chong Tow Chong. "The Fano resonance in plasmonic nanostructures and metamaterials.". *Nature Materials*, 9(9):707–15, 2010.

[190] M. I. Stockman. "Spasers explained". *Nature Photonics*, 2:327–329, 2008.

[191] E. Dulkeith, T. Niedereichholz, T. A. Klar, J. Feldmann, G. von Plessen, D. I. Gittins, K. S. Mayya, and F. Caruso. "Plasmon emission in photoexcited gold nanoparticles". *Phys. Rev. B*, 70:205424, 2004.

[192] T. V. Shahbazyan, I. E. Perakis, and J.-Y. Bigot. "Size-Dependent Surface Plasmon Dynamics in Metal Nanoparticles". *Phys. Rev. Lett.*, 81:3120–3123, 1998.

[193] Dhrubajyoti Basak, Santanu Karan, and Biswanath Mallik. "Size selective photoluminescence in poly(methyl methacrylate) thin solid films with dispersed silver nanoparticles synthesized by a novel method". *Chemical Physics Letters*, 420(13):115 – 119, 2006.

[194] J Zhang, K. F. MacDonald, and N. I. Zheludev. "Nonlinear dielectric optomechanical metamaterials". *Light: Science & Applications*, 2, 2013.

[195] Nathan C Lindquist, Prashant Nagpal, Kevin M McPeak, David J Norris, and Sang-Hyun Oh. "Engineering metallic nanostructures for plasmonics and nanophotonics". *Rep. Prog. Phys.*, 75:036501, 2012.

[196] FEI. "An introduction to electron microscopy", 2010.

[197] C. A. Volkert and A. M. Minor. "Focused Ion Beam Microscopy and Micromachining". *MRS Bulletin*, 32:389–399, 2007.

[198] Comsol AB. *Comsol Multiphysics User's Guide, version 3.5 a*, 2008.

[199] E. D. Palik, editor. *Handbook of Optical Constants of Solids.* Academic Press, Orlando, 1984.